UNIVERSITY OF BRISTOL

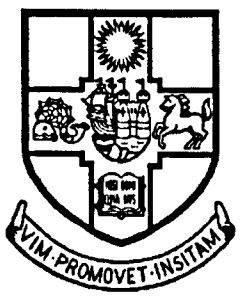

DEPARTMENT OF AEROSPACE ENGINEERING

Investigation of the Dynamic Wake of a Model Rotor

Thomas Jochen Ellenrieder B.Eng.

October 1995

A thesis submitted to the University of Bristol in accordance with the requirements of the degree of Doctor of Philosophy in the Faculty of Engineering

Abstract

In this study the dynamic induced velocity field of a model helicopter rotor - excited in collective and cyclic pitch at frequencies extending to 1.5 times the nominal shaft speed - is investigated using mainly hot-wire and laser Doppler anemometry.

The dynamic induced velocities are found to vary significantly with radial station and frequency. For cyclic excitations, azimuthal variations are also observed. The results point to the dynamic induced flow being influenced by the distribution of shed vorticity in the wake and cannot be explained using simple momentum theory. Vertical variations of the measured inflow response are also observed, with phase changes possibly partly due to transmission type delays. At frequencies above shaft speed a change in character of the induced flow is seen and around shaft speed an increase in the general level of turbulence is found. The available data on the dynamic induced velocity field of a rotor under controlled excitation, are substantially extended.

The measured induced flow response was compared to that predicted using the Pitt and Peters dynamic inflow model. In the 'collective' case good agreement was found, suggesting that the primary inflow model parameters such as the inflow gain and apparent mass are correct with some evidence that a higher order inflow representation might be desirable.

A novel method is used to infer the aerodynamic hub loading, which could not be directly measured, from the blade flapping data. This is used to isolate the inflow response using the Pitt and Peters dynamic inflow model and the results are compared with experimental measurements. The method shows the Pitt and Peters dynamic inflow representation to be adequate in the 'collective' case. In the 'cyclic' case, the inferred hub loads were very sensitive to the blade model and hence conclusions for this case are limited.

A literature survey and review of the Pitt and Peters dynamic inflow model are also given.

Dedication

Für Meine Eltern

Acknowledgements

I would like to express my sincere thanks to my Mr. P.R. Brinson for his many hours of advice, assistance and encouragement, whilst acting as adviser on this project.

Special thanks must also go to all the technicians in the Department of Aerospace Engineering; Alan Bishop, John Burns, Ken Crabtree, Tom Hawkins, Dick Harvey, Andy Kinsman, John Morrison, Steve McQueen, Phill Waller, Gordon Young and particularly to Keith Firks who spent many hours working on the rotor rig and provided many invaluable suggestions.

I would also like to thank Westland Helicopters plc, who sponsored this project as part of a CASE award in conjunction with the SERC, particularly David Tyler, Colin Massey and David Haddon. Further thanks also go to Gareth Padfield and Andy McCallum at the DRA for their helpful advice and interest in my work.

Declaration

The work presented herein was carried out solely by the author, under the supervision of Mr. P.R. Brinson, in the Department of Aerospace Engineering at the University of Bristol, in partial fulfilment of the requirements for the degree of Doctor of Philosophy.

The ideas and results are original except where otherwise acknowledged or referenced, and no part of this work has been submitted previously to any university, college or other institute.

Note that the views expressed in the dissertation are those of the author and are not necessarily those of the University of Bristol.

Thomas Jochen Ellenrieder

Permission to Copy

Thomas Jochen Ellenrieder

Investigation of the Dynamic Wake of a model Rotor

Adviser: Mr. P. R. Brinson

Department of Aerospace Engineering

University of Bristol

I, the undersigned, am willing that this thesis should be made available for consultation in Bristol University Library, for inter-library lending, for use in another library or for photocopy in part or in full - at the discretion of the Librarian - on the understanding that users are made aware of their obligations under copyright.

Thomas Jochen Ellenrieder

Table of Contents

List of Figures and Tables

List of Symbols

β	coning or blade flapping angle, positive upwards [rad]
β_0	tip path plane 'collective' degree of freedom
β_C	longitudinal tip path plane degree of freedom, positive nose side down
β_S	lateral tip path plane lateral degree of freedom, positive retreating side down
ε	normalised hinge offset, $\varepsilon = \frac{e}{R}$
γ	Lock number, $\gamma = \frac{\rho a c R^4}{I_\beta}$
$\eta(r)$	radial mode shape
θ_0	collective pitch perturbation [rad]
λ	non-dimensional inflow perturbation , $\lambda = \frac{v}{\Omega R}$
λ_0	non-dimensionalized 'collective' inflow degrees of freedom in the non-rotating frame
λ_C	non-dimensional fore-aft inflow degrees of freedom
λ_m	non-dimensional momentum induced velocity, $\lambda_m = \sqrt{\frac{C_T}{2}}$
λ_S	non-dimensional side-to-side inflow degrees of freedom
μ	advance ratio
v	inflow perturbation , positive downwards [m/s]
ρ	air density [kg/m^3]
σ	solidity, $\sigma = \frac{bc}{\pi R}$
ψ	azimuth angle, 0 over tail
Ω	rotor rotational speed, anti-clockwise from above [rad/s]
ΔAl	effective moment arm area ratio of a hydraulic motor [m^3]
ΔV	volumetric displacement [m^3/rad]
A	system matrix in state-space description of model
a	lift curve slope
B	state space model control matrix, or tip loss factor
b	number of blades
C^*	lift deficiency factor, (used in blade flapping equation), $C^* = \frac{1}{1+\frac{\pi\sigma}{4\lambda_m}}$
C_*	thrust deficiency factor (used in thrust equation), $C_* = \frac{1}{1+\frac{a\sigma}{16\lambda_m}}$
C_f	valve flow coefficient
C_L	coefficient of aerodynamic roll moment, positive more lift on retreating side (Pitt / Peters Model)
C_M	coefficient of aerodynamic pitch moment, positive more lift on nose side (Pitt / Peters Model)
C_{pitch}	coefficient of aerodynamic pitch moment, positive more lift on nose side
C_R	non-dimensional root cut out
C_{roll}	coefficient of aerodynamic roll moment, positive more lift on advancing side
C_T	thrust coefficient, $C_T = T/\rho(\pi R^2)(\Omega R)^2$

c blade chord [m]

d_v valve spool opening diameter [m]

e hinge offset [m]

F_z aerodynamic loading on a radial blade segment

f_R flap frequency ratio

I_β flapping moment of inertia [Kg m^2], $I_\beta = \int_e^R mr^2 dr$

J rotational inertia [Kg m^2]

K_β equivalent hinge spring stiffness [Nm/rad]

K_m, K_x valve flow gains

k reduced frequency, $\frac{f\frac{c}{2}}{\Omega r}$

L motor leakage [m^3/ N/m^2]

M_β blade moment about flapping hinge [Kg m], $M_\beta = \int_e^R mrdr$

M_{11} non-dimensional apparent additional air-mass, $M_{11} = \frac{m_a}{\rho \pi R^3}$

M_{aero_0} 'collective' aerodynamic loading degree of freedom

M_{aero_c} longitudinal aerodynamic loading degree of freedom in the non-rotating reference frame, positive more lift at rear of disc

$M_{aero}{}^m$ individual aerodynamic blade moment at root

M_{aero_s} lateral aerodynamic loading degree of freedom in the non-rotating reference frame, positive more lift on advancing side

$m(r)$ distributed blade mass [kg/m]

m_a apparent additional air-mass [Kg]

N number of blades, or bulk modulus of fluid [N/m^2]

P_a, P_b valve pressures [N/m^2]

P_m pressure difference across hydraulic motor [N/m^2]

P_s, P_r hydraulic supply and return pressures [N/m^2]

q_{in}, q_{out} valve flows [m^3/s]

R rotor radius [m]

r radial station

T thrust [N], or rotor torque [Nm]

u control vector in state space description

V flow parameter in Pitt & Peters inflow model

Vt trapped hydraulic volume [m^3]

x state vector in state space description, or valve opening

Subscripts and Superscripts

$\cdot\cdot_{aero}$ subscript implies aerodynamic loading only, i.e. no inertial terms

$\cdot\cdot^m$ superscript implies individual blade quantities

Chapter 1
Introduction and Theoretical Background

1.1 Introduction

Despite significant progress in helicopter mathematical modelling over the past few decades, helicopter models that are typically used for flight mechanics and control work are still known to be deficient in a number of key areas. From the point of view of control and handling qualities, greatest uncertainty exists in the high frequency region where the complex dynamic and aerodynamic coupling of the rotor come into play and a lack of fidelity in the representation of this dynamic coupling inevitably leads to conservatism in any high performance control system design.

This thesis is primarily concerned with a detailed experimental investigation of rotor dynamic inflow. The term dynamic inflow refers to the induced-velocity response delay associated with changes in rotor loading. In other words, dynamic inflow theory is concerned with the induced velocity delay experienced when the operating conditions of the rotor are changed.

Dynamic inflow was first observed as a transient thrust increase occurring when collective pitch was rapidly increased. During the period of time before the induced flow has reacted to the increase in pitch, the angles of attack on the blades are not decreased by the downward induced flow, so creating a transient increase of thrust, above that of the final increase due to the larger blade pitch.

A similar effect can be observed with the tail rotor. A sudden increase in pitch of the tail rotor blades will cause an increase in the effective blade angle of attack above that of the final steady state value, achieved once the flow has responded. Temporary stalling of the blades and the associated high tail-rotor torque have been observed, and in the past, unexpected high torque transients have led to cases of twisted tail rotor drive shafts [Prouty 1992].

More recently, problems have been encountered with high-gain fly-by-wire height hold systems [Prouty 1992]. These automatically adjust the blade pitch rapidly in an attempt to maintain a precise altitude. If the dynamics associated with delayed inflow response are not incorporated correctly in the model used for control law design, significant reductions in the stability margins may occur.

Dynamic inflow also introduces couplings between roll and pitch that have previously not been included in helicopter mathematical models used for flight mechanics research. As it has been shown that dynamic inflow can destabilise rotors this has implications for the design of automatic control systems.

This chapter will first examine the literature concerned with dynamic inflow and then review the Pitt and Peters [Pitt & Peters 1983] dynamic inflow model, which has been widely used, particularly in the area of flight mechanics. From this and the literature review principal areas of investigation will be identified.

1.2 Review of Literature

1.2.1 Introduction

The purpose of this review is to assess the work that has been undertaken in the field of helicopter rotor dynamic inflow so that the current research work and planned future programme may be placed in context.

Summaries of most of the papers included in the review below, with the emphasis on issues relevant to the modelling of dynamic inflow, are given in Appendix A. It is hoped that these will allow rapid identification of relevant reports in future dynamic inflow research. A complete bibliography and list of references are given at the end of this thesis.

The literature was initially complied from known references and subsequently an on-line literature search was performed to uncover most of the relevant references. After this the

literature base was extended through regular searching of pertinent journals in the field of helicopter research and an on-line computer search.

1.2.2 Historical Development and Review of Literature

Based on momentum theory, the simple models of the helicopter rotor wake assumed a uniform velocity over the entire rotor disc. Soon this was modified for forward flight, to allow a first harmonic inflow variation, which increases from the leading to the trailing edge of the rotor disc in the longitudinal direction with a given gradient.

The start of the development of dynamic inflow theory dates back to 1950 when it was discovered that the roll and pitch damping of a helicopter were not predicted well by theory. Work by Sissingh [Sissingh 1951] showed that variations in the then assumed steady and uniform inflow distribution could account for the damping discrepancies. In Sissingh's model the variations in inflow were assumed to be linked to the pitch and roll moments of the rotor, but occurred instantaneously. This is often referred to as quasi-steady inflow, where changes in rotor loading are assumed to cause immediate variations in the induced flow.

Two years later, in 1953 Carpenter and Fridovich [Carpenter & Fridovich 1953] showed that the induced flow does not respond instantaneously to sudden pitch changes in collective. The basis for this work can be found in a manoeuvre practised by helicopter pilots to get heavily overloaded aircraft airborne, by suddenly increasing the blade pitch. This causes a temporary increase in lift that can be sufficient for take-off. Theoretically this was modelled by including an apparent mass term in the inflow formulation. Hence, a delay is introduced between the application of blade pitch, which accelerates the air, and the resultant response. The lag in the downwash response was shown to provide the temporary increase in lift observed in the experiments. The magnitude of the air mass participating in the acceleration process was modelled by a term equal in magnitude to that which would be affected by an impermeable disc during accelerations. Although the analogy between a rotor disc and an impermeable disc

are not strictly valid, it was found to give good results. This work introduced the idea of time varying downwash in response to rotor load changes.

A further development was made in 1953 by Mangler and Squire [Mangler & Squire 1953], who found a potential pressure distribution that satisfies Laplaces equation and gives a pressure discontinuity, i.e. lift, across the rotor disc. Hence if the pressure field around a rotor can be established, which produces the correct rotor loads, then the induced flow distribution can be found from this pressure field, the intention being to link the induced flow field to the rotor loads. Using a predetermined rotor load distribution it was shown that the induced velocity field could be calculated. Ormiston [Ormiston 1972] tried to link the load distribution, induced flow field and flapping dynamics of the blade in a closed loop form, but this became excessively complex. Significantly this work established that the induced flow response of the rotor affects the dynamics of the blade and rotor loading, which in turn affect the induced flow response.

Ormiston and Peters [1972] returned to the effects of quasi steady induced flow and showed that inclusion of non-uniform inflow significantly improved the correlation of theory with experimental flapping data of a non-articulated rotor in forward flight. The model was mostly of empirical nature. Of importance to the later development of dynamic inflow theory, it was established that the effects of the quasi-steady inflow changes due to rotor loading were greatest at low disc loading and that the quasi-steady induced flow response was driven by the aerodynamic rotor loads. A distinction has to be made between the loads seen at the rotor hub, which are due to the dynamics of the moving blade, and those which are purely a result of the aerodynamic loads acting along the blade.

Later on Ormiston [1976] returned to the concept of dynamic inflow. The magnitude of the change in inflow response was linked to the aerodynamic rotor loading, both in the collective and cyclic case, using simple momentum theory. The dynamic effects of the inflow are modelled again by apparent mass terms, which are obtained from an analysis of the air that would be accelerated by an impermeable disc, but now both for changes in thrust (vertical

movement of the disc) and pitch and roll (rotation of the disc) moments. Two significant advances in terms of dynamic inflow modelling were made. Firstly, both variations in aerodynamic thrust and pitch/ roll moments are related to the dynamic response of the flow. Secondly, the effect of this on the rotor dynamics overall is examined. It is found that dynamic inflow can significantly affect the flapping dynamics of the blades and may also be important in the analysis of ground resonance. The link between dynamic inflow, which is essentially an aerodynamic effect, on the dynamics of helicopters was established. What remains to be found is a consistent formulation and derivation of the magnitude of the inflow response and time delay associated with the mass of the affected air. The effect of dynamic inflow on flapping dynamics was further investigated by Chen [Chen 1980] and the effects on the flap-lag dynamics of rotors by Peters and Gaonkar [Peters & Gaonkar 1980].

Bannerjee [Bannerjee et al 1979] identified the inflow parameters from data of a model helicopter rotor and found that at low advance ratios an inflow model, including inflow time delays, performed best, whereas at high advance ratio a quasi-steady approach was sufficient.

In 1981 Pitt and Peters [Pitt & Peters 1981] examined the induced flow problem from a flight dynamics point of view. They again assumed that the inflow distribution could be represented assuming both fore-aft and side-to-side variations plus a uniform component. Again potential flow theory as by Mangler and Squire [Mangler & Squire 1953] was used to link the degrees of freedom of the inflow distribution to the aerodynamic forces acting at the rotor hub, essentially an open-loop problem. Furthermore, by extending this theory to the unsteady case (unsteady actuator disc theory), they could take account of apparent mass effects. The gains and time constants for the inflow distribution degrees of freedom could thus be found for flight conditions between hover and forward flight, purely from a mathematical analysis of the relationship between the pressure field surrounding a rotor and the aerodynamic rotor loading. Analytical expressions give the variation of the inflow parameters with forward flight speed. The Pitt and Peters inflow formulation subsequently became the standard dynamic inflow model. Due to its importance and complex derivation, a full review of this model, its mathematical derivation and its application are given later in this chapter.

Peters [Peters & Chen 1982] also found that the dynamic inflow model indirectly predicted the instability seen in the vortex ring state. The inflow derivatives and time constants from various inflow models are considered by Pitt and Peters in 1983 [Pitt & Peters 1983]. Particular attention is paid to the differences in the obtained inflow when either assuming superposition of pressure or velocities. The Pitt and Peters [Pitt & Peters 1983] dynamic inflow model assumes superposition of pressures, and results in a more flexible model as it allows analytical expressions for the gain matrix as a function of angle of attack. The differences between the two approaches are discussed in the detailed review of the Pitt and Peters dynamic inflow model later in this section. Gaonkar [Gaonkar & Peters, 1984] further compares the results obtained from an approach considering superposition of pressures and velocities and finds little difference between the simpler superposition of pressures and the more complex superposition of velocities. The improvement gained from incorporating the Pitt and Peters dynamic inflow model in rotor analyses, when considering the predicted pitch and roll moments of a rotor under cyclic excitation, is demonstrated. There is also a suggestion that tip loss factors may be included in the dynamic inflow formulation. The use of experimental rotor coning response data over a range of frequencies at advance ratios up to 0.51 is further used to illustrate the improvement gained from theoretical models if the Pitt and Peters dynamic inflow model is included [Gaonkar & Peters, 1986]. It is not sufficient to model dynamic inflow solely with a lift deficiency factor [Peters 1987], it needs to be incorporated as a separate degree of freedom in rotor models.

A thorough review of dynamic inflow modelling is given by Peters in 1988 [Peters & Gaonkar, 1988]. The report also addresses the difficulty in validating dynamic inflow models and concludes that without inflow data pure rotor flapping is most useful. The relevance of dynamic inflow, not only to stiff rotor hubs, is stressed. This is due to the inflow being driven by the aerodynamic loading of the rotor and not the total loading at the hub, which for an articulated rotor will be significantly less. Furthermore, the inclusion of tip deficiency factors in the inflow model is rejected as it is argued that this is already accounted for in the assumed rotor loading function, which has no load at the tip. Finally Peters and HaQuang [Peters &

HaQuang 1988] reformulated the Pitt and Peters dynamic inflow model for practical applications using a rotor co-ordinate frame and a non-linear formulation, which does not use small perturbation quantities.

Chen and Hindson [Chen & Hindson, 1987] examined the effect of dynamic inflow on the vertical response and blade flapping of a helicopter in hover. In the resulting simple rotor body models apparent mass factors, as found by Pitt and Peters [Pitt and Peters 1981], using a corrected pressure distribution, and the larger value originally found by Carpenter [Carpenter & Fridovich 1953], are considered. The different apparent mass factors found by Pitt and Peters using a corrected or an uncorrected rotor loading function are discussed later in this chapter together with the Pitt and Peters model. The results are compared to experimental flapping and vertical response data from a CH-47B helicopter and good correlation, particularly with the larger apparent mass factor, is found. Some of the experimental results would not be easily compared with the theory as during the experiments the rotor speed could not be kept constant, as is assumed in the theoretical models.

The parameters of rotor/ body/ inflow models similar to those developed by Chen [Chen & Hindson, 1987] are inferred using system identification from vertical acceleration and coning data gathered during flight tests of a Puma helicopter, by Houston [Houston 1989, Houston & Tartellin 1989]. Previously it was found that models using quasi-steady inflow severely underestimated the vertical gain and damping. Again the larger apparent mass factor as first found by Carpenter [Carpenter & Fridovich 1953] gives better results. Furthermore, it is suggested that real wake effects need to be incorporated in the models. The limited range of the linear models could be demonstrated by large step responses, which correlated worse with theory than responses with smaller step inputs, although the poor speed-governing of the helicopter was also a contributing factor. The identifiability and robustness of these models obtained from experimental data are examined by Houston and Black in 1990 [Houston & Black 1990]. Without inflow data the inflow derivatives had to be fixed when an output error method was used. It was found that the identified parameters were sensitive to the frequency range over which the identification was carried out and to a prori parameter estimates.

The identification of rotor/ body models incorporating dynamic inflow is further considered by Bradly [Bradly et al, 1989]. Without inflow measurements an equation-error approach was not possible and output-error techniques had to be adopted. Leith [Leith et al 1991] concludes that without inflow measurements some parameters always need to be determined using a prori information. As far as frequency input was concerned the need for excitation frequencies up to at least shaft speed with good definition was identified. This would be difficult to achieve using pilot generated inputs.

In 1989 Peters [Peters, Boyd & He, 1989] developed a more sophisticated dynamic induced flow model. This was further extended and validated by Su [Su, Yoo & Peters 1992]. In this model the flow field is described by the coefficients of azimuthal harmonics and radial shape functions, which are the degrees of freedom of the model. The number of degrees of freedom, and hence the allowed complexity of the wake is user defined. The degrees of freedom of the flow field are linked by ordinary differential equations to the circulatory lift distribution over the rotor. The difference in comparison to the Pitt and Peters dynamic inflow model, is that the forcing function is no longer the aerodynamic hub loading but the pressure coefficients of the assumed loading obtained from the circulatory lift distribution along the blade. The chosen complexity of the wake determines the accuracy to which the aerodynamic loading is required. The link between blade loading and flow field is established through a pressure field that satisfies the rotor boundary conditions and Laplace's equation, but in contrast to the Pitt and Peters models can vary with rotor azimuth position. The basis is therefore created to predict the flow behaviour associated with blade passage. Theoretical results are compared to limited dynamic inflow data obtained from a two-bladed tail rotor under a 4-per-revolution, 1 deg. collective excitation. It is found that the flow variation due to collective excitation is very small, and this highlights the lack of measured rotor downwash that includes dynamic variation due to rotor loading. The radial inflow distribution under steady conditions is also examined and an increase in inflow up to the tip is seen. This is not shown in the experimental results, which show a sharp drop in the inflow in the tip region due to tip effects and wake contraction. The effect of blade passage is however captured well.

Efforts to remedy the lack of measured dynamic inflow data were made by Liou [Liou & Komerath 1994]. A two-bladed tail rotor is excited at one frequency of exactly 4-per-revolution and the induced flow recorded using Laser Doppler Anemometry.

1.3 Review of the Theoretical Development of the Pitt & Peters Dynamic Inflow Model

1.3.1 Introduction

Throughout this thesis reference will be made to the widely accepted Pitt and Peters [Pitt & Peters 1981] dynamic inflow formulation. Due to the importance of this work and the fact that much of the other work is based on it, a detailed discussion of its derivation is given below. The model derivation and applications are given by Pitt and Peters [Pitt & Peters 1981, Peters & HaQuang 1988, Peters & Gaonkar 1988, Pitt & Peters 1983], with the majority of the theory covered in the first of these papers. Equations which are identical to those given by Pitt [Pitt & Peters 1981] are numbered in bold, using the numbering in the original paper, which should allow easy cross-reference with that paper. Particular attention has been paid to explaining the steps left out of derivations in the 1981 [Pitt & Peters 1981] paper and to some of the subtleties and logical development of the original model. The original paper often uses a complicated mathematical notation and an attempt to explain this more clearly has been made. It is intended that this section will systematically explain the dynamic inflow model and its theoretical basis. This section uses the symbols as used in the original paper [Pitt & Peters 1981] and not as given in the list of symbols at the beginning of this thesis. A reader not interested in a detailed explanation of this dynamic inflow model, may wish to skip sections 1.3.3 to 1.3.12..

1.3.2 General Representation

The dynamic inflow model [Pitt & Peters 1981] is concerned with finding a relationship between the induced velocity in the wake and the rotor loading. This is essentially a closed

loop problem, the rotor loading determining the induced flow and this in turn affecting the rotor loading. The blade response is also affected by the wake, the rotor loading and the dynamics of the blade. An illustration of the structure of this closed loop problem is shown below.

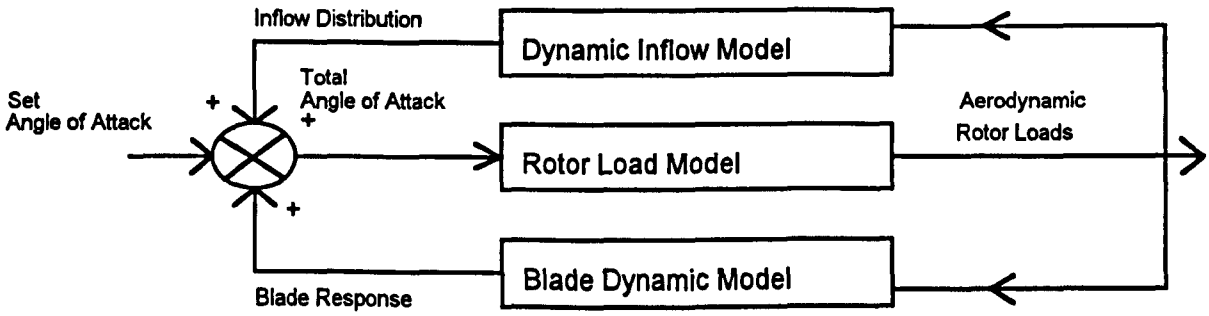

The model relates the inflow distribution to the aerodynamic rotor loads, and is given below in its general small perturbation form.

$$[\mathrm{M}]\begin{Bmatrix}\dot{\lambda}_0\\ \dot{\lambda}_s\\ \dot{\lambda}_c\end{Bmatrix} + [L]^{-1}\begin{Bmatrix}\lambda_0\\ \lambda_s\\ \lambda_c\end{Bmatrix} = \begin{Bmatrix}C_T\\ C_L\\ C_M\end{Bmatrix}_{\text{aero}} \tag{1-1}$$

This merits some further explanation. The wake model assumed by the Pitt-Peters model is uncomplicated. It is assumed that the variations in the induced flow due to changes in the rotor loading can be represented by the following relationship.

$$\lambda = \lambda_0 + \lambda_s r\sin\psi + \lambda_c r\cos\psi \tag{1-2}$$

The small perturbations in the induced flow are thus assumed to be modelled by a uniform component λ_0, and by fore-aft λ_c and side-to-side λ_s variations. This suggests than in undisturbed hover when the side-to-side and fore-aft variations would normally be zero the perturbations in the wake would be uniform over the area of the rotor. For moment perturbations, the resulting inflow changes are assumed to be linear with radial station.

The aerodynamic thrust and pitch/roll coefficients (C_T, C_L, C_M) are also small-perturbation quantities. They represent the *aerodynamic* lift and pitch/roll moments acting at the rotor hub in non-dimensionalised form. These must not be confused with the total thrust and pitch/roll moments acting at the hub which, apart from aerodynamic contributions, also contain terms

due to the dynamic motion of the blade, including centripetal as well as inertial and gravitational terms.

The Pitt/Peters model thus relates the wake perturbation degrees of freedom $(\lambda_0, \lambda_c, \lambda_s)$ to the perturbations in rotor aerodynamic loading (C_T, C_L, C_M), by two matrices L and M, in a linear, first-order structure. The M matrix can be associated with the apparent mass terms needed to model the time-delay nature of the wake degrees of freedom. The L matrix determines the magnitude of the inflow distribution due to rotor loading. The time derivatives are with respect to non-dimensional time $\frac{d}{d\Omega t}$.

In this form the Pitt and Peters dynamic inflow model is a linear model relating the inflow perturbations to the perturbations in rotor loading. A non-linear form of the model [Peter & HaQuang 1988] also exists and will be discussed briefly at the end of section 2-11.

1.3.3 Kinner Pressure Distribution

The main achievement of the work by Pitt and Peters [Pitt & Peters 1981] was to find the elements of the L and M matrices from a purely analytical standpoint and this will be examined below.

The analysis is based on finding a pressure field around a rotor which includes a pressure discontinuity across the rotor disc, which gives the desired rotor lift. Having found a suitable pressure distribution this can be used to find the relationships among the loading on the rotor , the magnitude and distribution of the pressure discontinuity, and the resulting flow field, which can be found by integrating the pressure field. This method is often referred to as potential flow actuator disc theory. It combines the assumptions within the actuator disc theory (that the rotor with a discrete number of blades and individual blade aerodynamics can be modelled as a continuous disc with a pressure discontinuity across it) with potential flow theory which allows the flows resulting from a given pressure distribution to be calculated.

The pressure distribution used was discovered by Kinner and used by Joglekar [Joglekar 1970] and the non-dimensional pressure distribution - non-dimensional with respect to density and tip speed $\left(\phi = {}^{P}/_{\rho(\Omega R)^2}\right)$ - is given as a function of an ellipsoidal co-ordinate system and satisfies Laplace's equation. Flows which satisfy Laplace's equation are assumed to be irrotational and incompressible and inviscid. In a Cartesian co-ordinate system Laplace's equation is given by:

$$\nabla^2\phi = \frac{\partial^2\phi}{\partial x^2} + \frac{\partial^2\phi}{\partial y^2} + \frac{\partial^2\phi}{\partial z^2} = \phi_{xx} + \phi_{yy} + \phi_{zz} = 0 \tag{1-3}$$

$$\underline{\phi_{ii}, e = 0} \tag{1-3a}$$

As can be seen, various notations exist. In the Pitt and Peters paper [Pitt & Peters 1981] the **Laplace equation** is expressed in an ellipsoidal co-ordinate system and a rarely used notation is applied, namely $\phi_{ii}, e = 0$, where the *ii* indicates second derivatives of ϕ in the three co-ordinate directions and the e indicates an ellipsoidal co-ordinate system.

The general form for Kinner's pressure distribution in an ellipsoidal co-ordinate system is given by Equation (1-5) below. A diagram of the ellipsoidal co-ordinate system and its relation to the rotor disc plane is shown below.

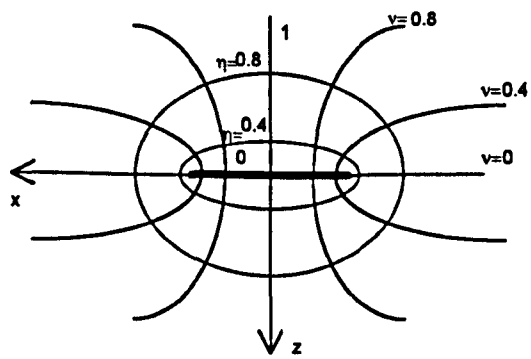

The relationship between the ellipsoidal co-ordinate system (ν,ψ,η) and a Cartesian co-ordinate system is given by the following.

$$\begin{aligned} x &= -\sqrt{1-\nu^2}\sqrt{1+\eta^2}\cos\psi \\ y &= \sqrt{1-\nu^2}\sqrt{1+\eta^2}\sin\psi \\ z &= -\nu\eta \end{aligned} \tag{1-4,[4a-c]}$$

The rotor azimuth ψ follows the usual counter-clockwise convention and on the rotor disc $\eta = 0, \nu = \sqrt{1-r^2}$,

$$\phi = -\sum_{m,n=0}^{\infty} P_n^m(\nu) Q_n^m(i\eta)\left[C_n^m \cos m\psi + D_n^m \sin m\psi\right]. \qquad \text{(1-5,[3])}$$

As already stated Kinner's potential pressure function ϕ is a solution to Laplace's equation and is given in an ellipsoidal co-ordinate system. The coefficients P_n^m, Q_n^m are Legendre Functions associated with the ellipsoidal co-ordinate system. The Kinner pressure distribution looks very complicated, but is essentially simple. It is a general potential function in the ellipsoidal co-ordinate system, which fulfils the Laplace equation. The C and D coefficients are initially arbitrary functions which need to be chosen so that the potential pressure function gives the desired rotor loading. For instance the thrust of the rotor is given by integrating the pressure at the rotor over the rotor disc, with the following conditions for the ellipsoidal co-ordinate system $\left(\nu = \sqrt{1-r^2}, \eta = 0\right)$. The integration yields the following result:

$$C_T = \iint \phi \, dA = \tfrac{4}{3} C_1^0. \qquad \text{(1-6[5a])}$$

Therefore only one of the C coefficients C_1^0 affects the thrust of the rotor. All other coefficients have no effect on the thrust produced by the rotor. This is a very important result, as it suggests that different pressure distributions will produce the correct thrust as long as C_1^0 equals $\tfrac{3}{4} C_T$. Substituting this coefficient back into the Kinner pressure distribution, with the conditions at the rotor disc $\left(\nu = \sqrt{1-r^2}, \eta = 0\right)$ gives the following pressure at the rotor disc,

$$\phi = -\sqrt{1-r^2}(-1)\left[\tfrac{3}{4} C_T\right]. \qquad \text{(1-7).}$$

This can be plotted against radius and is shown in Fig. 3 of Pitt and Peters paper [Pitt & Peters 1981]. The pressure difference at the rotor hub ($r = 0$) is non-zero, i.e. lift is being predicted at the hub. Pitt and Peters refer to this as the *uncorrected* pressure distribution as it does not fulfil the boundary condition that the loading and rate of change of loading be zero at the rotor hub. It has been suggested that the *uncorrected* distribution models the pressure loading of an ideally twisted rotor, where the pitch of the blade increases to infinity at the root to

compensate for the loss of lift due to reducing air speed. Further terms can now be added to the Kinner pressure distribution, so that the boundary conditions are fulfilled. We have already seen that these other C and D terms will not affect the thrust produced. By considering further terms in the Kinner distribution it is possible to obtain a pressure distribution that satisfies the boundary conditions, and this is referred to a the *corrected* pressure distribution by Pitt and Peters [Pitt & Peters 1981]. For the rotor thrust this is the C_3^0 term and the resulting pressure distribution at the rotor is plotted in Fig. 3 of their 1981 paper, and it can be seen that at the root there is now zero pressure loading.

Similar results can now be found for the pitch and roll moments. These are again uniquely defined by the D_2^1 and C_2^1 terms. If the boundary conditions are to be fulfilled the additional terms are the D_4^1 and C_4^1 terms. Thus a Kinner distribution consisting of the C_1^0, C_3^0, C_2^1, D_2^1, C_4^1, D_2^1 and D_4^1 terms given by Pitt and Peters, and the appropriate Legendre functions will give a pressure distribution which, when integrated gives the desired rotor thrust, pitch and roll moments and also satisfies the boundary conditions. This analysis can be extended to take into account second or higher harmonic pressure integrals and this will then lead to further C and D terms.

To summarise, an analytic pressure distribution in an elliptical co-ordinate system, which fulfils Laplace's field equation has been found in terms of a few coefficients which give not only the desired rotor loading but also pressure distributions at the rotor disc which fulfil the boundary conditions. Solutions to Laplace's field equation can be used to find the velocity at a point in the field using integration.

1.3.4 Continuity and Momentum Equations

The next step is to find the velocity at any point on the rotor disc from the given pressure distribution.

If we consider the fluid flow in a region with the velocity v and density ρ which is only dependent on the location in the region, say in a two-dimensional Cartesian co-ordinate system

[x y], then the velocity consists of two individual velocity components v_1 and v_2. The fluid flow has to adhere to the conservation-of-mass law. This is also called the continuity condition of a fluid flow. The mathematical expression is given by:

$$\frac{\partial \rho}{\partial t}+\frac{\partial \rho v_1}{\partial x}+\frac{\partial \rho v_2}{\partial y}=0 \tag{1-8}$$

$$\underline{q_{ij}=0}. \tag{1-8a}$$

The derivation of this can be found in most fluid mechanics text books. If the flow is incompressible and the density is thus constant this reduces to:

$$\frac{\partial v_1}{\partial x}+\frac{\partial v_2}{\partial y}=0 \tag{1-9}$$

$$q_{ij}=0. \tag{1-9a}$$

An alternative method of writing this is $\mathrm{div}\, v=0$. Essentially this expresses the fact that the inflow and outflow at a given point must be equal. In the Pitt and Peters paper the **continuity equation** is written in a non standard form as $q_{ij}=0$, meaning that the partial derivatives of the induced velocity components q_i in the chosen co-ordinate system, in the direction i must satisfy the continuity equation, where i represents all the unit vectors defining the co-ordinate system.

Similarly the conservation of momentum in a fluid flow can be expressed mathematically. For a two-dimensional, incompressible flow in a Cartesian co-ordinate system, the conservation of momentum equations in each direction of the unit co-ordinate system are given by:

$$\begin{aligned}
&\frac{\partial \rho v_1}{\partial t}+\frac{\partial \rho v_1^2}{\partial x}+\frac{\partial \rho v_1 v_2}{\partial y}=-\frac{\partial p}{\partial x} \quad \text{x-direction} \\
&\frac{\partial \rho v_2}{\partial t}+\frac{\partial \rho v_2^2}{\partial y}+\frac{\partial \rho v_1 v_2}{\partial x}=-\frac{\partial p}{\partial y} \quad \text{y-direction}
\end{aligned}, \tag{1-10}$$

where v_1, v_2 are the velocity components in the x and y directions and p is the pressure function. The partial derivatives can be further expanded giving, for the x-direction for example:

$$\frac{\partial \rho v_1}{\partial t}+v_1\frac{\partial \rho v_1}{\partial x}+v_1\frac{\partial \rho v_1}{\partial x}+v_1\frac{\partial \rho v_2}{\partial y}+v_2\frac{\partial \rho v_1}{\partial y}=-\frac{\partial p}{\partial x}\quad \text{x-direction}$$

$$\frac{\partial \rho v_1}{\partial t}+v_1\frac{\partial \rho v_1}{\partial x}+v_1\left(\frac{\partial \rho v_1}{\partial x}+\frac{\partial \rho v_2}{\partial y}\right)+v_2\frac{\partial \rho v_1}{\partial y}=-\frac{\partial p}{\partial x} \qquad (1\text{-}11)$$

$$\frac{\partial \rho v_1}{\partial t}+v_1\frac{\partial \rho v_1}{\partial x}+v_2\frac{\partial \rho v_1}{\partial y}=-\frac{\partial p}{\partial x};\quad \frac{\partial \rho v_1}{\partial x}+\frac{\partial \rho v_2}{\partial y}=0 \ \left(\text{from continuity } \frac{\partial \rho}{\partial t}=0\right)$$

If the velocity in the 2 dimensional co-ordinate system, consisted of only one component , say in the x direction, i.e. v_1 then the momentum equations would become

$$\frac{\partial \rho v_1}{\partial t}+v_1\frac{\partial \rho v_1}{\partial x}=-\frac{\partial p}{\partial x}$$
$$\frac{\partial \rho v_2}{\partial t}+v_1\frac{\partial \rho v_2}{\partial x}=-\frac{\partial p}{\partial y}. \qquad (1\text{-}12)$$

In the Pitt & Peters model the pressure function is given by the non-dimensional field function ϕ. The co-ordinate system is a three dimensional elliptic one, with the free stream velocity υ coming from the negative ξ direction. The individual velocity components in the unit directions of the elliptical co-ordinate system are collectively written as q_i .The above **momentum equations** can then be written in a different mathematical notation as:

$$\underline{q_{i,0}-\upsilon q_{i,\xi}=-\phi_i}. \qquad (1\text{-}13[7b])$$

This equation effectively establishes a relationship between the time-varying pressure field around the rotor and the velocity components within this field, and solutions to this equation will give the induced flow at any point. Various specialisations of the **momentum equation** are considered by Pitt and Peters to find the induced velocity response. For each it is shown that the respective specialisation of the momentum equation together with the continuity equation satisfy Laplace's equation, and therefore the Kinner pressure distribution, which is a solution to Laplace's equation, is always a valid solution.

1.3.5 Induced Flow Calculation

Now the relationship between the loading ϕ and the induced flow at the disc q_z, with η=0 needs to found. The next step is to find the induced flow at all points on the rotor in terms of

the applied loading. Once this has been done the inflow degrees-of-freedom response to the applied rotor loading can be found with the integrals below.

$$\lambda_0 = \frac{1}{\pi}\iint \lambda \, da$$
$$\lambda_s = \frac{4}{\pi}\iint \lambda \sin\psi \, da \qquad \text{(1-14[6a-c])}$$
$$\lambda_c = \frac{4}{\pi}\iint \lambda \cos\psi \, da$$

Higher harmonic inflow distributions are also considered in the Pitt and Peters paper and are discussed later.

Several special cases of the **momentum equation** can be considered.

<u>**Steady Case with Time Invariant Velocities**</u>

The first case considered is the steady case. The velocity components q_i do not vary with time. Pitt and Peters write this as $q_{i,0} = 0$ meaning that the rate of change with non-dimensional time of the velocity vector q is zero or $\frac{\partial q}{\partial \Omega t}$=0. The **momentum equation** (1-13) then simplifies to $q_{i,k} = \frac{1}{\upsilon}\phi_j$. The aim is to find the normal q_Z velocity on the disc , i.e. in the z direction at a point (x_0,y_0) on the disc. Then with i=z , $\upsilon q_{z,k} = -\phi_j$, or in a more usual notation $\upsilon\frac{\partial q_z}{\partial \xi} = \frac{\partial \phi}{\partial z}$. The velocity q_Z can now be found from $q_z = \frac{1}{\upsilon}\int \frac{\partial \phi}{\partial z}\, d\xi$, where dξ implies an integration along the free stream direction from infinity to the point (x_0,y_0) on the disc, i.e.

$$q_z = \lambda(x_0, y_0) = \frac{1}{\upsilon}\int_{-\infty}^{0} \frac{\partial \phi}{\partial z} d\xi. \qquad \text{(1-15[9])}$$

The z derivative of the potential field can be expressed as partial derivatives of the Kinner distribution in the elliptical co-ordinate system.

Two specialisations of this case, which are useful for finding the closed form results are available.

Axial Flow Specialisation of the Steady Case

If the free stream flow is directly from above the rotor, i.e. axial flow, the free stream ξ direction is parallel but opposite to the z direction, giving $\upsilon\frac{\partial q_z}{-\partial z}=\frac{\partial \phi}{\partial z}$. For this case the induced flow can be found without integration. (see also Equation (1-15))

$$\lambda(x_0,y_0)=-\frac{1}{\upsilon}\phi\big|_{\eta=0\ \text{(on rotor disc)}} \tag{1-16}$$

Edgewise Flow Specialisation of the Steady Case

Similarly if the flow is edgewise, then the ξ is in the x direction. Part of the integration will be over the disc. The partial differential equation $\upsilon\frac{\partial q_z}{\partial \xi}=\frac{\partial \phi}{\partial z}$ now becomes $\upsilon\frac{\partial q_z}{\partial x}=\frac{\partial \phi}{\partial z}$. Using the relationship between the partial derivative of pressure potential in the z direction and the partial derivatives of the pressure with respect to (w.r.t.) the ellipsoidal co-ordinate system as given by Pitt and Peters, the results of the integration are:

$$\phi_z=-\frac{\eta(1-\nu^2)}{\nu^2+\eta^2}\frac{\partial \phi}{\partial \nu}-\frac{\nu(1-\eta^2)}{\nu^2+\eta^2}\frac{\partial \phi}{\partial \eta} \tag{1-17[11]}$$

$$\lambda(x_0,y_0)=-\frac{1}{\upsilon}\int_{\infty}^{\sqrt{1-y_0^2}}\frac{\partial \phi}{\eta\partial \nu}\bigg|_{\nu=0}dx-\frac{1}{\upsilon}\int_{\sqrt{1-y_0^2}}^{\infty}\frac{\partial \phi}{\nu\partial \nu}\bigg|_{\eta=0}dx. \tag{1-18[13]}$$

Again the integration is from infinity to (x_0,y_0) in the direction of the free stream and a part of the integration is on the disc

Simple Harmonic Pressure Distribution with No Free Stream

In the next case considered, the free stream velocity υ is zero. The **momentum equation** (1-13) becomes $q_{i,0}=-\phi_{,i}$. A simple harmonic pressure distribution $\phi=\bar{\phi}e^{i\omega\Omega t}$ and $q_i=\bar{q}_i e^{i\omega\Omega t}$ is assumed. It should be remembered that the time derivative in the momentum equation is w.r.t. non-dimensional time Ωt and ω is the frequency of the oscillation. Taking the time derivative of the oscillating velocity vector $\frac{\partial q}{\partial(\Omega t)}=i\omega\bar{q}_i e^{i\omega\Omega t}$ and substituting this and the expression for ϕ back into the **momentum equation** $q_{i,0}=-\phi_{,i}$ gives:

$$i\omega\bar{q}_i e^{i\omega\Omega t} = -\bar{\phi}_{,i} e^{i\omega\Omega t}$$
$$i\omega\bar{q}_i = -\bar{\phi}_{,i} \qquad [1\text{-}19]$$

Remembering that $\frac{1}{i} = -i$ and writing the **momentum equation** in the z direction gives $\bar{q}_z = \frac{i}{w}\bar{\phi}_{,z}$ Both partial derivatives are w.r.t. the z direction and the induced flow at the disc can be found without integration, using the potential z derivative as given in Equation 1-17, i.e.

$$\lambda = \left.\frac{-i\partial\bar{\phi}}{wv\partial\eta}\right|_{\eta=0\ (\text{at disc})} . \qquad (1\text{-}20[\mathbf{15b}])$$

Simple Harmonic Velocity Field with Free Stream Flow

In this case we now assume that the induced velocities are oscillating but are always mutually in phase. The analysis is not restricted to the *no free stream* condition. The induced velocity vector is represented by $q_i = \bar{q}_i e^{i\omega w}$ where $\bar{q}_i$ is real. The potential pressure field however is allowed to have both real (in phase) and imaginary (out of phase) components. This is represented by $\phi = (A+Bi)e^{iw\Omega t}$. The expressions for the velocity and pressure field are substituted in the **momentum equation**:

$$\begin{gathered} q_{i,0} - \upsilon q_{i,\xi} = -\phi_{,i} \\ \left(\bar{q}_i e^{i\omega\Omega t}\right)_{,0} - \upsilon\left(\bar{q}_i e^{i\omega\Omega t}\right)_{,\xi} = -\left((A+Bi)e^{i\omega\Omega t}\right)_{,i} \\ iw\bar{q}_i e^{i\omega\Omega t} - \upsilon e^{i\omega\Omega t}\bar{q}_{i,\xi} = -A_i e^{i\omega\Omega t} - iB_i e^{i\omega\Omega t} \end{gathered} \qquad (1\text{-}21)$$

Equating the real and imaginary parts, after dividing by $e^{i\omega\Omega t}$ gives:

$$-\upsilon\bar{q}_{i,\xi} = -A_i \Rightarrow \bar{q}_{i,\xi} = \frac{1}{\upsilon}A_i \ \text{(real)} \qquad (1\text{-}22a)$$

$$w\bar{q}_i = -B_i \Rightarrow \bar{q} = -\frac{1}{w}B_i \ \text{(imaginary)}. \qquad (1\text{-}22b)$$

Taking the derivatives of the above equations[1] w.r.t. i and then using the continuity equation $q_{ij} = 0$ gives $A_{,ii} = B_{,ii} = 0$, which is the Laplace equation in A and B.

From Equation (1-22a) it can be seen that with a pressure field that has an in-phase and out-of-phase component the velocity response to the in-phase component is the same as that for the *"Steady Case with Time Invariant Velocities"*, and the velocities at the disc are given by Equation (1-15) and its specialisations.

From Equation (1-22b) it follow that the velocity response due to the out of phase pressures is analogous to the case of *"Simple Harmonic Pressure Distribution with No Free Stream"* and the velocities at the disc can be found from Equation (1-20).

It follows from this, that the in-phase induced velocities, have a corresponding potential pressure field which is made up of a steady pressure ($\omega = 0$) and an out of phase pressure or apparent mass pressure field ($\upsilon = 0$), which is one of the underlying assumptions in the Pitt and Peters model, and justifies the use of a steady gains matrix L and an apparent mass matrix M. This method is also called ***superposition of pressures.***

Simple Harmonic Pressure Field with Free Stream Flow

There is another possibility for solving the **momentum equation** for the unsteady case. Now the pressure field and not the induced velocities is assumed to be mutually in phase. The induced flow is expressed by $q = (u + iw)e^{i\omega t}$, i.e. it has both real and imaginary components (superposition of velocities). The potential pressure is given by $\phi = \bar{\phi}e^{i\omega t}$ where $\bar{\phi}$ is now purely

---

[1] This is important, because it allows the use of the Kinner pressure distribution as a valid solution for the unsteady case, both for the real and imaginary parts. This can be shown also for the other cases already considered, by the same method of differentiating the q_i expression and using the continuity relationship, and confirms that the Kinner distribution is always a valid solution, since all equations satisfy the Laplace equation.

real. Substitution in the **momentum equation** and separation between the real and imaginary parts then gives expressions for the induced flow as a function of the potential field strength.

$$\begin{aligned} \omega^2 u_i + \upsilon^2 u_{i,\xi\xi} &= \upsilon \bar{\phi}_{i,\xi} \\ \omega^2 w_i + \upsilon^2 w_{i,\xi\xi} &= \omega \bar{\phi}_i \end{aligned} \quad \text{(1-23[18a-b])}$$

Pitt and Peters [Pitt & Peters 1983] show that by taking the derivative of Equation 1-23 w.r.t. i and using the continuity equation, results in the Laplace equation, i.e. Kinner's pressure distribution is also a valid solution for this case, as before.

Now the real and imaginary components can again be found from an integration. The steps are given in detail by Pitt and Peters [Pitt & Peters 1984], and only the results quoted here:

$$\begin{aligned} u_s &= \frac{1}{\upsilon}\int_{\infty}^{0} \bar{\phi}_s \cos(k\xi) d\xi \\ w_s &= -\frac{1}{\upsilon}\int_{\infty}^{0} \bar{\phi}_s \sin(k\xi) d\xi \end{aligned} \quad \text{(1-24[19a-b])}$$

The integration is similar to that of *"Steady Case with Time Invariant Velocities"* Equation 1-15 , except that the cosine and sine factors have been added for the in-phase and out of phase components respectively. The factor k is a reduced-frequency factor based on the free stream velocity $\left(\frac{\omega}{\upsilon}\right)$. Since k is only a function of the frequency of the pressure field oscillation and free stream velocity the integration needs only be carried out for all values of k of interest for each given angle of attack. This approach to the solution of Equations 1-13 is also called the ***superposition of velocities*** as it assumes that the velocities are made up of in phase and out of phase components, and will be discussed in section 2-10 with regard to the superposition of pressures method.

1.3.6 L-Matrix Elements

By integrating the Kinner pressure distribution, along a streamline to the rotor disc, the velocities at the disc for the *"Steady Case with Time Invariant Velocities"* can be found from:

$$q_t = \lambda(x_0, y_0) = \frac{1}{\upsilon}\int_{-\infty}^{0} \phi_s d\xi. \quad \text{(1-15[9])}$$

The above integration is used to find the induced flow at 720 positions on the rotor disc. The induced flow at each point will be a function of the loading of the rotor in terms of C_t, C_l and C_m. The integration goes from (x_0,y_0) to infinity along the direction of the free stream, called the streamline in the paper:

$$\begin{aligned} x &= x_0 + \xi\cos\alpha \\ y &= y_0 \\ z &= -\xi\sin\alpha \end{aligned} \quad . \qquad \text{(1-25[10a-c])}$$

The final step is to find the induced flow degrees of freedom from the inflow over the disc using the following integrals:

$$\begin{aligned} \lambda_0 &= \frac{1}{\pi}\iint \lambda \, da \\ \lambda_s &= \frac{4}{\pi}\iint \lambda \sin\psi \, da \\ \lambda_c &= \frac{4}{\pi}\iint \lambda \cos\psi \, da \end{aligned} \quad . \qquad \text{(1-26[6a-c])}$$

Higher-order inflow degrees of freedom are also given in the paper. The relationship between the aerodynamic loading and induced velocity degrees of freedom, the elements in the L-matrix, has now been obtained. These results are repeated for a range of conditions between axial flow and edgewise flow, using both a corrected and uncorrected pressure distribution and also for higher harmonic terms. Results requiring no numerical techniques were also available for the specialised cases of pure axial and pure edgewise flow and show that the numerical results have an inaccuracy no greater than 4 %.

1.3.7 M-Matrix Elements

The elements of the M Matrix can be found entirely from closed-form results using the equation below, for the specialisation of *"Simple Harmonic Pressure Distribution with No Free Stream"*. The potential pressure field which created the appropriate loading on the rotor now oscillates harmonically $\phi = \bar{\phi}e^{i\omega t}$, where $\bar{\phi}$ is the magnitude of the steady pressure field:

$$\lambda = \left.\frac{-i\partial\bar{\phi}}{w\,v\partial\eta}\right|_{\eta=0(\text{at disc})} \quad . \qquad \text{(1-20[15b])}$$

The inflow at positions on the disc $\lambda(x_o, y_o)$ can now be found from the steady pressure distribution and is out of phase with the harmonic variation. The final step is to apply the integrations below to find the inflow degrees of freedom:

$$\lambda_0 = \frac{1}{\pi}\iint \lambda \, da$$
$$\lambda_s = \frac{4}{\pi}\iint \lambda \sin\psi \, da \; . \qquad \text{(1-14[6a-c])}$$
$$\lambda_c = \frac{4}{\pi}\iint \lambda \cos\psi \, da$$

From these a relationship between the dynamic loading on the rotor and the in-phase response of the inflow degrees of freedom can be found, which are the elements of the M matrix in the Pitt and Peters [Pitt & Peters 1981] model and are given for both corrected and uncorrected pressure distributions.

Together the L and M matrices are then used to represent the *"Simple Harmonic Velocity Field with Free Steam Flow"* using the *Superposition of Pressures* approach to solving he momentum equation for the unsteady case (Equations 1-22a&b).

1.3.8 Models with Higher Harmonics

As briefly indicated earlier the model considered in the Pitt and Peters paper [Pitt & Peters 1981] is primarily directed towards finding 3x3 L and M matrices for Equation 1-1. However the case of higher harmonic variations in the induced flow and aerodynamic loading, resulting in 5x5 L and M matrices, are also considered. The additional degrees of freedom in this formulation are λ_{2s}, λ_{2c}, C_{2L}, C_{2M}. Pitt and Peters argue, however that these can be neglected since the numerical coupling terms between the second harmonic loading and the first-order inflow distribution degrees of freedom are small compared to the coupling terms between the first-order loading terms and first-order inflow distribution.

1.3.9 Corrected and Uncorrected Blade Loading Functions

As previously discussed, an uncorrected pressure distribution at the rotor, which does not fulfil the zero-loading condition of a rotor at the hub, and a corrected loading distribution which does, are considered in the Pitt and Peters paper. For both distributions numerical results for all the elements in the L and M matrices at values for alpha between 0° and 90° are calculated. Closed form results are available for the *uncorrected* L elements over the whole range of alpha, *corrected* elements of L, for the axial and edgewise flow conditions only, and the M elements both for the *corrected* and *uncorrected* loading.

In the final model proposed by Pitt and Peters the first column of L uses the closed-form results found for a corrected pressure distribution, since it assumes a more realistic loading of the rotor. For the other two columns of L the uncorrected results are used, because analytical expressions exist for these over the range of alpha. Furthermore the uncorrected loading distribution for the pitch and roll moments is closer to the corrected distribution, than is the case for the lift distribution, and this suggests that the uncorrected values may be used to good approximation.

For the M matrix elements similar arguments are used. These do not vary with alpha. For the first column the corrected values are used; for the remaining columns the uncorrected values are used.

1.3.10 Superposition of Pressures or Velocities

All the results presented above were obtained by using the simpler *superposition of velocities* approach, for which closed-form results could be found in special cases and otherwise numerical results were used. The true rotor, however, should behave somewhere between the *superposition of velocities* and *superposition of pressures* approach. Or in other words, the real rotor would have both out-of-phase pressures and out-of-phase velocities. The two solution methods represent the boundaries of the real case. A comparison between the results of both methods is given by Gaonkar and Peters [Gaonkar & Peters 1984] and suggests

significant variations in the L matrix obtained from both methods. The *superposition of pressures* method is however preferred by Pitt and Peters because of its mathematically simpler formulation. The dynamic inflow formulation for the *superposition of velocities* approach would be as follows $\{C_{aero\_loading}\} = L(k)^{-1}\{\lambda\}$, i.e. the relationship between the rotor loading and induced velocity is given by a complex L matrix, which varies with frequency and angle of attack. A detailed analysis of the differences between the two methods is given by Pitt and Peters [Pitt & Peters 1984] and concludes that '... the variations between the S.P. [superposition of pressures] and S.V. [superposition of velocities] method are not large enough to warrant the abandonment of the simple S.P. model.'.

It has to be remembered that the methods of superposition of velocities and of pressures are two solutions to the **momentum equation** (1-13) which governs the flow through the disc. The superposition of pressures method results in a simple mathematical formulation and is the basis of the Pitt and Peters [Pitt & Peters 1981] dynamic inflow model.

1.3.11 Final Model

Given below is the final linear model as proposed by Pitt and Peters, with analytical terms for all elements which vary with free stream angle of attack (α=90 in axial flow).

$$\begin{bmatrix} \frac{128}{75\pi} & 0 & 0 \\ 0 & \frac{-16}{45\pi} & 0 \\ 0 & 0 & \frac{-16}{45\pi} \end{bmatrix} \begin{Bmatrix} \dot{\nu}_0 \\ \dot{\nu}_s \\ \dot{\nu}_c \end{Bmatrix} + \left[\frac{1}{\upsilon} \begin{bmatrix} \frac{1}{2} & 0 & \frac{15\pi}{64}\sqrt{\frac{1-\sin\alpha}{1+\sin\alpha}} \\ 0 & \frac{-4}{1+\sin\alpha} & 0 \\ \frac{15\pi}{64}\sqrt{\frac{1-\sin\alpha}{1+\sin\alpha}} & 0 & \frac{-4\sin\alpha}{1+\sin\alpha} \end{bmatrix} \right]^{-1} \begin{Bmatrix} \nu_0 \\ \nu_s \\ \nu_c \end{Bmatrix} = \begin{Bmatrix} C_T \\ C_L \\ C_M \end{Bmatrix}_{aero} \tag{1-25}$$

According to the analysis presented so far, the υ in the L matrix elements is the free stream velocity. The angle of attack α is taken between the disc plane and the free stream. In the final section of the Pitt and Peters paper it is suggested that the term $\upsilon = \sqrt{\mu^2 + \bar{\lambda}^2}$, where μ is the advance ratio (non dimensionalized forward speed) and $\bar{\lambda}$ non-dimensional vertical component of the aircraft velocity be replaced by

$$\upsilon = \frac{\mu^2 + (\bar{\lambda} + \bar{v})(\bar{\lambda} + 2\bar{v})}{\sqrt{\mu^2 + (\bar{\lambda} + \bar{v})^2}}. \qquad \text{(1-26[23b])}$$

In the Pitt & Peters paper, there is a typographical error , with the second $\bar{v}$ term written without the bar. The significance of this is that the induced flow, due to the rotor lift, is taken into account through $\bar{v}$, which is the non-dimensionalised steady induced flow, obtainable from momentum theory and the steady thrust coefficient. For the hover case this reduces to $\upsilon = 2\bar{v}$. The definition of the angle of attack is also modified to

$$\alpha = \tan^{-1}\frac{\bar{\lambda} + \bar{v}}{\mu}. \qquad \text{(1-27[23c])}$$

A non-linear version of the dynamic inflow model, i.e. not formulated in perturbation quantities also exists [Peters & HaQuang 1988]. For the hover case this reduces to

$$C_T = \frac{M_{11}}{\Omega}\dot{\lambda} + 2V_T\lambda; \text{ where } \lambda = \frac{\upsilon}{\Omega R}, \qquad \text{(1-28)}$$

and where V_T is the total normalised velocity at the rotor. Linearizing this equation about initial conditions of λ_m [Appendix A] and using perturbation quantities gives

$$C_T = \frac{M_{11}}{\Omega}\dot{\lambda} + 2*2\lambda_m\lambda, \qquad \text{(1-29)}$$

which is the same as the linear model with $\upsilon = 2\lambda_m$. The complete non-linear model is given as

$$[M]\begin{Bmatrix}\dot{\lambda}_0\\ \dot{\lambda}_s\\ \dot{\lambda}_c\end{Bmatrix} + [L]_{nl}^{-1}\begin{Bmatrix}\lambda_0\\ \lambda_s\\ \lambda_c\end{Bmatrix} = \begin{Bmatrix}C_T\\ C_L\\ C_M\end{Bmatrix}_{aero}, \text{ with } [L]_{nl} = [L][V]^{-1} \text{ and } [V] = \begin{bmatrix}V_T & 0 & 0\\ 0 & V & 0\\ 0 & 0 & V\end{bmatrix}.$$ The mass flow matrix [L] has different flow parameters associated with the pitch and roll equations than those in the thrust equation. V_T is the total resultant velocity at the disc as in the linear model [Peters HaQuang 1988].

1.3.12 Comparison with Other Theories

There have been other analyses which have predicted the gains of the L matrix. The steady state response of the inflow degrees of freedom w.r.t. the aerodynamic loading can be fully

derived purely using momentum theory [Gaonkar & Peters 1986]. It should be noted that the values of the L22 and L33 terms depend on the wake assumptions used in that analysis [Chen 1989]. The details of this are explained by Chen [Chen 1989], but it suffices to say that for a rigid-wake assumption, in hover, the elements are twice a large as for a non-rigid wake assumption. The values obtained in the Pitt and Peters dynamic inflow model [Pitt & Peters 1983] correspond to the values obtained using a non-rigid wake assumption and Peters [Peters 1988] gives good arguments in favour of the non-rigid wake assumption.

One of the results of the Pitt & Peters inflow formulation in hover is that with $L_{11}=\frac{1}{2\upsilon}$ a lift deficiency function can be found for quasi-steady inflow. From Johnson [Johnson 1980] the following is given, which shows the effect that inflow perturbations have on the thrust produced by a rotor, $\frac{C_T}{\sigma a}=\left(\frac{C_T}{\sigma a}\right)_{steady}-\frac{1}{4}\delta\lambda$, where $\delta\lambda$ is the inflow perturbation. Substituting from the Pitt model in the hover case the relationship between inflow perturbation and hub loading, $\lambda=\frac{C_T}{2\upsilon}$, gives the following:

$$\frac{C_T}{\sigma a}\left(1+\frac{\sigma a}{8\upsilon}\right)=\left(\frac{C_T}{\sigma a}\right)_{steady}$$
$$\gamma=\frac{C_T}{\sigma a}\Rightarrow\frac{\gamma}{\gamma_{steady}}=\frac{1}{1+\frac{\sigma a}{8\upsilon}}. \qquad (1\text{-}30)$$

This is the reduced Lock number to account for the reduction in lift due to quasi-steady dynamic inflow and is the result given by Pitt and Peters [Pitt & Peters1983] and is the same lift deficiency found from several other analyses. Similarly, it can be shown that quasi-steady inflow results can be modelled using an increased equivalent drag coefficient.

1.3.13 Conclusions

The attractions of the Pitt and Peters dynamic inflow models are numerous. Its simple formulation gives the relationship between the induced flow degrees of freedom and the aerodynamic rotor loading. The lag between loading and inflow response is modelled through the use of an apparent mass matrix. The elements both of the gain and mass matrices can be found by considering a potential pressure field about the rotor. For the final model, the

variation of the gain and phase elements as a function of the angle of attack is given in analytical form. There are however some assumptions in the model which should be examined critically.

Firstly, the perturbation wake representation through the use of a uniform, side-to-side and fore-aft inflow variation needs to be examined, through comparison with experimental data. Furthermore the analysis is based on the assumption of inviscid and irrotational flow. This is an underlying assumption of using potential flow theory to predict the inflow response. The rotor wake is not likely to be irrotational and the viscosity effects of swirling flow could be considerable. Although there is much evidence that the superposition of pressures approach is valid this too needs to be examined from an experimental standpoint. Similarly the results obtained from corrected and uncorrected pressure distributions should be examined further. Experimental comparisons, particularly of experimentally determined inflow, with theoretical models should further improve confidence in Dynamic Inflow modelling.

1.4 Summary and Aims of Work

The aims of an extensive literature review and detailed discussion of the Pitt and Peters [Pitt & Peters 1981] dynamic inflow model were to give a detailed account of the strengths and weaknesses of previous work. From this, areas of interest and future research could be identified which, within the constraints of the proposed experimental rig, formed the basis of an experimental programme.

From the literature it is clear that the Pitt/Peters dynamic inflow model [Pitt & Peters 1983] has been extensively used in flight mechanics models [Gaonkar & Peters 1986, Peters & Gaonkar 1988, Chen 1990, Curtiss & Zao 1988]. The effect of including dynamic inflow, over steady or quasi-steady dynamic inflow, on the dynamics of rotor flapping, vertical response and hub moments has been demonstrated, and it is clear that rotor dynamic analyses are improved if a dynamic inflow degree of freedom is added.

For the case of hub moments, comparison with experimental data show much improvement when the Pitt and Peters dynamic inflow model is included [Gaokar & Peters 1986]. However other experimental validations show that although dynamic inflow theory improves the correlation there is further scope for improvement [Houston 1989]. In general the validation of dynamic inflow theory has taken place without regard to direct inflow measurements, usually using pure flapping data, and this is an area of work on which this thesis will focus.

Although it is clear that the simple wake model assumed in the derivation of the Pitt and Peters dynamic inflow model is only an approximation, it is important to examine the limitations of this wake model compared to experimental data. It is the induced velocities predicted by this wake model which are used in the prediction of the aerodynamic loading of the rotor, which in turn affect the inflow response.

The lack of inflow measurements which include dynamic variations due to changes in rotor loading have been highlighted frequently in work which has attempted to identify the rotor and dynamic inflow parameters from experimental data [Houston & Black 1990, Bradly et al 1986]. Although it is not intended to extend the comprehensive work in parameter identification studies, this is a further justification for a detailed examination of the induced velocity field. Even when rotor flapping and body movement data obtained from full size helicopters are used in identification strategies, the deficiency in both frequency range and content, limited by the physical capabilities of the control system and pilot are apparent [Leith et al 1991]. From this it is concluded that in any experimental investigation inflow and rotor flapping data need to be examined over a frequency range from near zero to above shaft speed, using a high bandwidth control and actuation system. The need to keep rotor speed constant during these experiments is also illustrated [Houston & Tartellin 1989, Leith et al 1991], and this will be considered in the experimental arrangement. Furthermore, conducting the experiments on a hover stand which eliminates vertical movement and in a more controlled environment than that of full-size flight testing, should allow isolation of the inflow / flapping rotor dynamics.

In addition to the work done by Chen/Hindson [Chen & Hindson 1987] into the effects of primary rotor parameters on coning in hover, a further parametric investigation examining the effects of hinge offset and flapping restraint as would be used to model a rigid rotor, should be conducted. This should also further provide evidence for the correct apparent-mass factor to be used.

The limited inflow data at a single frequency, including dynamic effects, which are available [Liou & Komerath 1994], highlight the difficulties in obtaining large velocity variations without jeopardising the fatigue limits of the model rotor. Consequently future experimental work needs to examine the inflow response over a large range of frequencies, and if the inflow variations prove to be small then they need to be captured over a long period.

The aims of this work therefore are to gain a better understanding of the dynamic induced velocity field of a rotor over a wide frequency range, and to examine the correlation of dynamic inflow models, and rotor model including dynamic inflow, with the experimental data.

Chapter 2
Experimental Apparatus and Procedure

2.1 Introduction

In this section the experimental facility including the rotor rig will be described in detail, with particular attention being given to the techniques of measuring the induced flow beneath the rotor. During the period of the research significant alterations to the rig were made and it was also moved from a rotor test chamber to a wind tunnel. A short review of the experiments carried out, and their consequences for the rig development, is given with the aim of putting the conducted experiments and modifications into a logical progression and chronological order.

2.2 Experimental Facility

The description of the model rotor facility will concentrate on the configuration used in the majority of the experiments, after it had been modified following the initial experiments described in Chapter 3. The modifications made to the original facility will be pointed out.

The experimental facility consists of a four-bladed rotor of 1.54 m diameter that is driven by a hydraulic motor. A fully actuated swashplate and associated control system allowed the collective and cyclic pitch of the rotor to be changed dynamically at frequencies up to 30 Hz. Strain gauges mounted on the blades were used to measure blade deflection, shaft encoders provided rotor azimuth position and pressure transducers and hot wires were used for flow measurements. The elements of the rotor relevant to this work are described below and further information is given by Brinson [Brinson 1991], who developed the rig to its initial state including the mechanical rotor hub and gimbal, actuation system, and the control system including 8 digital signal-processing boards and sophisticated on-line monitoring. Areas in which the rig was subsequently modified included further software developments (although

many of the required software routines particularly regarding on-line monitoring existed already) reduction of the gimbals, base plate and provision of flow instrumentation, data logging and analysis.

2.2.1 Gimbal

The rotor, swashplate and hydraulic motor assembly, are mounted onto a base plate, which is supported by a U-shaped gimbal. The gimbal allows the base plate and rotor assembly to pitch and roll freely, but can also be locked in position when required. The ability of the rotor to pitch and roll enables the rig to be used for rotor control studies, but for the purposes of the inflow studies the gimbals were locked in the level position. The hydraulic oil powering the motor was brought in through the gimbal axes with two rotating hydraulic unions. While the rotor is running up to speed, with the gimbals unlocked, a steel cable attached by a rotating bearing to the hub and pulling upwards keeps the rotor from pitching or rolling until the operating condition is reached. At this point a weight on the end of the cable is lifted and the rotor is then free to pitch and roll. Incremental shaft encoders provide positional information with an inaccuracy of only 0.005 degrees. As already stated, the original gimbal was redesigned after the preliminary work, to produce a more compact unit, with less aerodynamic interference. Fig. 2-1 and 2-2 show the old gimbal design and Fig. 2-3, 2-4 and 2-5 show the redesigned gimbal. The method of passing the hydraulic oil to the rotor was also changed. In the original base plate four hydraulic unions were used to feed the oil in and out of the outer and inner gimbals. On the new design, two dual port hydraulic unions were used which allowed a more compact gimbal arrangement and a reduction in the length of hydraulic pipes.

2.2.2 Rotor

The four-bladed rotor diameter was 1.54m and consisted of four glass fibre reinforced plastic Göttingen 436 section blades of 60mm constant chord, without twist. The active length of the blade from the tip to root attachment was 0.70m, with an approximate two dimensional lift curve slope of 6 per radian. The blade was mounted in the rigid hub without any mechanical

flap or lag degree of freedom and the pitch of the blade was directly controlled by pitch links to the swash-plate. The weight of the blade was given by the manufacturers as 0.171 Kg/m, and it was balanced so that its centre of gravity coincided with the centre of lift at the quarter-chord point. The design of the blade allowed a maximum operating speed of 1600 RPM. The normal operating point of the rotor was at 1200 RPM giving a tip speed of 97 m/s, with a nominal root pitch setting of 12 degrees. At this condition the rotor would be expected to be operating at a thrust coefficient of 0.014 providing about 300 N of lift[1]. The rotor is driven by a 10KW hydraulic motor powered from a hydraulic supply at pressures up to 3000psi. The Lock number of the rotor based on an average blade weight of 0.171 Kg/m was approximately 4. Figures 2-5 and 2-6 show the rotor, with the redesigned gimbal, mounted in the wind tunnel. Noticeable is the aerodynamically clean side of the rotor on the right side, and the 'sky hook' attachment from the tunnel roof.

2.2.3 Swashplate

The swashplate was of conventional design and is shown in Fig. 2-7, consisting of a lower section, which is rotationally fixed with respect to the base plate and an upper section which rotates with the hub, separated by a ball bearing. The inclination of the swashplate is determined by three actuators connected to the lower section. Upper and lower sections are connected to the hub and base plate respectively by scissor links. A spherical bearing allows the swashplate to be inclined about the main rotor shaft and move vertically. The initial swashplate is shown in Fig. 2-8. The conservative design of the lower and upper plates was reduced in the new swashplate shown in Fig. 2-7, making it lighter and more compact. This in turn allowed the base plate to be reduced and the gimbals to be brought in closer.

---

[1]These estimates were obtained from a rotor performance program developed internally at the University of Bristol, configured to the present rotor. [Bunniss 1984]

2.2.4 Actuation system

Three rare-earth electric actuators are connected to the lower swash-plate through planetary roller screws and, together with the swashplate, can provide blade-root pitch changes in excess of 500 degrees per second. The maximum movement of the actuators allows approximately 30 degrees of blade pitch movement. The actuators are controlled electronically and have individual incremental shaft encoders to monitor their positions to within 1μm. The bandwidth of the actuation system is approximately 60 Hz. Micro switches on the actuators provide limits to the movement of the actuators and allow a quick shutdown in the case of an actuator run-away.

2.2.5 Blade Instrumentation

Strain gauges on the blade provided blade deflection information. The signals from the strain gauges were brought from the rotating hub to the base plate using a high quality slip-ring. The slip-ring unavoidably introduced noise into these signals. Several locations of the strain gauges were tried to maximise the obtained signal. In the final design, silicon strain gauges were used located at 26 % R, which gave much increased signal levels. The signals were taken from the slip-ring into a multi-channel strain gauge amplifier.

2.2.6 Control System

The task of controlling the rig, monitoring its safe operation and gathering the data is performed by a computerised system consisting of a master processor and eight slave processors or digital signal processing boards (DSP). The detailed architecture and on-line safety monitoring are given by Brinson [Brinson 1991]. Additionally, the system consists of a 40 MB hard disk, floppy disk and 8-channel strain gauge amplifier and 16-channel analogue-to-digital converter. Each DSP has dedicated tasks, such as controlling the rotor speed, the swashplate position or reading the shaft encoders. The rig software runs at a frame rate of 500 Hz, which is the speed at which information about the blade flapping and induced flow are

gathered. All analogue data are fed through anti-aliasing low-pass filters, with cut-off frequencies of 238 Hz, before sampling by the analogue-to-digital converters.

Significant effort was put into the design of active safety monitoring of the rig [Brinson 1991] so that it could be shut down safely and quickly automatically, if there were a malfunction. A schematic of the control hardware configuration is shown below.

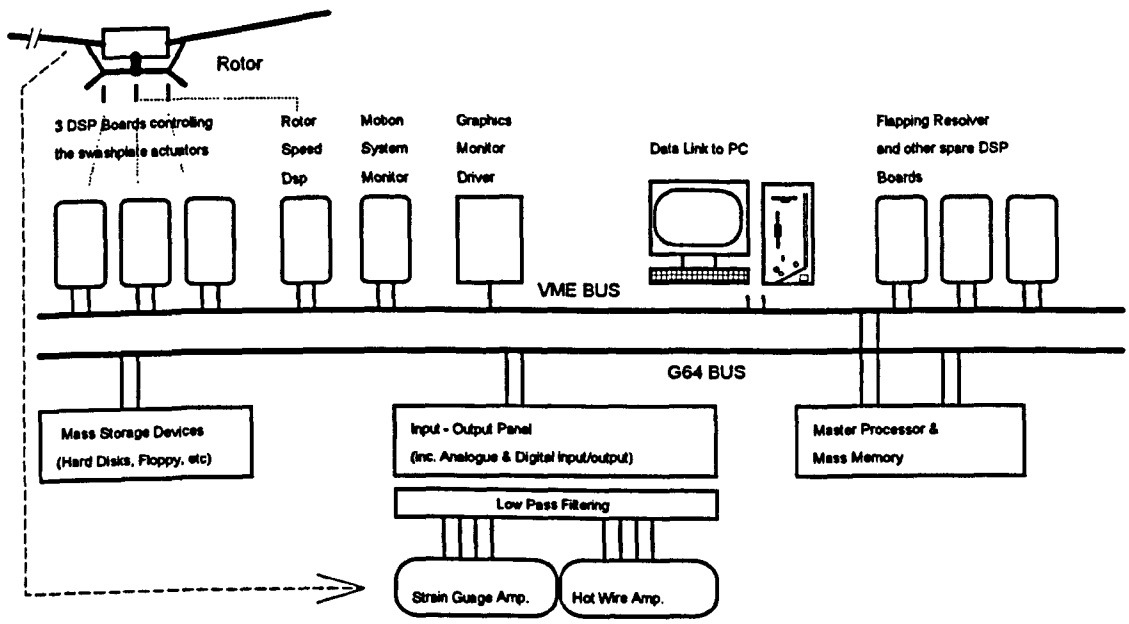

Schematic of Control Hardware

Fig 2-9 shows the control console mounted next to the wind tunnel.

2.2.7 Pressure Transducers

The use of pressure transducers and pitot-static pressure tubes in the measurement of steady airflow is covered well in the literature [Ower 1977]. Four pitot-static tubes and pressure transducers were available. The difference between the pressure of the flow brought to a standstill (total pressure) and the flow static pressure (measured on a surface tangential to the flow) is directly related to the speed of the flow, and this is measured by the pressure transducers. Theoretical analysis of this is given by [Ower 1977] , but essentially the relationship between flow speed and transducer output is given by:

$$V_{out} \propto 0.5\rho A V^2 . \qquad (2\text{-}1)$$

Care has to be exercised when using pitot-static tubes for the measurement of fluctuating flows, as the dynamics of the trapped air between the pitot static tube and pressure transducer need to be considered and experimental results corrected accordingly. The signal from the pressure transducer amplifier was digitised and a look-up table used to find the associated velocities.

2.2.8 Hot Wires

Most of the flow measurements were obtained from hot wires. Due to equipment constraints three different systems were used, however the operating principles of all are identical. A small heated wire approximately a micron thick and 5 mm long is placed in the flow. The flow dissipates heat or energy from the wire. The resistance of the wire is directly related to its temperature. Any change in resistance is registered by the hot-wire bridge and a closed loop feedback system increases the voltage applied to the wire to maintain a constant temperature. The power required to keep the hot-wire at a constant temperature is a measure of the velocity of the air. The signal from the hot-wire bridge is taken through an analogue-to-digital converter to the control system, where it is converted to velocities using look-up tables and then recorded. The detailed operation of hot-wires is given by Ower and Pankhurst [Ower 1977] and many other textbooks. The relationship between the output voltage of the bridge and the flow speed is given by the following relationship

$$V_{out} = V_0 + AU^{0.4}, \tag{2-2}$$

where V_0 is the output voltage for zero flow speed U. The constant A needs to be found for every individual hot-wire as it is material-dependent. It is worth noting that with a hot-wire the sensitivity $\left(\frac{\partial V_{out}}{\partial U}\right)$ decreases as mean velocity increases, whereas for a pitot-tube it increases with speed.

2.2.9 Laser Doppler Anemometry

2.2.9.1 General Theory

The operation of the Laser Doppler Anemometry (LDA) system will be explained here only in very general terms, sufficient for the understanding of the use of LDA anemometry in the context of this thesis. For a comprehensive explanation of the operating principles and practices the reader is referred to work conducted at the University of Bristol [Swales, Rickards, Brake, Barrett 1993].

A laser beam is split into two separate beams, which are focused through two optic heads to converge at a point in space. The intersection of the beams defines the measuring volume. The beams being of the same wave length and synchronisation, will form an interference pattern in the measuring volume due to peaks and troughs of the two beams reinforcing each other respectively. A particle passing through this interference pattern will reflect light at varying intensity as it passes through the peaks and troughs of the interference pattern. The frequency of reflections from the particle passing orthogonally through the measuring volume is related to the speed of the particle, the Doppler Effect, and is captured by photo detectors. The relationship between the Doppler frequency f_d, the wavelength of the laser light λ and the beam separation angle θ is given by:

$$f_d = u\frac{\sin(\theta/2)}{\lambda/2}. \tag{2-3}$$

The top schematic in Fig. 2-10 shows the interference pattern generated by two beams and the received Doppler Burst of a particle passing through the measuring volume.

Seeding

Impurities in the air cannot be relied on to provide sufficient contamination or seeding particles in the air flow, for the generation of frequent burst signals. Therefore artificial seeding, using vaporised oil injected into the flow, is used. Care has to be taken with the seeding, as too

much seeding will 'fog' the laser beams and particularly the reflected burst signal. Too little seeding will result in low data rates.

Burst Processing

The generated Doppler burst is detected using photo-multipliers and its frequency content examined to find the velocity of the particle. It has to be realised that the time at which a Doppler burst occurs, i.e. when a minute particle in the flow, passes through the measuring volume is entirely random, although over a given period a statistical mean of particles passing the measuring volume per unit time will be established.

A means of detecting valid Doppler bursts is provided by passing the detected signal through a series of band-pass filters, low-pass filters and rectifiers to extract two signals known as the Doppler burst 'pedestal' and 'envelope' signals, which are shown in Fig. 2-10. Once the pedestal and envelope signals exceed given thresholds the signal sampling is started, and the arrival time of the burst recorded. The sampled Doppler burst is then passed through extensive frequency analysis to obtain the frequency of the Doppler burst and hence the speed of the detected particle.

3D Coincidence

By using three sets of beam pairs, each pair of beams at a different frequency, and originating from different geometric positions, the measurement of a particle's velocity in three directions is made possible. Knowing the beam geometry it is possible to resolve the velocity components of the particle into the usual three-dimensional orthogonal velocity components with respect to a global co-ordinate system. For this to be possible it has to be ensured that the three photo multipliers examining the Doppler bursts generated from the three beam pairs are looking at the same particle, as otherwise the resolving of the global velocity components will not be possible. For this purpose it is necessary to synchronise the burst spectrum analysers so that in addition to the pedestal and envelope burst detection a valid signal is

accepted only if all detectors detect a valid Doppler burst at the same time. This is termed coincidence filtering.

If the three measuring volumes of the three beam pairs only partially overlap then it is likely that a burst detected by one photo-multiplier is not accepted by the other and hence no measurement is made. The accurate alignment of the three measuring volumes as well as the receiving optics to that same volume is crucial in establishing high data rates.

Advantages & Disadvantages

The advantages of the LDA lie predominantly in the capability of taking non-intrusive, three dimensional velocity measurements of a flow. In the case of rotor work a further advantage is that measurements can be made very close to the rotor where safety considerations prevent intrusive test techniques such as hot wires or pitot-static tubes.

The disadvantages of the system lie in its sophistication and sensitivity. The alignment of the transmitting and receiving optics requires meticulous set-up, special vibration resistant mounting structures and great caution when viewing the laser beams. Obtaining good performance from the system is possible only with careful optimisation of the beam and photo multiplier parameters.

In the case of dynamic tests, the fact that the received velocity information of the LDA is not equi-spaced in time, i.e. not at a constant sampling rate, demands that for techniques such as frequency analysis or time-correlation procedures, gathered data be re-sampled at twice the frequency that is associated with the longest period between two samples.

2.2.9.2 Application to Dynamic Inflow Measurements

The aim of using the LDA during the investigation of the dynamic response of the rotor induced velocity was to obtain data to verify the data taken by other means and to take data at positions closer to the blade than would have been possible with intrusive methods, due to the danger of striking the blades. The time available to use the LDA was very limited so that only

some basic investigations, as outlined in Section 2.4 could be done. Some of the problems and solutions, peculiar to the measurement of dynamic inflow will be discussed below.

The operating environment was not ideal for operation on an LDA system. It was found that the relatively flexible wooden tunnel floor made alignment of the system very difficult. In addition, the rotating rotor produced so much vibration that, over a period of time, the heads of the LDA would move slightly relative to each other, and hence the system would drift out of alignment. For safety considerations, should a blade fail, the LDA heads were kept at a level below the rotor plane. The range of the LDA was further limited to an area of only one quarter of the rotor disc due to travel limitations on the traverse. The area covered by the LDA traverse was thus the rotor quadrant extending from 0 to 90 degrees azimuth. Other areas would have been possible by relocating the laser equipment, but were not feasible given the time limitations.

For dynamic measurements of the air flow the data rate of the LDA had to be kept high. Usually a sampling rate at least twice the frequency of interest would suffice. As the LDA however is not an equally-spaced sampling system, with the Doppler burst occurring only at random intervals, it was decided to set the minimum acceptable average data rate at 300 Hz, some ten times as high as the highest frequency of interest. Through careful placement of the seeding generators a sampling rate of approximately 500 Hz to 600 Hz could be achieved. Recirculation in the tunnel, meant that occasionally the wake would not pass so as to take the maximum amount of seeding particles through the measuring volume, and the sampling rate would fall. Long record lengths were used in order to ensure good data repeatability.

Finally, the data taken by the LDA system had to be synchronised with the rotor control system. For the correlation procedure a direct relation between the inputs to the rotor and measured velocities had to be established. Initially the clock on the LDA system was reset at the start of a test run. As the rotor inputs were a known function of time, this should have been sufficient to synchronise the two. A difference in the observed phase for similar test cases was observed between the LDA and similar hot-wire results, and this is discussed in Chapter 6.

Subsequently it was found that the clock rates on the LDA and rig were slightly different, and this affected the phase results of the signal processing procedure. For further tests the synchronisation between the two systems was improved through continuous synchronisation pulses which were recorded with the laser data.

2.3 Frequency Response Method

Examination of the literature showed that there is very limited data looking at the dynamic response of the air, and the existing data deals with only one frequency, 4-per-rev in the case of the experimental work used by Su et al [Su, Yoo & Peters 1992]. The dynamic response of the air needs to be examined over a range of frequencies, not only multiples of the rotor frequency. For this reason a frequency response approach was used.

In this method the rotor was excited at various discrete frequencies and the response of the inflow at these frequencies examined. From this data the gain and phase, frequency response of the inflow with respect to the inputs on the rotor were established.

The advantages of this method, over other approaches such as examination of the time response, are that the rotor can be excited at the same frequency for a lengthy period. A correlation procedure can then be used to examine the inflow response at that frequency. Using long record lengths this approach is insensitive to noise and low signal strengths. This approach is particularly suited for comparisons with the Pitt and Peters dynamic inflow model, as this is a perturbation model, and once the rotor is at its operating condition sinusoids are added to the collective or cyclic actuators at the required frequency and the perturbation inflow response examined. However great care was taken to ensure as little as possible residual cyclic.

The range of frequencies over which the rotor was excited ranged from 0.5 to 30 Hz. In initial experimental work a total of 36 intermediate frequencies were used. This generated approximately 4.5 MByte of data for each run, which was unnecessarily large, and a reduced set of 12 frequencies was subsequently used. The table below lists the 12 frequencies used in

the majority of the work. In all results the frequencies are given as dimensional frequencies in units of Hertz. For comparison the table below also shows the non-dimensionalised frequencies (non-dimensionalised on shaft speed) for the three rotor speeds used in this work.

Frequency [Hz]	Non-Dimensional Frequency [1200 RPM]	Non-Dimensional Frequency [1300 RPM]	Non-Dimensional Frequency [1500 RPM]
0.5	0.025	0.023	0.020
1.0	0.050	0.046	0.040
5.0	0.25	0.231	0.200
10.0	0.50	0.46	0.40
12.5	0.62	0.58	0.50
15.1	0.75	0.70	0.60
17.2	0.86	0.79	0.69
20.0	1.00	0.92	0.80
21.7	1.08	1.00	0.87
27.7	1.38	1.28	1.11
29.4	1.47	1.35	1.18

Table 2-1 Experimental Rotor Excitation Frequencies

The inputs to the rotor for both the collective and cyclic experiments consisted of root pitch changes of 1.43 degrees. Ideally, larger pitch changes would have been used, which would have resulted in larger inflow perturbations, but fatigue considerations of the blade prevented this. From computational predictions of performance [Bunniss 1984] the expected amplitude of the low frequency inflow variation was 0.85 m/s for the above root pitch inputs. The frequency responses are given in the usual Bode plot format, where gain and phase are given over a frequency range shown logarithmically. The gain in Decibels is defined as the decimal log of the output response - the inflow or blade flapping perturbation - over the input - the rotor excitation - multiplied by 20. The table below gives the relationship between the gain and actual perturbations for the inflow and flapping response. The gain of the inflow response is always given in units of metres/second per radian and the coning gain as radian/radian.

Coning or Flapping Gain (Input Amplitude: 1.43 deg 0.025 rad)		
[dB] (rad/rad)	[rad]	[deg]
-20	0.0025	0.143
-15	0.0044	0.254
-10	0.0079	0.453
-5	0.0140	0.802
0	0.0250	1.432

Inflow Gain (Input Amplitude: 1.43 deg 0.025 rad)	
[dB] (m/s / rad)	[m/s]
0	0.0250
5	0.0444
10	0.079
15	0.140
20	0.250
25	0.444
30	0.790

Table 2-2 Coning & Inflow Gain Conversions

2.4 Review of Experiments

The original rig was initially mounted in a test chamber on a pedestal approximately 2m above ground level and 1.5m from the roof. The chamber was open to one side, with a wire safety mesh. All initial work was carried out here, and the results given in Chapter 3. The collective pitch of the rotor was excited over a range of frequencies between 0.1 and 30 Hz with 36 intermediate frequencies. The induced velocities were measured using four pitot static tubes with pressure transducers. The choice of pressure transducers was made purely from a practical and economic viewpoint. The aim was to measure the flow field at as many simultaneous positions as possible. Four pressure transducers were available. With hindsight, and for the reason given in Chapter 3, hot wires would have been a better choice had they been available. During the later stages of this first experiment one hot wire channel was added to the four pitot static tubes.

The initial experiments highlighted a number of areas of weakness in the experimental set-up. The large number of test frequencies and data taken for each at a sampling rate of 500 Hz over test periods lasting tens of seconds produced unwieldy amounts of data. Although this body of data was reduced when processed, it was thought prudent to keep the originally recorded test data, should it be needed at a later stage. Through careful spacing of the test frequencies, with only a few points at low frequency where the dynamic changes to the inflow and flapping were only occurring gradually, and by a concentration of points in the interesting region above 10 Hz, the number of test frequencies was reduced to twelve.

The original rotor gimbal, shown without rotor head and ancillaries (Fig. 2-1) was large and bulky compared to the area of the rotor. Flow visualisation showed that it significantly affected the flow of air beneath the rotor. This gimbal utilised four hydraulic unions, to bring the hydraulic oil in to the motor through the outer and inner gimbal axes. Fig 2-2 shows a side view of the gimbal, with some of the large bore hydraulic pipes. The aerodynamic environment of the test chamber, was relatively good, with only limited recirculation due to the height of the chamber and its open section on one side.

After the completion of this first set of experiments it was decided to address some of these deficiencies. The gimbal was redesigned and reduced to produce less aerodynamic interference. Replacing the initial strain gauges on the blades with ultra-high-gain silicon gauges gave an order of magnitude improvement in the signal to noise ratio. Additional hot wire channels were introduced so that at least 4 simultaneous flow measurements could be made. The software was also modified, to have fewer test frequencies, especially at low frequencies, where the coning and inflow behaviour were not changing. The design changes and modification to the software, given in detail in Chapter 3, took nearly a year to complete. During this time the rotor hub and swash-plate were also disassembled and inspected for wear.

For further tests, the rotor rig was moved from the rotor test section to the return section of a wind tunnel. The reasons for this were three-fold. The rotor test chamber was needed for other research; the rig needed to be moved to a wind tunnel for forward flight work on another

project; and it was also hoped that forward flight inflow measurements would also eventually be taken. The difficulty experienced in moving the rig, associated electronics and hydraulic power pack, meant that the rig was permanently kept in the return section of the tunnel. The tunnel measured 2.5m by 5m and was worse than the test chamber with regard to recirculation. A tunnel with an open bottom section as used by Liou [Liou, Komerath et al, 1994], to reduce circulation would have been better, but this was not available.

The next experimental case considered looked at the radial variation of the induced flow due to collective pitch variations, which had not been possible with the old rig. The hot wire could not be moved very close to the rotor blades, because of the danger of contact and catastrophic damage to the rotor and instrumentation. At this time a Laser Doppler Anemometer (LDA) became available for a short time and it was considered that the LDA, would be a useful tool for obtaining non-intrusive measurements close to the rotor and also confirm the hot wire results. However the set-up of the LDA, its operation in a very vibratory environment, and interfacing to the rig, posed severe problems, which are discussed in more detail in Chapter 6 together with the results obtained.

The next step was to consider the induced flow field due to cyclic inputs to the rotor. Again the rotor was kept in the return section of the wind tunnel and hot wires formed the primary source of instrumentation. Again the LDA was available for a limited period and measurements were taken to back up the hot-wire results. The cyclic input to the rotor was such that the maximum pitch of the blades was reached at azimuth positions of 15° and 195°. The maximum blade response occurred at approximately 70° and 250° azimuth resulting in predominantly rolling moments. In future work further cyclic inputs should be considered. Some work was also carried out with a tunnel speed setting of 2.5m/s, giving an advance ratio of 0.025. Much further work needs to be done away from the hover and some of the proposed further research outlined in Chapter 8 had to be abandoned due to failure of a hard disk on the control system.

2.5 Summary

The experimental facilities needed to measure the dynamic induced flow response are considerable, both in terms of the rotor model and the inflow instrumentation. A unique dynamic facility with reduced aerodynamic interference was developed from an existing sophisticated rotor rig. Dynamic tests could be performed at frequencies up to 1.5 times the shaft speed and several methods for measuring the dynamic inflow, including non-intrusive Laser Doppler Anemometry were available.

The induced flow was investigated primarily using hot-wires and Laser Doppler Anemometry, with some initial work being carried out using pitot-static probes. Fatigue and structural load limits resulted in relatively small rotor pitch changes. To examine the resulting inflow velocities long record lengths were used over a range of rotor excitation frequencies. The results were then analysed using a correlation procedure, which gave the inflow response in terms of gain and phase with respect to the input excitation. The measured coning response was similarly recorded.

Figure 2-11 shows a schematic of the rotor rig in the wind-tunnel with the orientation of the primary rotor axes and the inflow measurement positions.

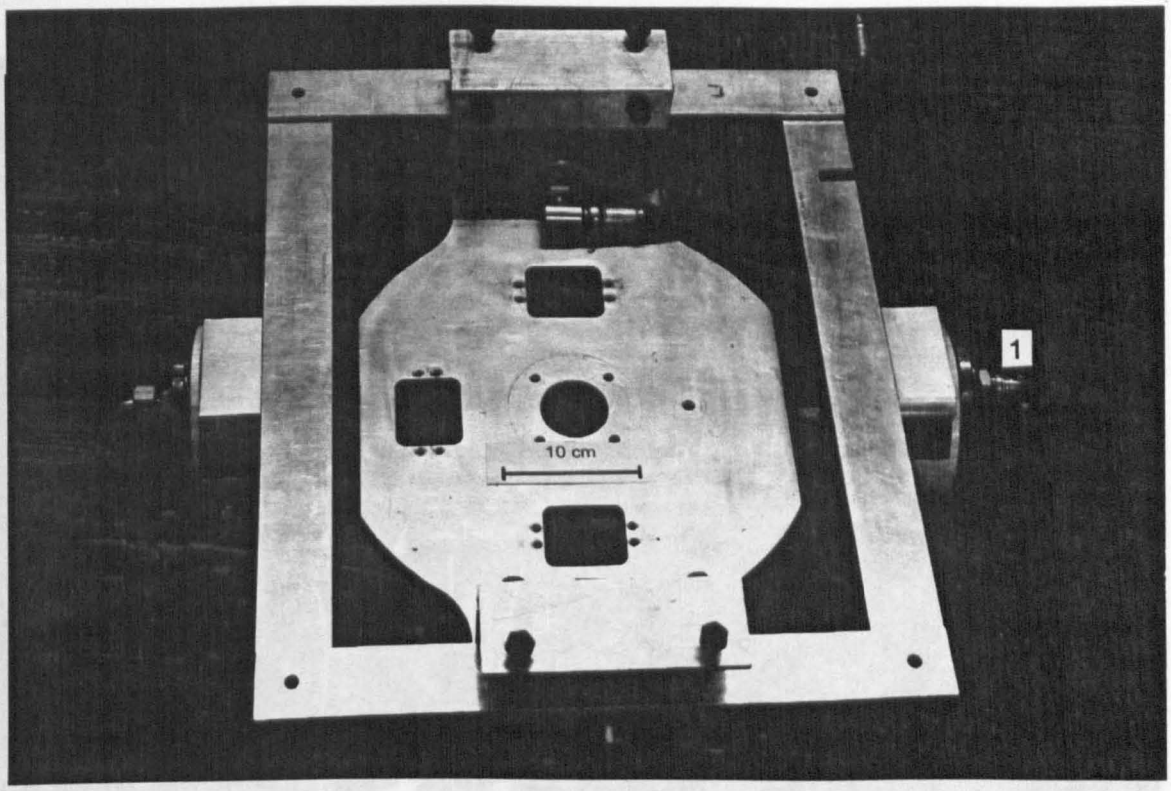

Fig. 2-1 Top View of the Old Gimbal showing Inner and Outer Gimbals
(Rotor Head Removed, 1- Single Line Hydraulic Union)

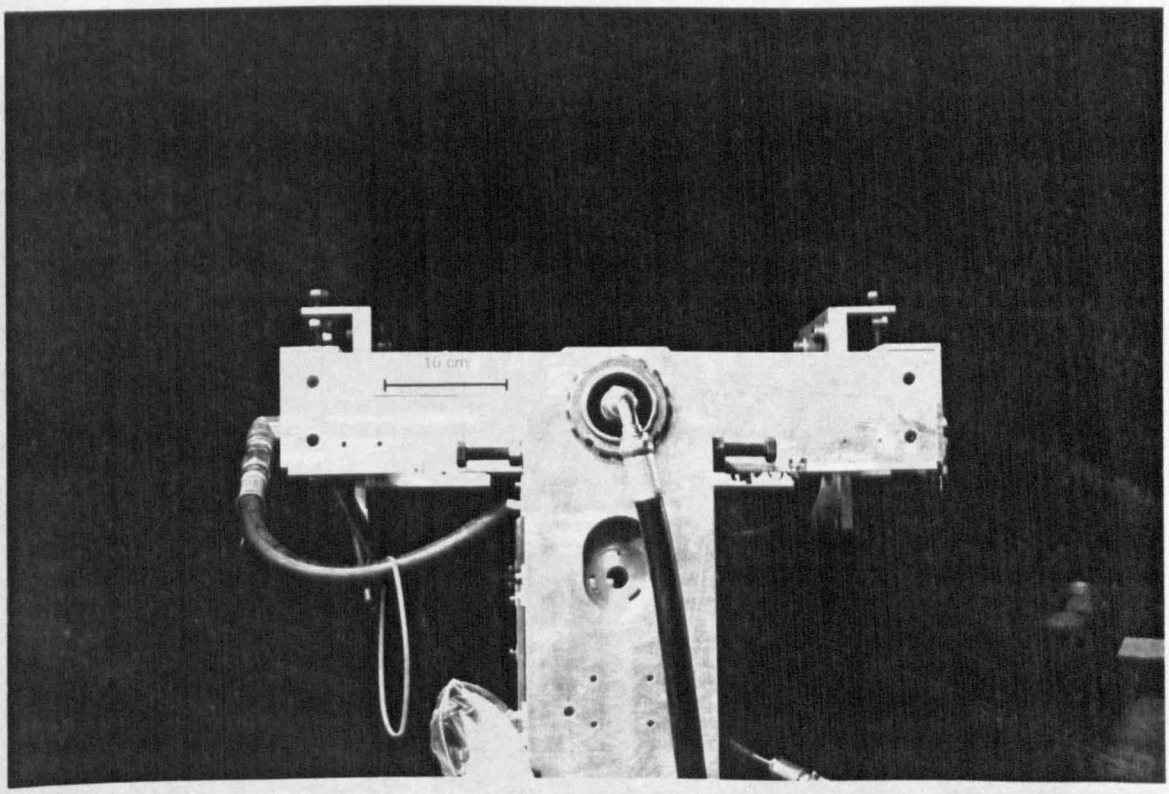

Fig. 2-2 Side View of the Old Gimbals with Single Line Hydraulic Unions

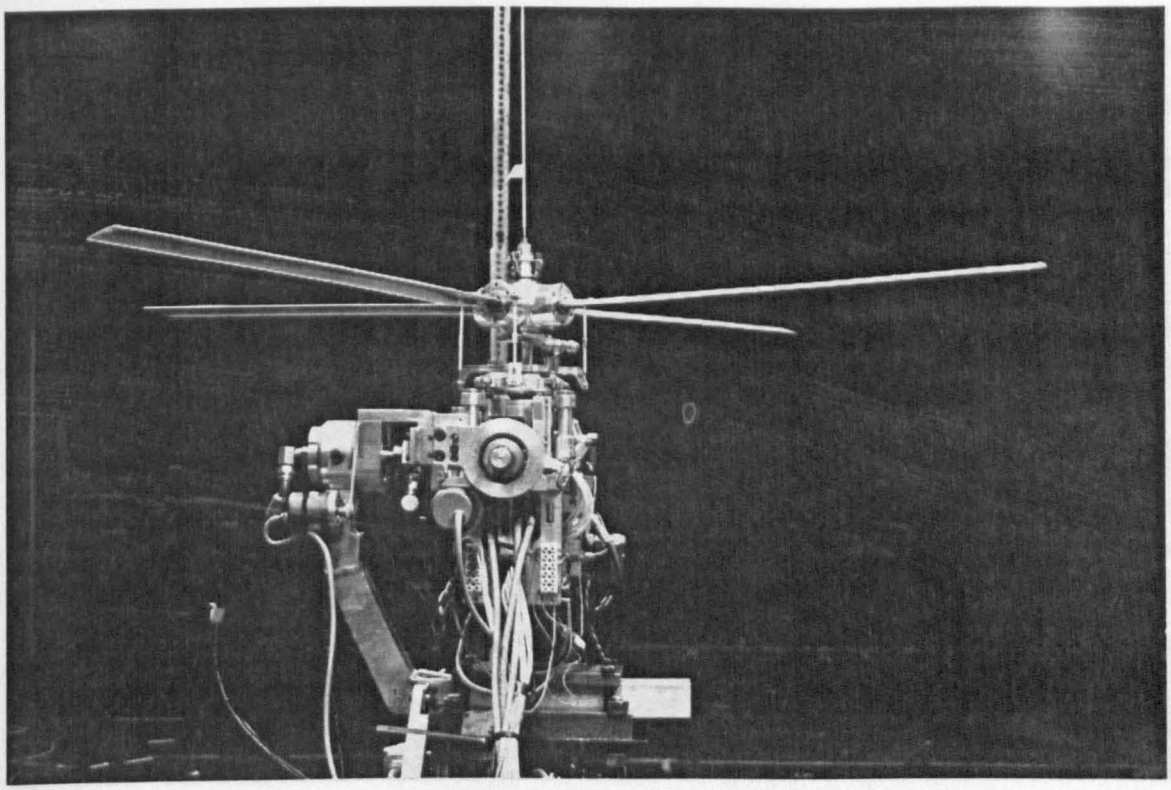

Fig. 2-3 View of the Rotor Rig with Redesigned Gimbal from Behind
(Aerodynamically Clean Side to Starboard)

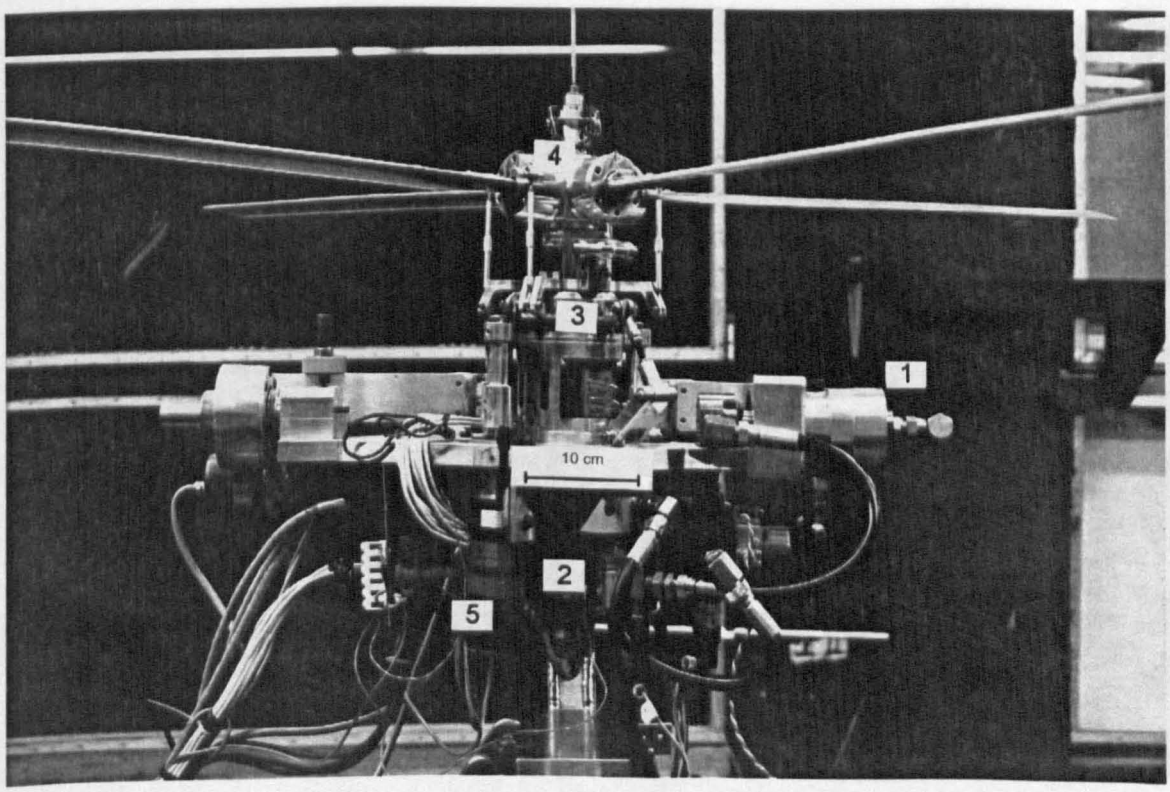

Fig. 2-4 Side View of the Rotor Rig with modified Gimbal
(1- Dual Line Hydraulic Union, 2- Hydraulic Motor, 3- Swash-Plate,
4- Hub, 5- Electric Actuators)

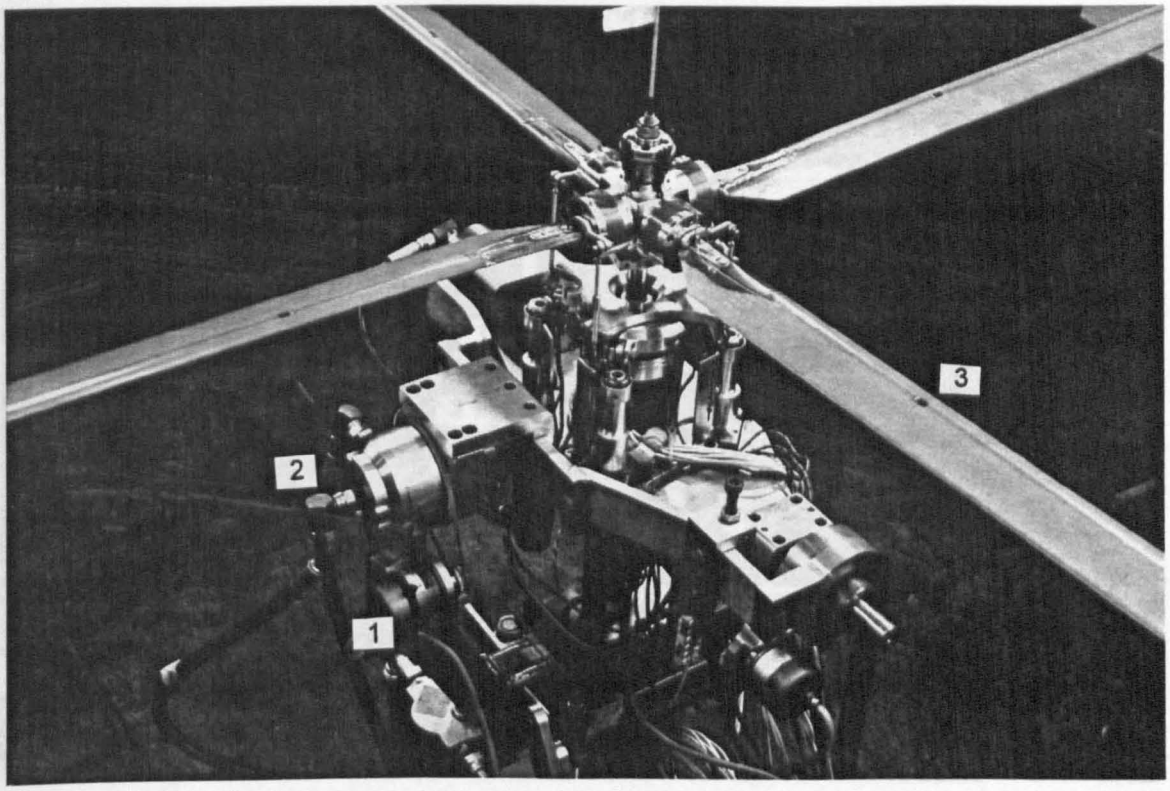

Fig. 2-5 Rotor Head and Actuators on the Redesigned Gimbal
(1- Shaft Encoder, 2- Hydraulic Union, 3- Strain Gauges)

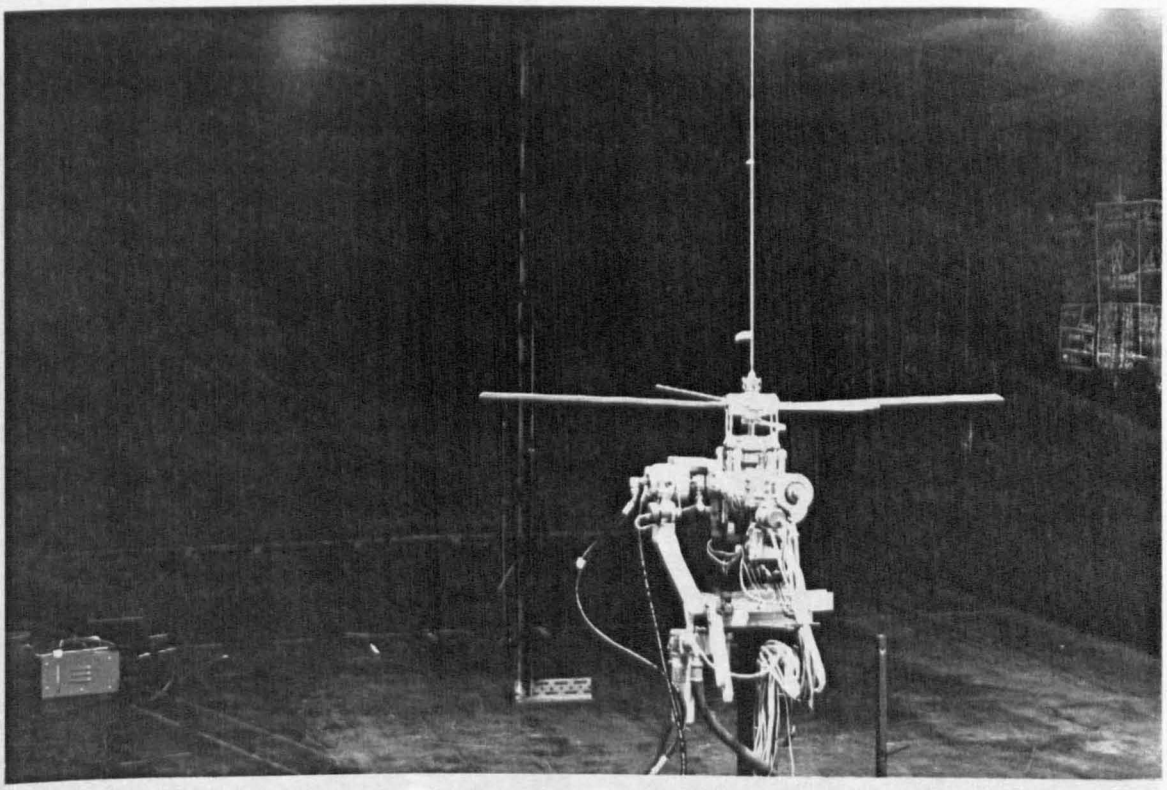

Fig. 2-6 Rotor with Redesigned Gimbal Mounted in the Wind-tunnel
(View Looking Upstream)

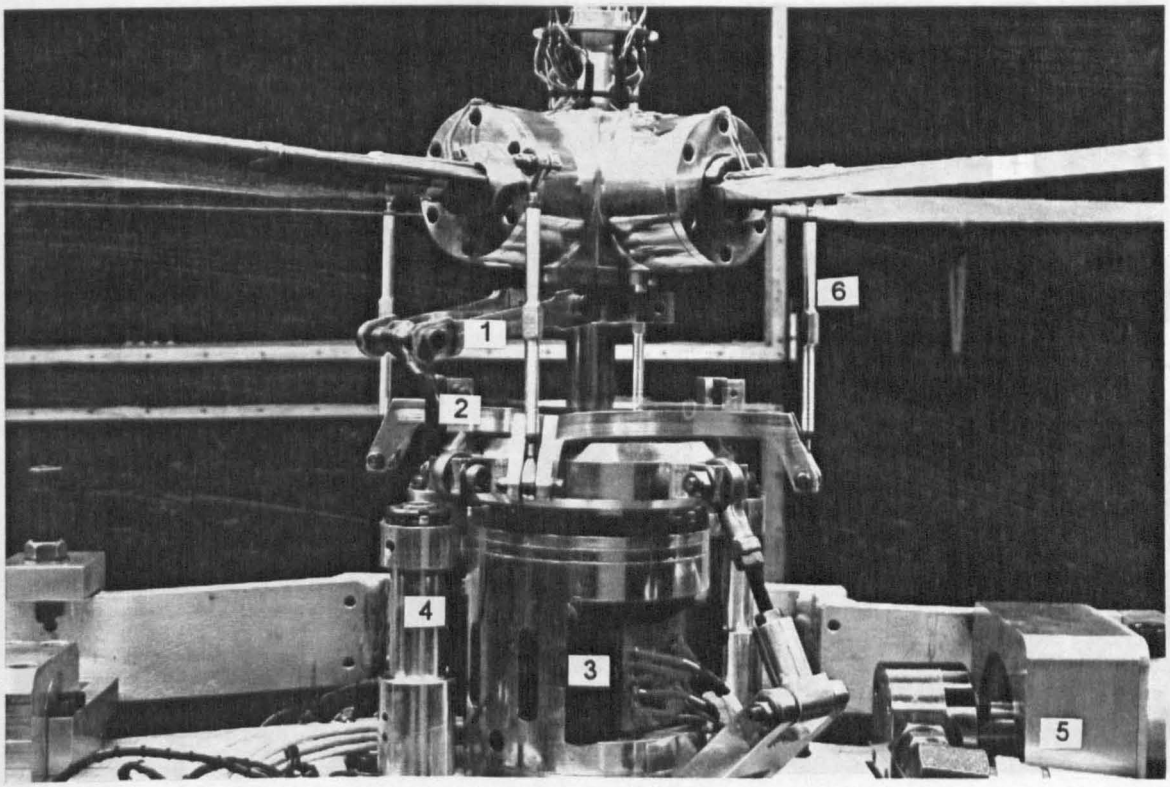

Fig. 2-7 Close-up of Redesigned Swash-plate and Rotor-head
(1- Upper Scissors, 2- Lower Scissors, 3- Slip-ring,
4- Planetary Roller Screw, 5- Dual Line Hydraulic Union,
6- Pitch Links)

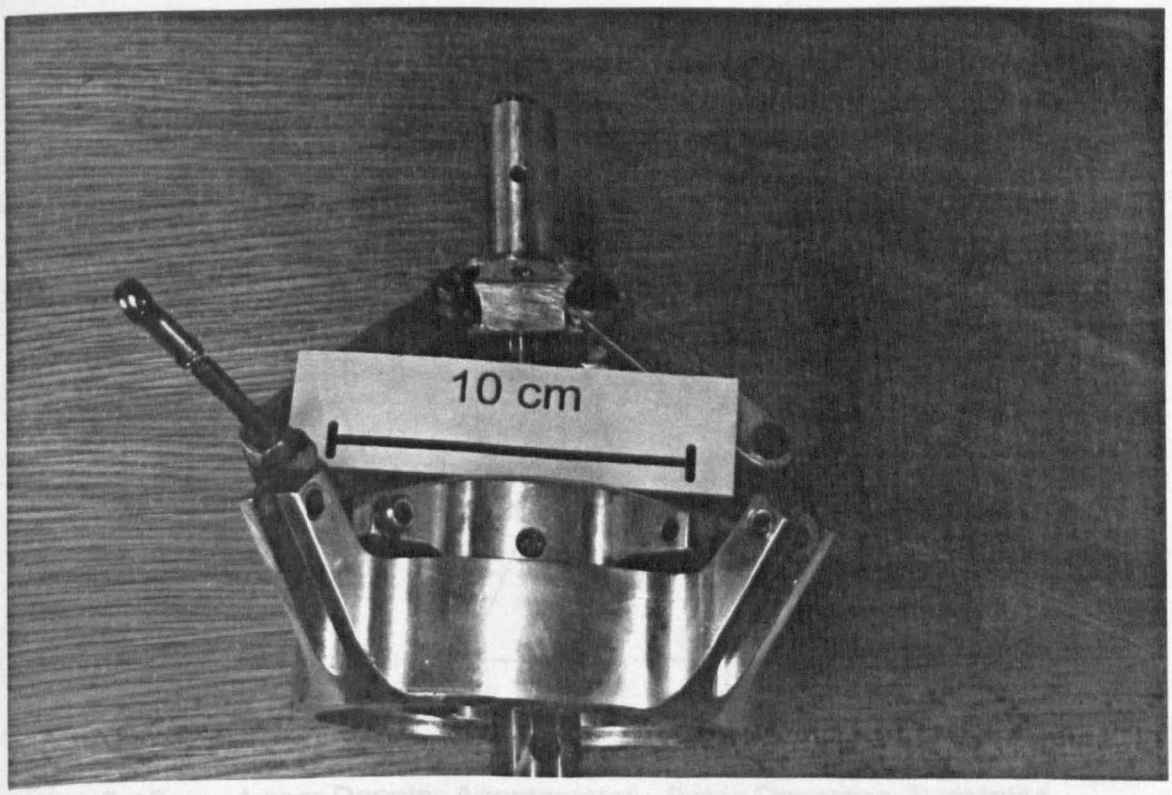

Fig. 2-8 Original Swash-Plate

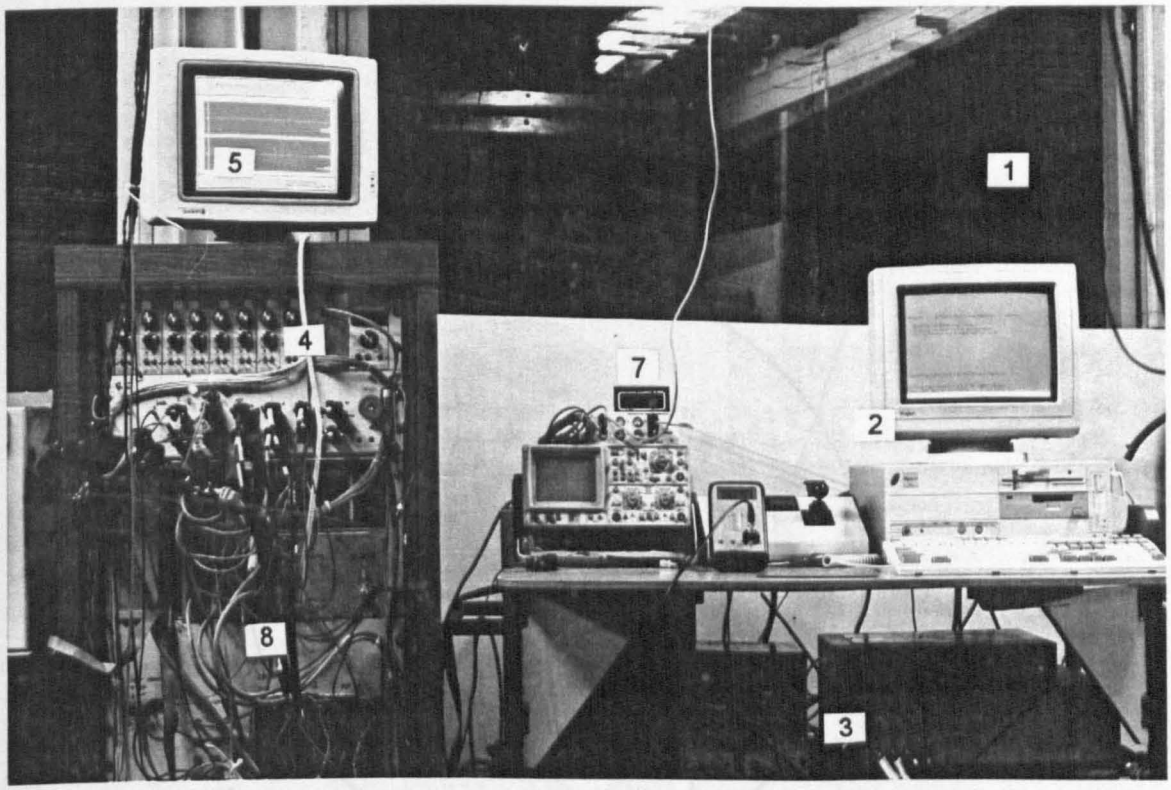

Fig. 2-9 Control Panels mounted near Wind-tunnel
(1- Bullet Proof Glass, 2- Data Processing PC, 3- Hot-Wire Amp.,
4- Strain Gauge Amp., 5- Graphics Display, 7-Flow Meter and Blade Signal
Monitor Scope, 8-Control Cabinet with DSP boards)

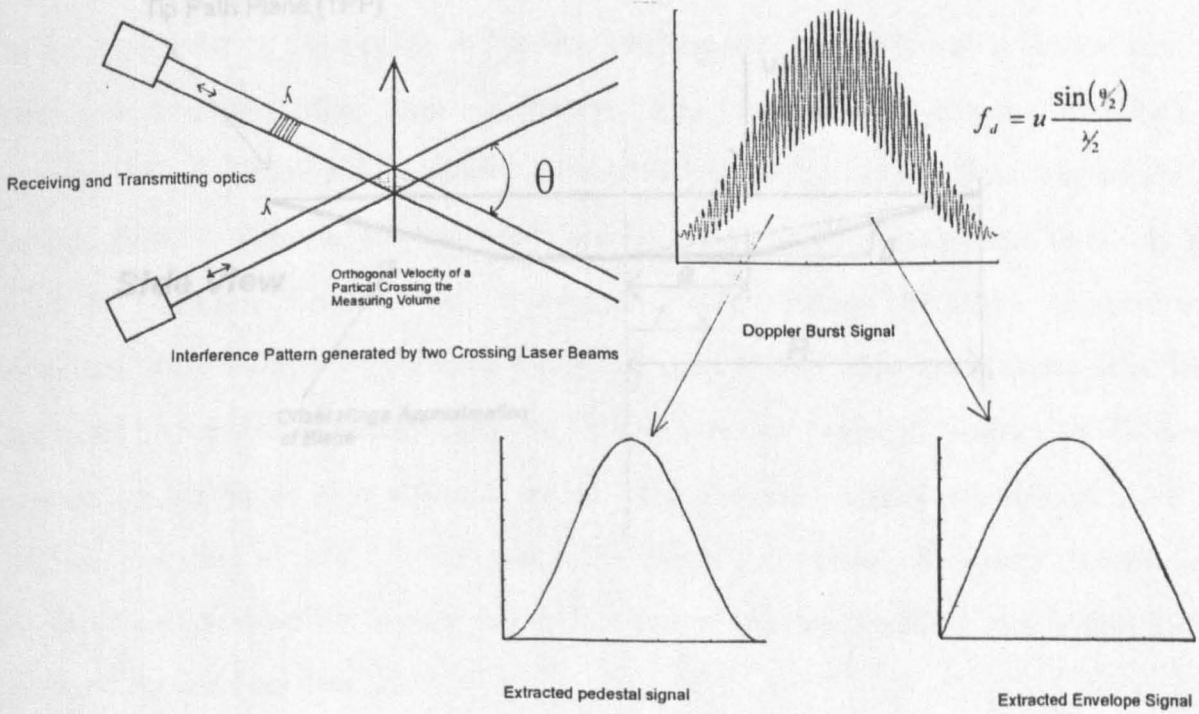

Fig. 2-10 Laser Doppler Anemometer - Basic Operation Principles

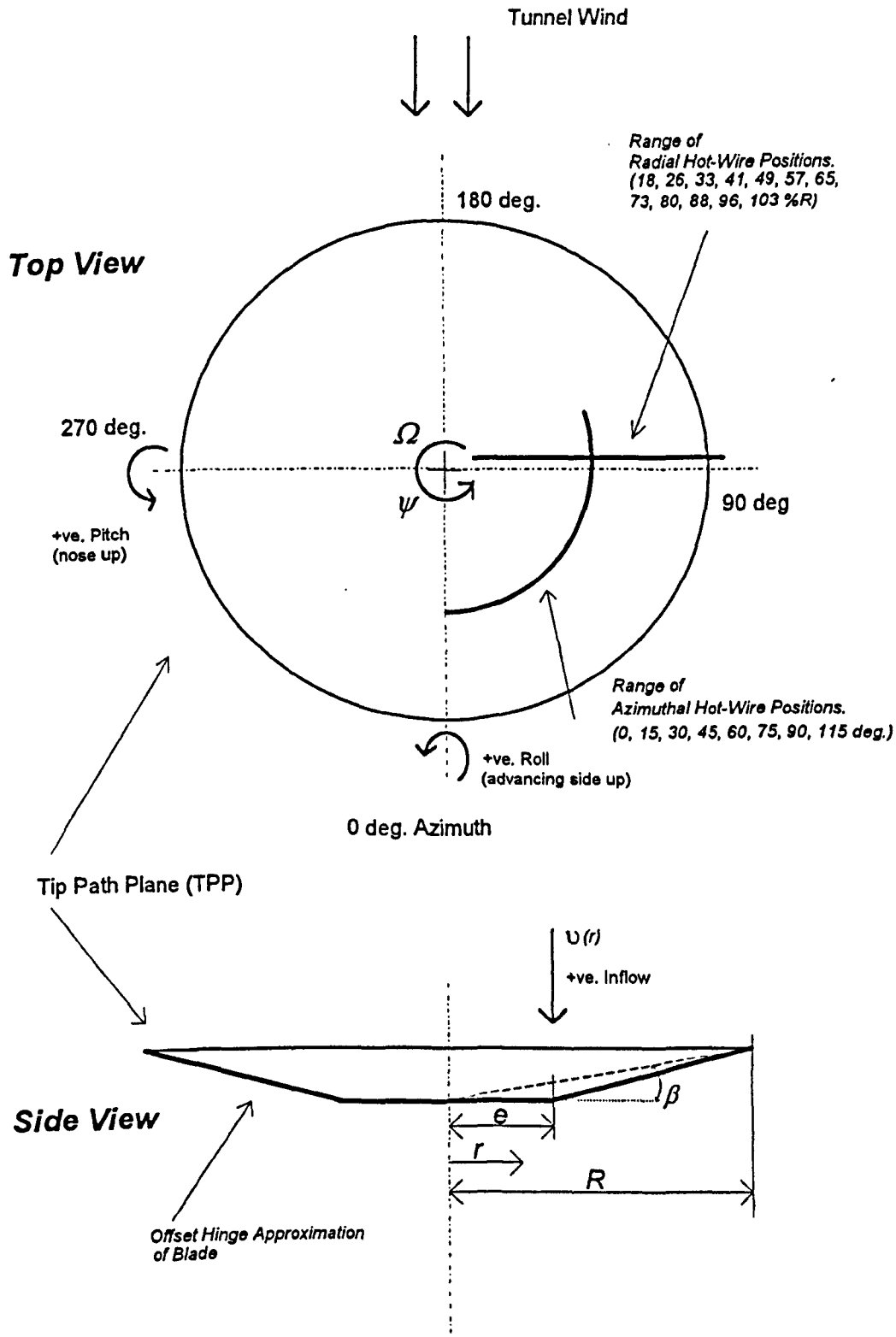

Fig. 2-11 Definition of Basic Rotor Geometry

Chapter 3
Initial Correlation of Coning / Inflow Models with Experimental Data

3.1 Introduction

This section documents the first efforts to obtain experimental dynamic inflow measurements beneath a rotor on a hover stand. The aims were to gather dynamic inflow data using suitable instrumentation and to compare the results with those predicted by simple coning / inflow models including dynamic inflow theory. This highlighted areas in which the rig and instrumentation could be improved. Changes to the initial models were made to account for the semi-rigid hub and real wake affects. The models were modified further as explained below.

3.2 Theoretical Coning / Inflow Models

In previous work by Chen [Chen & Hindson 1987] analytical models with a vertical motion, coning response and inflow degree of freedom (d.o.f.) were used to examine the effects of dynamic inflow. These 3 d.o.f. models are relatively simple to develop from first principles, include dynamic effects of the inflow and are easily formulated in state-space form. In the work by Chen and Hindson [Chen & Hindson 1987], although the inflow response was examined, there were no experimental data to compare it with. The models considered here are based on those developed by Chen, but without a vertical degree of freedom, as this is not present on the hover-stand mounted model. The analytical models are also modified to account for the semi-rigid rotor hub. The effects of various deficiency factors and improvements such as root cut-out and tip loss factors are also examined with respect to the gathered experimental data.

The general structure of a 2 DOF Coning/Inflow model with first-order inflow and second order coning, is given below:

$$\dot{x} = Ax + Bu,$$

$$A = \begin{bmatrix} \upsilon_\upsilon & 0 & \upsilon_{\dot{\beta}} \\ 0 & 0 & 1 \\ \beta_\upsilon & \beta_\beta & \beta_{\dot{\beta}} \end{bmatrix}; \quad B = \begin{bmatrix} \upsilon_\theta \\ 0 \\ \beta_\theta \end{bmatrix}. \tag{3-1}$$

$$x = \begin{bmatrix} \upsilon & \beta & \dot{\beta} \end{bmatrix}, u = \theta_0$$

The following section will focus on the main steps in the derivation of the model and identify principal improvements. A detailed derivation of all models is given in Appendix B.

The derivations rely on three steps, which are common to all five models discussed. Firstly, an expression relating the inflow to the thrust is needed. Secondly an expression for the thrust in terms of inflow and coning using blade-element theory is found. Lastly an equation describing the coning dynamics of the blades is required. All three equations are combined together to produce the two d.o.f. coning inflow models below.

3.2.1 Dynamic Inflow / Thrust Relationship

The Carpenter/Fridovich Representation

In 1953 Carpenter and Fridovich [Carpenter & Fridovich 1953] proposed that the dynamic behaviour of air flowing through a hovering rotor can be modelled by considering the analogy between the rotor and an impervious disc moved normal to its plane. The apparent additional mass of the fluid associated with an accelerating impervious disc was previously found as 63.7 % of the fluid mass in the circumscribed sphere. After formation of a slipstream this analogy is no longer strictly valid, but it was assumed that the apparent air mass was a good approximation to that which would be accelerated by the rotor. The force necessary to accelerate the air is simply given by the product of the apparent additional mass and the change in induced velocity. The momentum theory result for a rotor with no vertical velocity is thus modified accordingly and stated below, where υ is the velocity at the rotor:

$$T = m_a \dot{\upsilon} + 2\left(\pi R^2\right)\rho\upsilon(\upsilon). \tag{3-2}$$

The classical momentum theory result $T = 2\rho A \upsilon^2$, where υ is the velocity at the rotor disc is obtained by considering the power, momentum and mass flow equilibrium of a rotor, assuming that the flow velocity toward the rotor but far upstream is zero, and the thrust a result of the change in momentum between far upstream and downstream and also applying the energy balance between the thrust created by the rotor and the energy imparted to the flow. A good discussion of this is given by Johnson [Johnson 1980, 29ff].

In Equation 3-2, for a rotor with flapping blades the velocity υ is itself affected by the coning motion of the disc and this has to be taken into account. Considering a rotor disc coning about the centre of the hub, the velocity of annular elements of the rotor disc with respect to the rotor hub can be found. Integrating this over the rotor disc and dividing by the rotor area gives an average velocity of the rotor disc with respect to the hub of $\frac{2}{3}\dot{\beta}R$ [Appendix B] and Equation 3-2 is modified accordingly, giving:

$$T = m_a \dot{\upsilon} + 2(\pi R^2)\rho\upsilon(\upsilon + \frac{2}{3}\dot{\beta}R). \qquad (3\text{-}3a)$$

The coning motion of the hub is effectively treated as a vertical velocity component of the rotor disc, the relevant theory is expanded by Johnson [Johnson 1980].

This inflow expression forms the basis of the Carpenter and Fridovich formulation [Chen 1987]. The value of the affected air mass m_a is given as 63% of the mass of a sphere of air of radius R. Non-dimensionalized [Appendix B] Equation 3-3a becomes:

$$C_T = 0.849\frac{\dot{\lambda}}{\Omega} + 2\lambda(\lambda + \frac{2\dot{\beta}}{3\Omega}). \qquad (3\text{-}3b)$$

The Pitt/Peters Inflow Model

The Pitt and Peters dynamic inflow formulation is explained comprehensively in Chapter 1. For the hover case the relationship between the aerodynamic loading on the rotor and the inflow response is given by:

$$C_T = \frac{M_{11}}{\Omega}\dot{\lambda} + 2V\lambda; \text{ where } \lambda = \frac{\upsilon}{\Omega R}, \tag{3-4}$$

and where V is the total resultant flow through the disc, non-dimensionalised on rotor speed and radius. Note also that the M_{11} coefficient has been divided by rotor speed, as the Pitt / Peters model assumes non-dimensional time. As discussed in Chapter 1, two values for the apparent mass factor M_{11} in hover are considered, depending on the loading distribution used in the theoretical derivation of this parameter. For a *corrected* pressure distribution M_{11} is $128/75\pi$ and for a *uncorrected* pressure distribution M_{11} is given as $8/3\pi$.

3.2.2 Thrust from Blade Element Theory

In the above equations it is desirable to eliminate the rotor thrust explicitly. It depends on the local induced velocity, the vertical motion of the hub and the instantaneous blade flapping rate. Blade element theory can be used to develop an expression for the rotor thrust in terms of the above variables by considering the local velocities, angle of attack and lift characteristics of the blade. The differential thrust produced by an elemental annulus on the rotor disc can be expressed as [see Appendix B, Equation B-9]:

$$dT = \tfrac{1}{2}\rho(\Omega r)^2 bac\left(\theta_0 - \frac{\dot{\beta}}{\Omega} - \frac{\upsilon}{\Omega r}\right)dr. \tag{3-5}$$

This is then integrated over the rotor disc, taking root cut-out and tip losses into account.

3.2.3 Blade Flapping Equations

The blade flapping equations for a four-bladed rotor are taken from Chen [Chen 1980], where the following assumptions are made. The rotor blades are assumed rigid both in bending and in torsion, compressibility and stall effects are ignored and a uniform inflow distribution is assumed. The flapping equations were obtained by summing the moments acting on the blade about the flapping hinge. These were the centrifugal, inertia, Coriolis and hinge restraint forces. Further information on the derivation of the flapping equation is given in Appendix E and by Johnson [Johnson 1980]. The definition of the basic rotor geometry and axes are given

in fig. 2-11. The effect of hinge offset has been retained to the order of ε^2. The flapping equation for a four-bladed rotor is shown below:

$$\ddot{\beta}+\Omega\gamma\left(\frac{1}{8}-\frac{\varepsilon}{3}+\frac{\varepsilon^2}{4}\right)\dot{\beta}+\Omega^2\left(f^2{}_R\right)\beta=\Omega^2\frac{\gamma}{8}\left(1-\frac{4}{3}\varepsilon\right)\theta-\Omega^2\frac{\gamma}{2}\left(\frac{1}{3}-\frac{\varepsilon}{2}\right)\lambda. \tag{3-6}$$

The flapping equation may also be modified to include the effects of tip loss [Rosen 1983] which is not accounted for in 2D lifting line theories such as standard blade element theory. An approximate method to account for these tip losses is to assume that outboard of the radial station **R*B** no lift is produced. The tip loss factor used is this work is given by Johnson [Johnson 1980] as $B=1-\frac{\sqrt{2C_T}}{N}$, and is inserted in Equation (3-6) to produce:

$$\ddot{\beta}+\Omega\gamma\left(\frac{B^4}{8}-\frac{B^3\varepsilon}{3}+\frac{B^2\varepsilon^2}{4}\right)\dot{\beta}+\Omega^2\left(f^2{}_R\right)\beta=\Omega^2\frac{\gamma}{8}\left(B^4-\frac{4B^3}{3}\varepsilon\right)\theta-\Omega^2\frac{\gamma}{2}\left(\frac{B^3}{3}-\frac{B^2\varepsilon}{2}\right)\lambda. \tag{3-7}$$

Blade twist can be incorporated into these equations. If constant twist is assumed however, the resulting constant is neglected in small perturbation equations.

The blade flapping equations developed by Chen [Chen 1980] use the blade flapping angle at the location of the flapping hinge. As the centre of reference for the experimental data is taken at the hub centre a correction factor needs to be applied to the flapping angles obtained from the theoretical models.

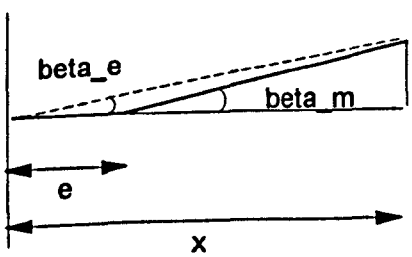

$$y=(R-e)\sin\beta_m$$
$$x=e+(R-e)\cos\beta_m$$
$$\beta_e=\tan^{-1}\left(\frac{(R-e)\sin\beta_m}{e+(R-e)\cos\beta_m}\right)$$
$$\beta_e=\beta_m\left(1-4/3\,\varepsilon\right)$$

This correction was incorporated in the numerical models and all flapping angles can be assumed to be referenced with respect to the rotor axis.

A flapping equation applicable to rotors with hinge offset was also developed by Johnson [Johnson 1980] and is given below. Interestingly although the equation is the same as that derived by Chen [Chen 1980] for a centrally hinged rotor, the terms incorporating hinge offset are different:

$$\ddot{\beta}+\frac{\Omega\gamma}{8}(D1)\dot{\beta}+\Omega^2\left(f^2{}_R\right)\beta=\Omega^2\frac{\gamma}{8}(C2)\theta-\Omega^2\frac{\gamma}{6}(C1)\lambda \tag{3-8}$$

The constants C1, C2 and D1 are given by the expressions below. It should be noted that $\eta=(r-\varepsilon)/(1-\varepsilon)$ is a mode shape which corresponds to rigid rotation about the flapping hinge and fulfils the boundary conditions that $\eta(r=1)=1$ and $\eta=r$ for $\varepsilon=0$ [Johnson 1980]. Since the mode shape is unity at the tip the flapping angle β can be interpreted with reference to the rotor centre and not the location of the flapping hinge, which explains the slightly different derivatives. The above mentioned correction to the flapping angle in the Chen flapping equation thus does not apply here. The coefficients in Equation 3-8 are found from integrations dependent on the mode shape, and are given by Equation 3-9 to 11.

$$C1=3\int_{\varepsilon}^{B}r\eta dr=\frac{3}{1-\varepsilon}\left(\frac{B^3}{3}-\frac{\varepsilon B^2}{2}+\frac{\varepsilon^3}{6}\right)\xrightarrow{B=1}1-0.5\varepsilon-0.5\varepsilon^2 \tag{3-9}$$

$$C2=4\int_{\varepsilon}^{B}r^2\eta dr=\frac{4}{1-\varepsilon}\left(\frac{B^4}{4}-\frac{\varepsilon B^3}{3}+\frac{\varepsilon^4}{12}\right)\xrightarrow{B=1}1-\frac{\varepsilon}{3}-\frac{\varepsilon^2}{3}-\frac{\varepsilon^3}{3} \tag{3-10}$$

$$D1=4\int_{\varepsilon}^{B}r\eta^2dr=\frac{4}{(1-\varepsilon)^2}\left(\frac{B^4}{4}-\frac{2\varepsilon B^3}{3}+\frac{\varepsilon^2B^2}{2}-\frac{\varepsilon^4}{12}\right)\xrightarrow{B=1}1-\frac{2\varepsilon}{3}+\frac{\varepsilon^2}{3} \tag{3-11}$$

Substituting into the flapping equation gives the flapping equation based on Johnson [Johnson 1988] given below:

$$\begin{aligned}&\ddot{\beta}+\frac{\Omega\gamma}{8}\left(\frac{4}{(1-\varepsilon)^2}\left(\frac{B^4}{4}-\frac{2\varepsilon B^3}{3}+\frac{\varepsilon^2B^2}{2}-\frac{\varepsilon^4}{12}\right)\right)\dot{\beta}+\Omega^2\left(f^2{}_R\right)\beta=\\&\Omega^2\frac{\gamma}{8}\left(\frac{4}{1-\varepsilon}\left(\frac{B^4}{4}-\frac{\varepsilon B^3}{3}+\frac{\varepsilon^4}{12}\right)\right)\theta-\Omega^2\frac{\gamma}{6}\left(\frac{3}{1-\varepsilon}\left(\frac{B^3}{3}-\frac{\varepsilon B^2}{2}+\frac{\varepsilon^3}{6}\right)\right)\lambda\end{aligned} \tag{3-12}$$

3.2.4 The Chen/Hindson Model - Model 1

The Chen & Hindson Coning/Inflow model combines the flapping equations for an articulated rotor with no hinge offset or restraint with the Carpenter/Fridovich or Pitt/Peters inflow formulation, the only difference in the inflow formulations being the different apparent mass values. Blade element theory is used in its simplest form to eliminate the thrust in the inflow equations. The system and input matrices are stated below and derived in detail in Appendix B.

$$\dot{x} = Ax + Bu$$

$$A = \begin{bmatrix} -\frac{4\Omega}{M_{11}}(\lambda_m + \frac{a\sigma}{16}) & 0 & -\frac{4\Omega R}{3M_{11}}(\lambda_m + \frac{a\sigma}{8}) \\ 0 & 0 & 1 \\ -\frac{\Omega\gamma}{6R} & -\Omega^2 & -\frac{\Omega\gamma}{8} \end{bmatrix} \quad B = \begin{bmatrix} \frac{4\Omega^2 Ra\sigma}{3M_{11}8} \\ 0 \\ \frac{\Omega^2\gamma}{8} \end{bmatrix}; \qquad (3\text{-}13)$$

$$x = \left[\upsilon, \beta, \dot{\beta}\right]'$$

Henceforth this model will be known as model (1).

3.2.5 The DRA Model - Model 2

The model developed by the DRA in 1989 by Houston [Houston 1989] is based on the Chen Hindson model. A number of improvements were made to improve correlation with experimental data. The uniform induced velocity is based on momentum theory and is corrected to account for actual non uniformity, tip losses and root cut-out. Unsteady effects in the real wake are considered through a lift deficiency factor. The flexibility of the blades is accounted for by a reduction in blade first moment of inertia. The full derivation of the equations of motion is detailed in Appendix B. Although the model assumes an articulated centrally hinged rotor, a blade flap frequency ratio is included, to take account of the small hinge offset of the Puma helicopter, but otherwise the offset is ignored. The other derivatives in the flap equation did not include the terms due to hinge offset. Thrust C* and lift C^* deficiency factors as given by Johnson [Johnson 1980] were also included in the inflow and flapping derivatives respectively, to take account of unsteady aerodynamic effects. The

inclusion of lift deficiency factors in the flapping equations are difficult to justify from a physical viewpoint since it can be argued that once the unsteady effects are included in the inflow derivatives, through a thrust deficiency factor, it is not necessary to include these again in the flapping equation [Houston 1993], through use of a lift deficiency factor. The inclusion of deficiency factors in the flapping equation did however significantly improve correlation with the experimental data obtained by the DRA.

$$\dot{x} = Ax + Bu$$

$$A = \begin{bmatrix} -\frac{4\Omega}{M_{11}}\left(\frac{C_\bullet}{k^2}\lambda_m + \frac{a\sigma}{16}\right) & 0 & -\frac{4\Omega R}{3M_{11}}\left(\frac{C_\bullet}{k}\lambda_m + \frac{a\sigma}{8}\right) \\ 0 & 0 & 1 \\ -\frac{\Omega\gamma}{6R}C^\bullet & -\Omega^2 f_R & -\frac{\Omega\gamma}{8}C^\bullet \end{bmatrix} \quad B = \begin{bmatrix} \frac{4\Omega^2 Ra\sigma}{3M_{11}8} \\ 0 \\ \frac{\Omega^2\gamma}{8}C^\bullet \end{bmatrix} \qquad (3\text{-}14)$$

$$x = \left[\upsilon, \beta, \dot{\beta}\right]'$$

Henceforth this model will be referred to as model (2).

3.2.6 Equivalent Non-Articulated Rotor Models - Models 3 & 4

For this formulation the flapping equations for a rigid rotor included an equivalent hinge offset and a hinge restraint [Chen 1980]. The blade element formulation has been improved to take account of the root cut-out and tip losses in the thrust equation, and a complete derivation is given in Appendix B.

$$\dot{x} = Ax + Bu$$

$$A = \begin{bmatrix} -\frac{4\Omega}{M_{11}}\left(\frac{C_\bullet}{k^2}\lambda_m + \frac{a\sigma}{16}(B^2 - C^2)\right) & 0 & -\frac{4\Omega R}{3M_{11}}\left(\frac{C_\bullet}{k}\lambda_m + \frac{a\sigma}{8}(B^3 - C^3)\right) \\ 0 & 0 & 1 \\ -\frac{\Omega\gamma}{2R}\left(\frac{1}{3} - \frac{\varepsilon}{2}\right)C^\bullet & -\Omega^2 f_R & -\Omega\gamma\left(\frac{1}{8} - \frac{\varepsilon}{3} + \frac{\varepsilon^2}{4}\right)C^\bullet \end{bmatrix} \quad B = \begin{bmatrix} \frac{4\Omega^2 Ra\sigma}{3M_{11}8}(B^3 - C^3) \\ 0 \\ \frac{\Omega^2\gamma}{8}\left(1 - \frac{4}{3}\varepsilon\right)C^\bullet \end{bmatrix}$$

$$x = \left[\upsilon, \beta, \dot{\beta}\right]'. \qquad (3\text{-}15)$$

This model will be referred to as model (3). Including tip loss effects in the flapping equation the following model is obtained. This model will be referred to as model 4:

$$A=\begin{bmatrix} -\frac{4\Omega}{M_{11}}\left(\frac{C_{\bullet}}{k^2}\lambda_m+\frac{a\sigma}{16}(B^2-C^2)\right) & 0 & -\frac{4\Omega R}{3M_{11}}\left(\frac{C_{\bullet}}{k}\lambda_m+\frac{a\sigma}{8}(B^3-C^3)\right) \\ 0 & 0 & 1 \\ -\frac{\Omega\gamma}{2R}\left(\frac{B^3}{3}-\frac{B^2\varepsilon}{2}\right) & -\Omega^2 f_R & -\Omega\gamma\left(\frac{B^4}{8}-\frac{B^3\varepsilon}{3}+\frac{B^2\varepsilon^2}{4}\right) \end{bmatrix} \quad B=\begin{bmatrix} \frac{4\Omega^2 Ra\sigma}{3M_{11}8}(B^3-C^3) \\ 0 \\ \frac{\Omega^2\gamma}{8}\left(B^4-\frac{4B^3\varepsilon}{3}\right) \end{bmatrix}. \tag{3-16}$$

Using Johnson's flapping equation with the improvements of root cut-out and tip loss factors model 4b is obtained:

$$A=\begin{bmatrix} -\frac{4\Omega}{M_{11}}\left(\frac{C_{\bullet}}{k^2}\lambda_m+\frac{a\sigma}{16}(B^2-C^2)\right) & 0 & -\frac{4\Omega R}{3M_{11}}\left(\frac{C_{\bullet}}{k}\lambda_m+\frac{a\sigma}{8}(B^3-C^3)\right) \\ 0 & 0 & 1 \\ \Omega\frac{\gamma}{6R}\left(\frac{3}{1-\varepsilon}\left(\frac{B^3}{3}-\frac{\varepsilon B^2}{2}+\frac{\varepsilon^3}{6}\right)\right) & -\Omega^2 f_R & \frac{-\Omega\gamma}{8}\frac{4}{(1-\varepsilon)^2}\left(\frac{B^4}{4}-\frac{2\varepsilon B^3}{3}+\frac{\varepsilon^2 B^2}{2}-\frac{\varepsilon^4}{12}\right) \end{bmatrix} \quad B=\begin{bmatrix} \frac{4\Omega^2 Ra\sigma}{3M_{11}8}(B^3-C^3) \\ 0 \\ \Omega^2\frac{\gamma}{8}\left(\frac{4}{1-\varepsilon}\left(\frac{B^4}{4}-\frac{\varepsilon B^3}{3}+\frac{\varepsilon^4}{12}\right)\right) \end{bmatrix}. \tag{3-17}$$

In an attempt to show the correctness of the models and also that of the numerical analysis software, all models were configured as the models in Chen and Hindson's report [Chen 1980] with appropriate values for rotor speed, Lock number and rotor radius and with the tip loss, lift deficiency and thrust deficiency factors set to unity while hinge offset or root cut out were set to zero. The results in Chen's report could thus be reproduced by all models. With no hinge offset, models 4b and 4 are equivalent.

3.2.7 Quasi Steady Model - Model 5

For comparison, model 4 is restated with quasi steady inflow dynamics. The value of the apparent mass factor is assumed to be zero giving instantaneous variations in inflow. The model is derived fully in Appendix B and is shown below.

$$A=\begin{bmatrix} 0 & 1 \\ -\Omega^2 f_R & \Omega\gamma\left[\frac{2\lambda_m C_{\bullet}C^{*}}{3kD}\left(\frac{B^3}{3}-\frac{B^2\varepsilon}{2}\right)+\frac{\sigma a C^{*}}{12D}\left(\frac{B^3}{3}-\frac{B^2\varepsilon}{2}\right)\left(B^3-C^3\right)-C^{*}\left(\frac{B^4}{8}-\frac{B^3\varepsilon}{3}+\frac{B^2\varepsilon^2}{4}\right)\right] \end{bmatrix}$$

$$B=\begin{bmatrix} 0 \\ \Omega^2\gamma\left[\frac{\sigma a C^{*}}{12D}\left(\frac{B^3}{3}-\frac{B^2\varepsilon}{2}\right)\left(B^3-C^3\right)+\frac{C^{*}}{8}\left(B^4-\frac{4B^3}{3}\varepsilon\right)\right] \end{bmatrix}$$

$$x=\left(\beta,\dot{\beta}\right)' \tag{3-18}$$

This quasi steady model should not be confused with models not incorporating dynamic inflow.

The table below summarises the differences between the models.

Model	Hinge Offset	Tip Loss Factor	Root Cut Out	Thrust Deff.	Lift Deff.
1	X	X	X	X	X
2	X	X	X	√	√
3	√(Chen)	√ (inflow equ.)	√ (inflow equ.)	√	√
4	√(Chen)	√ (infl. & flapping equ.)	√ (infl. & flapping equ.)	√	X
4b	√(Johnson)	√ (infl. & flapping equ.)	√ (infl. & flapping equ.)	√	X
5	√(Johnson)	√ (infl. & flapping equ.)	√ (infl. & flapping equ.)	√	X

Table 3-1 Summary of Model Differences

3.3 Experimental Set-up

3.3.1 Rig Description

The experimental facility for this work was essentially as described in Chapter 2, before any design changes to the gimbal were made. The rotor was operated in hover conditions in an open test chamber at 1200 RPM. The rotor was not allowed to pitch or roll. The collective pitch was varied sinusoidally at frequencies up to 30 Hz.

The real-time software operating the rotor control functions operated on a frame-time of 2 ms allowing 8 channels of coning and inflow data to be gathered at a sampling rate of 500 Hz.

From the literature review in Chapter 1 is was clear that it was desirable to keep the rotor speed constant during the collective excitation of the rotor, which had not been achieved in flight tests. Assuming a constant rotor speed also allowed the complexity of the theoretical models to be kept to a minimum. A rotor speed controller kept the speed at the desired value and the variations in root-mean-square of the rotor speed during collective tests is shown in Fig. 3-1. The best regulation of the rotor speed is achieved at collective excitation frequencies above 5 Hz, where the rotor inertia keeps speed variations to a minimum. The average variations in rotor speed were less than 1 per cent over the entire frequency range.

3.3.2 Coning Measurement

The instantaneous flapping angle of each blade was measured using a simple half-bridge arrangement with foil strain gauges located on the upper and lower surfaces of each blade at a radial station of 47 % and on the 25% chord line. This position was found to give a good representation of the first mode of blade flapping. The signals from the strain gauges were passed without local amplification through a slip-ring to the strain gauge amplifier. A static calibration between blade deflection and strain gauge amplifier was used to convert the sampled data into flapping angles used in the analysis. In the calculation of all flapping angles

the centre of blade rotation was assumed to be at the rotor shaft position. The bandwidth of the strain gauge amplifier was 15 kHz. and its effect was therefore ignored in the data analysis.

In order to confirm that the static calibration was valid when the rotor was operating and that blade twist did not significantly influence the output of the strain gauges a further dynamic calibration was used. A vertical, radially aligned laser light sheet was used to illuminate the blade tips as they passed through one azimuth position. A camera with a high speed film was focused on the position of the blade tips in the laser sheet and set with an exposure of 1s. This exposure setting was sufficient to capture the vertical blade position over approximately 20 revolutions. The resultant images showed a blurred vertical line representing the maximum vertical blade response over the time period. Using a calibration picture of the position of the blade tip in the laser light sheet, the vertical displacement and hence maximum flapping angles of the blade could be determined. This could then be compared with the values obtained from the strain gauges and good correlation was found. Fig. 3-2 shows a diagram of the rotor and camera. Images taken at 1 and 20 Hz., showing the blurred vertical movement within the laser light sheet are shown.

3.3.3 Inflow Measurement

The induced velocity was measured with four shrouded pitot-static tubes equally spaced at a radial station of 58% R about the rotor shaft axis and 0.165m below the root blade plane. The pitot and static pressure outlets were connected using 1 mm piping approximately 1m long to pressure transducers mounted in a vibration absorbent casing. The piping was kept as short as possible and mounted in such a way as to reduce any movement in the rotor wake which could introduce pressure fluctuations. A calibration between flow velocity and transducer output was conducted in a wind tunnel and is shown in Fig. 3-3. The bandwidth of the pressure transducer was well above 2000 Hz. The effect of the piping between the pitot tube and the pressure transducer on the attenuation and delay of pressure variations at the pitot tube needs to be considered. Fig. 3-4 shows the gain and phase relationships between pressure

disturbances at the pitot tube and at pressure transducer, obtained from a computer model, and all the inflow results have been corrected for this. The computer program was developed at the University of Bristol based on the theory by Bergh & Tijdeman [Bergh & Tijdeman 1965].

The mean induced velocity was measured using a vane anemometer. This was placed at two locations 0.545m radially 0.320m above and 0.50m radially 0.165m below respectively and this confirmed the steady state measurements taken by the pitot tubes.

3.3.4 Frequency Response Data Analysis

One method for examining the inflow and coning behaviour of the rotor is to obtain the frequency response of both inflow and coning over a frequency range. The collective pitch of the rotor was varied sinusoidally at a range of frequencies and the flapping and coning response recorded. The recorded data were analysed using a correlation procedure at the excitation frequency and the gain and phase obtained. This simple method was found to be effective despite low signal-to-noise ratios, because of the long record lengths used, which were only limited by the available computer storage space. In all experiments the collective pitch was varied by +/-1.43 degrees.

3.3.5 Power Spectral Density

The spectrum of data obtained at selected excitation frequencies was also examined. A mathematical package was used to convert the raw data to coning angles and inflow velocity and then a Power Spectral Density (PSD) analysis was undertaken. The PSD spectrum was normalised so that the gains of individual frequency components compared to the input excitation were shown. Details of this are given in Appendix C. This confirmed the quantitative results of the simple correlation procedure.

3.3.7 Experimental Data Corrections

Wake Contraction

The velocity in the far rotor wake increases downstream of the rotor to twice that at the rotor plane. Johnson [Johnson 1980] suggests the following variation of the induced velocity, based on actuator disc vortex theory, within the confines of the rotor wake:

$$\upsilon(z) = \upsilon(0)\left[1+\frac{z/R}{\sqrt{1+(z/R)^2}}\right]. \tag{3-19}$$

To obtain an accurate estimate of the gain of inflow perturbations at the rotor disc, the gain obtained from measurements some distance z below the rotor disc has to be reduced by, $20\log_{10}\left[1+\frac{z/R}{\sqrt{1+(z/R)^2}}\right]$ 1.6 dB or by a factor of 0.8 for the experimental set-up in question.

Blockage Effects

The measured velocities in the wake beneath the rotor were higher than would be predicted from the operating condition of the rotor and it was thought that this was due to the significant blockage of the wake caused by the rotor base plate, gimbal and attachments, which significantly blocked the rotor downwash, creating higher local induced velocities.

Fig. 3-5 shows a diagrammatic representation of the rotor from above and the amount of the wake area that is obstructed by the rotor gimbal and attachments. At the pitot tube measurement plane, the diameter of the wake region was determined using flow visualisation to be approximately 0.6m. From Fig. 3-5 it can be seen that the ratio of blocked area to wake area is 0.718. Assuming that the mass flow rate in the wake is unaffected by the blockage the mean velocity in the unblocked area of the wake has to increase by a factor $1/0.718 = 1.39$ which has to be taken into consideration.

Wake Transmission Effects

The vertical separation between the pitot tubes and the rotor plane means that velocity changes at the rotor do not instantaneously register with the pitot tubes. This significantly affects the phase information obtained form the pitot tubes and an appropriate correction needs to be made. The average velocity at the rotor was found to be 8m/s but 14m/s at the pitot tubes. Assuming a linear variation of velocity over the short separation distance, the time for small velocity perturbations at the rotor to be transported downward to the pitot tubes was found to be 0.015s. The necessary phase correction in degrees to apply to the inflow phase obtained from experimental data is given by: *freq*time_delay**360. This gives a correction of 162 degrees, 54 degrees and 5.4 degrees at 30Hz, 10Hz and 1 Hz respectively. Further work needs to be carried out in this area, probably using a laser anemometer, to verify the above correction for various transmission path lengths and this is discussed in Chapter 5.

Rotor Pitch Actuator Frequency Response

The main rotor actuation arrangement has a bandwidth of approximately 60 Hz. The measured attenuation of the actuator at 32Hz is less than 0.5dB and the phase lag is 18 degrees. The phase of the inflow and coning data has been corrected for the small actuation system phase lag.

3.4 Discussion of Results

3.4.1 Steady State Downwash Measurement

The expected downwash velocity at the rotor plane for a operating point of 1200 RPM with 11 degrees of collective pitch, calculated from the thrust coefficient is 8m/s. The velocity measured by the pitot tubes 0.2 m below the rotor plane was found to be in the region of 14m/s and this was confirmed using a vane anemometer. This was higher than was expected at the operating thrust of the rotor and suggests a velocity at the rotor of 12m/s after wake contraction (as outlined in 2.7.1) is taken into account. The high measured average velocity can be explained by considering the blockage effects of the rotor gimbals and associated

hydraulic assemblies. According to section 3.3.7 a factor of $\frac{1}{1.39}$ is applied to give the corrected velocity at the rotor of 8m/s.

To confirm that blockage was the cause of the high measured velocities, further steady-state measurements were taken 0.32m above the rotor as the blocked area here is minimal. The velocity was determined to be 6m/s at the same rotor operating point. After allowing for wake contraction the velocity at the rotor was determined to be 8m/s. Fig. 3-6 shows the variation of the induced velocity measured above and below the rotor for various rotor speeds. The induced velocity at the rotor disc calculated from theoretical rotor thrust coefficients and the blockage and contraction corrected velocities are also shown and good correlation was found.

The scaling factor, which accounts for wake contraction and blockage, has been applied to the measured frequency gain data, resulting in an overall gain reduction of 4.8 dB.

3.4.2 Experimental Data Quality

A data set was processed at selected frequencies using proprietary signal analysis software. The resulting power spectrums were examined to determine the inflow gain at the excitation frequencies and this information is shown on Fig. 3-7 together with the results from the correlation procedure. Very good agreement between the correlation procedure and the power spectral density is exhibited reinforcing confidence in the simple 'on line' analysis software. An important advantage of the correlation method, was that it could be performed 'on line' with significant data management advantages. A visual dynamic calibration of the coning gains was also conducted as described in 2.2. and the results are shown in Fig. 3-7. The visual calibration gives slightly higher gain values than the power spectrum or correlation procedures. This is to be expected as any recirculation in the tunnel and vibration of the rig will lead to larger blurred images. In the other methods temporary effects such as these will be inherently averaged out.

Fig. 3-8 shows spectral density plots at selected excitation frequencies. The spectrums have been normalised so that the amplitudes of signals are given as gains with respect to the input excitation. Details are given in Appendix C.

The inflow and coning signals at the excitations frequencies are clearly visible and have been labelled with approximate gain values.

In all of the inflow data a strong 80 Hz component is visible. This is due to flow disturbances caused by the passage of each individual blade over the pitot-static velocity sensor. During one revolution, four blades would pass over each sensor explaining the four-per-rev signal (80 Hz) at 1200 RPM (20 Hz).

A strong 80 Hz component is also present in the individual blade flapping data, which cannot be explained as a blade passage effect, as the flapping strain gauge sensors are located in the rotating frame of the rotor. In an attempt to explain this the natural frequencies of the blade in the rotating frame were examined and the analysis is given in Appendix H. The second blade bending mode is predicted to be at 79 Hz and this the most likely explanation for the strong 80Hz component in the flapping data.

The analysis of the rotating blade vibration modes also predicted a first torsion mode of the blade at approximately 160 Hz. This is interesting, as a frequency component at 160 Hz can be identified in the inflow data, which is not readily explained. Although torsional motion of the blade may introduce perturbations in the flow, it would be expected to occur with some blade flapping motion. Furthermore the inflow response at 160 Hz would be expected to be small. Aliasing effects are unlikely to be a contributing factor as an anti-alias low-pass filter at 238 Hz was used. A justification for the 160 Hz component was not found but in any case it lies well outside of the frequency range of interest.

A 20 Hz component in the flapping data is probably due to asymmetry of the rig and is generally 6 dB or more smaller than the excitation peak. At 25 Hz, which is very close to the rotating blade first flap mode, the inflow spectra seems to indicate a change in the level of

turbulence within the wake. Whilst it is difficult to explain why this should be the case, it does indicate that the structure of the dynamic wake is highly complex.

The coning and inflow frequency response data are shown in Fig. 3-9. The figure shows the average of 5 experiments conducted over several days. The 1 standard deviation confidence interval is also plotted. Generally the data variance is largest at low frequencies. For the coning gain data it is approximately +-1.5 dB at 0.2 Hz. This can be largely attributed to wake recirculation within the confined test chamber causing low frequency flow fluctuations. Confidence in the data is good over the entire frequency range for the coning data and up to 25 Hz for the inflow data.

The measured signal-to-noise ratios (SNR) for the data are also shown in Fig. 3-10. The signal-to-noise ratios were obtained by passing the raw data separately through a band-pass and band-stop filter at the excitation frequency resulting in signal and noise components of the raw data. The root mean square values of these signal were then obtained and the signal-to-noise ratios calculated. The inflow SNR decreases from an initial value of -0.5 dB at 0.1 Hz to -12.5 dB at 25 Hz only to recover to -7.5dB at 27 Hz. The coning SNR increases from -10 dB at 0.1 Hz to 2.5 dB at 25 Hz as the coning resonance peak is reached and the blade flapping reaches a maximum. It was intended to improve the signal-to-noise ratios for the flapping data by using high-gain silicone strain gauges. Rotor fatigue considerations did not allow increased pitch variations which would have resulted in larger inflow variations.

3.4.3 Model Correlation

3.4.3.1 Comparison of 3 coning/inflow models with experimental data

Fig. 3-11 and Fig. 3-12 compare the results obtained from models 3, 4 and 5 (as detailed in section 3) with experimental data. The location of the offset hinge to model the semi-rigid blade is not easy to obtain. Various combinations of offset hinge and spring stiffness will give the correct flap frequency ratio of 1.18 which gives a coning resonance peak of 23-24 Hz. The

two cases considered here will be a centre spring case, i.e. no offset, and the correct flap frequency ratio is achieved by an appropriate spring term at the centre of rotation. For the offset hinge case an offset hinge of 21 % R was chosen, with no spring stiffness, to give the correct flap frequency ratio. Another method, suggested by Johnson [Johnson 1980] is to locate the offset hinge at the intersection with the hub plane of the deflected blade tangent at 75% R. This was attempted using pictures of the statically deflected blade, the argument being that this would be similar to the rotating deflected shape. The hinge offset obtained by this method was found to be approximately 26%. An offset hinge location here would have produced a higher coning resonance frequency, than the experimentally determined 23-24 Hz. This could have been corrected by using a negative spring stiffness, but this seems physically hard to justify, and subsequently the nearest inboard position which gave the correct flap frequency ratio with no hinge spring was used.

A centre hinge representation is chosen in Fig. 3-11 and a offset hinge representation, with the hinge located at 21% R, is used in Fig. 3-12.

Centre spring representation.

For the centre spring representation it can be seen that both the quasi-steady model 5, which assumes no inflow dynamics, and model 4 capture the low frequency response very well. Between 0.1 and 2 Hz both models lie 1 dB above the experimental data. At higher frequencies the two models diverge and the quasi-steady model over-predicts the coning resonance peak by 9 dB. Although model 4 over-predicts the coning gain by 5 dB at 10 Hz it captures the resonance coning gain better than model 5, over-predicting it only by 3.5dB. Model 3 which is similar to model 4 except for inclusion of a lift deficiency factor in the flapping equation under-predicts the low frequency gain by 2.5 dB and over-predicts the coning resonance peak by 4 dB. The inclusion of the lift deficiency factor in the flapping equation in addition to inclusion of a thrust deficiency factor in the thrust equation [Houston 1993] did improve the correlation between theory and experiment for tests conducted by the DRA in 1989 [Houston 1989]. A likely explanation for this is that the model used by the DRA

did not include the effects of tip loss explicitly in the flapping equation, but that these were compensated by the lift deficiency factor.

The coning phase is predicted equally well by all three models. All over-predict the phase by about 15 degrees at approximately 4 Hz. Above 10.5 Hz the experimental phase drops off rapidly to 150 degrees at 30 Hz. Ideally the experimental frequency range should be extended further.

For the inflow gain only models 3 and 4 are shown as model 5 has no inflow dynamics. Both capture the low frequency gain to within 2 dB up to 10Hz. Above 10 Hz there is a slight resonance peak in the experimental inflow gain between 15 and 21 Hz before rapidly decreasing to 12 dB at 25Hz and then seemingly recovering. Due to experimental limitations it was possible to average only 2 data sets for frequencies above 15Hz , compared to the 5 data sets available at lower frequencies. For this reason the experimental behaviour of the inflow gain above 15 Hz should be regarded with due care. None of the models show the sharp drop in inflow gain and subsequent recovery at 25 Hz.

The inflow phase is again matched well by both models 3 and 4, up to 10Hz. Above 10 Hz the experimentally obtained phase drops off more rapidly than predicted by the models only to recover slightly just below 20 Hz to match the theoretical models.

Off-set hinge representation

The results of a model using an off-set hinge representation are shown in Fig. 3-12. It can be seen that models 3, 4 and 5 under-predict the low frequency coning gain. Models 4 and 5 both give results which are 6dB below the experimental data for frequencies below 4 Hz. Model 3 under-predicts the coning gain by 10 dB. Model 4b, (model 4 with a flapping equation based on Johnson [Johnson, 1980]), captures the low frequency coning gain up to 1 Hz before increasing above the experimental data at higher frequencies. Above 4Hz the quasi-steady model rises very quickly to over-predict the resonance coning gain by more than 15 dB. Model 4 and Model 4b over-predict the coning resonance gain by only 4.5 dB.

The coning phase response of all 4 models is very similar. Model 5 has the sharpest phase transition at the coning resonance frequency indicating that the absence of inflow dynamics has decreased the coning damping with respect to the other models. This is in agreement with the high coning resonance gain peaks exhibited by the quasi-steady model. Models 3,4 and 4b have virtually identical phase responses. The experimentally determined phase drops off earlier than predicted by the models. At 10 Hz the experimentally determined phase lag is 30 deg whilst models 3 and 4 suggest an average of 8 degrees. In the area of 5 Hz the theoretical models 4 and 5 predict a slight phase lead. The smoother roll-off observed in the experimental data also suggests a further deficit in damping.

The inflow gain of models 3 and 4 lies 5 dB below the experimental for frequencies unto 8Hz. Model 4b shows a significant improvement predicting the inflow gain to within 2dB. The response of models 3 and 4 is again very similar. Model 3 predicts a higher recovery in gain at the coning resonance frequency. Interestingly the experimental data shows a recovery in gain somewhat before the resonance coning frequency. Model 4b is different from models 3 and 4 in that it does not show any resonance peak at 25 Hz, just a change in the slope of the roll off. At the resonance coning frequency there is a sharp drop in the experimental gain. As discussed previously, due to experimental limitations the data above 15 Hz have to be treated with less confidence than that at lower frequencies.

The inflow phase response of models 3, 4 and 4b is very similar. The experimental phase drops off rapidly at 10 Hz before recovering slightly at 20 Hz. This is not captured by any of the models, and further experimental data need to be gathered here.

In conclusion, model 4 and model 4b approximate the experimental data best for the central and offset-hinge case respectively. Model 4b is the same as model 4 when the hinge offset is set to zero.

3.4.3.2 Effect of Apparent Mass Factor

Centre spring representation.

The value of the apparent mass factor has been previously examined. The theoretical value initially suggested by Pitt and Peters [Pitt & Peters 1981], for a *corrected* pressure distribution of 0.542, is contrasted with the value of 0.849 proposed by Carpenter and Fridovich [Carpenter & Fridovich 1953] , which has been found to give the best results compared to experimental data [Houston 1989, Houston & Black 1990].

Fig. 3-13 shows the effect of various apparent mass factors on model 4 using a central hinge representation. The effect of changes in the apparent mass on the coning gain is minimal. The resonance coning gain peak is affected by less than 2 dB for values of M11 ranging between 0.2 and 1.0. The predicted coning peak becomes steeper with increasing M11 and the coning gain is reduced most, in this respect the model using an apparent mass value of 1.0 matches the experimental data most closely.

The coning phase response of model 4 for all four values of M11 is very similar. Only the lowest value of M11 does not show a slight phase lead in the frequency range between 2 Hz and 9 Hz.

The most significant effect of the value of the apparent mass factor is on the inflow gain shown in Fig. 3-13. The effect of M11 is only visible at frequencies above 2 Hz. At higher frequencies the value of the apparent mass determines the shape of the inflow gain. For the case of lowest M11 the gain increases to 30dB at 22 Hz before falling. For the other three models the gain decreases above 4Hz. The larger the value of apparent mass the lower the frequency at which the fall in gain starts and the larger the drop. All of the theoretical models show a slight change in the rate of gain loss at 27Hz. None of the theoretical models show the rapid drop in gain at 25 Hz and subsequent recovery suggested by the experimental data.

Off-set hinge representation

For comparison, the above results have been repeated for model 4b, which uses an offset hinge representation to model the rigid hub rotor and the results are shown in Fig. 3-14.

The effect of hinge offset on the coning gain for various apparent mass factors is to increase the steepness of the resonance coning gain slightly. With M11=0.542 at 10 Hz the theoretical value is 5 dB above the experimental results for an offset hinge, compared to 9 dB for the centre spring case.

The inflow gain response is also affected by the hinge offset. The effect of the hinge offset is only visible for frequencies above 20 Hz. For the case of M11=0.2 the peak of the inflow gain at 23 Hz has been increased by 3 dB. Similarly the response for M11=0.542 now has a slight peak at 22 Hz whereas previously there was none.

From this examination no clear conclusion can be reached on the suitability of either central or offset hinge location in modelling the semi-rigid rotor arrangement. The most obvious deficiencies in the models is their overprediction of the coning gain at the damped resonance frequency and failure to reproduce the character of the inflow gain at frequencies above shaft speed.

3.4.3.4 Model Response with Increased Coning Damping

The coning gain resonance peak is primarily determined by the coning rate derivative and the apparent mass. The previous section has shown that the various values of M11 do not significantly reduce the size of the coning peak. The conclusion is that there must be some deficiency in the coning gain damping derivative shown below both for a centrally hinged and offset hinged rotor.

$$\beta_{\dot{\beta}} = \frac{-\Omega\gamma}{8}\left(\frac{B^4}{1}\right)$$

$$\beta_{\dot{\beta}} = \frac{-\Omega\gamma}{8}\frac{4}{(1-\varepsilon)^2}\left(\frac{B^4}{4} - \frac{2\varepsilon B^3}{3} + \frac{\varepsilon^2 B^2}{2} - \frac{\varepsilon^4}{12}\right) \qquad (3\text{-}20)$$

To affect the damping either γ, Ω or B needs to be changed or the structure of the derivative altered. Changing the rotor speed or the Lock number will significantly affect the low frequency coning gain, which has been captured very well.

Justification for an increased coning derivative can be found by examining the derivation of the flapping equation. For a comprehensive derivation the reader is referred to Johnson [Johnson 1980]. In small perturbation form and using non-dimensional quantities the flapping equation is given by:

$$\ddot{\beta}+f_R^2\dot{\beta}=\gamma M_F;\quad M_F=\int_\varepsilon^1 \eta\frac{F_Z}{ac}dr \tag{3-21}$$

where F_Z is given by:

$$\frac{F_Z}{ac}=0.5\left(U_T^2\theta-U_PU_T\right). \tag{3-22}$$

U_P and U_T are the normalised air velocity at the blade section perpendicular and tangential to the rotor disc plane, respectively. The rigid rotation about a flap hinge is presented by η, which is normalised is such a way that for no hinge offset $\eta=r$ and then the deflection of the blade is given by $\beta\eta$.

$$U_p=\lambda+\eta\dot{\beta} \text{ and } U_T=\Omega r; \tag{3-23}$$

The expression for M_F (Equation 3-21) is then integrated over the disc with substitution of Equations (3-22 & 3-23) and the following result is obtain from Johnson for the zero forward speed case:

$$M_F=\frac{1}{8}C_2\theta_0-\frac{1}{6}C_1\lambda-\frac{1}{8}D_1\dot{\beta} \tag{3-24}$$

The expressions for the constants C_1, C_2 and D_1 are given by Johnson and integrated from the location of the offset hinge to the blade tip, i.e. from ε to 1. The D_1 coefficient incorporates the reduced aerodynamic force created by the blade due to its flapping motion, which acts to decrease the local angles of attack on the blade. The D_1 coefficient therefore primarily affects the flap damping. To include the effect of tip loss it was previously suggested by Johnson

[Johnson 1980] that the integrals are evaluated from ε to B. A tip loss factor is used to approximate the decrease in lift over a finite distance at the blade tip. Over the length of blade outside the tip loss factor the lift and thus inflow are assumed zero.

It can be argued however that the air velocity perpendicular to the blade outside of the tip loss factor due to the flapping motion is still present and acts to damp the flapping motion of the blade. The expression for Up, local non-dimensionalized vertical velocity as referenced to the blade is then given by:

$$U_p = \begin{cases} \lambda + \eta\dot{\beta}; & r <= B \\ \eta\dot{\beta}, & r > B \end{cases} . \tag{3-25}$$

It can be seen that the velocity relative to the blade due to the flapping motion is present outside the limits of the wake assumed by the tip loss factor. It can be argued therefore that the limits of the integral for D1, which accounts for the relative velocity due to blade flapping, are thus ε to 1, whilst the other integrals are only evaluated up to the tip loss factor. The new coning damping derivative for the centrally and offset hinge cases are thus given by:

$$\begin{aligned} \beta_{\dot{\beta}} &= \frac{-\Omega\gamma}{8} \\ \beta_{\dot{\beta}} &= \frac{-\Omega\gamma}{8}\frac{4}{(1-\varepsilon)^2}\left(\frac{1}{4} - \frac{2\varepsilon}{3} + \frac{\varepsilon^2}{2} - \frac{\varepsilon^4}{12}\right) \end{aligned} . \tag{3-26}$$

Dropping the tip loss factor from the coning damping derivative has increased this derivative by 25 %. The effect of this increase in coning damping derivative, based on physical examination of the flapping equation, is shown in Fig. 3-15 for a central and offset hinge representation. Only the coning gain and inflow gain responses are shown as the effect on the phase was found to be minimal. It can be seen that the resonance coning peak has been reduced by approximately 2 dB for both cases and the range of apparent mass values examined. Significantly however, although the effect on the coning gain response is relatively small, the increased coning damping derivative has dramatically affected the inflow gain response between 20 and 30 Hz. Whereas previously the inflow gain response with M11=0.2 showed a resonance peak of 5 dB at 24 Hz, it now has virtually no peak. Similarly the curves

for the other values of M11 fall off much more rapidly after 20 Hz than previously. A value of M11=0.2 gives the best fit between the theoretical and experimental data for the coning gain. This value of M11 however gives a poor correlation between the observed and predicted inflow gain above 10 Hz. A value of M11=0.849 gives much better results. Before a conclusion on the most appropriate value of apparent mass factor can be reached the coning damping should be increased further, to give a coning response which matches the experimental resonance peak, as it has been shown that even slight increases in coning damping can significantly change the inflow gain response.

Artificially Further Increased Coning Damping Derivative

The effect of further increasing the coning damping derivative by a factor of 1.5 is shown in Fig. 3-16. The damped resonance coning peak is now at the same height as that of the experimental data, both for the centre and offset hinge representation. The effect of the apparent mass value used on the inflow response is minimal. As previously discussed the lower apparent mass value gives a steeper coning peak which matches the experimental data marginally better.

The most significant effect of the apparent mass is on the inflow gain. The use of a centre or offset hinge representation has little effect on the inflow response. The inflow response for both values of apparent mass (M11=0.8 and M11=0.3) shows a sharp dip in gain at the 25 Hz, with subsequent recovery. The curves obtained using an apparent mass value of M11=0.8 give a good overall fit to the data, with the inflow gain reducing from 3 Hz onwards. The response obtained with the lower value of M11, although not providing such an overall good fit, does capture the magnitude of the inflow dip to within 4 dB and gives most inflow gain recovery. Neither model matches the recovery of the experimental inflow gain accurately.

It would seem necessary to obtain further inflow data in the frequency range 10 to 100 Hz and to compare this with the theoretical models. It would be particularly useful if this data could be obtained by means other than pressure transducers to eliminate any possibility of unmodelled sensor dynamics affecting the inflow response. The results obtained from model

4b for a centre and offset hinge representation together with an apparent mass factor of 0.849 suggest that this model can be used to examine the coning and inflow behaviour with good fidelity up to rotor shaft frequencies.

3.5 Conclusions and Further Work

3.5.1 Conclusions

1. The coning/inflow model below gives a good approximation to the experimental coning and inflow frequency responses over a frequency range of 0.1 to 20 Hz, i.e. up to one-per-revolution. All models display less flapping damping than the experimental data. The damping of the coning response has been increased by approximately 25% based on physical arguments outlined in section 4.3.2. The best correlation with data for the offset hinge case was found when flapping Equation (3-12) was used. This reduces to Equation (3-7) when no hinge offset is used.

$$A=\begin{bmatrix} -\frac{4\Omega}{M_{11}}\left(\frac{C_o}{k^2}\lambda_m+\frac{a\sigma}{16}(B^2-C^2)\right) & 0 & -\frac{4\Omega R}{3M_{11}}\left(\frac{C_o}{k}\lambda_m+\frac{a\sigma}{8}(B^3-C^3)\right) \\ 0 & 0 & 1 \\ \Omega\frac{\gamma}{6R}\left(\frac{3}{1-\varepsilon}\left(\frac{B^3}{3}-\frac{\varepsilon B^2}{2}+\frac{\varepsilon^3}{6}\right)\right) & -\Omega^2 f_R & \frac{-\Omega\gamma}{8}\frac{4}{(1-\varepsilon)^2}\left(\frac{B^4}{4}-\frac{2\varepsilon B^3}{3}+\frac{\varepsilon^2 B^2}{2}-\frac{\varepsilon^4}{12}\right) \end{bmatrix} \quad B=\begin{bmatrix} \frac{4\Omega^2 Ra\sigma}{3M_{11}8}(B^3-C^3) \\ 0 \\ \Omega^2\frac{\gamma}{8}\left(\frac{4}{1-\varepsilon}\left(\frac{B^4}{4}-\frac{\varepsilon B^3}{3}+\frac{\varepsilon^4}{12}\right)\right) \end{bmatrix};$$

2. Both the offset and centre spring representations provide good fidelity over the frequency range. The offset hinge representation gave low frequency gain results which matched the experimental data very well, lying some 2 dB below that predicted by the centre spring representation. All models failed to capture the steepness of the coning gain resonance peak. Lower values of apparent mass give slightly better results, but the improvement is marginal.

3. Further experimental data need to be gathered, particularly at higher frequencies. This should resolve the behaviour of the inflow response above 25 Hz in which confidence is limited due to the small amount of data obtained at these higher frequencies. Ideally the separation between the pitot tubes and pressure transducer will be greatly reduced to improve frequency response in phase and gain. Direct dynamic measurements of the airflow should be made,

using hot wires or laser anemometry to support the results obtained using the pressure transducers.

4. The magnitude of the coning resonance peak and thus the damping of the coning formulation significantly affects the inflow response at the coning resonance frequency. All models exhibit insufficient damping of the coning response. Artificially increasing the coning damping produces a rapid decrease in inflow response and subsequent recovery at 25 Hz, which is similar to that exhibited by the experimental data. If further high frequency experimental data support this inflow behaviour the theoretical models need to be improved accordingly.

5. The overall fit of the data up to the shaft frequency is best when an apparent mass factor of 0.85, as suggested by Carpenter and Fridovich, is used. This reinforces previous results [Chen 1989, Houston 1989] suggesting that the apparent mass factor given by Pitt and Peters for a twisted bade or *corrected* pressure distribution [Pitt & Peters 1981] is best replaced with the mass factor of 0.85 found for a un-corrected pressure distribution, which is also the value obtained by Carpenter and Fridovich.

3.5.2 Further Work and Improvements

As a result of this work a number of improvements and areas of further investigation came to light, and these will be summarised here.

1 The aerodynamic interference of the large gimbals needs to be reduced if reliable inflow measurement are to be taken. Particularly, the need for smaller gimbals is obvious so that inflow measurements can be made over a large proportion of the rotor radius. Smaller gimbals should also produce less turbulence in the wake, which would aid in the determination of the real inflow response. As a result of this initial study, it was decided to redesign the gimbal mounting. Redesigning the gimbal would also allow the volume of oil between the gimbals and rotor to be reduced. This together with a higher performance speed control loop should allow tighter control of rotor speed.

2 Although compensation for the dynamic response and associated piping was incorporated, the sensitivity to pitot system geometry was found to be high. The pitot tube instrumentation also suffered from temperature drift. This problem was partially overcome by mounting the transducers in a large padded foam box, which isolated them from vibration and kept them thermally stable. This however resulted in long tubing lengths, between the transducers and actual pitot-static tube. The initial choice of pitot static tubes and pressure transducers was due to a lack of access to alternative instrumentation. However, it was felt that further inflow measurements should be made using hot wires and LDA.

3 In this initial study the location of the pitot-tubes was limited for safety reasons to 15cm below the tip path plane of the rotor. It is desirable to take further measurements closer to the rotor blades, particularly so that the effect of transmission delays can be assessed. This can be achieved by redesigned hot wire or pitot tube mountings, but a more elegant solution may be realised using a LDA system. The radial variation of the dynamic flow field should also be investigated.

4 Improvements to the blade instrumentation are also desirable. The output from the initial strain gauges was relatively small, compared to the noise produced by the slip rings. Silicon strain gauges produce resistance changes of an order of magnitude larger than conventional gauges and would significantly improve the signal-to-noise ratios of the blade flapping data.

3.6 Summary

Experimental coning and inflow data have been obtained using a rotor with a semi-rigid hub mounted on a hover stand. Collective pitch was varied dynamically over a frequency range of 0.1 to 30 Hz. The results have been compared with theoretical coning/inflow models utilising a first-order inflow and second-order coning representation. Theoretical models incorporating a lift deficiency factor in the flapping equation, tip loss factors and hinge offset compared well with the experimental data. The models generally display lower damping in the coning

response than the experimental data, particularly when an offset hinge representation is used and some physical arguments are advanced to account for this apparent deficiency of the mathematical model. The inflow magnitude response at the coning damped natural frequency is strongly affected by the damping of the coning mode. Further experimental inflow data need to gathered at frequencies above the coning resonance frequency to define the inflow behaviour clearly. Preliminary results suggest that there is a sharp drop in inflow gain and subsequent recovery, at the damped coning resonance frequency. This behaviour is reproduced by a linear mathematical model when the coning damping is increased by a factor of 1.5. The results also provide further evidence that an apparent mass factor of 0.85, as suggested by Carpenter and Fridovich [Carpenter & Fridovich 1953], produces the best correlation between theory and experiment and a model applicable to articulated or offset hinge rotor is presented which gives good results up to shaft frequency.

Significant improvements need to be made to the experimental facility both in terms of the rig itself and the instrumentation, through the use of a aerodynamically optimised gimbal and reliable flow instrumentation. Several theoretical models including dynamic inflow were evaluated against experimental data, and areas for further work identified.

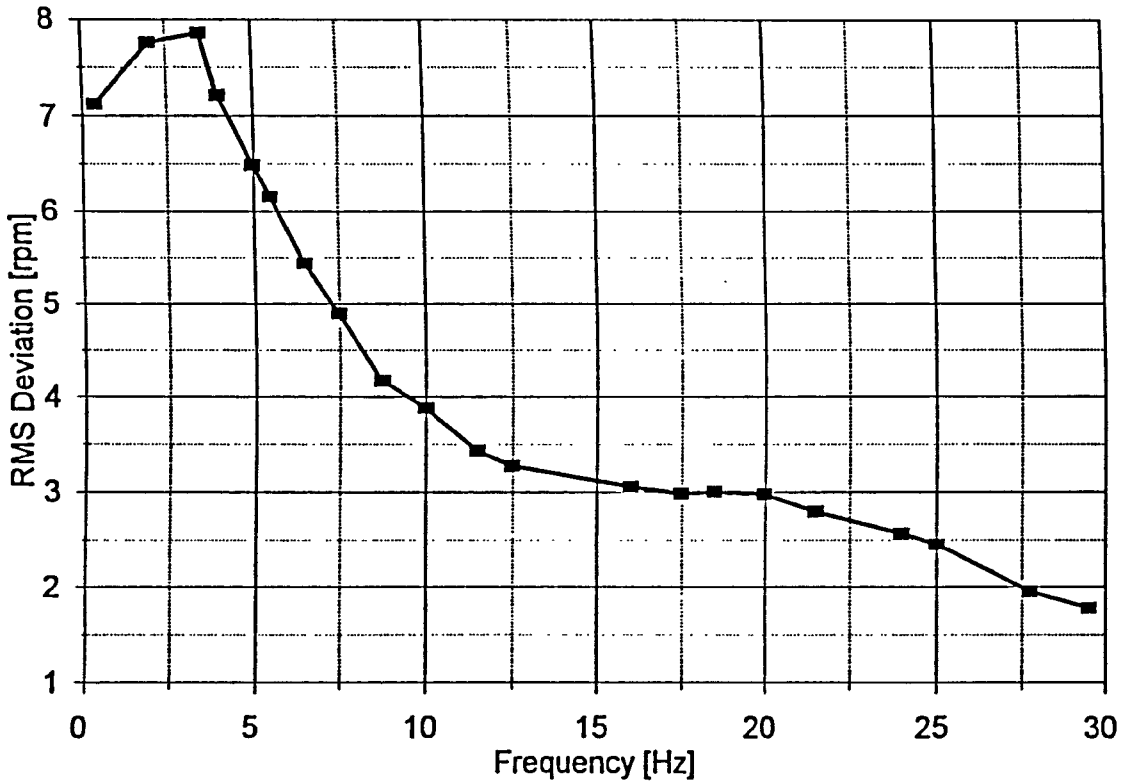

Fig. 3-1 RMS Change in Rotor Speed at Collective Excitation Frequencies (1200 rpm)

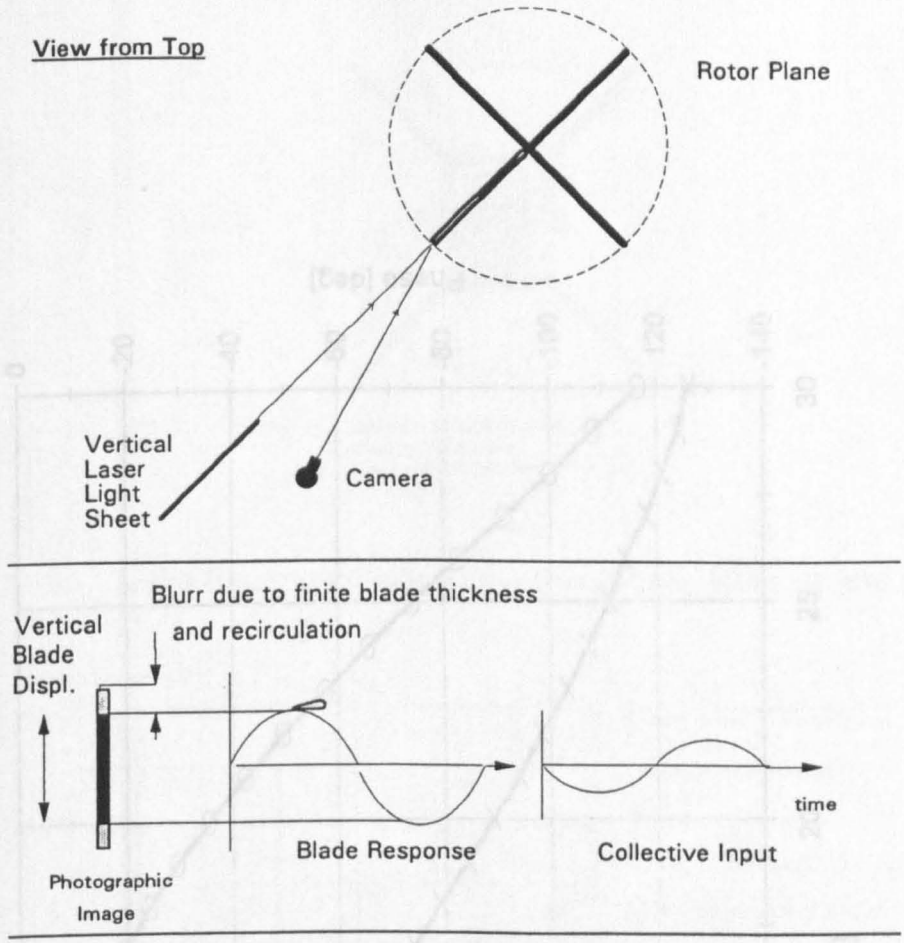

Actual Photographic Images Showing a Coning Gain of -12 dB and -5 db at 1Hz and 20 Hz Respectively

Fig. 3-2 Visual Determination of Blade Coning

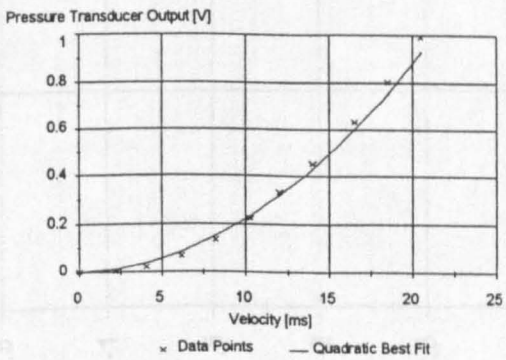

Fig. 3-3 Pitot-Static Velocity Calibration

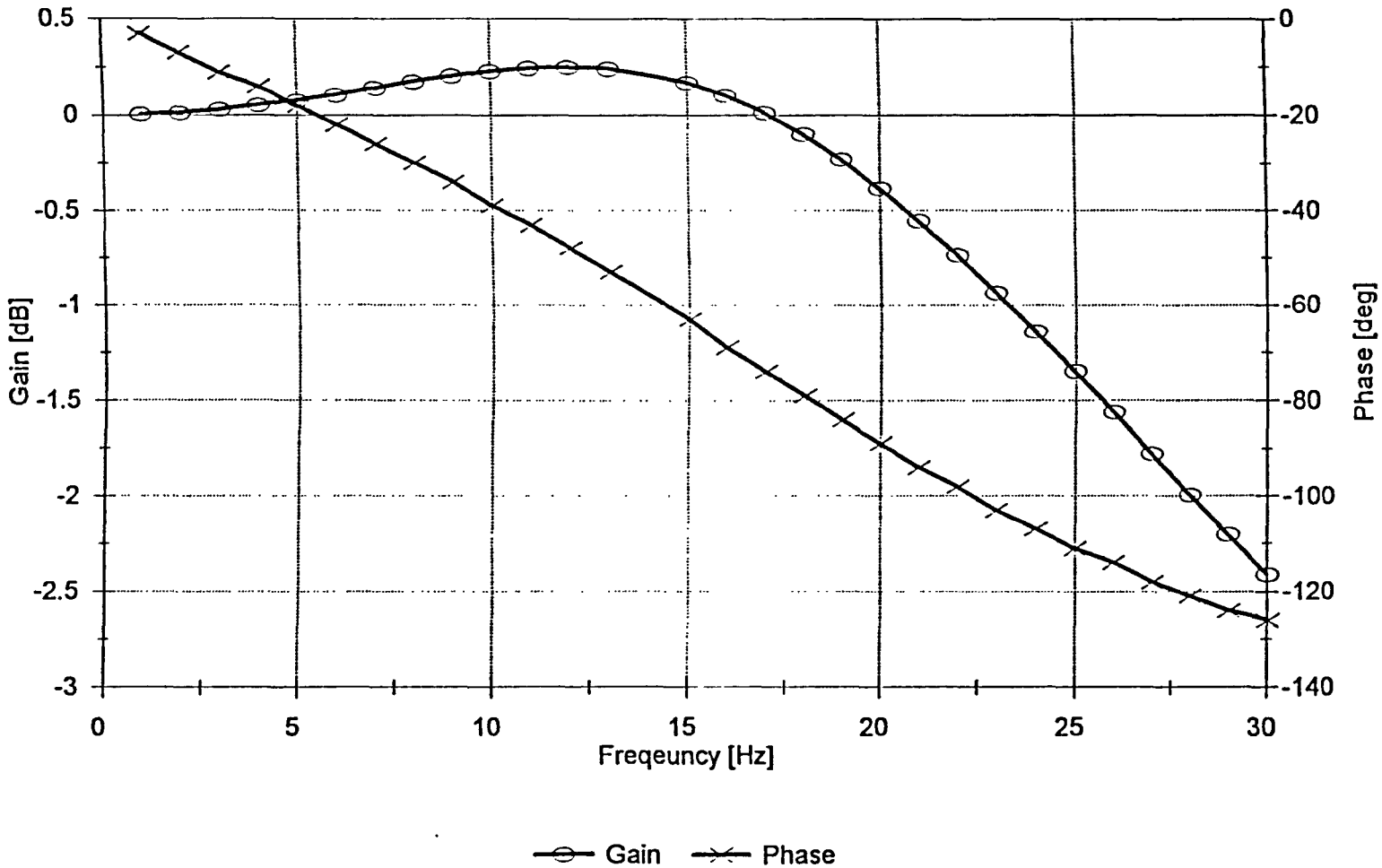

Fig. 3-4 Pressure Sensing System Frequency Response
(based on a computer program developed at the University of Bristol
for theory by Bergh [Bergh & Tijdeman 1966])

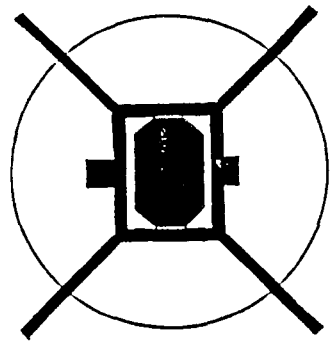

Fig. 3-5 Wake Blockage due to Rotor Base-Plate, Gimbals and Pitot Mountings

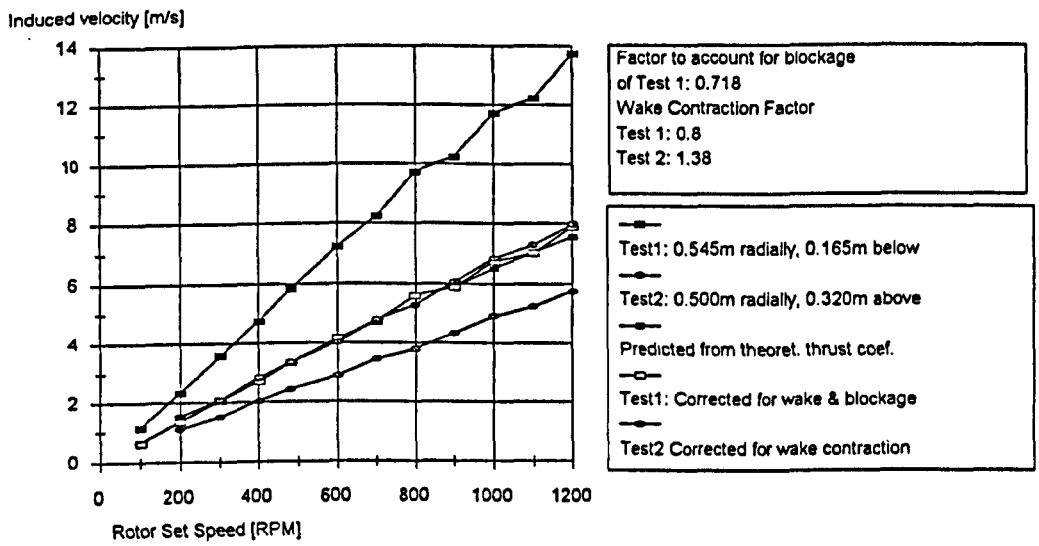

Fig. 3-6 Effect of Blockage on the mean Wake Velocities

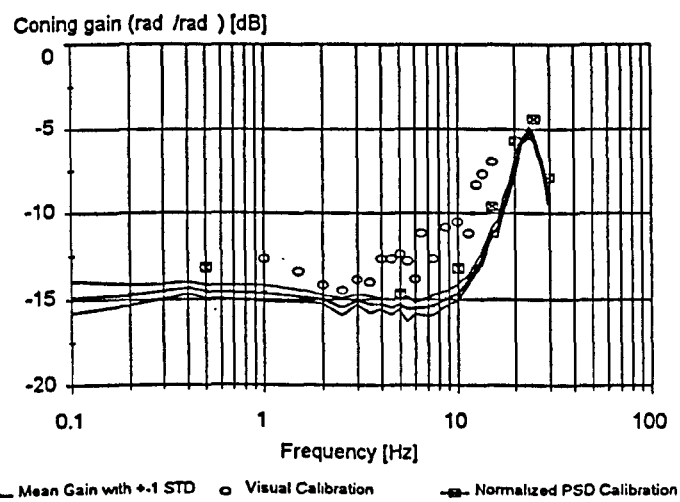

Fig. 3-7 Comparison of Coning Gain obtained from Correlation Procedure Power Spectrum Analysis and Laser Dynamic Calibration

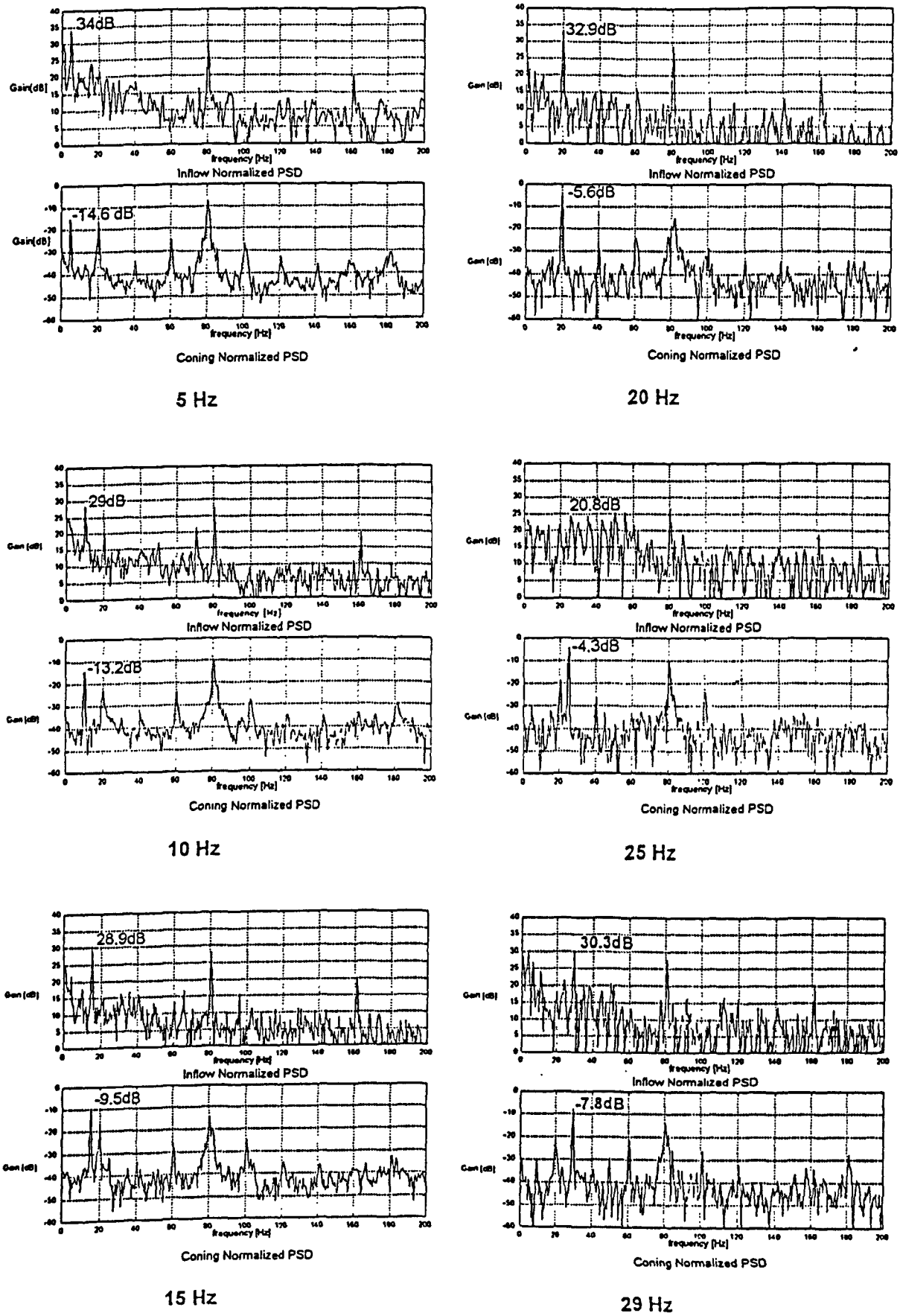

Fig. 3-8 Power Spectral Density Plots obtained from Inflow & Coning Data
(data have been normalised to show gains compared to input amplitude)

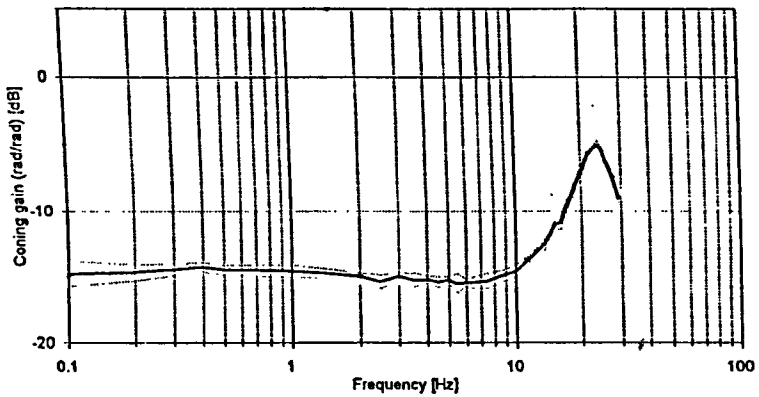

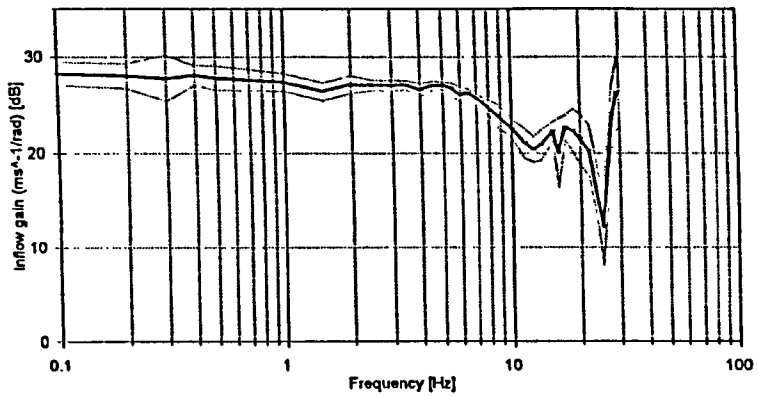

Coning

Inflow

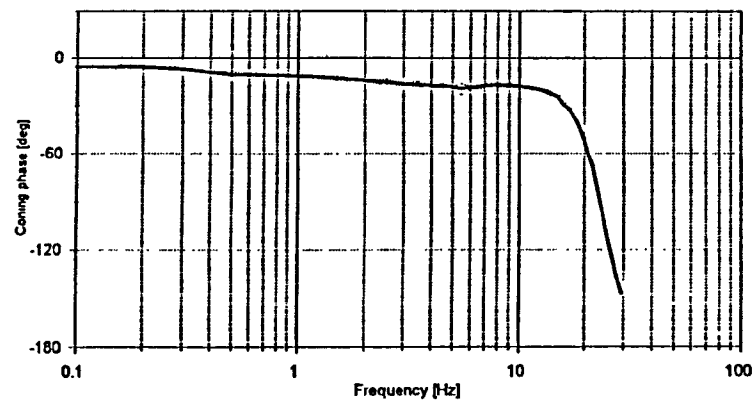

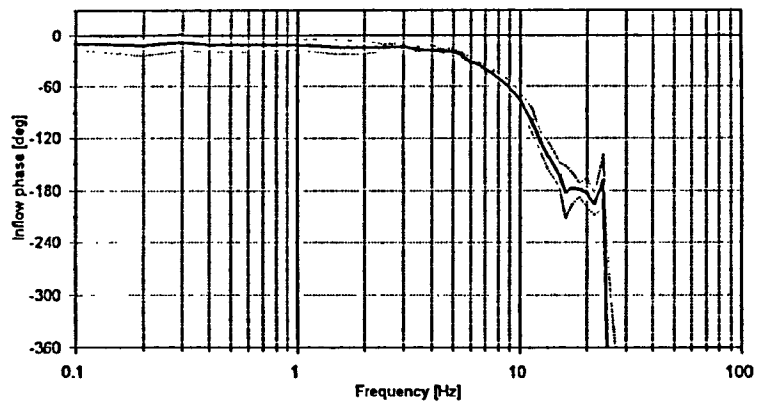

(Corrected for actuator lag)

(Corrected for blockage, tansmission delays, actuator lag and transducer dynamics)

Fig. 3-9 Experimentally determined Coning and Inflow Frequency Response with Confidence Intervals
(1200 rpm, 0.16m below, 58% R))

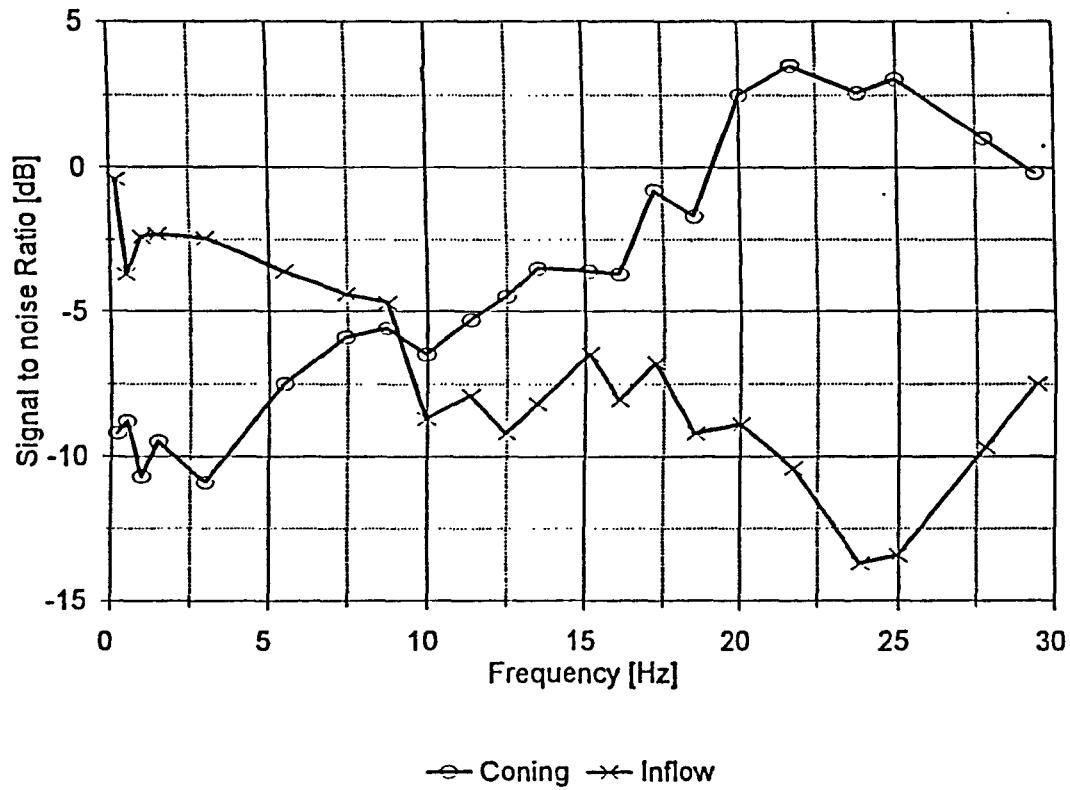

Fig. 3-10 Signal-to-Noise Ratios for the Coning and Inflow Data

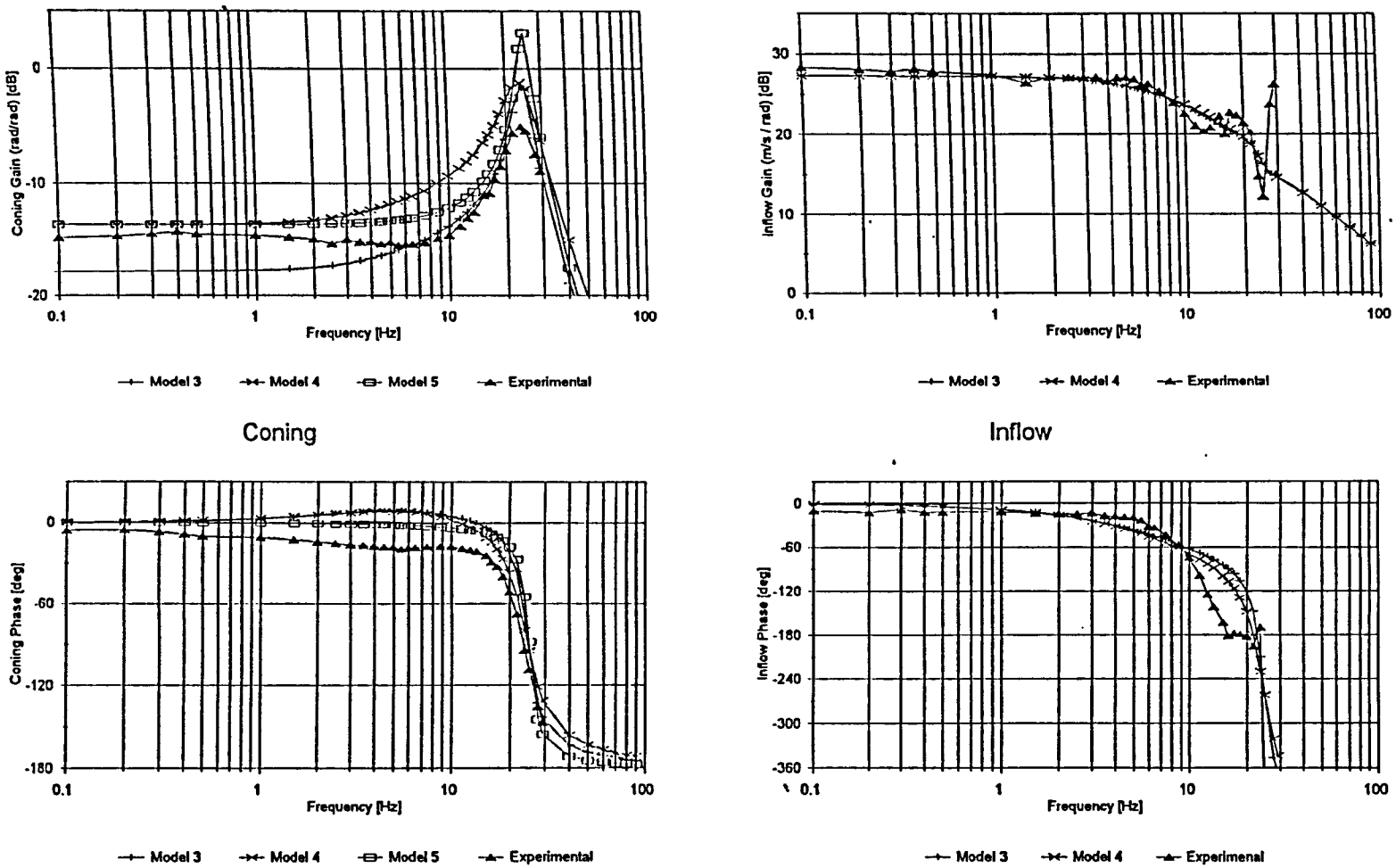

Fig. 3-11

Correlation of 3 Coning/Inflow Models with Experimental Data
(1200 rpm, 0.16m below, 58% R, M_{11}=0.849, central hinge)

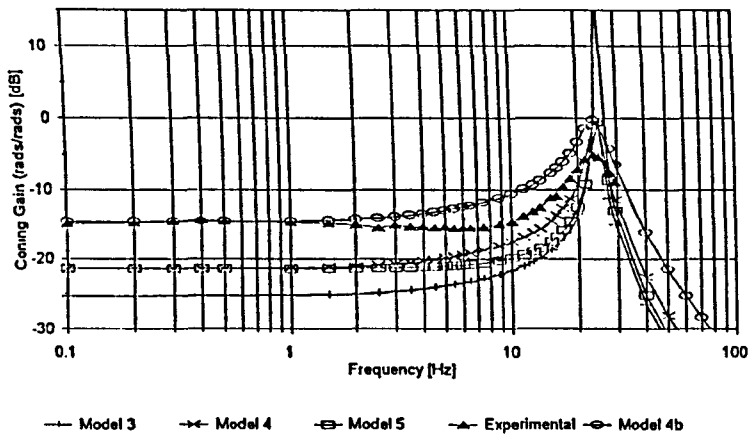

Coning

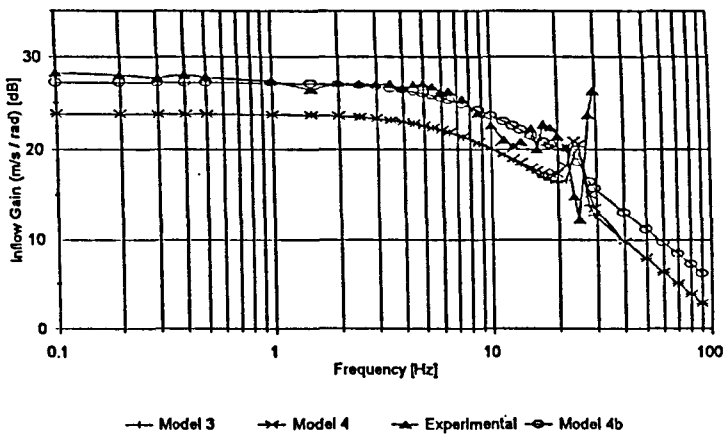

Inflow

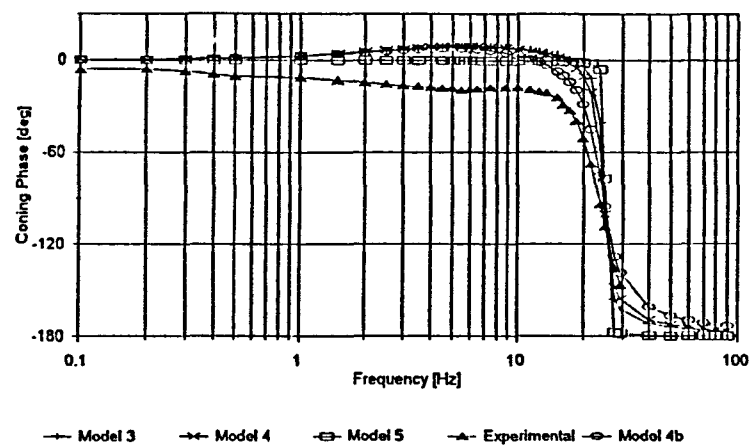

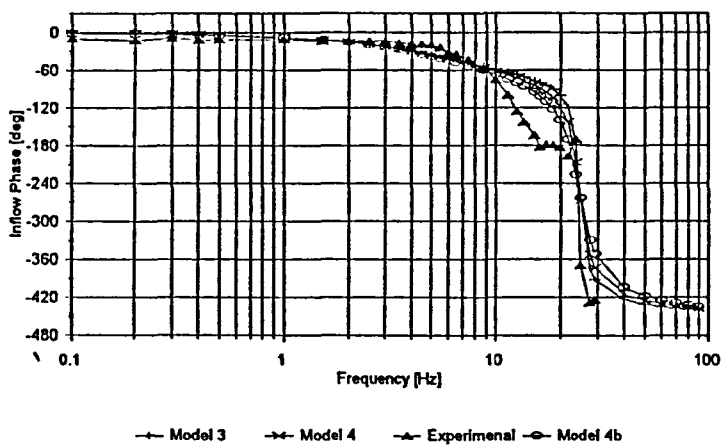

Fig. 3-12 Correlation of 3 Coning/Inflow Models with Experimental Data (1200 rpm, 0.16m below, 58% R, offset hinge)

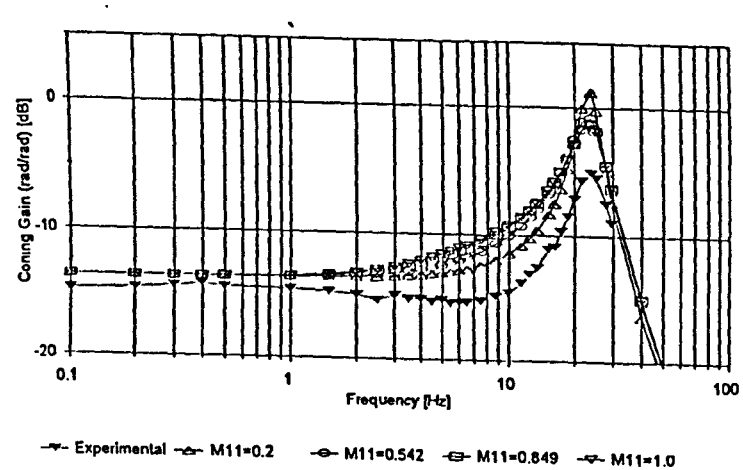

Coning

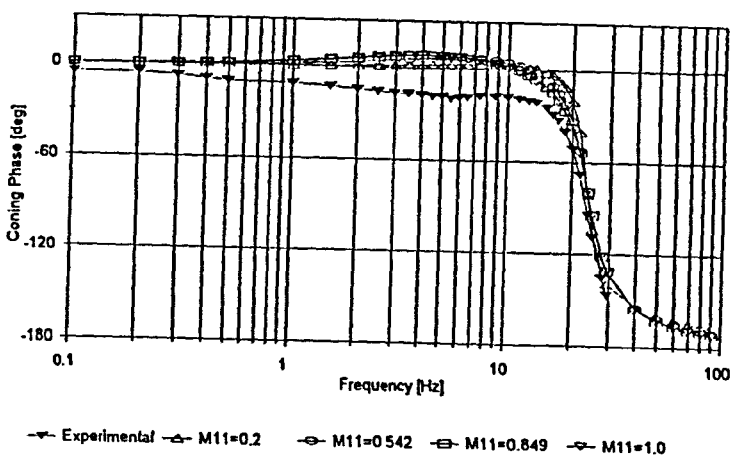

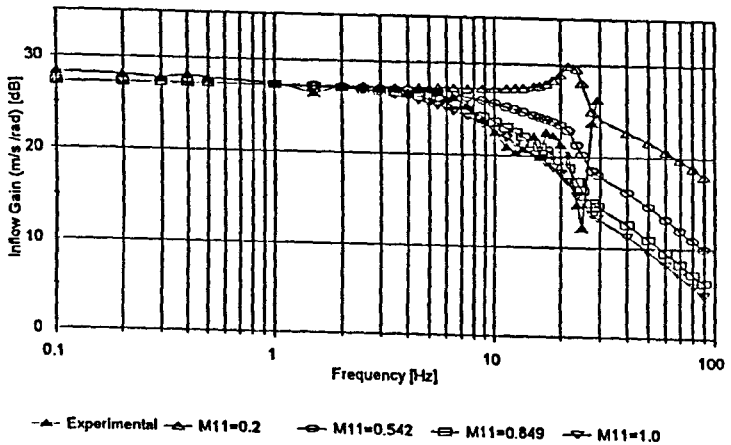

Inflow

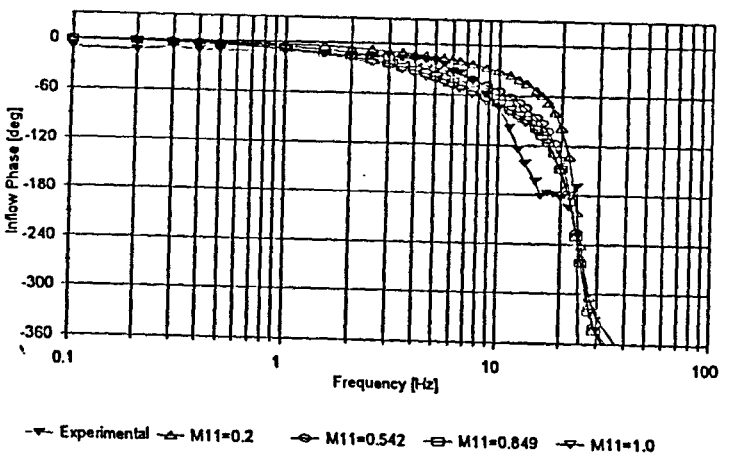

Fig. 3-13

Effect of apparent Mass on the Correlation of Model 4 with Experimental Data
(1200 rpm, 0.16m below, 58% R, central hinge)

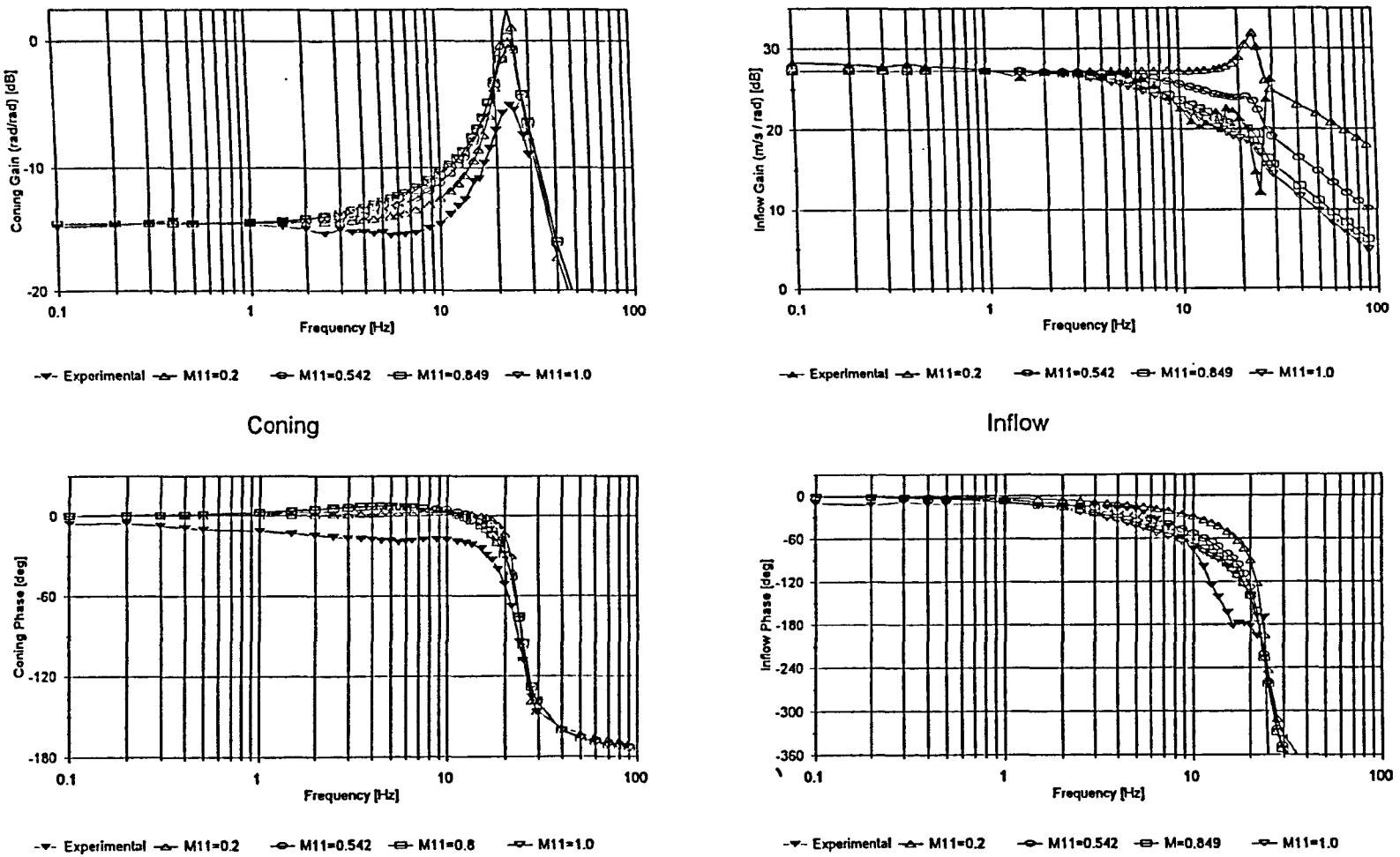

Fig. 3-14 Effect of Apparent Mass Factor on the Correlation of Model 4b with Experimental Data (1200 rpm, 0.16m below, 58% R, offset hinge)

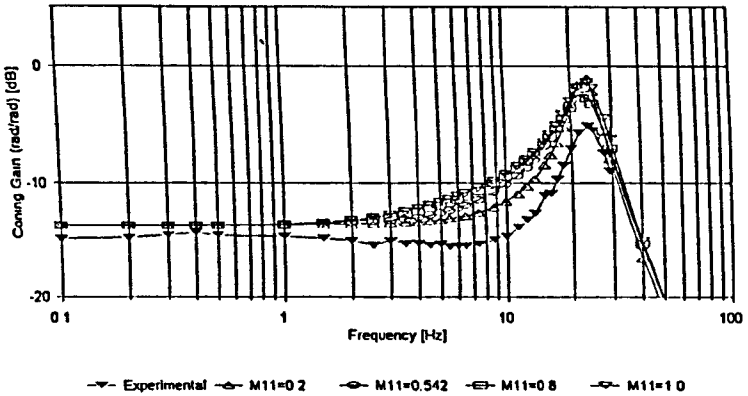

Coning

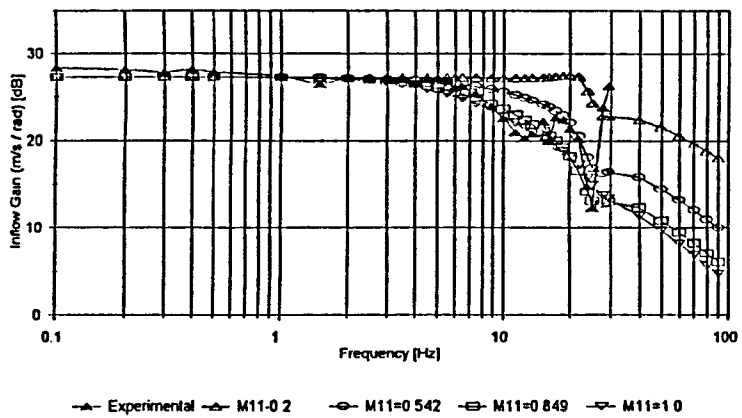

Inflow

Gain Response of the Central Hinge Model

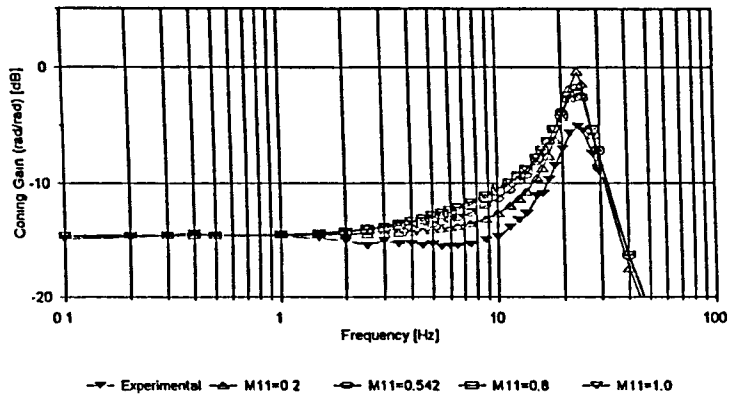

Coning

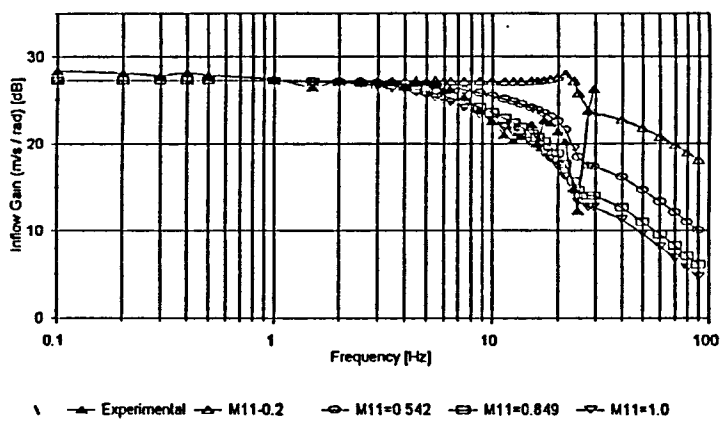

Inflow

Gain Response of the Offset Hinge Model

Fig. 3-15 Effect of Apparent Mass Factor on the Correlation of Model 4 with Exp. Data using Increased Damping (1200 rpm, 0.16m below, 58% R)

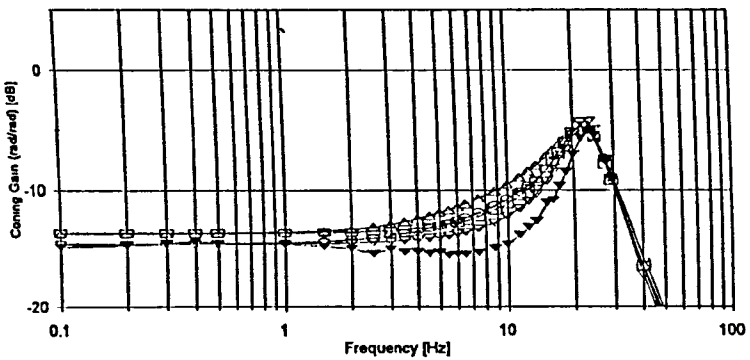

Coning

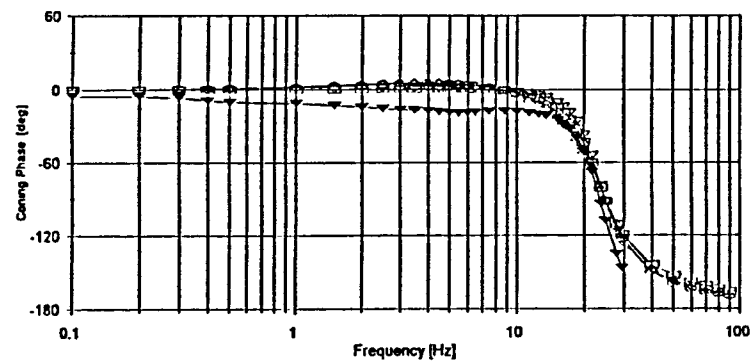

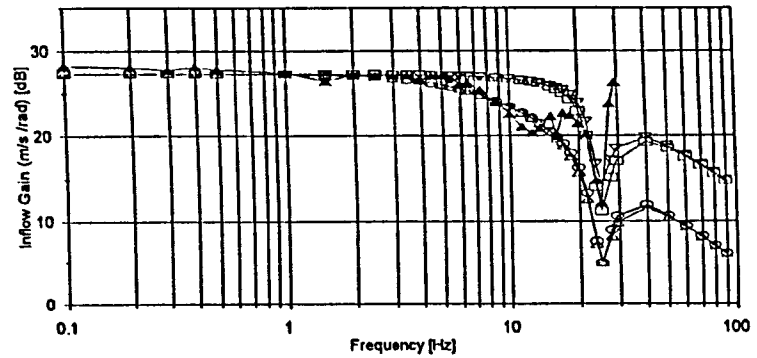

Inflow

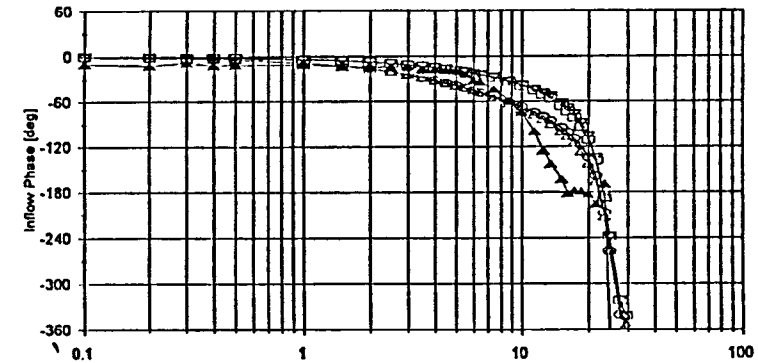

Fig. 3-16 Effect of artificially Increased Damping on the Correlation of Model 4b with Experimental Data (1200 rpm, 0.16m below, 58% R, central hinge)

Chapter 4
Design of a Rotor Speed Control System

4.1 Introduction

The mathematical models that have been used throughout this research study to represent inflow dynamics do not contain a rotor speed degree of freedom. Accordingly, it was necessary to design a control system that would hold rotor speed constant despite changes in collective pitch demand and hence rotor torque requirements. The need for good rotor speed control was highlighted in the literature review of Chapter 1 [Houston & Tartellin 1989, Leith et al 1991].

Torque is supplied to the rotor by a 3000 psi hydraulic motor that is controlled by an electro-hydraulic-servo valve (EHSV). Maximum continuous torque at 3000 psi is 50 Nm giving a maximum input power of 6.3 kW at the nominal operating speed of 1200 rpm.

A mathematical model of the speed control loop was produced and validated against data from the rotor rig. Once the mathematical model had been established an optimum controller was designed and the effects of proposed rig modifications were assessed.

4.2 Hydraulic System Model

A complete block diagram of the speed control loop is shown in Fig. 4-1. The main elements that make up this model are the EHSV, hydraulic motor, speed sensor, EHSV drive amplifier and digital control law. Speed information is provided from a shaft encoder mounted on the hydraulic motor. The loading on the motor consists of inertial loads (the motor and rotor) and aerodynamic drag acting on the rotor. Bearing friction and viscous loads were neglected. The modelling of the individual components will be discussed in detail below.

Electro-Hydraulic-Servo Valve (EHSV)

The EHSV converts an electrical input current into a spool displacement, which in turn determines the output flow of oil from the valve. The mass of the spool introduces an effective time lag, and damping is present in the form of friction on the moving spool. The spool cuts the magnetic field in the coil at a rate related to its axial velocity and this produces a back electro-magnetic force in the coil that acts against the applied current, and thus acts to damp the motion of the spool. The magnitude of the back current is related to the spool diameter, number of coil turns, flux density and core velocity.

The EHSV can be theoretically modelled [Stringer 1976] using a third order representation. Inspection of frequency response diagrams provided by the manufacturer suggest that over a frequency range of interest (0 Hz to 100Hz) the behaviour of the valve can be approximated sufficiently by a second order model. The gain, natural frequency and damping ratio of this model were then chosen to give the best fit with the frequency and time response data supplied by the manufacturer. A natural frequency of 300 rad/s and a damping ratio of 1.4 gave an acceptable fit as shown in Fig. 4-2.

As part of the programme to upgrade the rig it was planned to replace the EHSV with one of higher bandwidth. Limited manufacturers' data were available on the replacement valve and again a second order model was approximated to this as shown in Fig. 4-3.

Valve Spool Flow Analysis

To complete the model of the EHSV valve, a relationship between the spool displacement and resulting flow has to be found. The flow through either side of the valve (Equation 4-1a) is given by the square root relationship pressure drop, orifice opening, flow coefficient C_f and density ρ [Stringer 1976]. In the following analysis it will be assumed that the EHSV will be used to drive a hydraulic motor and that the magnitude of both flows will be equal and that the return pressure is negligible [Stringer 1976]. The supply pressure P_S can be assumed constant

and the return pressure P_r to be zero. The pressure across the motor P_m is given as the difference of P_a and P_b, the pressures either side of the motor between the EHSV.

$$q_1 = \frac{C_f}{\sqrt{\rho}} d_v X_v (2P_s - 2P_a)^{1/2} \qquad q_2 = \frac{C_f}{\sqrt{\rho}} d_v X_v (2P_b - 2P_r)^{1/2} \tag{4-1a}$$

$$\begin{aligned} &\text{If } q_1 \equiv q_2 \text{ then } P_s - P_a = P_b - P_r \text{ but with } P_r \cong 0 \text{ and } P_m = P_a - P_b \\ &\qquad \text{it follows that } P_s - P_m = 2P_b;\ P_s + P_m = 2P_a \\ &\qquad \text{and thus if } q = q_1 = q_2 = \frac{C_f}{\sqrt{\rho}} d_v X_v (P_s - P_m)^{1/2} \end{aligned} \tag{4-1b}$$

$$\text{we have } q = Ax(P_s - P_m)^{1/2}, \text{ where } A = C_f d_v X_v \quad 0 \le x \le 1. \tag{4-1c}$$

In practice, the valve displacement X_v will be much smaller than the valve opening diameter d_v. Stringer [Stringer 1976] suggests that the pressure across the motor P_m will rarely exceed 2/3 of the supply pressure and hence the following binomial approximation can be made with less than 10% error.

$$(P_s - P_m)^{1/2} = P_s^{1/2}\left(1 - \frac{P_m}{P_s}\right)^{1/2} \approx P_s^{1/2}\left(1 - \frac{P_m}{2P_s}\right) \tag{4-2a}$$

$$\text{then from (4-1c) } q = AxP_s^{1/2} - AxP_m \frac{1}{2\sqrt{P_s}} \tag{4-2b}$$

$$\text{or } q = K_x x - K_m P_m$$

$$K_x = A\sqrt{P_S};\ K_m = A\frac{x}{2\sqrt{P_s}};\ 0 \le x \le 1 \tag{4-3}$$

From the above analysis we then have a flow gain K_x that is constant with supply pressure and can be predicted from manufacturers' data. The gain K_m is related to the pressure across the motor and varies with spool displacement x, which is unsuitable for a linear analysis. The effect of K_m is to reduce the ideal valve flow in proportion to the pressure across the motor or load and is thus effectively a source of damping. As the valve is opened the displacement and thus damping is increased. The minimum damping occurring when the valve is near its null point. In the proposed model the flow due to the value of K_m is added to the leakage of the motor as their effects are the same (see 4.2.2). The value for K_m is found from the operating point of the linear model. In the model the spool displacement is represented as a percentage of the fully open value.

For a fully open valve the table below gives the flow through the valve for various supply pressures taken from the manufacturer's data sheet and corresponding values of $A = \frac{q}{\sqrt{P_s}}$ can be found.

Pressure [bar]	Flow [l/min]	Pressure [N/m^2]	Flow [m^3/s]	A $\left[\frac{m^3/s}{\sqrt{N/m^2}}\right]$
0	0	0	0	-
50	32	5e6	5.3e-4	2.4e-7
100	46	1e7	7.6e-4	2.4e-7
150	56	1.5e7	9.3e-4	2.4e-7
200	64	2e7	10.6e-4	2.4e-7

Table 4-1 EHSV Pressure and Flow for a fully open Valve

Hydraulic Motor

A schematic representation of the hydraulic vane motor is shown below together with its block diagram approximation.

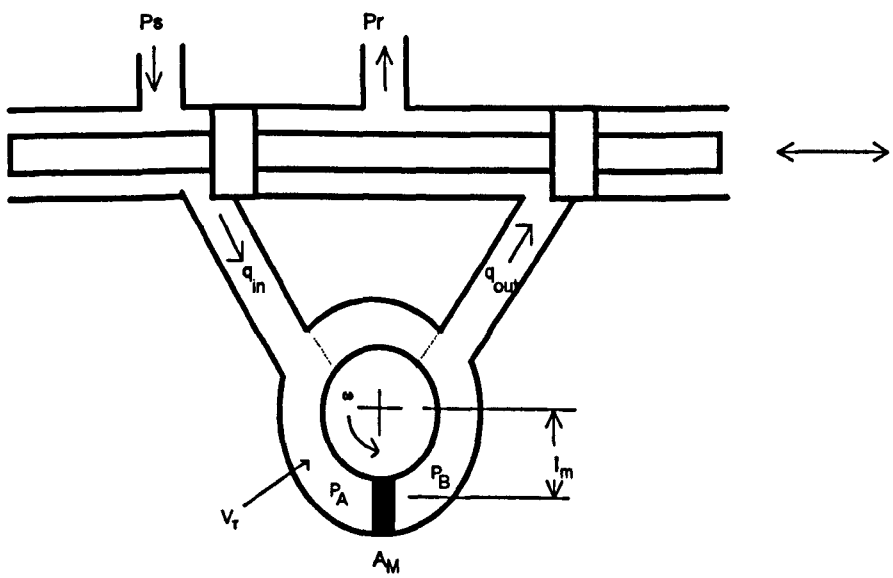

Schematic of the Rotary Hydraulic Motor

The flow from the EHSV into the motor and attached piping has two contributions, that due to the motor advancing and that due to the compressibility of the oil. The principal flow through the motor is given by the product of its rotational speed ω and volumetric displacement ΔV. Flows due to fluid compressibility are related to the total trapped volume of fluid V_T, the fluid bulk modulus N and the pressure changes acting on the fluid.

$$q_{in} = \omega\Delta V + \frac{\dot{P}_a V_T}{2N} \;,\; q_{out} = \omega\Delta V + \frac{\dot{P}_b V_T}{2N}$$
$$\dot{P}_a = [q_{in} - \omega\Delta V]\frac{2N}{V_T} \;,\; \dot{P}_b = [q_{out} - \omega\Delta V]\frac{2N}{V_T} \qquad (4\text{-}4)$$

The flow into and out off the EHSV is given by the valve opening and the pressure drop across the EHSV as developed in section 4.2.1.:

$$q_{in} = \frac{c_f}{\sqrt{\rho}} X_V d_v \sqrt{2P_S - 2P_a} \;,\; q_{out} = \frac{c_f}{\sqrt{\rho}} X_V d_v \sqrt{2P_b - 2P_R} \;. \qquad (4\text{-}1a)$$

The torque of the rotor T, which is due to the pressure difference across the effective surface A_M and moment arm l_M, is reacted by the inertia of the rotor, motor and aerodynamic torque:

$$T = (P_a - P_b) A_M l_M \qquad (4\text{-}5)$$

$$T = (I_M + I_R)\dot{\omega} + T_{Aero} \;. \qquad (4\text{-}6)$$

From this the non-linear block diagram of the hydraulic motor can be developed.

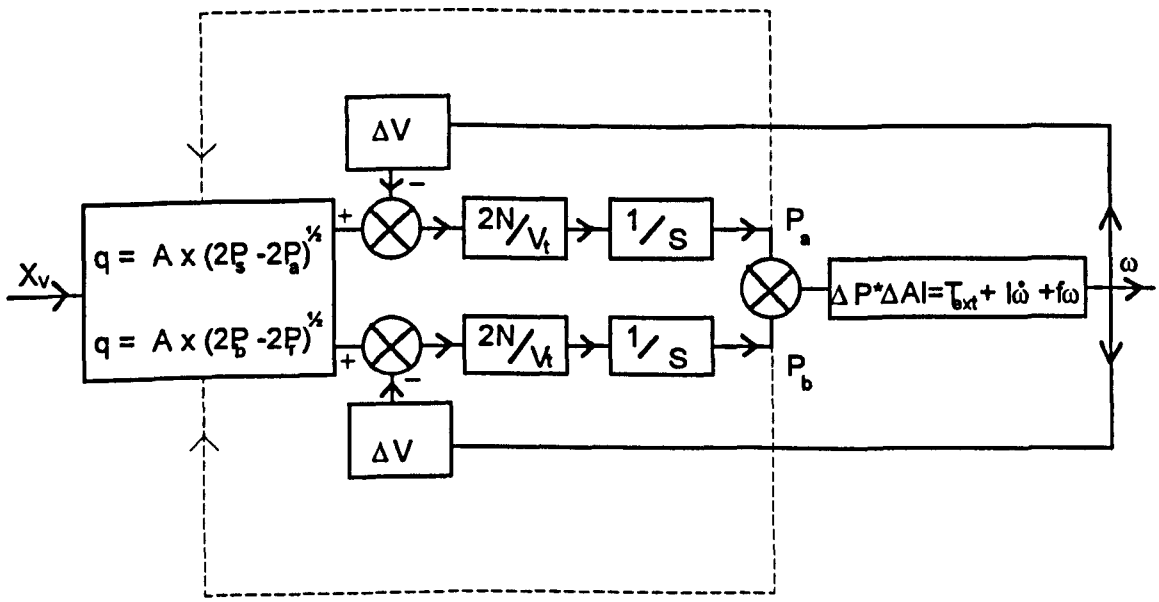

Non-linear Block Diagram Representation of the Hydraulic Motor

This results in a fairly complex non-linear analysis. The flow into and out of the EHSV valve depends on the pressure either side of the motor and similarly the rates of change of these pressures affect the flows due to compressibility. If it is assumed that half the total pressure loss will occur either side of the motor [Stringer 1976] the flow into and out of the motor and

valve will be equal and opposite. From this it follows that the motor pressure variations will also be equal and opposite and Equation (4-4) simplifies to the following:

$$\dot{P}_a = -\dot{P}_b \; ; \; \dot{\Delta P} = \dot{P}_a - \dot{P}_b \Rightarrow \dot{P}_a = \frac{\dot{\Delta P_a}}{2}$$
$$q = \omega \Delta V + \frac{\dot{\Delta P} V_T}{4N} \; , \; \dot{\Delta P} = [q - \omega \Delta V]\frac{4N}{V_T} \tag{4-7}$$

The flow from the EHSV can now be represented as a function of the pressure across the motor and valve opening as given in Equation 4-2b.

$$q = K_x x - K_m P_m \tag{4-2b}$$

The following simplified block diagram of the hydraulic motor results.

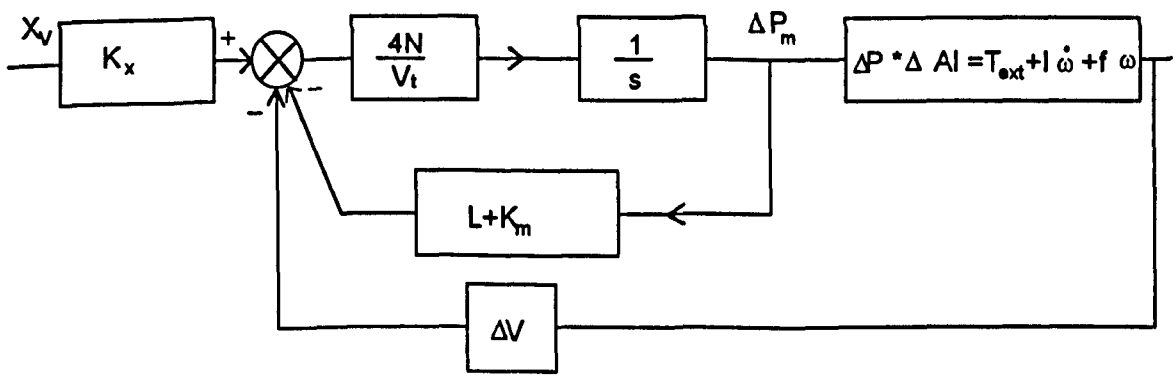

Block Diagram of the Linearised Hydraulic Motor

There will also be some leakage L through the motor which does not contribute to the rotation of the rotor and this should be considered. The leakage L is proportional to the pressure across the motor and effectively reduces the amount of flow which is used to turn the motor. The reduction in flow due to leakage and the effect of Km as discussed in section 2.1.1 have been included in the block diagram.

Power Amplifier

The power amplifier converts an input demand voltage to a EHSV coil current. The circuitry of the amplifier is such that a first-order delay may be introduced to make the response more sluggish, with a time constant of 0.5s. The amplifier may be modelled as a simple first-order

time delay with time constant T_a and gain K_a, if the delay circuitry is used, or as a simple gain K_a if it is not.

Rotor Speed Estimator

The rotor speed estimator is band-limited using a simple first-order low-pass filter and the transfer function representation between actual and estimated speed is given below. The time constant was chosen to be 0.004 to provide adequate bandwidth.

$$T.F._{\cdot} = \frac{60}{2\pi} \frac{1}{T_s s + 1} \tag{4-8}$$

Speed Controller

The controller initially implemented in the speed control loop, and subsequently modified, was a proportional-plus-integral gain controller. Although on the rotor rig the controller was implemented in digital form for the speed loop simulation, the controller was modelled in continuous time. This can be justified on the basis that the control law frame-rate was much larger than the desired speed control bandwidth. The controller parameters were then converted into their digital equivalents. The transfer function of the controller is shown below.

$$T.F._{\cdot} = \frac{K_P s + K_I}{s} \tag{4-9}$$

Aerodynamic Torque

The aerodynamic torque developed by the rotor was found using a rotor performance program developed internally at the University of Bristol [Bunniss 1984]. The torque of the rotor is proportional to the square of the rotor velocity and shown in Fig. 4-4, and a quadratic is fitted to each of the curves. The rotor is normally operated at conditions about a collective root pitch of approximately 12 degrees and the linearised torque in Nm is thus given by the following, about the operating point of 1200 rpm:

$$\begin{aligned} T &= 0.17 * 10^{-4} * rpm^2 \\ T' &= 0.34 * 10^{-4} * rpm \\ T_{@1200RPM} &= 0.17 * 10^{-4} * rpm_0^{\,2} + 0.34 * 10^{-4} * rpm_0 (rpm - rpm_0) \end{aligned} \quad , \tag{4-10}$$

or alternatively with the rotor speed in radians per second:

$$T_{@1200RPM} = 15.5*10^{-4}*\omega_0^2 + 3.1*10^{-3}*\omega_0(\omega-\omega_0). \tag{4-11}$$

Pressure Drop in Pipes

Flow through small bore pipes can cause considerable pressure losses. The flow resistance is governed by the tube diameter, the volume flow rate and the properties of the oil. Theoretically the flow will be either laminar or turbulent depending on the Reynolds number of the flow, which is primarily determined by the flow speed because pipes are generally fixed in size. In practice however it can be assumed that the flow will be turbulent. This is because the fluid will be continuously passing sharp bends, valves, filters and the hydraulic motor. Approximate oil properties at room temperature and expressions for the pressure drop per meter length of piping are given below and based on manufacturers data sheets.

$$p_{laminar} = \frac{0.32 w \nu \rho}{d_i^2 * 10^3} = \frac{6.79 V \nu \rho}{d_i^4 * 10^3} \left[{}^{bar}/_{m}\right]$$

$$p_{turbulent} = \frac{0.281 w^{1.75} \nu^{0.25} \rho}{d_i^{1.25} * 10^3} = \frac{59 V^{1.75} \nu^{0.25} \rho}{d_i^{4.75} * 10^3} \left[{}^{bar}/_{m}\right]$$

$$w = \text{flowspeed}[\text{m}/\text{s}],\ \nu = \text{kinematic viscosity}[mm^2/s] \tag{4-12}$$

$$V = \text{volume flowrate}\ [l/\text{min}],\ \rho = \text{density}\ [kg/m^3]$$

$$d_i = \text{pipe internal diameter}[mm]$$

Oil Properties

$$\nu = 50*10e{-}6\ \ [m^2/s] = 50\ \ [mm^2/s] \tag{4-13}$$

$$\rho = 870\ \ [kg/m^3]$$

The following graph shows the pressure drop in psi per meter length of various internal diameter pipes.

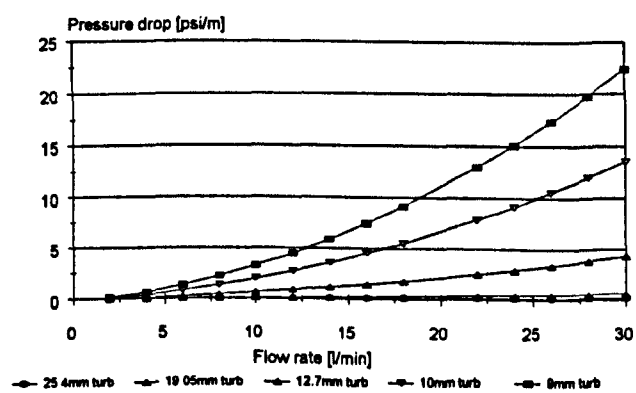

Pressure Losses in Piping assuming Turbulent Flow

The feed pipes between the EHSV and hydraulic power pack were of ¾ inch (19.05mm) internal diameter pipe of approximately 8m length. At the maximum flow speed of 30 l/min the pressure drop in these would be 5 psi assuming turbulent flow, which is negligible compared to the supply pressure of 3000 psi. In the initial rig design the flexible piping between the EHSV and motor was approximately 5m long and of ½ inch (12.7mm) internal diameter. For this piping the maximum pressure drop would be 25 psi, which again is small compared to the supply pressure. It was intended that in the modified rig the flexible piping between the motor and EHSV would be replaced by solid piping with an internal diameter of 10 mm and 0.7 m length. The expected pressure drop would be 10 psi. The pressure losses were therefore not considered further.

4.3 Model Validation

To validate the mathematical model of the speed control loop various tests, both open and closed loop, were conducted and the time and frequency responses were compared with the theoretical model. The results are shown in Fig. 4-5 to 4-8.

Fig. 4-5 shows the open-loop step response of the rotor from 280 rpm to 380 rpm. The mathematical model follows the overall shape of the experimental curve very well. The experimental data show a pulsating torque which occurs at shaft speed. Initially, it was thought that this could be due to pump dynamics but a detailed examination of the pump specification rules this out. A natural resonance in the hydraulic system is another possible explanation but would not account for the observed dependence of the oscillation on shaft speed. An analysis leading to a 1.5 Hz estimation of the first hydraulic mode frequency, for the unmodified rig, is given in Appendix E.

The experimental open-loop frequency response of the system at an operating point of 1200 rpm is shown in Fig. 4-6. Again the correlation between theoretical model and experimental data is good. Fig. 4-7 shows the closed-loop frequency response of the system at 1200 rpm. For this comparison, the proportional-plus-integral controller gains were set to the values used

in the original control system. The effect of the first hydraulic mode (1.5 Hz) is not apparent in the responses given because of the high damping due to leakage associated with the hydraulic servo motor.

Fig. 4-8 shows step responses at initial speeds from 1000 rpm to 1200 rpm with various controller settings of the rig compared with the mathematical model. The data in Fig. 4-8 have been re-sampled and the small speed ripple effect has therefore been suppressed. The correlation between the model and experiment is very good and together with the previous results suggests that the mathematical model can be used to design a more aggressive control scheme and to examine the effects of possible changes to the rig configuration on the dynamic performance of the speed regulation system.

4.4 Control Law Design

It was decided to use a frequency domain based approach to design the controller, since software to perform frequency response testing already existed as part of the software suite used on the rig. A proportional-plus-integral controller was chosen in order to improve gain in the low frequency region and hence improve speed regulation.

The transfer function and frequency response of a simple proportional-plus-integral controller are shown below.

$$T.F. = \frac{K_P s + K_I}{s} \qquad (4\text{-}14)$$

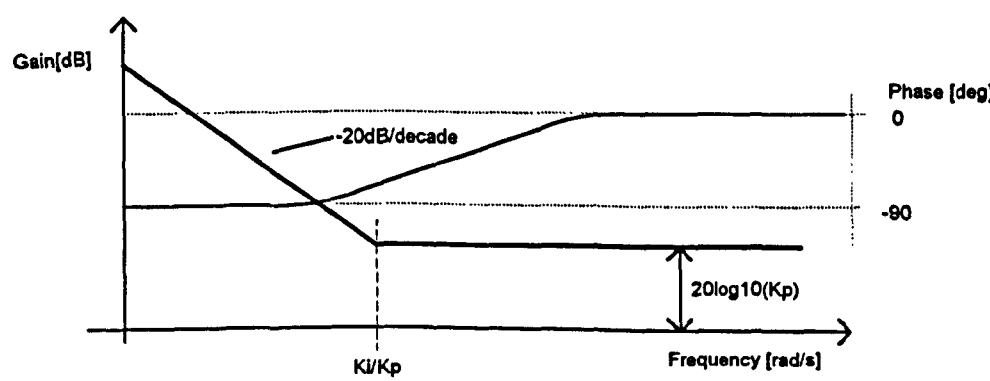

The integral term in the P+I controller lifts the low frequency gain by 20dB per decade at frequencies below a frequency of K_i/K_p radians per second, at higher frequencies the gain of the P+I controller remains constant. Similarly a phase lag of 90 degrees is introduced at low frequencies that gradually reduces to zero at higher frequencies. The frequency at which the phase loss due to the P+I controller can be considered negligible is one decade above the K_i/K_p ratio.

Before a new controller is developed the performance of the original controller on the un-modified rig was considered, which was a proportional-plus-integral controller with values of 4 and 6 for K_i and K_p respectively. The frequency and time responses for this controller are shown in Fig. 4-9 and 4-10. The controller gains were scheduled with speed to avoid instabilities in the speed loop at low rotor speeds due to reduced damping, and the new control scheme would have to take this into account.

In Fig. 4-11 the effect of reduced and solid piping on the open loop frequency response of the original controller are shown . It can be seen that reducing the volume has the most significant effect on increasing the bandwidth, and that the increased bulk modulus with solid piping only contributes marginally to the bandwidth improvement. From this is was decided to use small bore flexible piping in the new rig design that would decrease the trapped volume, and hence improve performance. The new controller would have to be designed with this in mind.

4.4.1 Optimised Proportional plus Integral Control

Knowing the open loop transfer function of the speed control loop with reduced trapped volume, the following optimum P+I controller was chosen.

The gain margin and crossover frequency at 135 degrees phase lag were found to be approximately 30 dB and 30 Hz respectively for the original open-loop response (Fig. 4-12). A 135 degree phase lag, as opposed to 180°, was chosen to give a safety margin.

To lift the gain at the crossover frequency to 0 dB a proportional gain of 31 is needed. To ensure that the integral gain does not introduce any phase loss at 30Hz the K_i/K_p ratio should give a frequency of an order of magnitude less (3Hz or 19 rad/sec). Thus a suitable value of K_i would be 589 (589/31=19). The open loop response with this controller is shown as a) in Fig. 4-12.

These gains are high and would result in very aggressive control of the helicopter rig, which in the event of a run away could result in damage to the blades, so and initially lower gains were used. The cross-over frequency was chosen to be at 4 Hz, which is close to that of the original set-up. The gain margin here is 15dB and thus K_p=5.6 . The required K_i/K_p ratio is 2.5 giving K_i=12, using rounded down values. The open loop response with a controller of K_p=5, K_i=12 is shown as b) in Fig. 4-12.

An intermediary controller with a crossover frequency of 10 Hz was also chosen and the appropriate values for K_p and K_i found using the above methods gives 12 and 75 respectively.

Thus three controllers of varying aggressiveness were developed, and the closed loop frequency and step response of the rotor operating at 1200 rpm are shown in Fig. 4-13 and 4-14.

The target closed-loop bandwidth of 10 Hz could be achieved using an optimised proportional-plus-integral controller on the modified rig with reduced trapped volume and higher performance servo valve. More sophisticated control schemes such as phase advance networks were therefore not necessary.

4.4.2 Torque Disturbance

The effect of torque disturbances on the rotor speed is shown in Fig. 4-15, for the original design and the reduced trapped volume design with different controllers. From Fig. 4-4 it can be seen that a pitch change of 1 degree about a nominal pitch of 12 degrees would produce an approximate variation in torque of 3 Nm. From the experiments described in Chapter 3 the

average change in speed over a series of sinusoidal collective inputs of 1 degree was obtained. The following table compares the observed and predicted root-mean-square changes in rotational speed during collective tests, for the unmodified rig.

Frequency [Hz]	Experiment [rms rpm]	Theoretical [rms rpm]
2	11	9.5
5	10.5	9.3
10	5.6	3.7
15	4.2	2.4

Table 4-2 Experimental & Predicted Speed Variations due to Torque Disturbances (Original Rig)

The low-frequency results correlate very well, whereas at higher frequencies the experimentally obtained variations are larger than those of the model.

For the improved rig design with reduced trapped volume the disturbance response is improved over the frequency range of interest. The effects of three different controllers are shown in Fig. 4-15. The main improvement lies in the low frequency range below 10 Hz. At frequencies above 20 Hz the choice of controller does not affect the disturbance response. The most aggressive controller a) (K_p=31; K_i=580) obviously has the best performance at low frequencies but features a frequency peak at 20 Hz.

4.4.3 Gain Scheduling

The reduced aerodynamic torque and smaller valve opening reduce the damping of the speed response at low speeds and thus the gain needs to be decreased at these speeds (see 4.2.1). Fig. 4-16 shows the open-loop frequency response at speeds of 200, 400, 792 and 1000 rpm. Gains were chosen with reference to gain and phase margin criteria. The following maximum allowable proportional gains are found for the above speeds respectively: K_p=2, 3.5, 7, 9. For speeds below the nominal operating speed of 1200 rpm only, the integral term was not used.

Demands on processing time meant that the scheduling of the controller gains with speed had to be kept to a minimum, and the finally implemented scheme had a controller gain of 2 up to speed 800 rpm and a proportional gain of 5 from 800 to 1000 rpm.

To confirm the viability of this simplified gain scheduling scheme, the closed loop speed response using the above controller gain is shown in Fig. 4-17, for speeds of 200, 400, 792 and 1000 rpm. Once above 1000 rpm the full proportional-plus-integral controller as discussed above is implemented.

4.5 Conclusions

A linear mathematical model of a helicopter rotor-rig speed-control loop was developed and validated against measured data. Using the theoretical model, a speed controller was designed that kept the speed variations of the rotor to a minimum. This was essential, as the dynamic inflow models considered in this work ignored the rotor speed degree of freedom. Furthermore, the model was used to examine the effects of future design changes on the rotor speed control performance.

At low speeds the proportional and integral gains had to be decreased significantly to avoid instabilities in the speed loop, and consequently these were thus scheduled with speed. The reduced gain at low speeds is due to the greatly reduced aerodynamic torque and valve opening, which decrease system damping. It was found that a reduction of the trapped volume between the motor and EHSV would increase performance of the rotor speed loop. Future design changes should aim to reduce the trapped volume by approximately one tenth, using small-bore hydraulic connections. The increased resistance to dilation of the solid mild steel piping and associated effects on the system bulk modulus, were found to be small. Therefore it was decided to use small bore flexible aerospace hosing for the hydraulic connections. The effect on pressure losses, of the reduced diameter piping, was found to be negligible.

In its initial state a torque disturbance, due to a 1 degree pitch change about the nominal root pitch, causes rotor speed variations of at worst 10 rpm. For the reduced volume design the speed changes could be reduced to 4 rpm at 1200 rpm using a controller with K_p=12 and K_i=75, scheduled with speed. The most aggressive controller was not implemented because of safety considerations, in case of component failures in the speed control loop.

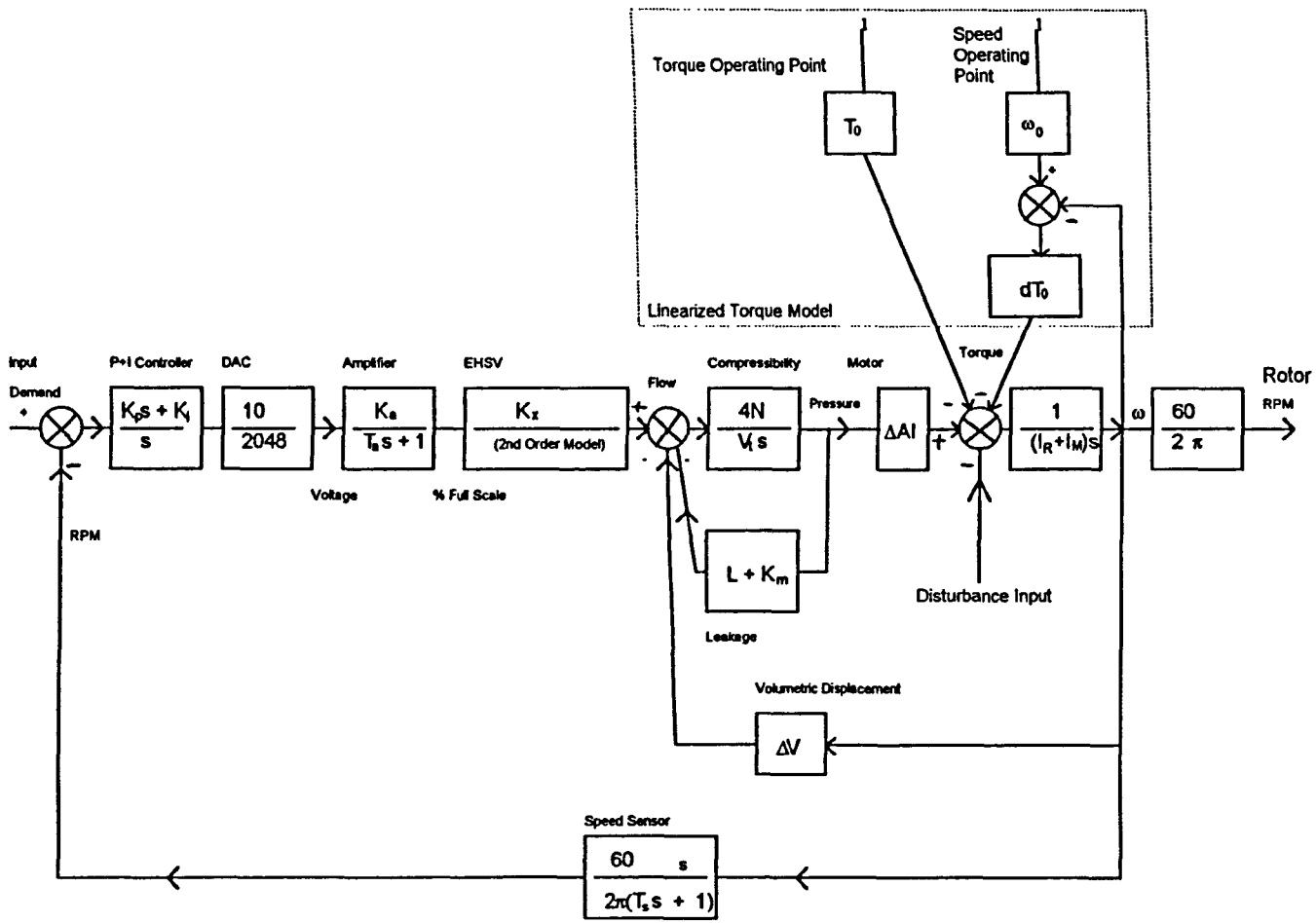

Fig. 4-1 Block Diagram of the Speed Control Loop

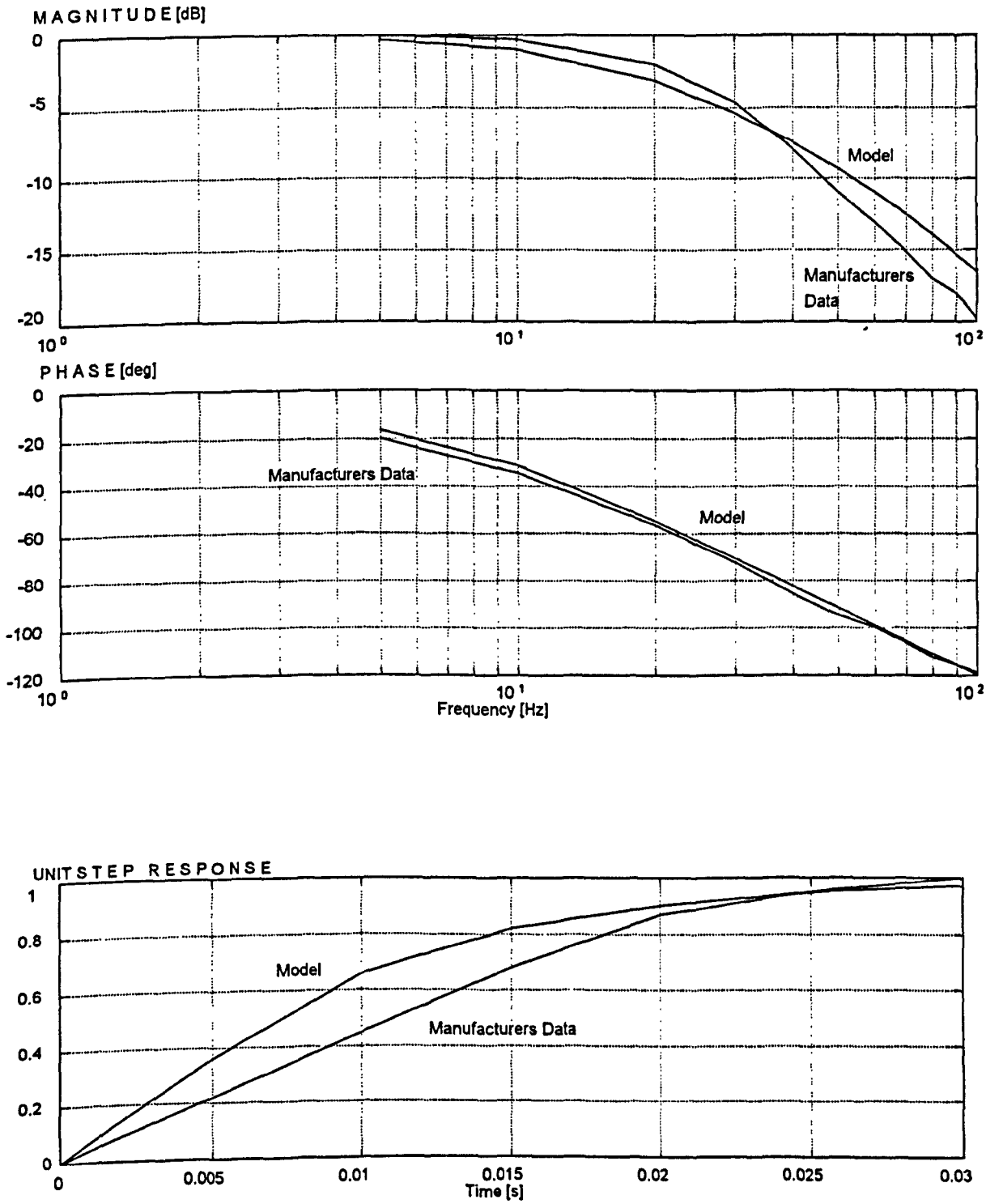

Fig. 4-2 Second Order EHSV Model Approximation using Manufacturer's Data
(natural frequency 300 rad/s, damping ratio = 1.5)

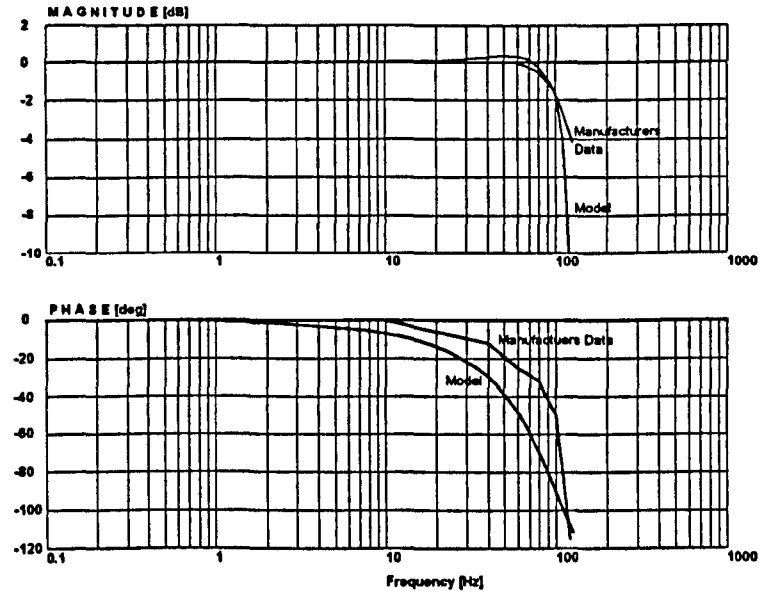

Fig. 4-3 Improved Bandwidth EHSV, Second Order Approximation
(natural frequency 600 rad/s, damping ratio = 0.6)

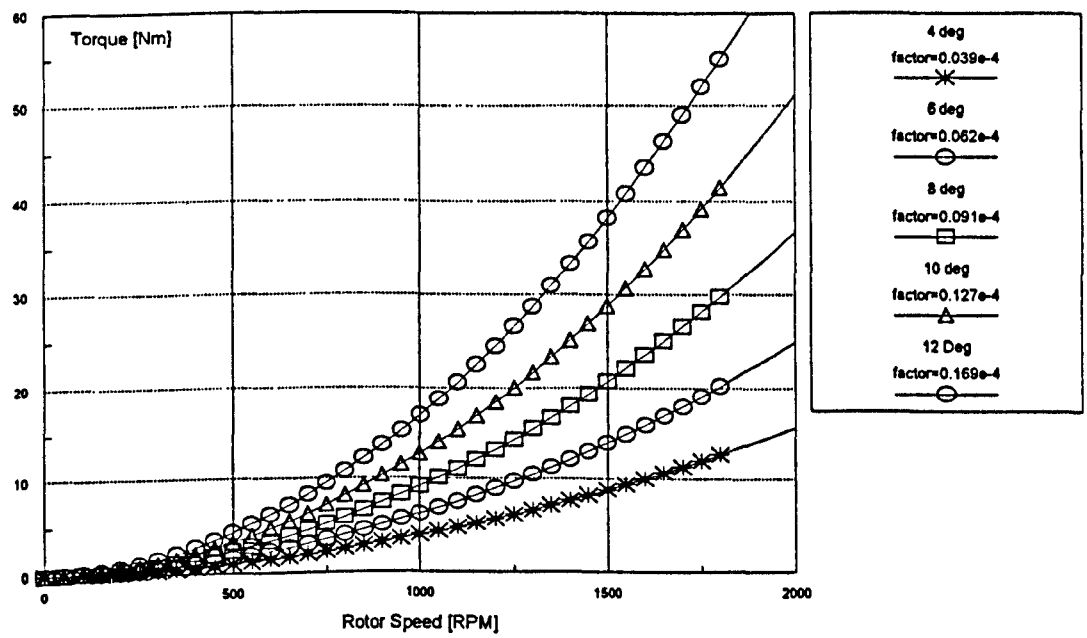

Fig. 4-4 Prediction of the Aerodynamic Rotor Torque at Various Pitch Pitch Settings with Quadratic Curves fitted to the Data
(based on SPROTAN [P.C. Bunniss 1984])

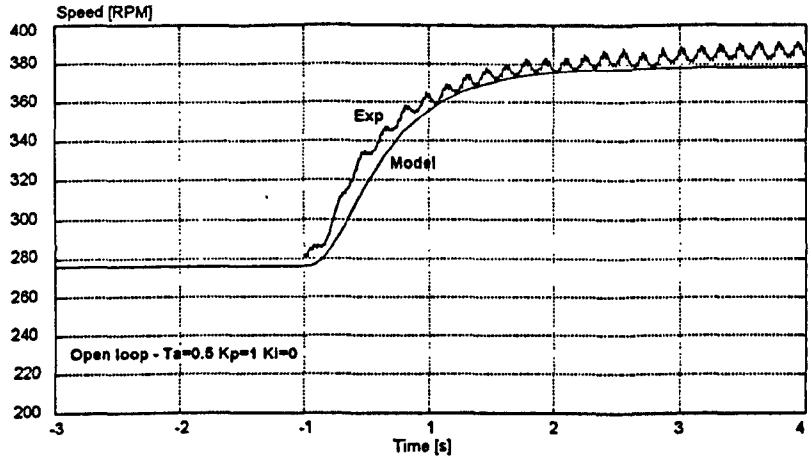

Fig. 4-5 Open Loop Step Response of Rotor and Model at Low Speed

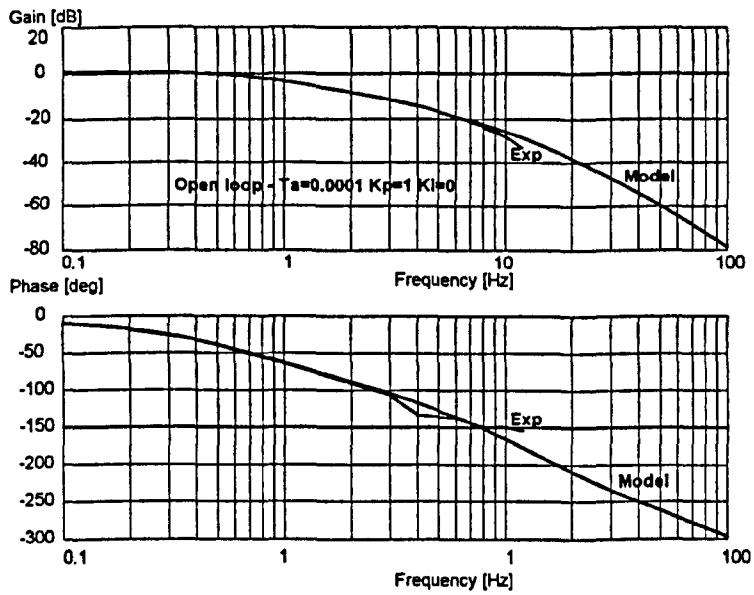

Fig. 4-6 Comparison of Open Loop Frequency Response of Model and Experimental Data

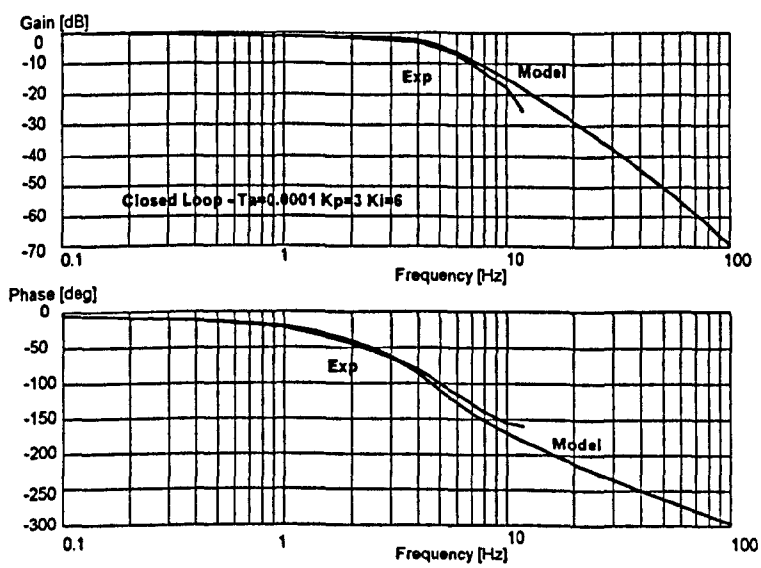

Fig. 4-7 Comparison of Closed Loop Frequency Response of Model with Experimental Data

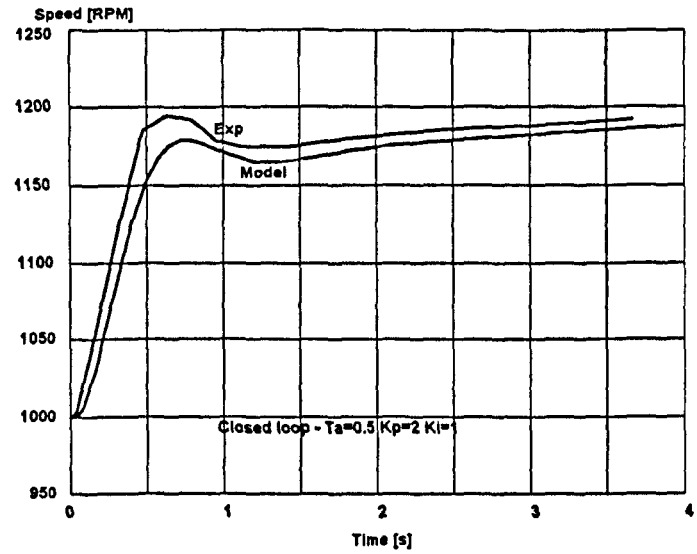

(a)

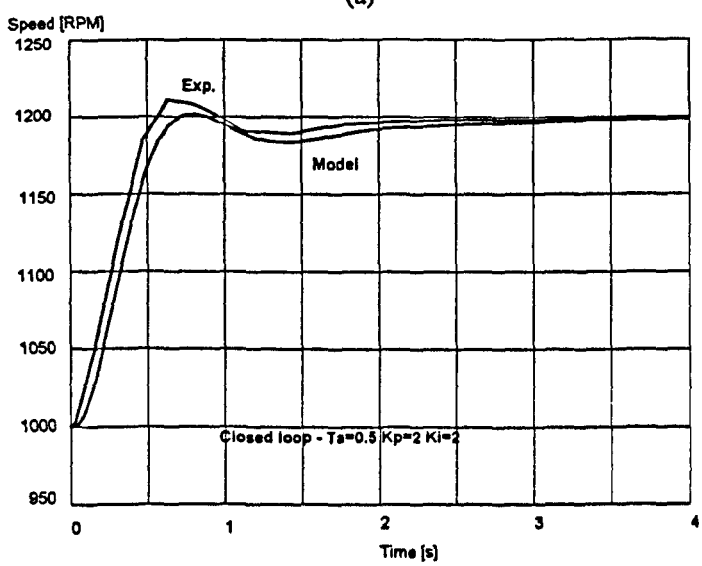

(b)

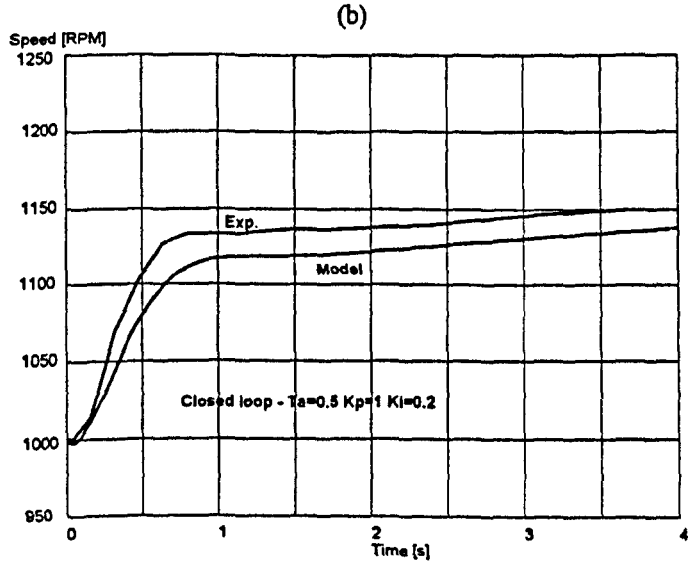

(c)

Fig. 4-8 Comparison of Model Step Response at 1000 rpm with Experimental Data using various Controller Settings

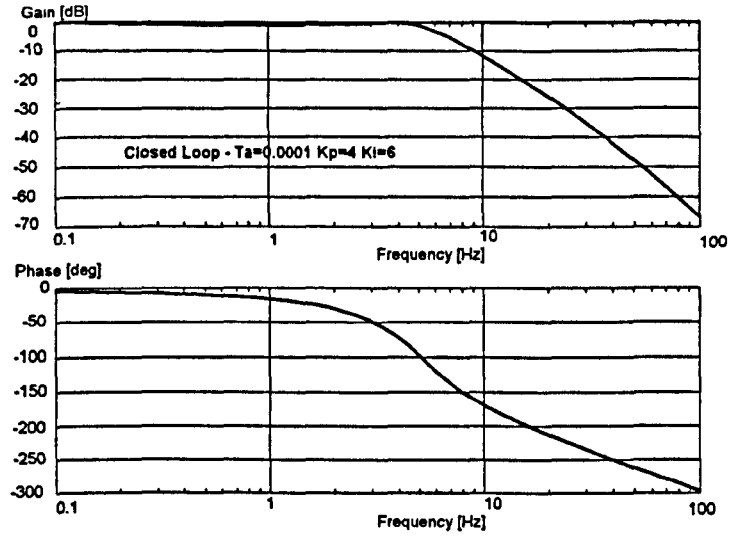

Fig. 4-9 Speed-Loop Frequency Response with Proportional & Integral Control

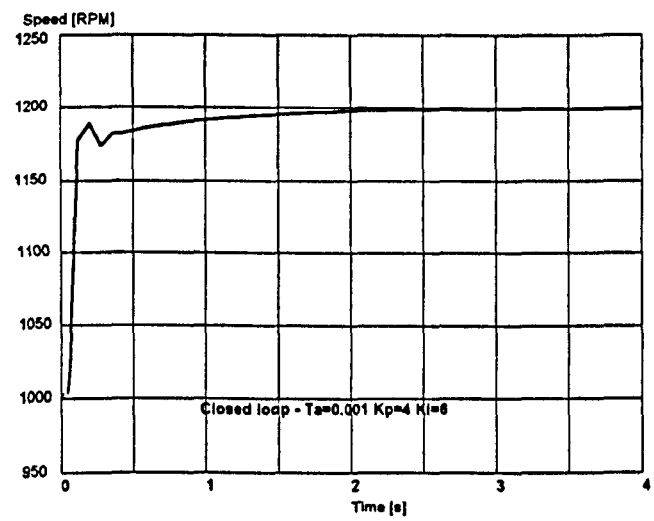

Fig. 4-10 Experimental Rotor Response to a Step Input at 1000 rpm

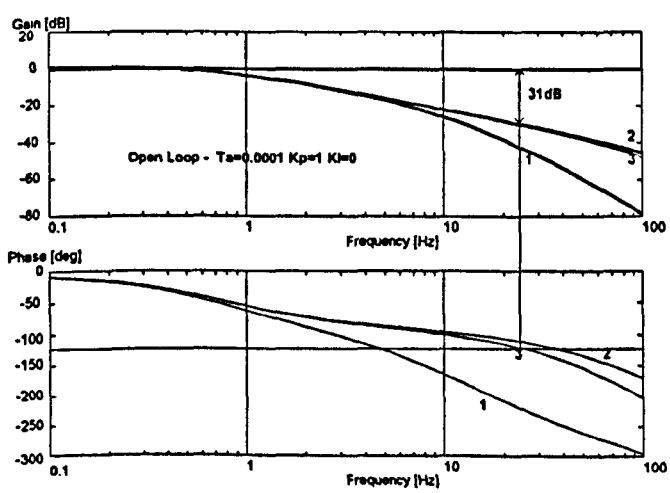

Fig. 4-11 Effect of Reduced Volume and Solid Piping
(1Original trapped volume with flexible piping; **2** Reduced trapped volume with solid piping; **3** Reduced trapped volume with flexible piping)

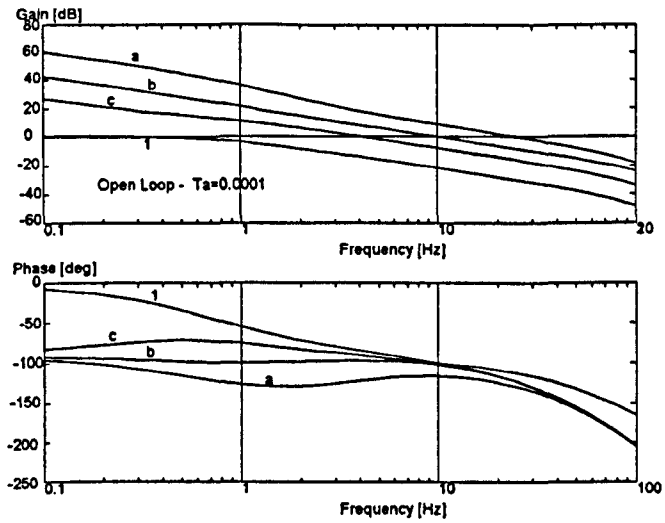

Fig. 4-12 Open Loop Frequency Response with three Controllers (1 Original, a Kp=31;Ki=580,b Kp=12;Ki=75, c Kp=5;Ki=12)

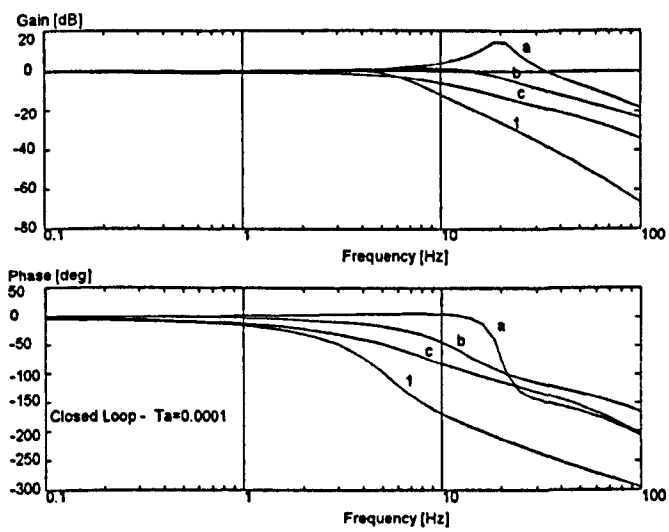

Fig. 4-13 Comparison of Closed Loop Response of Improved Rig with earlier Results (1 Original, a Kp=31;Ki=580,b Kp=12;Ki=75, c Kp=5;Ki=12)

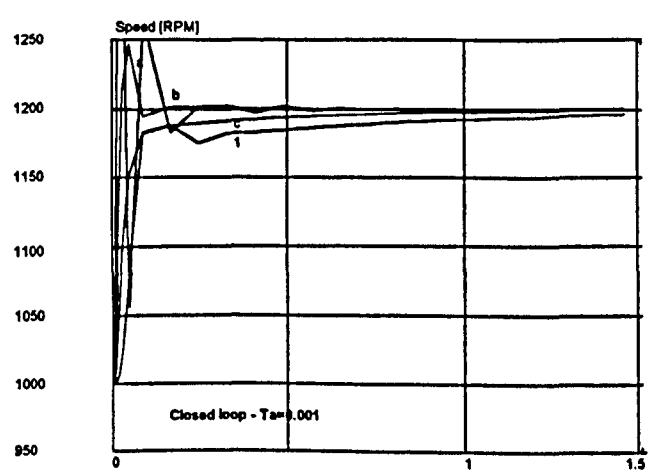

Fig. 4-14 Comparison of Closed Loop Step Response of Improved Rig with Original (1 Original Rig, a Kp=31;Ki=580,b Kp=12;Ki=75, c Kp=5;Ki=12)

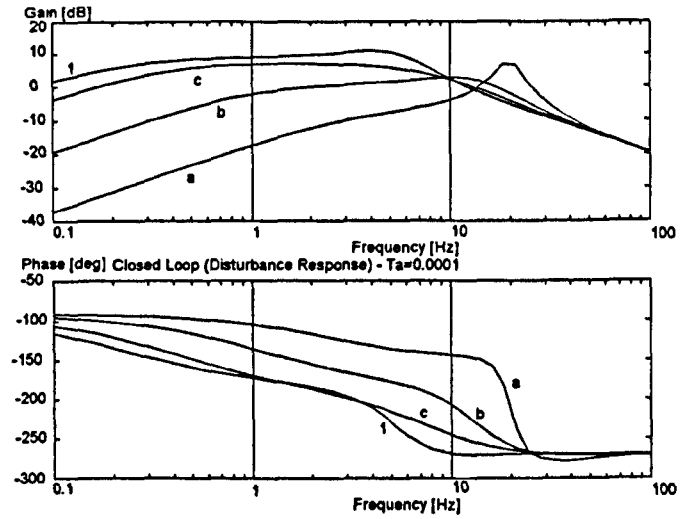

Fig. 4-15 Rotor Speed Response to Torque Disturbances for the Original and New Rig Design (Gain is given as rpm/Nm)
(1 Original Rig, a Kp=31;Ki=580,b Kp=12;Ki=75, c Kp=5;Ki=12)

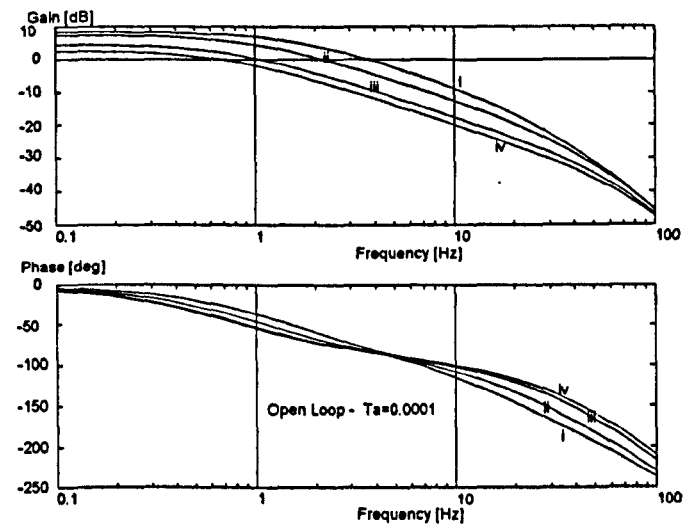

Fig. 4-16 Open Loop Frequency Response at various Speeds with Kp=1,Ki=0
(i 200rpm ii 400rpm iii 792rpm iv 1000rpm)

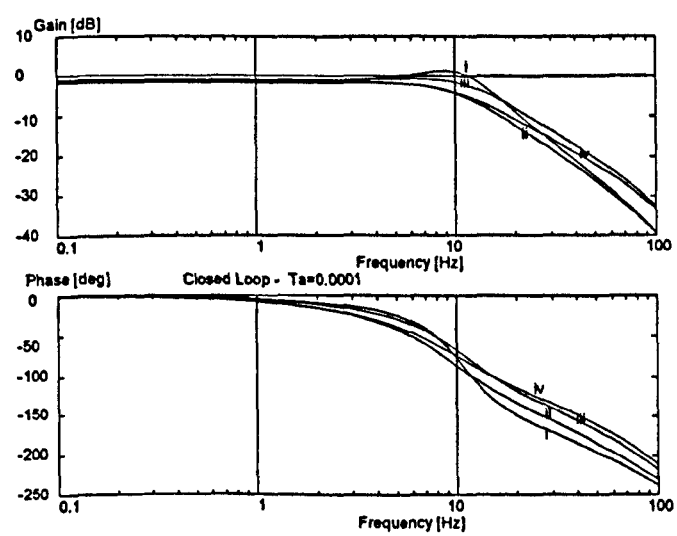

Fig. 4-17 Closed Loop Frequency Response using a Speed Scheduled Gain
(i 200rpm ii 400rpm iii 792rpm iv 1000rpm)

Chapter 5
Dynamic Inflow with Collective Excitation in Hover

5.1 Introduction

In this section results will be presented which examine the radial variation of the induced flow beneath the rotor, while it is being excited collectively. Most of the results were obtained at an operating speed of 1200 rpm, but results for 1000 rpm and 1500 rpm cases are also given. The inflow measurements taken by hot-wire anemometry were supplemented by measurements using a Laser Doppler Anemometer (LDA), which allowed measurements closer to the blades. The measurements were taken at one azimuthal position (90 deg.), and radial stations ranging from 18% to 103% of the rotor radius. The use of hot-wire anemometry is discussed in Chapter 2. Some discussion of the problems associated with taking dynamic measurements using a LDA will be given. For the test cases considered the rotor was mounted in the return section of the wind tunnel but operated in simulated hover, i.e. at zero wind speed. The radial variation of the induced flow in a dynamic case should be of interest with regard to the validation of the Pitt and Peters [Pitt & Peters 1981] dynamic inflow model as this assumes no radial variation of the dynamic inflow due to collective excitation of the rotor. An area of concern that was highlighted in Chapter 3 was the variation of the inflow phase with vertical separation from the rotor blade plane, and this will also be examined in detail. The input to the rotor was 1.43 degrees of collective pitch over a frequency range of 0.5 to 30 Hz. Finally, the results from the 2 DOF coning / inflow models developed in Chapter 3, will be briefly re-examined with reference to the extensive hot-wire dynamic inflow data.

5.2 Inflow Measurements using Radially Spaced Hot-Wires

5.2.1 Hot Wire Anemometry

The hot wires were located radially beneath the rotor at the 90 degree azimuth position, some 0.15m below the rotor. Previously, the hot wires had been calibrated in a wind tunnel. Twelve

radial positions were covered from 18%R to 103%R, with 5 measurements being taken at each taken.

5.2.2 Inflow Response Variation with Radial Station

The gain of the inflow response, due to the collective excitation of the rotor, as a function of the radial station is shown in Fig. 5-1, 5-2 and 5-3. Three rotor speed settings of 1000 rpm, 1200 rpm and 1500 rpm are shown respectively. The curves show the average inflow distribution obtained over 5 runs, and the standard deviation, for the 12 frequencies considered. It can be clearly seen that the dynamic inflow distribution is not constant with radius and also changes with frequency. Considering the 1200 rpm case, the inflow distribution is constant with radius at 0.5 Hz up to approximately 80 % R and then drops off rapidly. The reduction of gain outboard of 80% R is shown at all frequencies. This can be explained from results obtained by flow visualisation which put the extent of the turbulent tip region at approximately 90 % R. As frequency is increased a peak in the gain at 80-90% R develops and then becomes even more pronounced. In the mid-frequency range, approximately 10-20 Hz, a secondary peak in the gain at approximately 35% R appears, with a pronounced trough between the two peaks. Above 20 Hz this secondary peak disappears. This behaviour is reproduced at all three rotor speeds and is shown in Fig. 5-4, using three-dimensional carpet plots.

The variation of the induced inflow phase with radius is shown in Fig. 5-5 for the 1200 rpm case. The upper graph shows the frequencies 0.5 to 15.1 Hz and the lower graph the remaining frequencies to 30 Hz. With increasing frequency the inflow phase lag at a radial station generally increases, together with a trend of increasing inflow delay towards the inboard station. The variation for the higher frequencies is shown in Fig. 5-5 on the bottom graph , the trend here is much less clear.

For the lowest frequency considered at 0.5 Hz the inflow phase distribution over the radius is nearly constant with a slight phase lag of 10 degrees over the range of 45 to 80 % radial

station. The reliability of the phase measurements will deteriorate above 80 % R, as this lies outside the wake and also at the innermost radial stations due to the small induced velocities there. At the next frequency of 1 Hz the inflow phase response is still reasonably constant with radial station, particularly over the centre section of the blade. For the higher frequencies of 5 Hz, 10 Hz, 12.5 Hz and 15 Hz a clear increase of phase lag in the inboard direction can be seen. As the frequency is still further increased this trend persists but the behaviour of the phase with radius becomes more erratic. The rate at which the phase reduces towards the inboard section increases with frequency. The reduction is not strictly linear, but approximate rates are given for a range of frequencies below, which were calculated from an approximate linear gradient over the centre (0.4 to 0.8R) section of the blade.

Frequency [Hz]	5.0	12.5	25.0	27.0
Rate of Phase Loss [deg/m]	110	200	700	980

Table 5-1 Radial Inflow Phase Loss Gradient at 4 Frequencies

The rate of phase loss is not proportional to the excitation frequency. Possible explanations for the radial inflow gain behaviour will be given in section 5.2.6.

5.2.3 Inflow Frequency Response

To obtain a better understanding of the inflow response and its dependence on frequency, the gain and phase Bode plots are shown in Fig. 5-6 and Fig. 5-7 for various radial stations at 1200 rpm.

The gain response with frequency averaged over 5 runs, together with the standard deviation, for the 1200 rpm case is shown in Fig. 5-6. At the innermost radial stations and particularly at low frequency the standard deviation is poor compared to the response at other radial stations probably due to recirculation and small velocities. All the frequency responses essentially show a constant gain in the region 0.5 Hz to 10 Hz followed by a drop in gain at around 10 Hz. After the gain has dropped by some 10 dB there is a recovery of the gain at approximately 23 Hz. For the outermost radial stations the results are less repeatable because they were taken

outside the wake region of the rotor. The gain at low frequency is well below the gain at the inboard section of the blade, but the results imply that at high frequencies the outboard section of the blade is still producing inflow variations.

Fig. 5-7 shows the phase response at various radial stations. For the innermost radial station (18 % R) the phase response is erratic. This is most probably due to the small absolute changes in velocity caused at this inboard station. Moving outboard the repeatability of the response improves. Shown on the plot is the average over 5 runs together with the one-standard-deviation confidence interval. From these results, repeatability is seen to be good for all but the inner and outermost two radial stations. The problem with the outermost stations is that they lie outside the primary wake and are therefore in the turbulent region produced by the tip. Particularly interesting is the recovery in phase in the region of 20-24 Hz which can be seen for radial stations 49%R outward. The magnitude of the recovery increases with increasing radial station. Comparing the 65%R and 80 %R cases with those of Fig. 5-8, which has many more frequency points and is part of a different data set (gathered over a different period) very good agreement is found.

The phase response of the inflow at two other rotor speeds of 1000 rpm and 1500 rpm respectively are shown in Fig. 5-9 and Fig. 5-10. The corresponding gain response at these rotor speeds is shown in the 3D graphs of Fig. 5-4.

5.2.4 Effect of Rotor Speed on Inflow Frequency Response

The effect of rotor speed on the frequency response of the inflow is shown in Fig. 5-4, 5-9, and 5-10. Together these figures give a picture of the inflow gain and phase response with frequency at various radial stations at three different rotor speeds.

Fig. 5-11 shows how the gain response at one radial station changes with rotor speed. Considering the response for frequencies up to 20 Hz, it can be seen that at the higher rotor speed, the gain falls later than for the lower speed setting, but at the lower frequencies the overall values of the gains converge at just under 30 dB for all 3 speeds. The transfer function

between the aerodynamic loading perturbations and induced flow, assuming the Pitt and Peters dynamic inflow model, is given by, $\frac{\lambda}{C_T} = \frac{1}{\frac{M_{11}}{\Omega}s + 4\lambda_m}$ (from Equation 1-29) and the steady state gain is given by, $\frac{\lambda}{C_T} = \frac{1}{4\lambda_m}$.

It can be seen that in the steady case as the rotor speed is increased the average induced velocity will also increase and therefore the gain of the inflow response to thrust perturbations will decrease. However, for the same pitch perturbations it would be expected that the aerodynamic hub moment perturbations would increase with rotor speed, and it is therefore quite possible that the steady induced flow perturbations are the same at low frequencies as shown in the data.

Furthermore in the Pitt and Peters model the dynamics of the air are governed by the apparent mass factor (M11 for the hover case) which in the model is divided by the rotor speed. Therefore the higher the rotor speed the smaller the ($\frac{M_{11}}{\Omega}$) parameter and the smaller the effective apparent mass, which in turn results in reduced inflow dynamics. This correlates with the upper graph of Fig. 5-11, where the inflow gain falls off more slowly at the higher shaft speed.

The bottom two graphs of Fig. 5-11 show the variation of gain plotted against rotor speed. Their frequencies are split into two graphs, the upper showing frequencies between 0.5 Hz and 15 Hz and the lower showing the remaining frequencies to 30 Hz. Again it can be seen that for the frequencies up to 20 Hz the gain increases consistently, nearly linearly with rotor speed, whereas at higher frequencies this is not the case. There are distinct differences between the character of the inflow responses at frequencies above and below shaft speed.

The effect of rotor speed on the inflow phase response is shown in Fig. 5-12. The upper graph shows the phase variation over the frequency range for the three rotor speeds considered. On the two lower graphs the phase is plotted against rotor speed. For frequencies below 17 Hz it can be clearly seen that the phase lag depends linearly on rotor speed, with decreasing phase

lag for increasing rotor speed. At higher rotor speeds the air responds more rapidly to loading changes.

This conclusion needs to be examined with respect to the Pitt and Peters inflow formulation. As rotor speed, and hence rotor loading for a given collective setting, increases the delay of the induced velocity decreases. From the Pitt and Peters model we have the following relationship, between the unsteady induced velocities and the rotor loading: $C_T = \frac{M_{11}}{\Omega}\dot{\lambda} + 4\lambda_m\lambda$; The value of $\frac{M_{11}}{\Omega}$ is the effective apparent mass term. The larger this is the more sluggish the inflow response. Thus at higher rotor speeds the dynamic inflow would be expected to respond more rapidly. This is consistent with the above experimental results and goes some way to validate the Pitt and Peters model.

For the higher frequencies the phase variation with frequency is not so well behaved, but the general trend is still decreasing phase lag with increasing rotor speed.

5.2.5 Phase Jump Corrections

A major problem when looking at the phase data obtained from both hot wire and LDA data was to determine where phase jumps over 360 degrees occurred. The correlation procedure could resolve phase delays only between 0 and 360 degrees. To give confidence that phase jumps over 360 degrees occurred and that these were not recoveries in phase or vice-a-versa, 3 data sets were obtained with collective excitation between 0.5 and 36 Hz which had twice as many sampling frequencies as the normal experiments. The results are shown in Fig. 5-8, for two radial positions of 65 % R and 80 % R. It can be clearly seen that in both cases there is a phase jump between 20 and 25 Hz. The phase jump for the outer radial positions occurs at a higher frequency than that of the inboard station. This result confirms a radial variation of the induced flow phase and shows that the inflow phase falls more rapidly towards the inboard station of the rotor. The area around 20 Hz is particularly interesting, with the recovery in phase around this frequency, appearing as a sharp decrease in phase lag in the usual phase plots with twelve frequency points. This occurs at 20 Hz for both radial stations, also the standard

deviation of the data set which is very good over most of the frequency range is poorer around the area of 20 Hz. The information obtained from these results was used to determine where phase jump corrections in the other phase data were made. It was not always entirely clear were phase jumps were occurring and judgement based on other results and trends had to be exercised.

The frequency scale of the upper two graphs shown in Fig. 5-8 is exaggerated, running only from 10 to 100 Hz on the logarithmic scale. To aid in comparison with the previous results the same graphs are shown to the same scale as earlier results on the lower portion of the figure. It can be clearly seen that the recovery of gain in the vicinity of 20 Hz is the characteristic sharp peak seen in the graphs of Fig. 5-7, 5-9 and 5-10 .

5.2.6 Effects Contributing to the Radial Inflow Variation

These results show that at high frequencies the outer section of the blade produces the highest induced velocities and thus also most lift. Several effects may contribute and are briefly discussed here. Further work will be needed to isolate the individual effects.

The Reynolds number of the flow as referenced to the blade at a certain radial station varies along the span of the blade, increasing outboard as the relative velocity of the air over the blade increases linearly with radius. It is know that the lift characteristics of an aerofoil section vary with Reynolds number and this may be a contributory cause for the redistribution of the induced flow with radial station.

Furthermore, it is also known that the dynamic lift characteristic of an aerofoil depends on the non-dimensional reduced frequency of its oscillation. Work by Lal [Lal 1994, Liou et al 1994] has examined the chordwise pressure distribution of an aerofoil exited in pitch at various radial stations. It is found that the reduced frequency $k = \frac{b\omega}{\Omega}$, where b is the blade semi-chord and ω the excitation frequency, affects the pressure distribution. Again, because of the rotating nature of the blade the reduced frequency based on frequency of oscillation and relative airspeed over the blade will vary with radial station and excitation frequency providing a

further possible explanation for the three-dimensional inflow changes shown in the three-dimensional carpet plots (Fig. 5-4). In this experimental set-up the reduced frequency at the blade tip varies from 3.8e-2 to 1.2e-4 over a range of frequencies from 30 to 0.1 Hz. An effective means of isolating the reduced frequency effects would be to use blades of different chord at the same operating conditions. This is discussed under 'Future Work' in Chapter 8.

Work by Liou [Liou, Komerath et al 1994] which examined the induced flow response over a radial range at only one excitation frequency observed hysteresis when the induced flow at a point is plotted against the excitation root pitch. It is also found that this hysteresis effect diminishes toward the tip and seems to be predominantly affected by the inboard shed vorticity, the shed vorticity being due to the time-varying lift circulation at a radial station, in comparison to bound vorticity which is due to geometric changes in lift and predominantly found at the tip. Further work needs to be done to investigate this effect and is outlined in Chapter 8.

The increase in inflow response and subsequent sharp drop on the area of 80 % R is most probably due to tip effects. Work on a two-bladed teetering rotor by Liou [Liou, Komerath et al 1988] using laser sheet flow visualisation showed that the vortex cores have formed some 60 degrees behind the blade tip. Subsequently they move inboard to the 85% radial station staying within 6 cm of the rotor plane, for the first 180 degrees of rotor rotation, before moving down 13cm by the end of one revolution. The tip region is therefore strongly affected by the tip vortices of recent preceding blades. Another possible explanation may be that the strong downward velocity component in the tip region will convect any shed vorticity (vorticity due to time-varying circulation) rapidly away from the blade tip thus diminishing its effects. The increase in inflow phase delay from the tip inboard as shown in Fig. 5-5 in section 2.2 could also be due to tip effects. If the inflow is affected by the circulation of the strong tip vortex then further away from the tip this effect would be smaller and the response of the air more sluggish.

A comprehensive computational fluid dynamic approach, which tracks the time-varying shed vorticity and trailing vorticity from each blade for several revolutions, should be useful in

showing how the frequency of collective excitation affects the distribution of shed vorticity in the wake and whether this reproduces the observed radial and frequency dependent variations of the inflow gain and phase.

5.2.7 Inflow Response at Several Vertical Stations

An important question in this work was to examine how the measured induced velocity response varies with vertical separation from the blade. The Pitt and Peters [Pitt and Peters 1981] model predicts the velocity at the rotor disc, and as the velocities can only be measured some distance below, they need to be corrected for this vertical variation. The work in Chapter 3 assumed that the necessary correction was a pure transmission delay. That is to say that the difference between the measured response and the response at the disc is only due to the finite time it takes the flow to travel from rotor disc to measuring point. Given the mean flow speed this should be easy to correct. The correction seems quite plausible, but does contradict the idealised conceptualisation of the air behaving similar to a lumped mass, which is accelerated by the rotor. In this case it would be expected that the response of the air at the disc and at the measuring point would be very similar as they form part of the same mass of air which is being accelerated.

The induced flow was measured at the positions beneath the rotor at one radial position of 57% R . The vertical separation from the rotor plane was 9cm, 15cm and 27 cm. The frequency response of the inflow at these three vertical positions is shown in Fig. 5-13.

The gain measured at three vertical separations over the frequency range is essentially the same at low frequencies with the gain of the hot-wire furthest from the rotor being some 2dB larger than that of the closest hot wire. Particularly interesting is the fact that the measurements closest to the blade show the sharpest fall in gain in the area of 20 Hz, and the hot-wire furthest away shows the least.

The phase response is shown in the lower graph of Fig. 5-13. Again at low frequencies the phase responses are very similar. As frequency increases, the phase of the hot wire furthest

away from the rotor drops off earliest. The hot wire closest to the blade also has the most pronounced characteristic phase recovery at 20-25 Hz.

In Fig. 5-14 the gain and phase are plotted against vertical separation from the blade. The gain and phase plots have been split into two, one showing the frequency range 0.5 to 15 Hz, the other 17 to 30 Hz, for clarity.

The gain at low frequency increases significantly with vertical separation, for the 0.5 and 1 Hz case. The increases over 18 cm is about 3 and 4 dB respectively. Between 5 and 12 Hz the gain is at first constant with distance and then decreases slightly (1.5 dB over 18cm at 12Hz). The next two frequencies of 15 and 20 Hz again show an increases in gain of about 4 dB over the same distance. In all the results considered so far, the behaviour of the gain with distance has been essentially linear, typified by the straight lines in Fig. 5-14 for the gain cases of 0.5 to 15 Hz. At higher frequencies (20-29 Hz) this apparent linearity is lost and no clear gain tendency with vertical separation can be found, again showing the change in character of the inflow response at frequencies near and above the rotor shaft speed.

The lower two graphs of Fig. 5-14 show the induced flow phase variation with vertical separation. For frequencies between 0.5 and 17 Hz the phase variation is linear with distance and increases in steepness with frequency. This is as would be expected for a pure transmission delay. For the remaining higher frequencies the variation is not so linear but still increases in steepness with frequency.

The time delay between two observations of a flow with mean speed u a distance s apart is,

$$t_d = s/u. \tag{5-1}$$

As a function of rotational frequency and expressed in terms of phase of the excitation frequency f this time delay then becomes:

$$phase_{delay} = 360 f\, s/u. \tag{5-2}$$

Assuming a transmission delay, the phase difference between the cyclically varying flow between two measurement points expressed as a phase delay, is linearly dependent on the frequency and distance between the two points.

The upper graph in Fig. 5-15 shows the same data points as Fig. 5-14 for frequencies between 0.5 and 17 Hz, namely the phase delay as a function of vertical separation. Least-squares-error linear fit lines have been plotted on this graph and the gradients are given in the table below.

Frequency [Hz]	Gradient [deg/m]
0.5	30
1	-25
5	-187
10	-483
12.5	-779
15.1	-959
17.2	-966

Table 5-2 Inflow Phase gradient with Vertical Separation

The lower graph in Fig. 5-15 now plots the gradient and offset obtained from the least squares linear fit against frequency. The behaviour suggests linearity so again least squares error-linear fit, lines are fitted to the data and shown in the graph. The gradient and offset of the vertical phase variation are given as -63 deg/m /Hz and -4.8 deg /Hz respectively.

The slope of the inflow phase variation with frequency (gradient line) can be predicted assuming a pure transmission delay from the previous result (equation 5-2). The change in phase per unit distance and frequency is then

$$phase_d\left[{}^{deg}/_{m/Hz}\right] = 360/u. \tag{5-3}$$

Assuming the average velocity is 8.3 m/s (see Fig. 5-16) the appropriate slope is then 43.4 deg/m/Hz. The linearity of the observed phase lag with vertical separation and frequency, strongly suggests a transmission type delay although the theoretically predicted gradient is smaller by a factor of 0.7 than the experimentally obtained value of 63.4 deg/m/Hz.

Figure 5-17 finally shows the difference in phase between the three measuring points against frequency. The predicted difference assuming a transmission delay is also shown. Again the correlation up to 17 Hz is very good, above that, the experimental phase drops off much more quickly.

In conclusion, the phase variation with vertical separation can be partly corrected assuming a pure transmission delay for frequencies up to 17 Hz, although the free wake velocity implies a smaller phase gradient than that observed in the experimental data. At frequencies above 17 Hz a transmission delay alone does not explain the experimental data. The fact that the transmission type delay model is not fully satisfactory is not surprising when one considers the real structure of the wake. It is over-simplistic to assume that the flow behaves like a cohesive mass flowing between points. The flow at and beneath the rotor is strongly influenced by the shed and trailing vorticity in the wake.

In Chapter 3 it was suggested that the magnitude of the inflow perturbations might behave similarly to the average induced velocity, which increases with distance from the rotor disc due to wake contraction. The suggested correction for the mean induced velocity was as given below [Johnson 1980]:

$$\upsilon(z) = \upsilon(0)\left[1+\frac{z/R}{\sqrt{1+(z/R)^2}}\right]. \qquad (5\text{-}4,3\text{-}19)$$

If it is assumed that the induced velocity perturbations increase with distance from the disc, then the correction that would need to be applied is shown in Fig. 5-18. This suggests that the wake contraction effects, may account for approximately a 2 dB increase over a distance of 18cm. It was already shown in Fig. 5-14 that the inflow gain for the 0.5 Hz and 1 Hz cases increased by 3 to 4 dB over 18cm, and further that the rate of increase was dependent on frequency. Thus it is difficult to suggest an appropriate modification to existing theory that will take into account the inflow gain dependence on vertical separation.

5.3 Laser Doppler Anemometry Results

5.3.1 Laser Doppler Anemometer (LDA)- Experimental Limitations

The details of the Laser Doppler Anemometer system (LDA) are given in chapter 2 together with a brief description of its operating principles. Some of the problems encountered using the LDA specific to this work will be described here.

The accurate focusing of the six laser beams on one point in space and the subsequent focusing of the receiving optics on the same point requires considerable skill. The quality of the alignment of the LDA determines the average data rate of the velocity measurements. During the experiments it was found that although the LDA was mounted on a solid steel structure standing on the wind tunnel floor the vibrations in the tunnel, and aerodynamic buffeting of the LDA while the rotor was running, resulted in a gradual shift in the alignment of the optic heads. The fact that the floor of the tunnel was not sufficiently stiff and free from vibration added to this problem. The net effect was that the LDA had to be continuously realigned, which took up valuable tunnel time. The gradual misalignment also resulted in varying data rates during tests.

Another factor affecting the sampling rate of the laser was the seeding of the flow with fine smoke particles. It is the velocity of these oil droplets of only a few microns diameter that the LDA measures. The oil vapour was introduced using two seeding machines located above the rotor. It was difficult to achieve even and continuous seeding at all the measuring locations, due to re-circulation in the tunnel causing the seeding to vary constantly. It was possible to obtain information from only one point beneath the rotor at any time, which compares unfavourably with the four simultaneous measurements using the hot-wire system. Together, these three factors made the use of the LDA very inefficient.

The most serious drawback of the laser is fundamental to its operating principle, in that as velocity measurements depend on a droplet of oil passing through the measuring volume, the time between samples and hence the frequency of measurements is essentially random. Even

when a droplet of oil passes through the measuring volume it is registered as a valid data point only if all three velocity component analysers register the occurrence, within very tight time limits. The significance for experimental work is that the data provided by the laser are not equi-spaced, or taken at a predetermined sampling rate, and thus the data are not easily used with standard signal processing procedures.

For most steady-state work this is not a drawback as the data obtained at one measuring position are simply averaged over a long period. For dynamic analysis this is not possible and equi-spaced signals at a given sampling rate are required. To overcome this problem the laser data are re-sampled. However since the sampling rate of the laser was difficult to maintain at high level (above 700 Hz) and because the re-sampling has to be performed at a rate lower than the lowest effective sampling rate of the laser, final sampling rates of only 300 Hz were common. This compares unfavourably with the constant data rate of 500 Hz of the other rig instrumentation systems.

As measurements were attempted closer to the blade, the data rate dropped rapidly to unacceptably low levels. This was probably due to difficulties in maintaining a sufficient concentration of seeding in the vicinity of the blade.

The final problem that had to be addressed during the operation of the LDA was associated with the synchronisation between the LDA and the rotor rig control system. Both are independent systems, which run off their own internal clocks. The data taken by the LDA had to be linked to the pitch inputs generated on the rotor system. This was done through the use of timing markers generated by the rotor rig which appeared in the raw LDA data.

Once the raw data were taken by the laser they were re-sampled and then an identical correlation procedure to that used with the hot-wire data was applied.

The most valuable use of the LDA was in confirming the hot-wire results and obtaining some limited information closer to the blades and this will be discussed below.

5.3.2 Comparison of LDA and Hot-Wire Results

The gain and inflow data obtained using LDA is shown in Fig. 5-19, Fig. 5-20 and Fig. 5-21. The limited freedom of the traverse meant that only 0.6m could be surveyed, radially. This meant that some of the data positions covered with the hot-wire anemometry were excluded from the laser work. The six radial positions considered were 33%, 41%, 49%, 57%, 65% and 73 % R. Two vertical stations were possible 100 mm and 50 mm below the rotor. Time constraints meant that it was possible to obtain only one set of LDA data, and averaging was therefore not possible. The gain response data shown in Fig. 5-19 taken 0.1m below the rotor are very similar to that obtained from the hot wires, which reinforces the validity of the data obtained from the hot wires. For the data obtained close to the blade, the fall in gain at around 20 Hz is much sharper than that of the data gathered some 0.15 m below the blade, which is consistent with the findings in section 5.2.7 looking at the vertical variation of the gain.

The LDA phase data are shown in Fig. 5-20. The phase delay of the inflow response measured further away from the rotor is greater than that measured closer to the rotor. This reinforces the assumption of a wake velocity-dependent transmission-type delay. There is evidence of a recovery in the phase in the outer three radial positions, particularly for the measurements 0.1m below the rotor. The recovery is not as obvious or consistent as with the hot-wire data. A more detailed comparison between the hot-wire and laser data will be given in Fig. 5-21. The other feature clearly visible in the laser phase data of Fig. 5-20 is that the drop in phase decreases towards the outboard section of the rotor. Or in other words the air closer to the tip responds more quickly than that further inboard, and this is as seen before.

The upper two graphs of Fig. 5-21 compare the gain and phase information obtained from the LDA system with the data obtained from the hot wires at the same radial station but 0.05m further away from the rotor, with good correlation. The phase lag of the LDA data is, for all but the lowest three frequencies, slightly larger than that of the data from the hot-wires. This is contrary to what would be expected assuming a transmission delay as shown in section 5.2.7, since the LDA data were taken closer to the blade.

Initially synchronisation between the two independent systems running on their own internal clocks was achieved using a synchronisation pulse at the beginning of a data run. A detailed examination of the operating schedules for the LDA and rig systems showed that they ran at slightly different clock rates and the bottom graph of Fig. 5-21 shows the effect that timing differences have on the results obtained from the correlation procedure (LDA inflow phase data, 0.1m below 73% R). If the rig runs at a clock speed 1.0024 times (0.24% error) as fast as the LDA then the analysed phase drop is even larger than that for the datum case. If the rotor rig runs at a clock speed of 0.993 (0.7% error) times that of the LDA then the phase drop over the frequency range is less than that of the datum case. Considering the latter case it can be seen that even small timing changes (0.7%) can significantly effect the phase (90 deg at 10 Hz) obtained from the correlation procedure. Several measurements showed that the rotor rig ran on average some 0.4 % slower than the LDA.

For subsequent data obtained from the LDA an improved synchronisation method was used, where synchronisation pulses exchanged between the two systems are inserted within the LDA data continuously, and this was discussed further in Chapter 2. Timing inaccuracies presented no problem for the data obtained from the rotor rig as here the input frequencies and rate of taking data were always synchronised by the frame rate at which the system was running.

5.4 Dynamic Inflow Correlation with 2 DOF Coning/Inflow Models

It has already been shown in this chapter that some of the underlying assumptions made in Chapter 3 with respect to the conceptualised wake model in the Pitt and Peters inflow model are not valid. The dynamic inflow response is not constant or a function of the radial station alone, but its shape also depends strongly on the frequency of excitation. The phase and gain corrections made to the inflow data, determined using pitot-static tubes as quoted in Chapter 3 have been shown to be of only some validity, over the frequency range of interest. With the new and extensive hot-wire data, the previous results from the two-degree-of-freedom coning / inflow modelling are briefly re-examined [Ellenrieder 1994]. Only the best two models from Chapter 3 are used for this study and these are reiterated in 5.4.2.

5.4.1 Comparison between Hot-Wire and Pitot-Static Sensors

The measured inflow obtained from the hot wires can be compared to that obtained earlier (Chapter 3) using pitot-static tubes. This is shown in Fig. 5-22. The original data from pitot tubes was obtained at a distance of 0.165 m below the blade at a radial station of 58 % R., with the nearest corresponding hot-wire position being 57%R and 0.15m below the rotor.

The comparison between the data from the hot-wires and data obtained from the pressure transducers is not straight forward. The pitot tubes on the old rig were placed at different vertical and also slightly different radial stations than the later hot wires. This was due to the redesign of the rig between experiments and the need for different mounting structures. It was initially not appreciated that even small changes in measuring position significantly affected the measured inflow response.

As no consistent correction for the phase and gain information with vertical separation over the *whole* frequency range is practical, and the differences in vertical and radial position are small, Fig. 5-22 compares the uncorrected pitot and hot-wire data.

At low frequencies it can be seen that the pitot inflow gain is some 2.5 dB higher than that found from the hot-wires. This is due to the much higher induced velocities on the original rig which caused significant blockage because of the bulky gimbal. The phase at frequencies up to 5 Hz matches well. The significant difference between the hot-wire and pitot probes in terms of gain is in the 10 to 20 Hz area. Here the pitot tubes show a recovery in gain which is not shown in this area by the hot-wire data. This discrepancy can only be explained by some dynamic effect of the pitot-static tube, piping and transducer, which was not adequately corrected according to the theory in Chapter 3. The phase of the pitot data also falls off more rapidly than that of the hot-wire data.

The frequency content, using spectral analysis, of the inflow response obtained with the hot-wires and LDA will be examined and contrasted to that obtained in Chapter 3, Fig. 3-8. It was found that apart from the signal at excitation frequency there were also significant signals at

80, 160 and 20 Hz. Figure 5-23 shows the power spectrums obtained from the hot-wire and LDA data at a radial station of 57%. The laser data were taken some 10 cm and the hot wire data at 15 cm below the rotor. The power spectrums have been normalised as in Chapter 3, and outlined in Appendix C.

Both the hot wire and LDA data show components at 80 Hz which are due to the blade passage of the four-bladed rotor. The LDA data, which were taken closer to the blade, show a larger four-per-rev. component than the hot-wire data, which illustrates that the effect of blade passage is greater nearer the blade. The peaks from the hot-wire data, which were taken near the same vertical and radial position as the pitot-static data, are smaller. During initial measurements with the pitot-static velocity sensors it was observed that they were sensitive to pressure fluctuations and this might explain the larger four-per-rev. component at 80 Hz, with the pitot-static sensors picking up the pressure pulses of the passing blades.

The 160 Hz component which is thought to be due to the blade torsion mode is also shown in both the hot-wire and LDA data. An analysis of the natural frequencies of the rotating blade is given in Appendix H.

At around 25 Hz the excitation signal in the inflow is lost in the surrounding turbulence. At 30 Hz the inflow signal is again clearly visible. This is similar to the original results obtained with the pitot-static tubes.

5.4.2 Two DOF Coning / Inflow Theoretical Models

The derivation of two-degree-of-freedom coning / inflow models, is given in Chapter 3 and Appendix B. Only two models from Chapter 3 are considered here, both given in the standard state space form shown below.

$$\dot{x} = Ax + Bu,$$

$$A = \begin{bmatrix} \upsilon_{\upsilon} & 0 & \upsilon_{\dot{\beta}} \\ 0 & 0 & 1 \\ \beta_{\upsilon} & \beta_{\beta} & \beta_{\dot{\beta}} \end{bmatrix} \quad B = \begin{bmatrix} \upsilon_{\theta} \\ 0 \\ \beta_{\theta} \end{bmatrix}. \tag{5-5}$$

$$x = \begin{bmatrix} \upsilon & \beta & \dot{\beta} \end{bmatrix}'$$

$$u = \theta_0$$

Both models use the widely accepted Pitt & Peters [1983] inflow formulation. Classical blade element theory is used to relate the rotor thrust to blade pitch perturbations, local induced velocity and blade flapping. Model A is based on the formulation developed by Chen [Chen & Hindson 1987] and Houston [1989], but has been modified to include an offset hinge representation with spring restraint, root cut-out and tip loss factors. The structure of the resulting model in state space formulation is given below, which is identical to model 3 in Chapter 3, Equation 3-15:

$$\dot{x} = Ax + Bu$$

$$A = \begin{bmatrix} -\frac{4\Omega}{M_{11}}\left(\frac{C_{\bullet}}{k^2}\lambda_m + \frac{a\sigma}{16}(B^2 - C^2)\right) & 0 & -\frac{4\Omega R}{3M_{11}}\left(\frac{C_{\bullet}}{k}\lambda_m + \frac{a\sigma}{8}(B^3 - C^3)\right) \\ 0 & 0 & 1 \\ -\frac{\Omega\gamma}{2R}\left(\frac{1}{3} - \frac{\varepsilon}{2}\right)C^{\bullet} & -\Omega^2 f_R & -\Omega\gamma\left(\frac{1}{8} - \frac{\varepsilon}{3} + \frac{\varepsilon^2}{4}\right)C^{\bullet} \end{bmatrix} \quad B = \begin{bmatrix} \frac{4\Omega^2 Ra\sigma}{3M_{11}8}(B^3 - C^3) \\ 0 \\ \frac{\Omega^2\gamma}{8}\left(1 - \frac{4}{3}\varepsilon\right)C^{\bullet} \end{bmatrix}.$$

$$x = \begin{bmatrix} \upsilon; \beta, \dot{\beta} \end{bmatrix}' \quad u = \theta_0$$

(5-6)

Model B introduces tip loss factors in the flapping equation, but discards the lift deficiency factor in the flapping equation. The inclusion of lift deficiency and thrust deficiency factors in the formulation is discussed in Chapter 3. The fact that a lift deficiency factor did improve correlation with flight test data during previous experimental work using the PUMA [Houston 1989] is probably due to the fact that its overall effect is similar to that of the tip loss factor. The formulation for the offset hinge in the flapping equation of model B is based on Johnson [1980] and contains the hinge offset terms to a higher order than that of Chen [Chen & Hindson 1987]. Model B is given below and is identical to model 4b in Chapter 3, equation 3-17:

$$A=\begin{bmatrix} -\frac{4\Omega}{M_{11}}\left(\frac{C_*}{k^2}\lambda_m+\frac{a\sigma}{16}(B^2-C^2)\right) & 0 & -\frac{4\Omega R}{3M_{11}}\left(\frac{C_*}{k}\lambda_m+\frac{a\sigma}{8}(B^3-C^3)\right) \\ 0 & 0 & 1 \\ \Omega\frac{\gamma}{6R}\left(\frac{3}{1-\varepsilon}\left(\frac{B^3}{3}-\frac{\varepsilon B^2}{2}+\frac{\varepsilon^3}{6}\right)\right) & -\Omega^2 f_g & \frac{-\Omega\gamma}{8}\frac{4}{(1-\varepsilon)^2}\left(\frac{B^4}{4}-\frac{2\varepsilon B^3}{3}+\frac{\varepsilon^2 B^2}{2}-\frac{\varepsilon^4}{12}\right) \end{bmatrix} B=\begin{bmatrix} \frac{4\Omega^2 Ra\sigma}{3M_{11}8}(B^3-C^3) \\ 0 \\ \Omega^2\frac{\gamma}{8}\left(\frac{4}{1-\varepsilon}\left(\frac{B^4}{4}-\frac{\varepsilon B^3}{3}+\frac{\varepsilon^4}{12}\right)\right) \end{bmatrix}. \quad (5\text{-}7)$$

5.4.3 Comparison of Coning / Inflow Models with Experimental Data

In this section the experimentally determined coning and inflow frequency responses will be compared with the results obtained from the theoretical models. The rotor was modelled assuming an offset hinge at 21% of the blade span and a spring stiffness to provide the correct flap frequency ratio. The location of the equivalent offset hinge was determined from the mode shape of the deflected blade. The datum value of the apparent mass was taken to be 0.85 and the tip loss and lift deficiency values where chosen in accordance with the appropriate thrust and mean induced flow values.

A typical set of experimental data is shown in Fig. 5-24. These data have been averaged over three runs and the one-standard-deviation confidence interval is shown. Fig. 5-24 clearly shows that the data repeatability is excellent. The very slight deterioration in repeatability at low frequency is due to recirculation effects within the tunnel. At frequencies above 20 Hz the signal-to-noise ratio of the inflow data is poor and the data should therefore be treated with some caution. Despite the poor signal-to-noise ratio on the high frequency inflow data, the results have been found to be very repeatable. The data have been corrected for actuation lag, which at 30 Hz is approximately 20 degrees. Additionally, the inflow data which were taken some 15 cm below the rotor disc have been corrected for wake contraction and wake transport delay. The data set depicted in Fig. 5-24 is taken from a hot wire measurement station at 57% blade span.

Figure 5-25 compares the frequency responses obtained from models A and B with the experimental data. It can be seen that model B captures the low frequency coning gain very well, but the magnitude of the coning resonance peak is over-predicted by 5 dB. Model A

under-estimates the low frequency coning gain and similarly under-estimates the damping of the coning mode.

The low frequency inflow response is again best captured by model B. At higher frequencies the inflow gain falls off rapidly and this behaviour is not matched by either theoretical model. Consistent with the underprediction of low frequency coning gain, model A also underestimates the low frequency inflow gain. There is no difference in the inflow formulation contained in both models, and this highlights the strong coupling between the coning and inflow low frequency behaviour. A slight recovery in the high frequency inflow gain shown in Fig. 5-25, although in an area where the signal-to-noise ratio is poor, is consistently apparent in the experimental data but not reproduced by either of the mathematical models. The inflow phase is very well captured by both models.

5.4.4 Effect of Changes in the Apparent Mass Term

The value of the apparent mass factor has been studied previously. The theoretical value initially suggested by Pitt and Peters [Pitt & Peters 1983], for a corrected pressure distribution, is 0.54 and may be contrasted with the value of 0.85 proposed by Carpenter and Fridovich [Carpenter & Fridovich 1953]. Previous studies of the PUMA hover dynamics [Houston 1989, Houston & Tartellin 1989] have suggested that an apparent mass term of 0.85 gives better results.

The effect of variation of the apparent mass term is shown in Fig. 5-26. As would be expected the primary effect of the apparent mass term is on the inflow response and not on the coning response. The lowest value of M11 studied causes the coning resonance peak to increase by approximately 1.5 dB. Variation in apparent mass causes no appreciable change in the coning phase.

The primary effect of the apparent mass factor is to change the bandwidth of the inflow response, and values of M11=0.54 cause a slight resonance peak to appear in the theoretical results at just over 20 Hz. This increases as M11 is decreased. As the apparent mass factor is

increased to 0.85, which is the value originally suggested by Carpenter and Fridovich, the inflow gain and phase start to roll off more rapidly, providing better agreement with the experimental data. From this it can be concluded that a larger proportion of the surrounding air is being influenced by the pitch perturbations than that suggested using a corrected pressure distribution. Using an apparent mass term of M11=0.85 the theoretical model remains deficient in characterising the coning damping and fails to capture the steep reduction in inflow gain at 10Hz. The latter of these two apparent deficiencies of the theoretical model is probably more serious because of the implications for 'tight' heave axis hover control, as a rapidly falling inflow response indicates higher rotor thrust transients.

5.4.5 Model Response with Increased Coning Damping

As suggested in Chapter 3 the effect of increasing the coning damping derivative is examined, the derivative being

$$\beta_{\dot{\beta}} = \frac{-\Omega\gamma}{8}\frac{4}{(1-\varepsilon)^2}\left(\frac{B^4}{4}-\frac{2\varepsilon B^3}{3}+\frac{\varepsilon^2 B^2}{2}-\frac{\varepsilon^4}{12}\right). \qquad (5\text{-}8;\ 2\text{-}20)$$

For the physical justification of dropping the tip loss B from this derivative the reader is referred to Chapter 3, and the modified derivative is given below:

$$\beta_{\dot{\beta}} = \frac{-\Omega\gamma}{8}\frac{4}{(1-\varepsilon)^2}\left(\frac{1}{4}-\frac{2\varepsilon}{3}+\frac{\varepsilon^2}{2}-\frac{\varepsilon^4}{12}\right). \qquad (5\text{-}9;\ 3\text{-}26)$$

Clearly, the effect of this modification to the flapping equation is to increase the coning rate derivative by approximately 25%, and the result is depicted in the graphs on the left hand side of Fig. 5-27. Only the coning gain and inflow gain responses are shown as the effect on the phase was found to be minimal. It can be seen that the resonance coning peak has been reduced by approximately 2 dB for all cases of apparent mass considered. Significantly however, although the effect on the coning response is relatively small, the increased coning damping has increased the rate at which the inflow gain rolls off. Once again, a value of 0.85 for the apparent mass provides the best agreement between the theoretical and experimental data.

The effect of further increasing the coning damping derivative to match the damping of the coning mode to the experimental data is shown in the graphs on the right of Fig. 5-27. Here, the coning rate derivative has been increased by 3.5dB. The inflow response now shows a sharp dip in gain at the coning resonance frequency, and interestingly, also shows a slight recovery in the response at high frequency. The frequency response obtained using an apparent mass value of 0.85 gives a good overall fit to the experimental data, with the inflow gain reducing from 3 Hz onwards and this model may be used to examine the coning and inflow behaviour with reasonably good fidelity up to rotor shaft frequencies.

5.4.6 Conclusions

The coupled coning/inflow theoretical models tested underestimate the damping of the coning mode. The magnitude of the coning damping significantly affects the character of inflow response and artificially increasing the coning damping reproduces the rapid decrease in the inflow response seen in the experimental data. Subsequently there is a slight recovery at the coning resonance frequency again, as seen in the experimental data. A modification to the blade flapping equation has been suggested and this partially rectifies the deficiency in coning damping.

The rapid decay in inflow response at high frequency is responsible for the characteristic increase in rotor thrust which accompanies high rates of application of collective and this feature is therefore especially important in control system design studies where "tight" heave axis control is sought.

The coning/ inflow model B when adjusted to strengthen the flapping rate derivative provides a good approximation to the experimental coning and inflow frequency responses over a frequency range extending to rotor shaft speed.

The best model-fit to the experimental data is obtained when an inflow apparent mass factor of 0.85 is used and this is in agreement with previous studies of the PUMA hover dynamics conducted by Houston [Houston 1989, Houston & Tartellin 1989].

5.5 Summary

In this investigation, it was found that the radial inflow distribution varies with radial station and also with collective excitation frequency. At high frequencies it is the outer portion of the blade which produces the largest contribution to the induced flow.

The inflow phase lag, at a given frequency, increases from the outer blade towards the rotor hub. An interesting recovery in the inflow phase frequency response, of the outer sections at frequencies of approximately 23 Hz can also be observed. The repeatability of the data obtained from hot-wire anemometry is good for all but the outermost and innermost regions and this is due to tip effects and small induced velocities respectively. A Laser Doppler Anemometry system was used to complement the data obtained from the hot-wire and although the LDA system presents significant operational difficulties it gave added confidence in the results from the hot-wires.

Further data obtained at rotor speeds higher and lower than the datum case of 1200 rpm showed similar trends. It was possible to examine the gain and phase variation at one radial station with rotor speed, and for frequencies below 20 Hz the results are reconcilable with the dynamic inflow theory by Pitt and Peters [Pitt & Peters 1983].

Examination of the vertical variation showed that the assumption of a transmission type delay to model the difference between the inflow phase measured beneath the rotor and that at the rotor disc is good approximation for frequencies up to 17 Hz. At higher frequencies the required correction and variation with vertical displacement is not clear. The variation of the gain with vertical distance was also investigated, but no consistent correction can be proposed. The assumptions, that the variation of the gain with vertical separation is proportional to the change in average induced velocities due to wake contraction, was found to be unsupported. The fact that a transmission delay does not fully explain the vertical phase variation of the inflow response points to the wake not moving as a uniform mass, from one point to the next, and suggests that it is influenced mainly by the shed vorticity distribution in the wake.

The mechanisms for the radial variation of the induced flow are not easily identified, but several possibilities exist. These include Reynolds number effects, reduced frequency effects of the aerodynamic response of the blade and shed and trailing vortex effects. Particularly the strong inflow response in the outer blade region and the drop of phase from the outer region of the blade inboard suggest that the trailing vortices from the blade tip significantly affect the inflow response over the outer blade region. The gain of the overall inflow frequency response decays rapidly at frequencies above shaft speed. This could be a factor in explaining why the dynamic inflow data by Su et all [Su, Yoo & Peters 1992], which used a collective excitation frequency of four times shaft speed, showed little dynamic inflow effect.

The measured induced flow was also compared to that obtained on the earlier rig, using pitot-static tubes, before it was moved to a wind tunnel and before the gimbals were reduced in size to lessen the effects of aerodynamic interference. Some of the discrepancies between the results could be attributed to dynamic effects of the pressure transducers, which introduced additional dynamic effects which were not adequately corrected. Rig geometry may also have played an important part in early pitot system results.

The extensive hot-wire data are used to re-examine the results from the coning / inflow model developed in Chapter 3, with similar conclusions. The final proposed model showed good agreement with the experimental data when using an apparent mass factor of 0.84. Increasing the coning damping improved the correlation significantly.

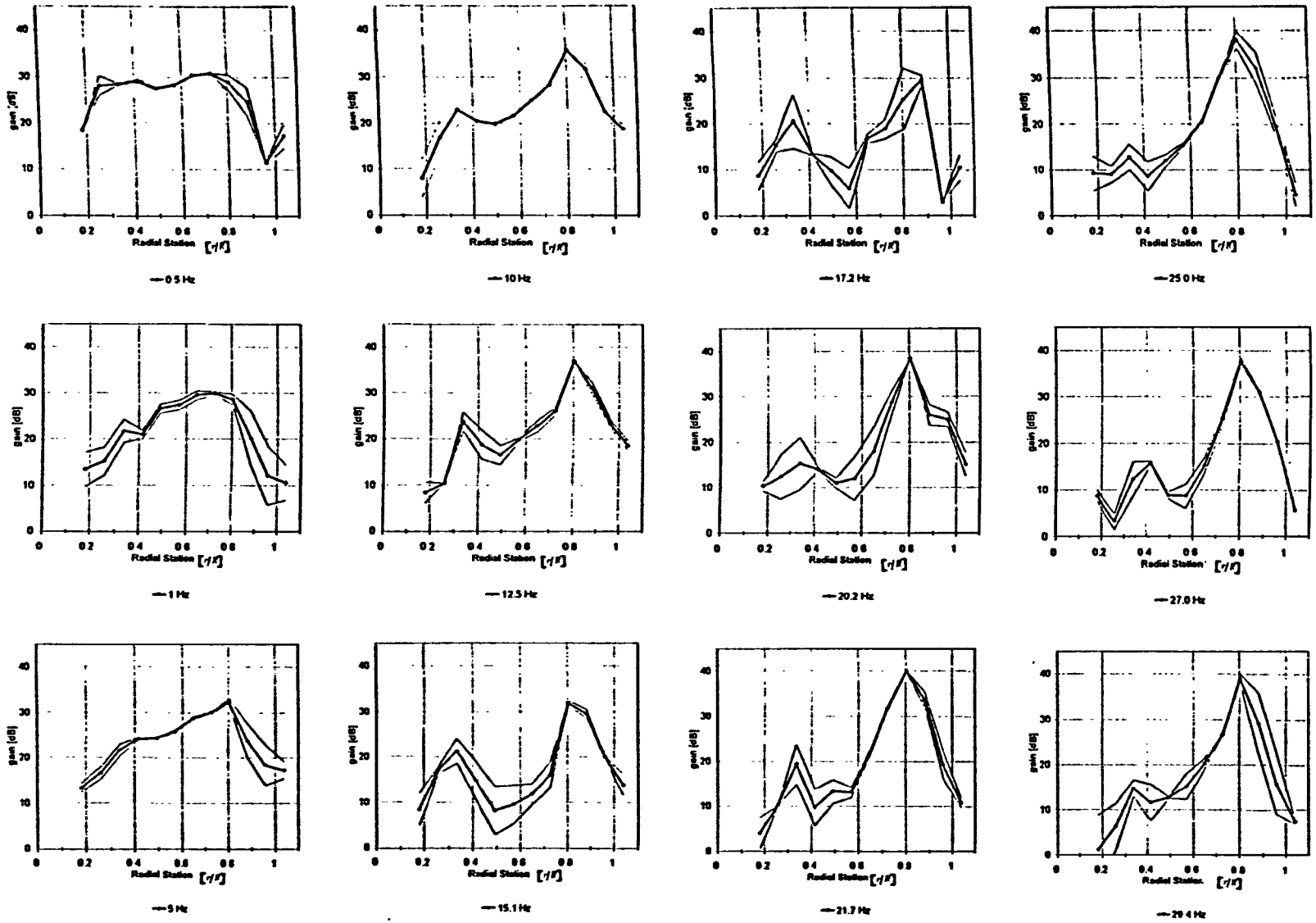

Fig. 5-1 Variation of Induced Flow Gain Response with Radial Station over a range of Frequencies at 1000 rpm
(Hot Wire, 0.15m below rotor, Collective Excitation)

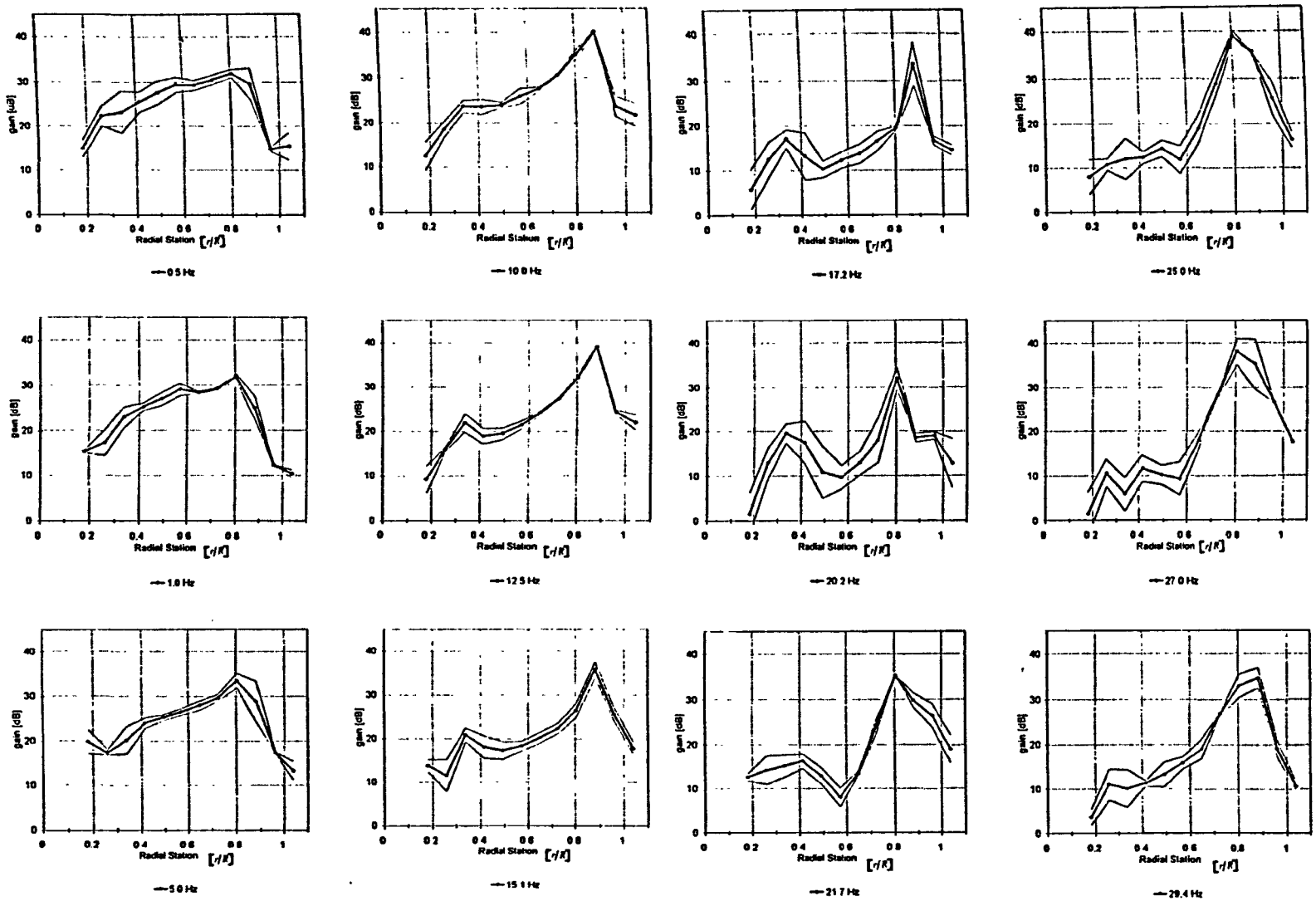

Fig. 5-2 Variation of Induced Flow Gain Response with Radial Station over a range of Freqencies at 1200 rpm
(Hot Wire 0.15m below rotor, Collective Excitation)

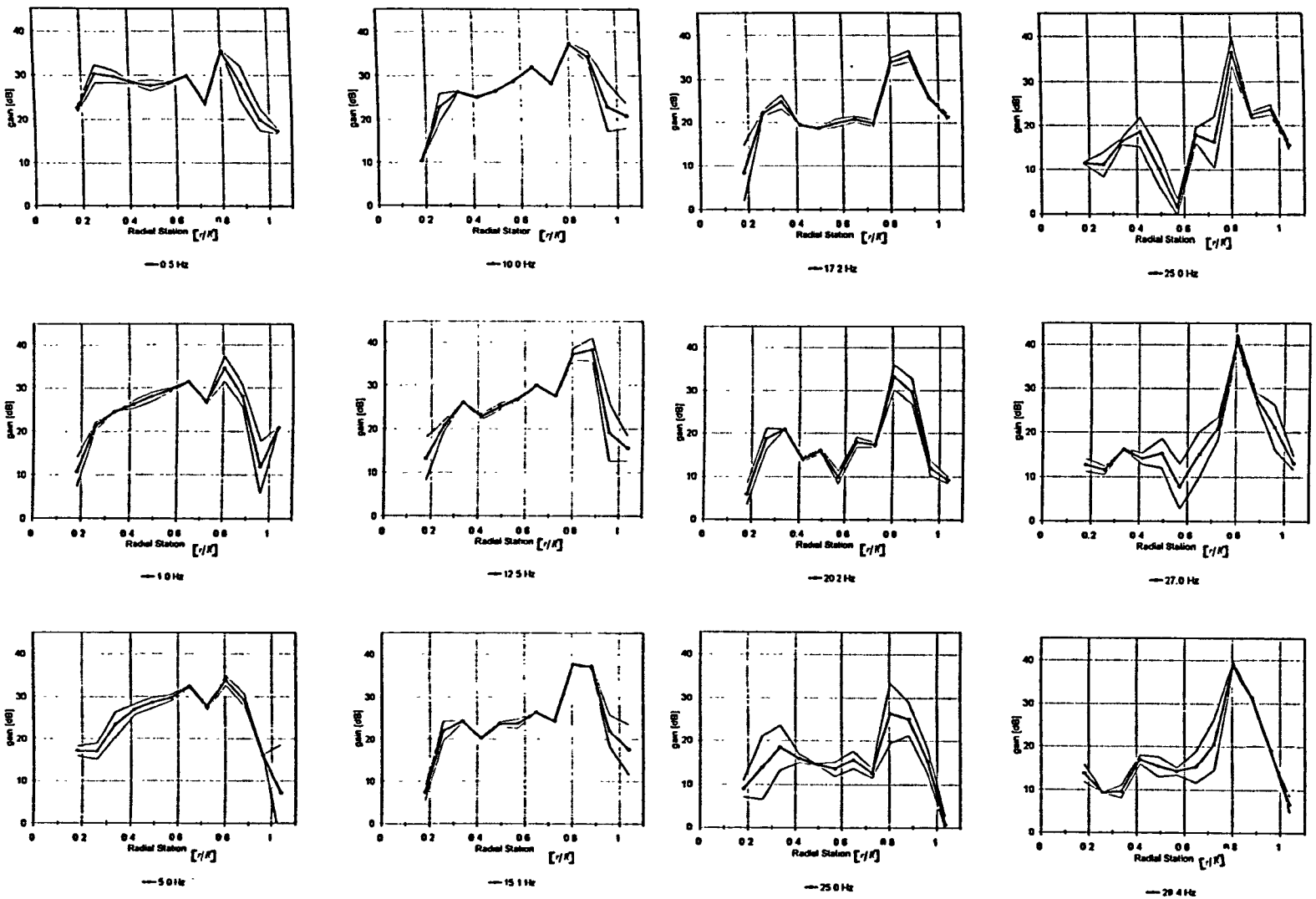

Fig. 5-3 Variation of Induced Flow Gain Response with Radial Station over a range of Frequencies at 1500 rpm
(Hot Wire 0.15m below, rotor, Collective Excitation)

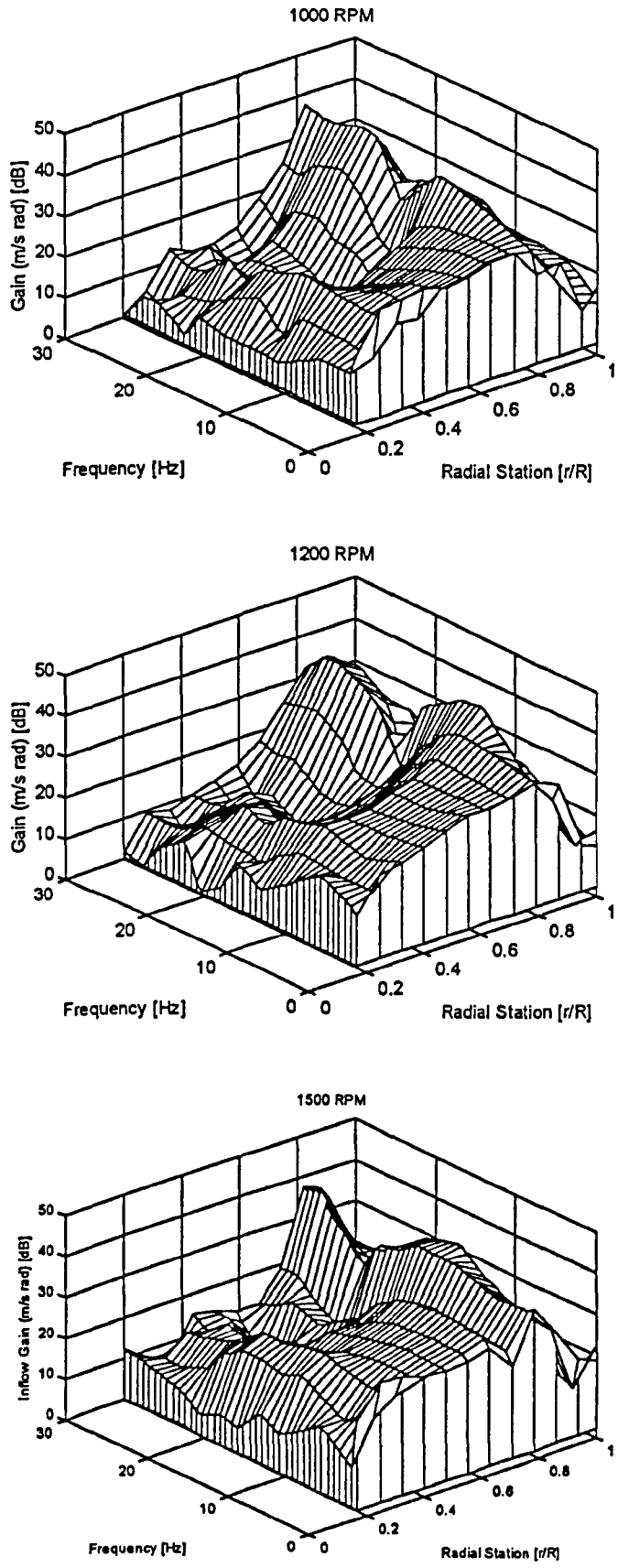

Fig. 5-4 Induced Flow Variation with Frequency and Radial Station at three Rotor Speed Settings

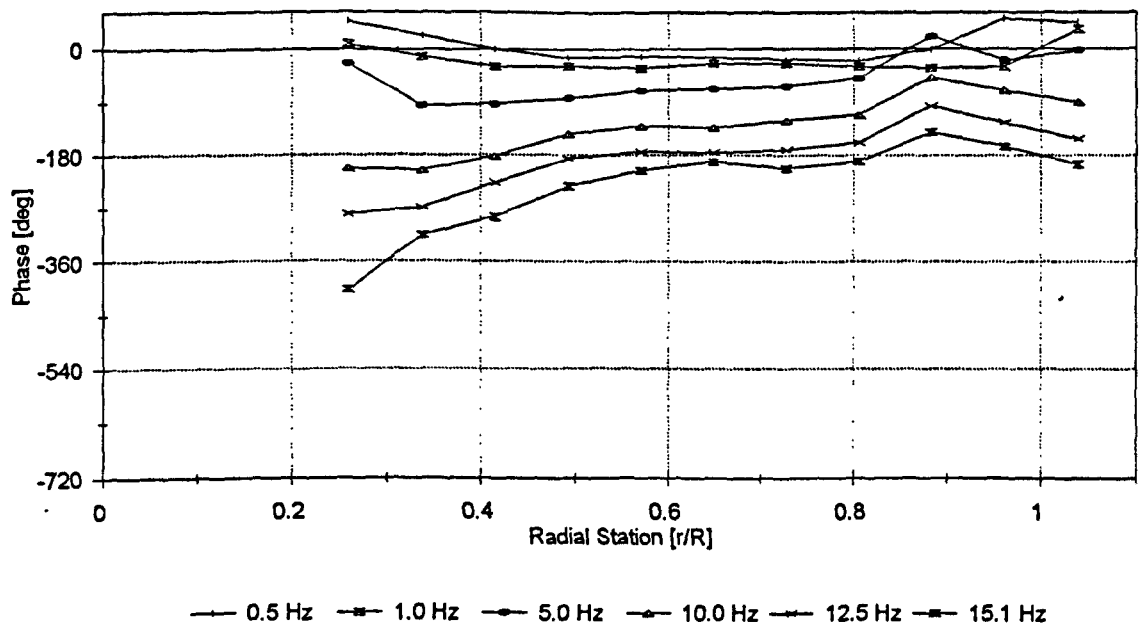

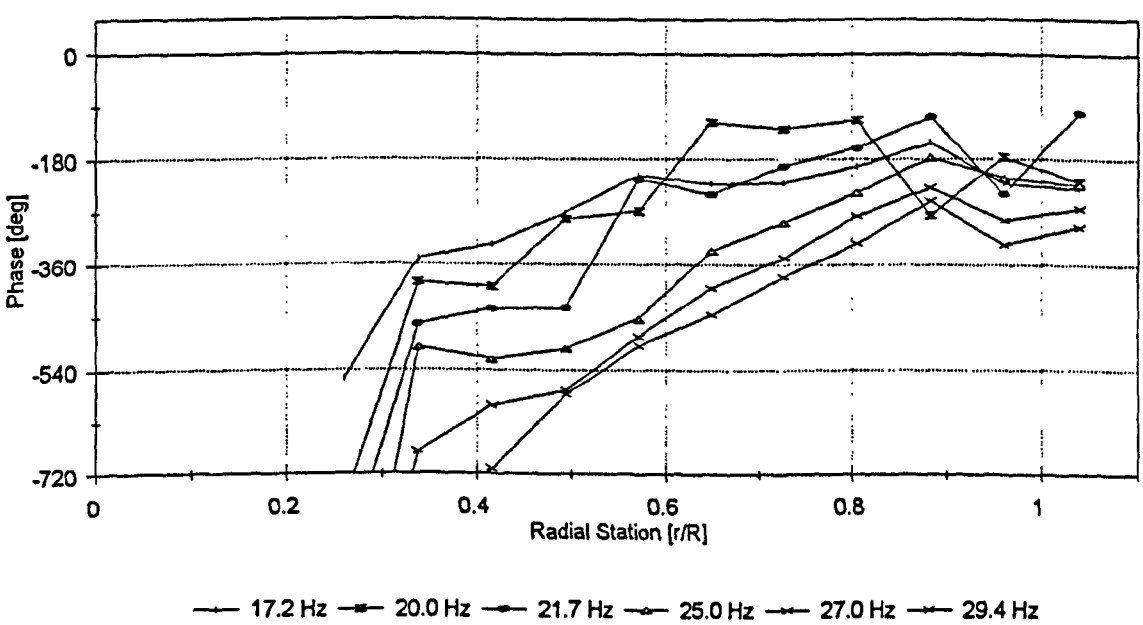

Fig. 5-5 Induced Flow Phase Response with Radial Station
(1200 rpm, Hot Wire 0.15m below, Collective Excitation)

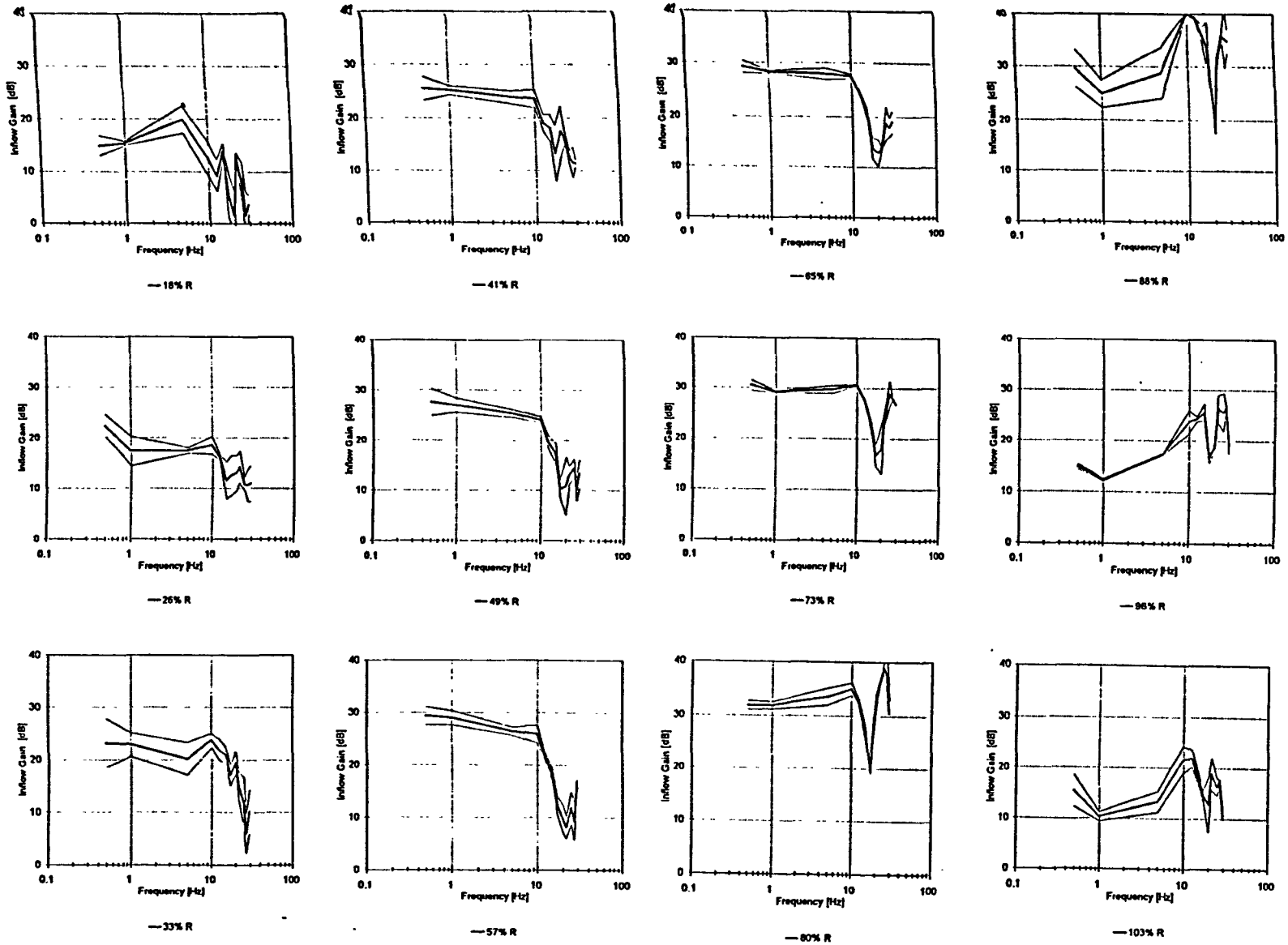

Fig. 5-6 Induced Flow Gain Response at selected Radial Stations at 1200 rpm
(Hot Wire, 0.15m below Rotor, Collective Excitation)

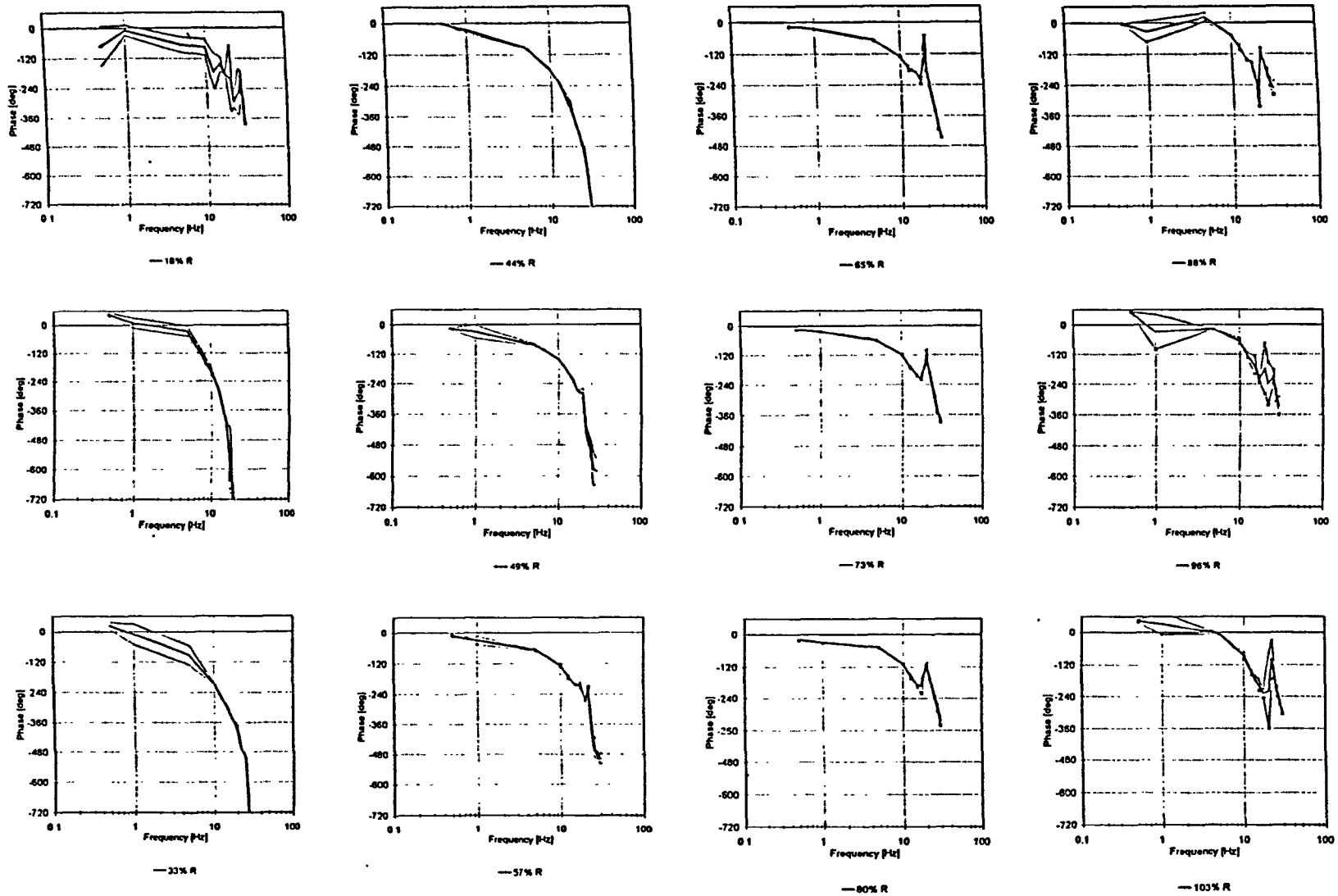

Fig. 5-7 Induced Flow Phase Response at selected Radial Stations at 1200 rpm
(Hot Wire, 0.15m below Rotor, Collective Excitation)

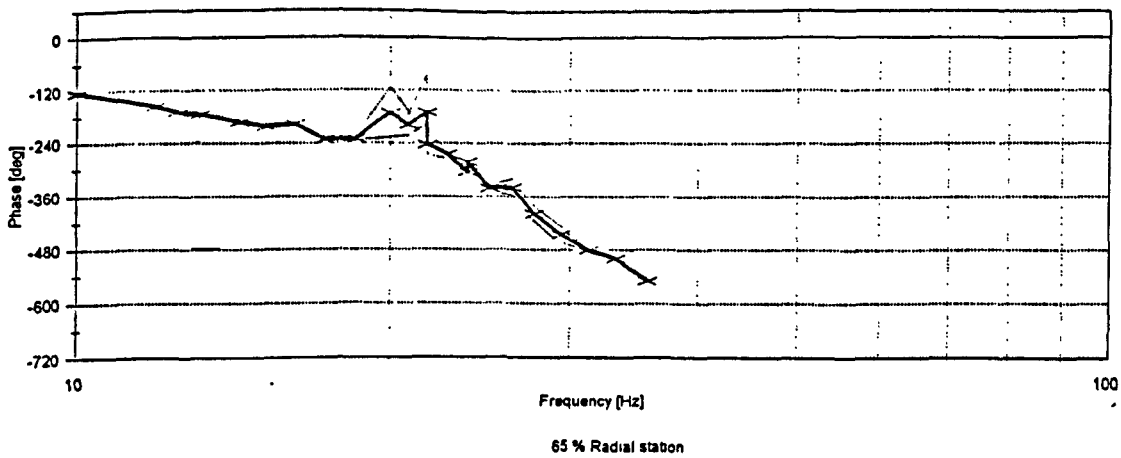

(Expanded Frequency Axis - 24 Data Points, 10Hz to 36Hz)

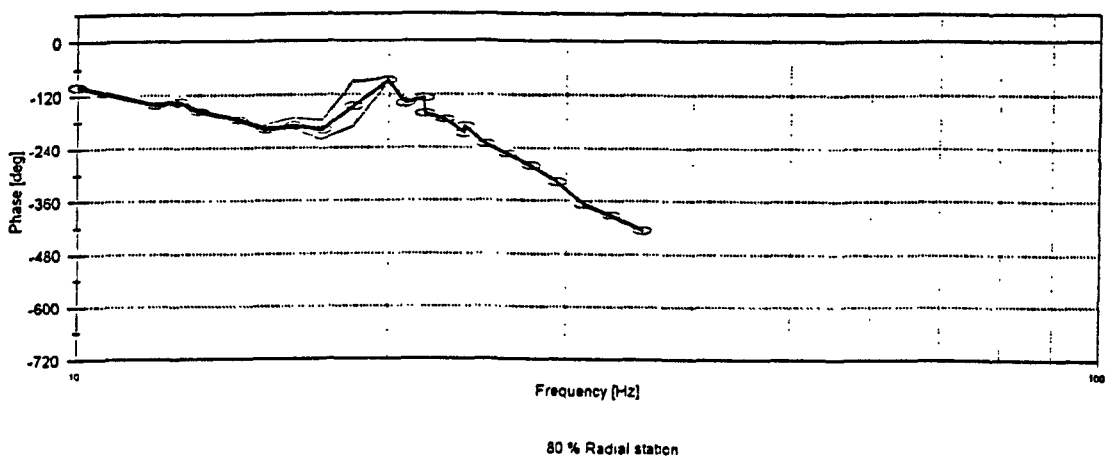

(Expanded Frequency Axis - 24 Data Points, 10Hz to 36Hz)

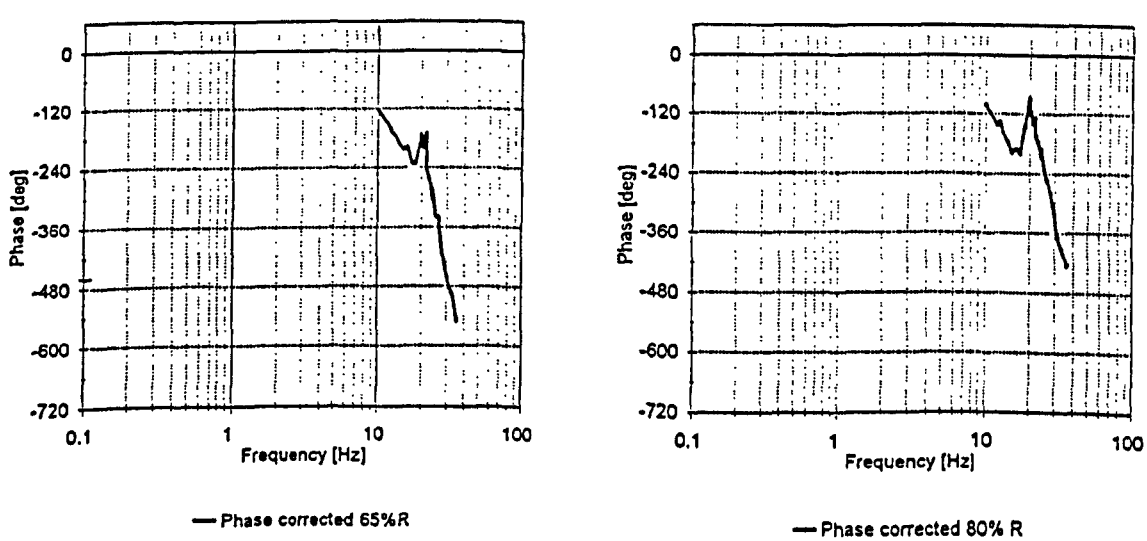

Fig. 5-8 High Resolution Inflow Phase Response Measured at Radial Stations of 65% and 80% Blade Radius
(1200 rpm, Hot Wire 0.15m below, Collective Excitation))

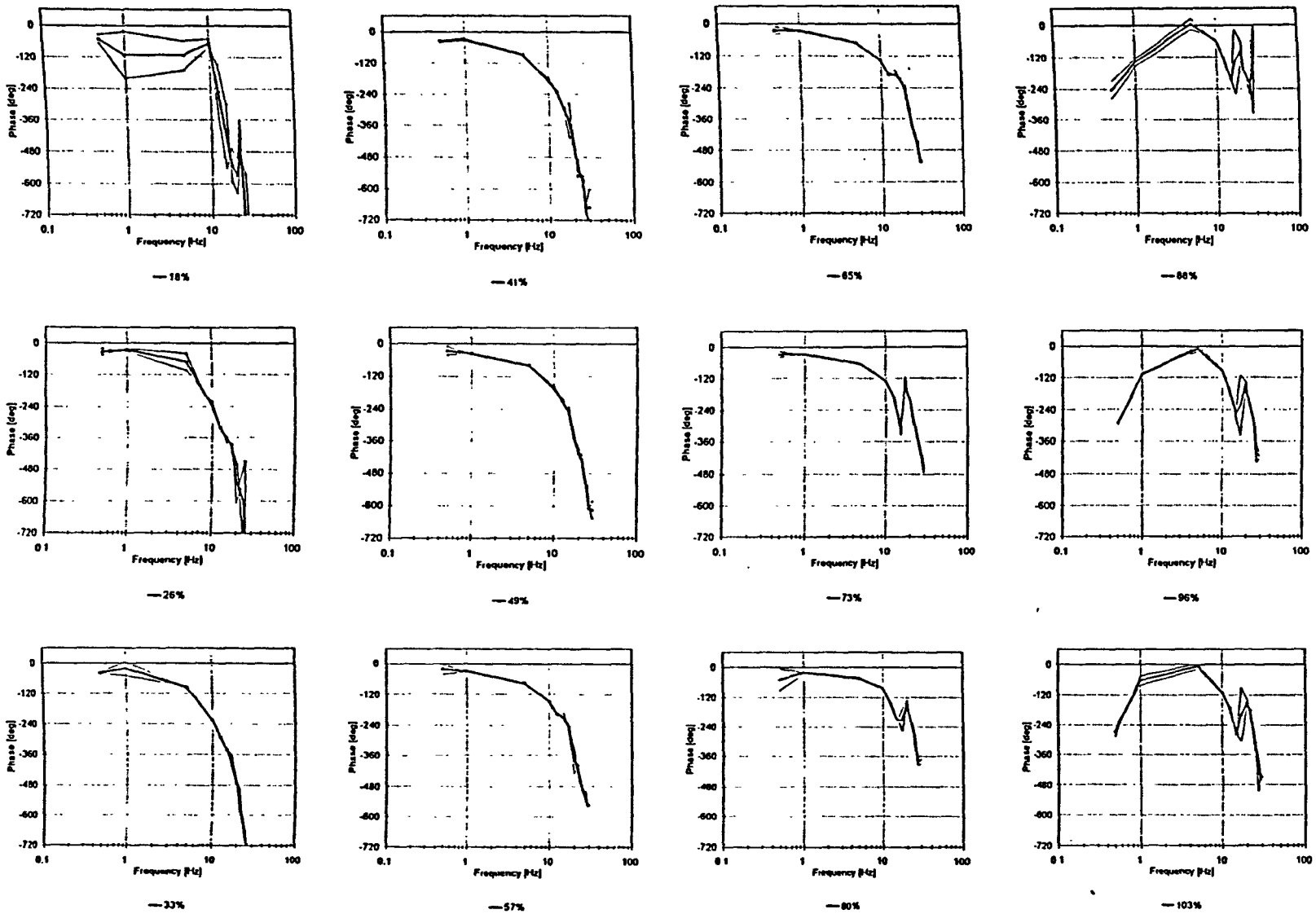

Fig. 5-9 Induced Flow Phase Response at selected Radial Stations at 1000 rpm
(Hot Wire, 0.15m below Rotor, Collective Excitation)

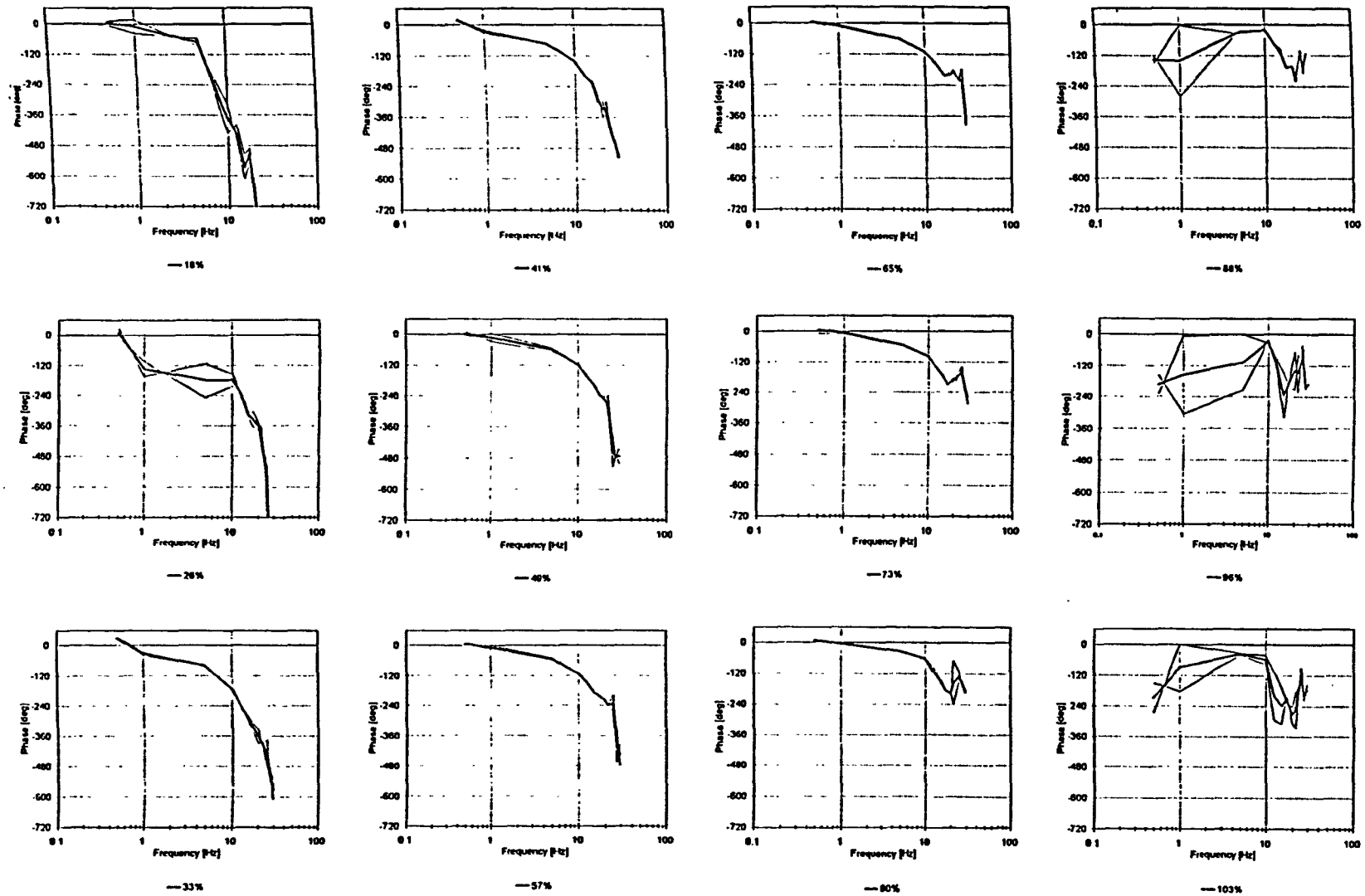

Fig. 5-10 Induced Flow Phase Response at selected Rdial Stations at 1500 rpm
(Hot Wire, 0.15m below Rotor, Collective Excitation)

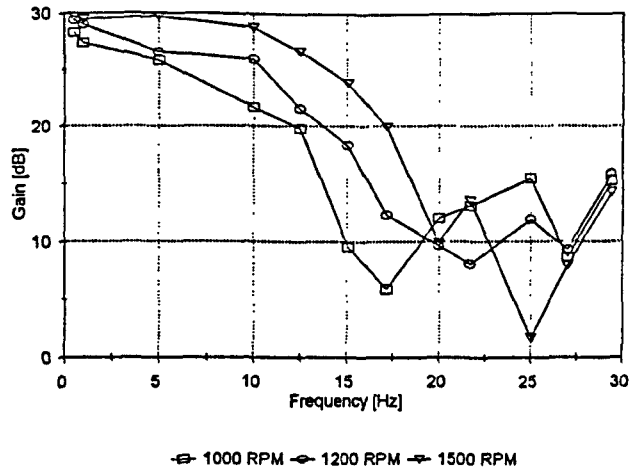

Frequency Response (1000, 1200, 1500 RPM)

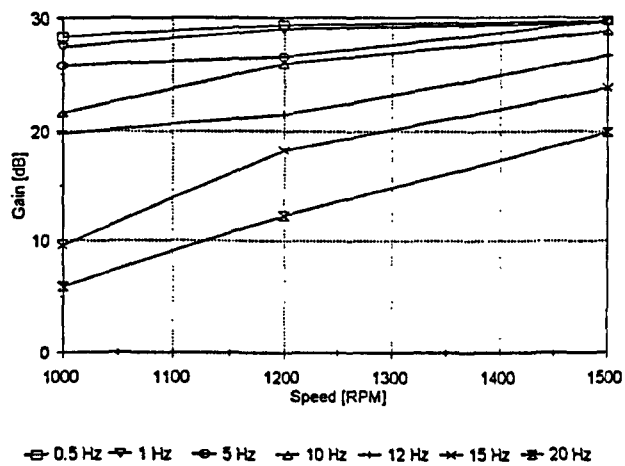

Variation with Rotor Speed (0.5-17Hz)

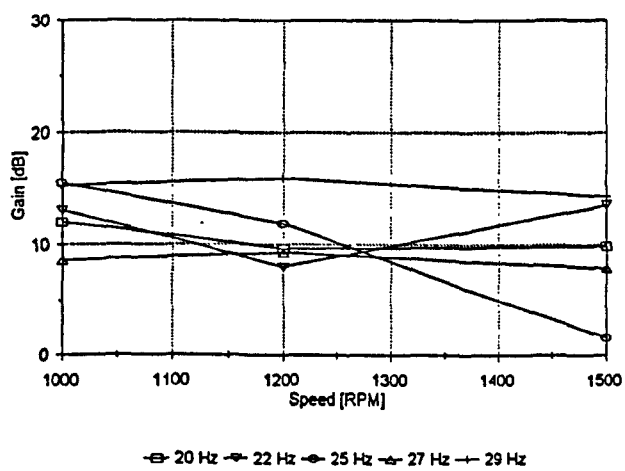

Variation with Rotor Speed (20-30Hz)

Fig. 5-11 Induced Gain Response Variation with Rotor Speed
(Hot Wire, 0.16m below Rotor, 57% R, Collective Excitation)

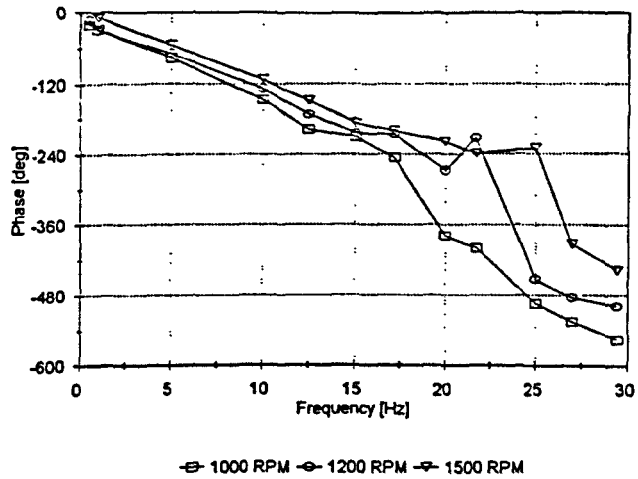

Frequency Response (1000, 1200, 1500 RPM)

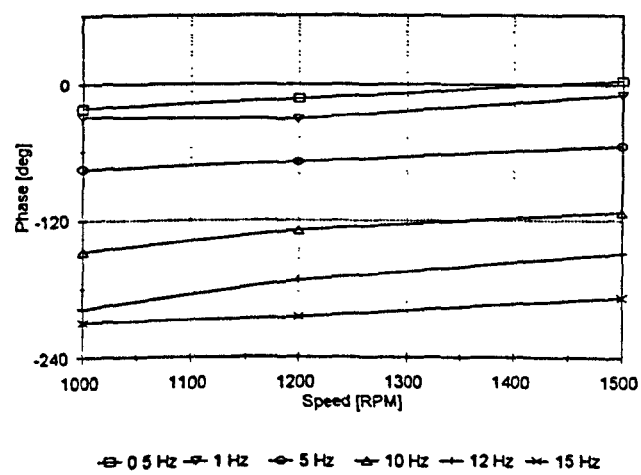

Variation with Rotor Speed (0.5-15Hz)

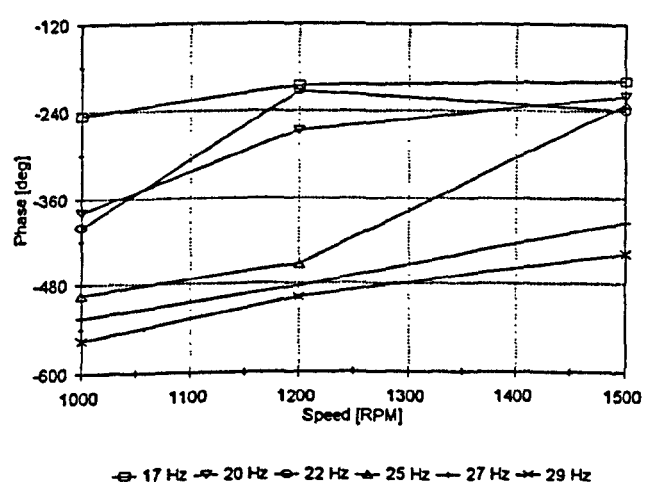

Fig. 5-12 Induced Phase Response Variation with Rotor Speed
(Hot Wire, 0.15m below Rotor, 57% R, Clooective Excitation)

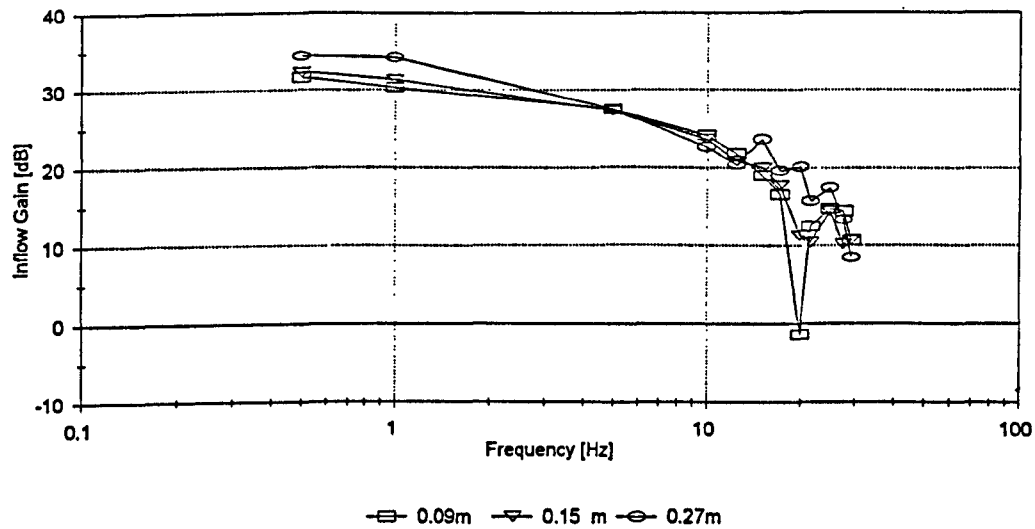

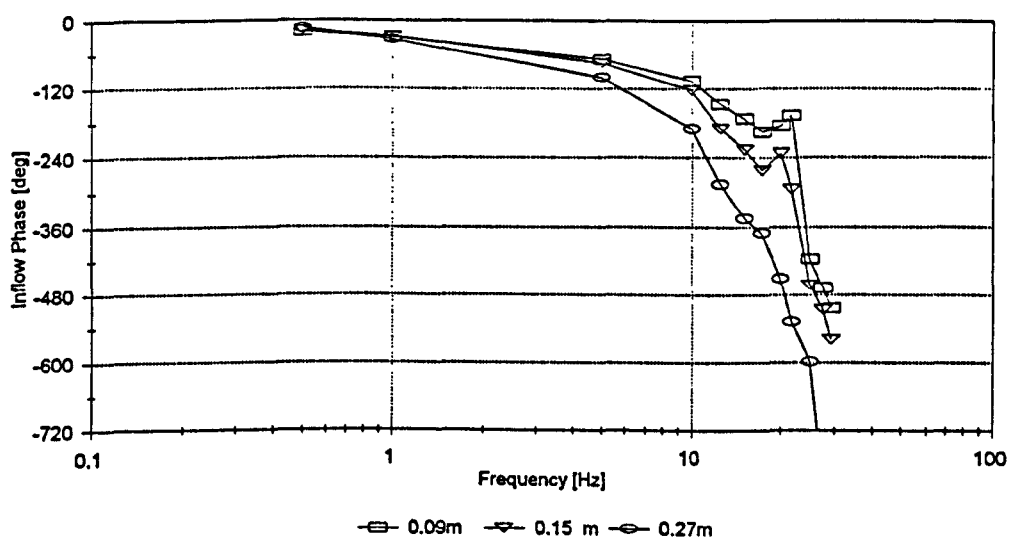

Fig. 5-13 INflow Gain and phase Response at three Vertical Stations
(1200 rpm, Hot Wire at 57% R, Collective Excitation)

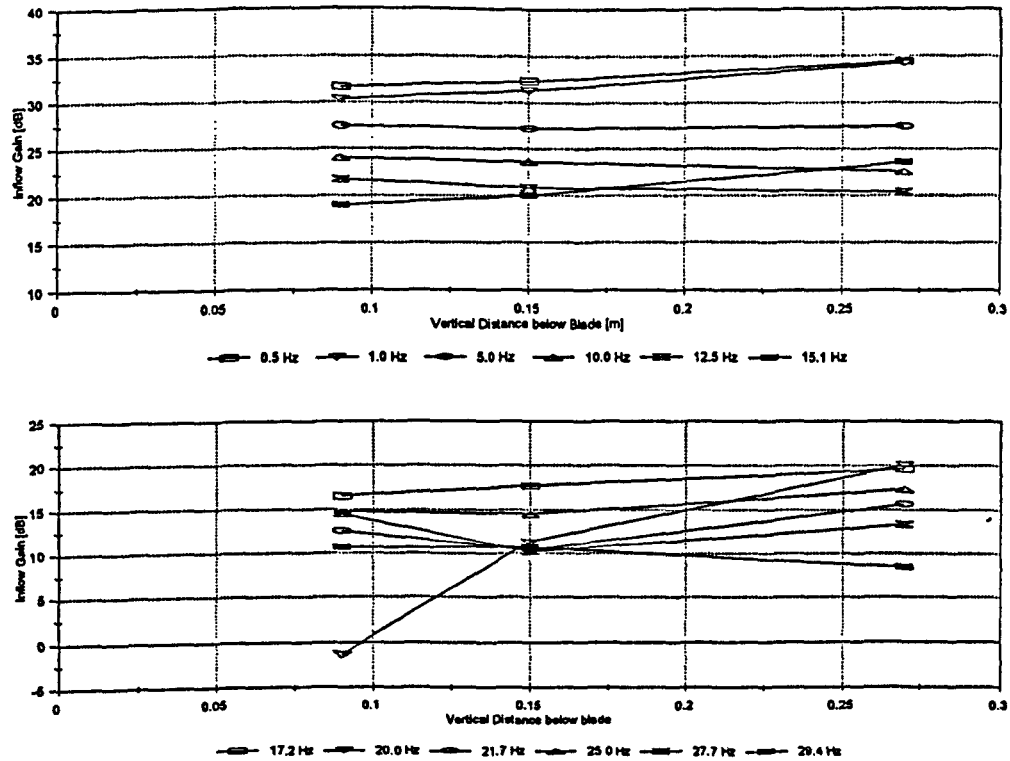

Inflow Gain

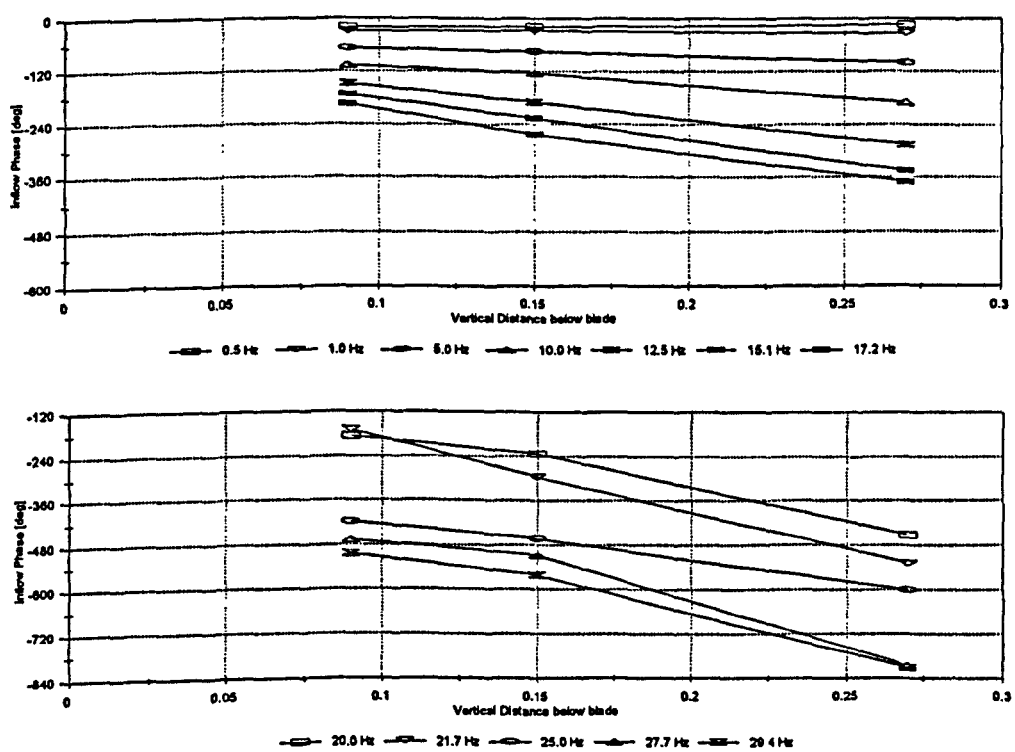

Inflow Phase

Fig. 5-14 Inflow Gain and Phase Characterstics with Vertical Separation
(1200 rpm, Hot Wire at 57% R, Collective Excitation)

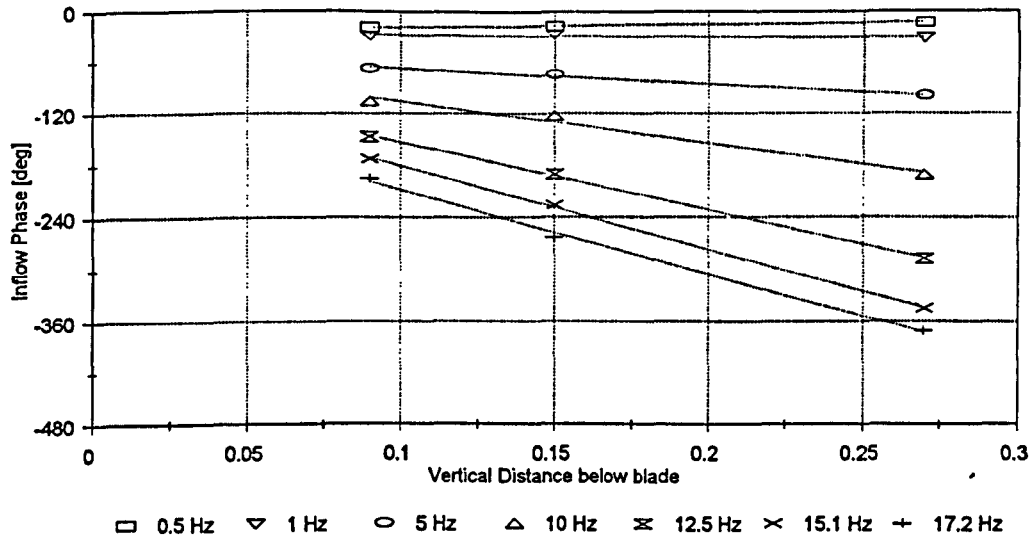

Least Squares Error Fit (LSEF) to Phase Variation

Freq. [Hz]		Gradient [deg/m		Offset [deg]
0.5		30		-21
1		-25		-25
5		-187		-49
10		-483		-58
12.5		-779		-75
15.1		-959		-85
17.2		-966		-112

Table of LSEF Parameters

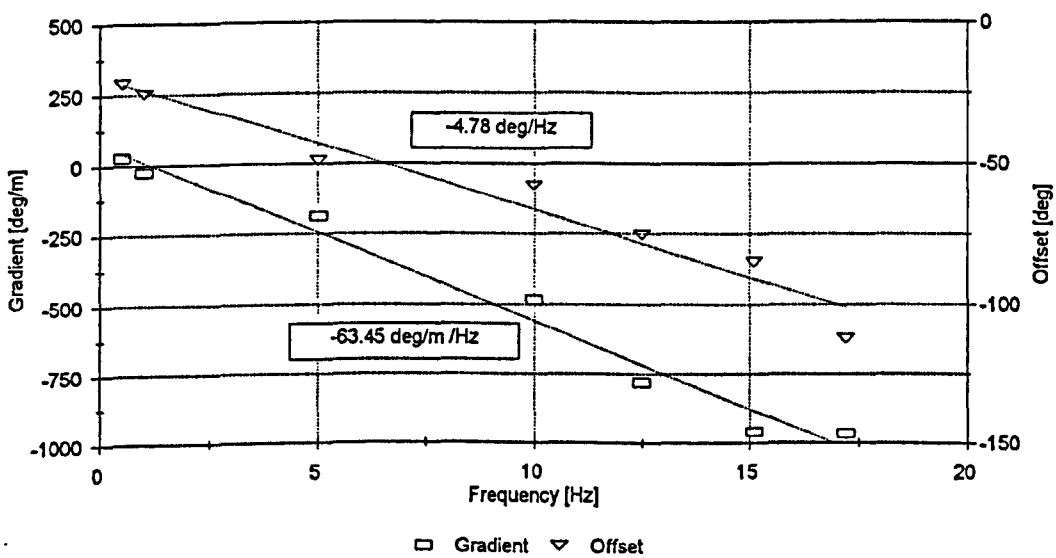

Variation of LSEF Parameters with Frequency

Fig. 5-15 Evidence for a Transmission Type Delay for the Axial Phase Variation
(1200 rpm, 0.16m below, 58% R)

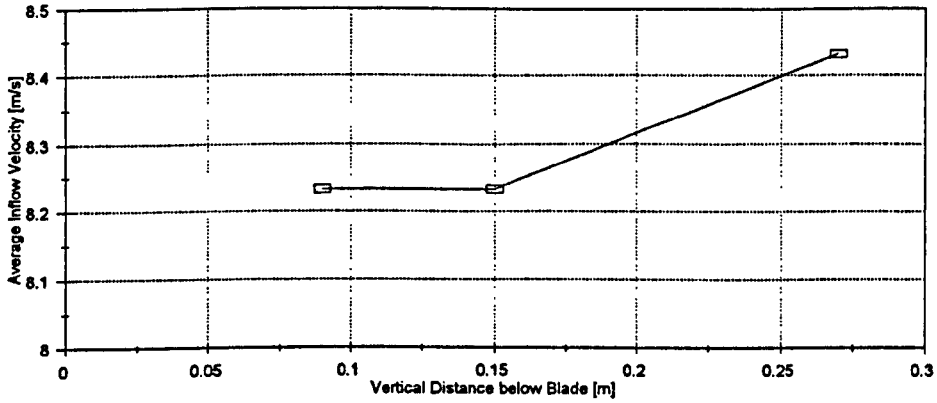

Fig. 5-16 Average Induced Velocities: Axial Variation

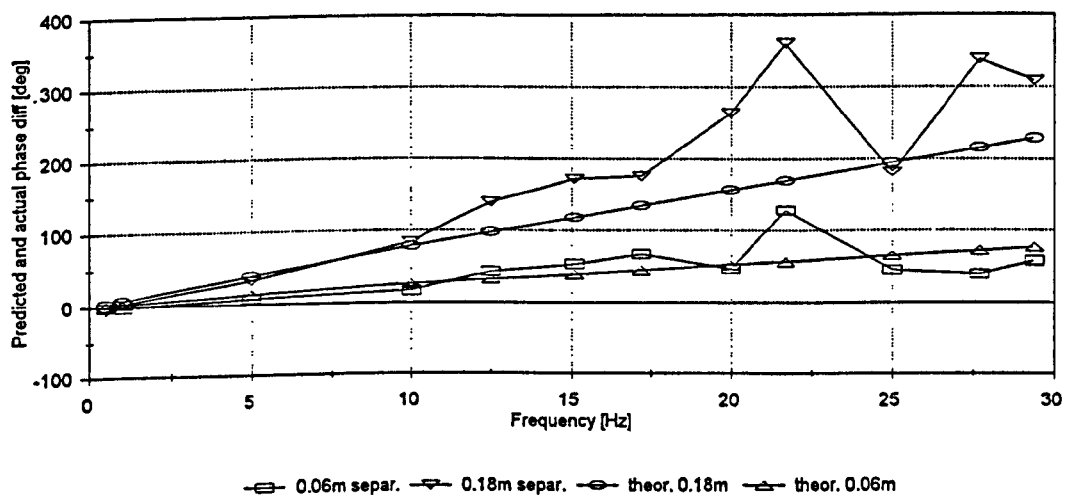

Fig. 5-17 Comparison of Theoretical and Experimental Axial Phase Change

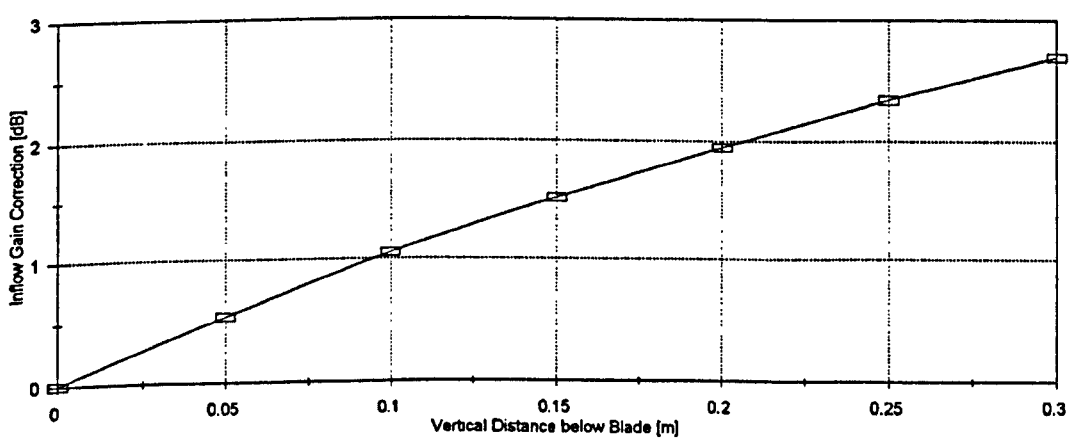

Fig. 5-18 Theoretical Inflow Gain Correction due to Wake Contraction

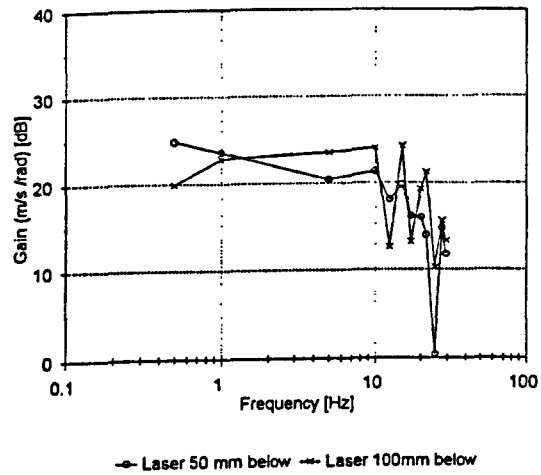

33% R

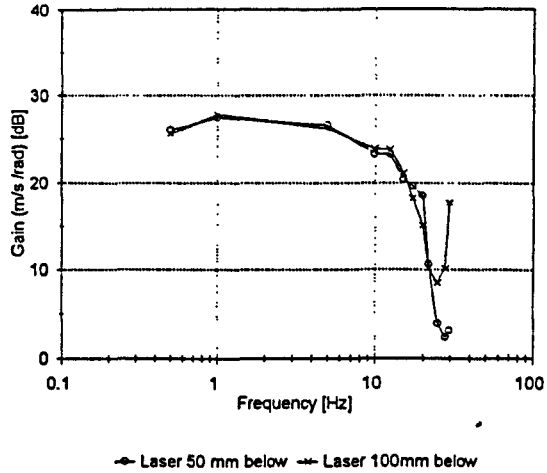

57% R

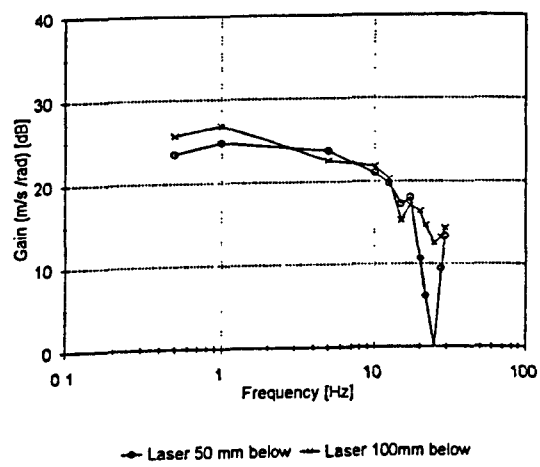

41% R

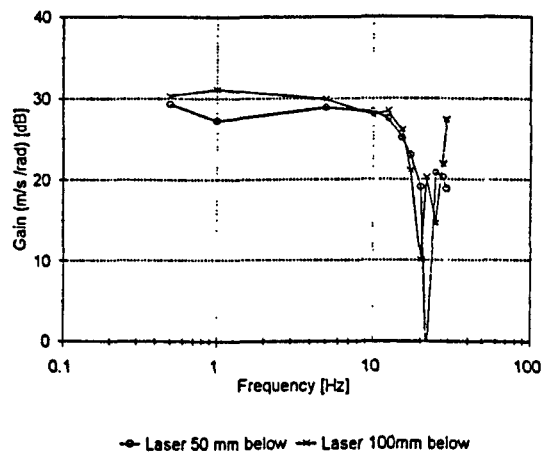

65% R

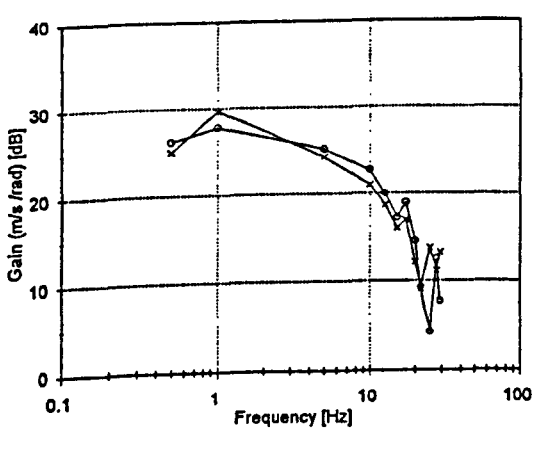

49% R

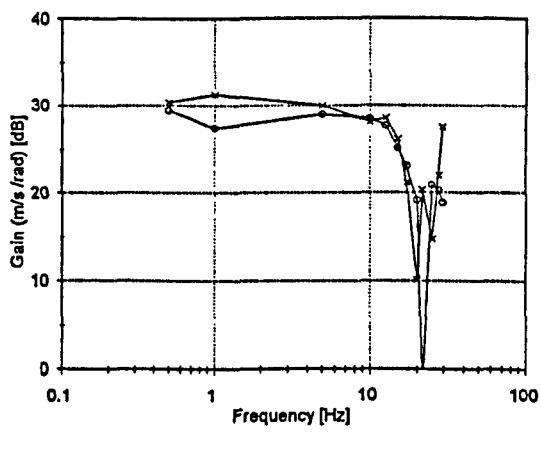

73% R

Fig. 5-19 Induced Flow Gain Response obtained from the LDA
(1200 rpm, LDA 0.05m & 0.1m below Rotor, Collective Excitation)

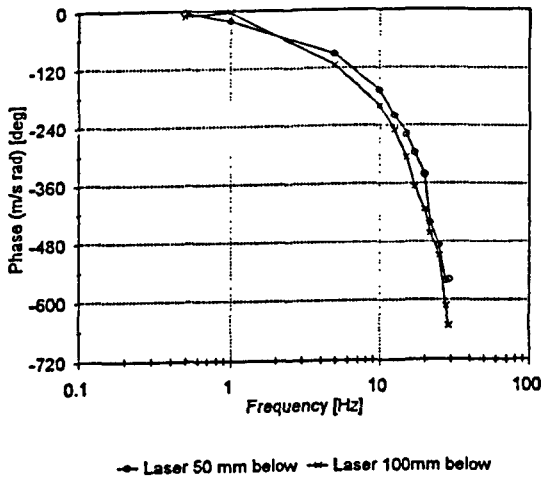

33% R

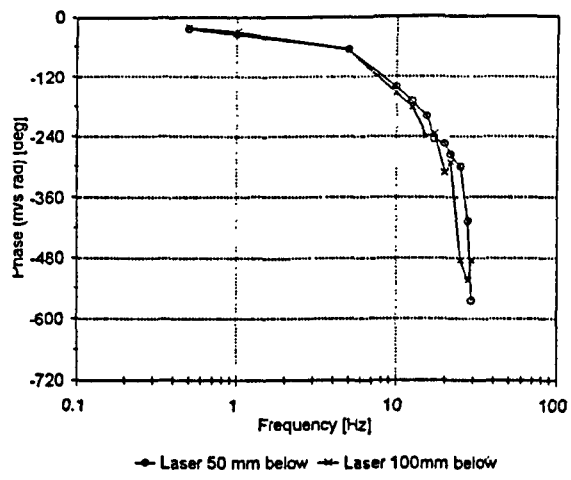

57% R

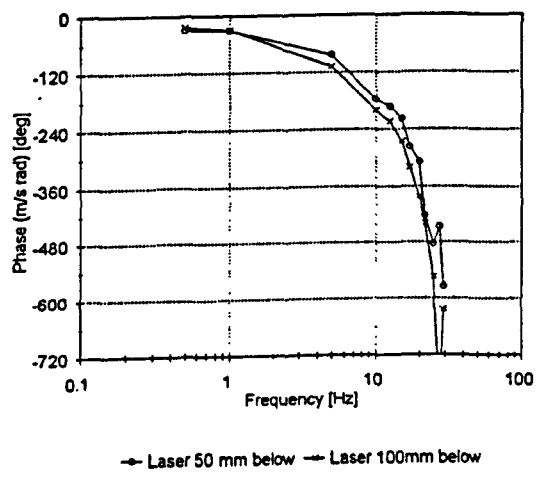

41% R

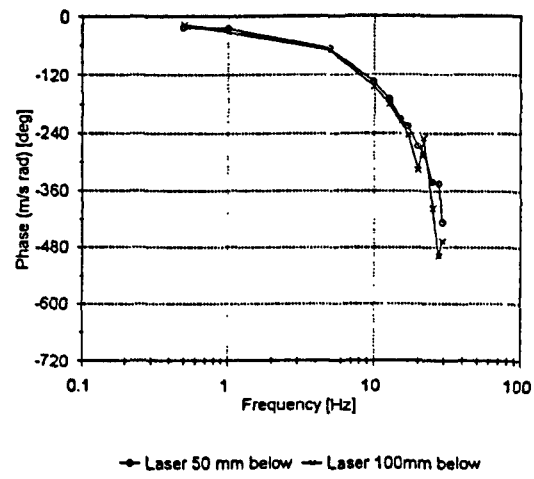

65% R

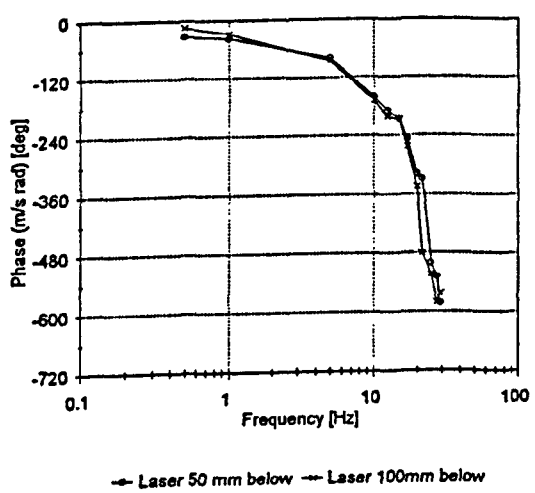

49% R

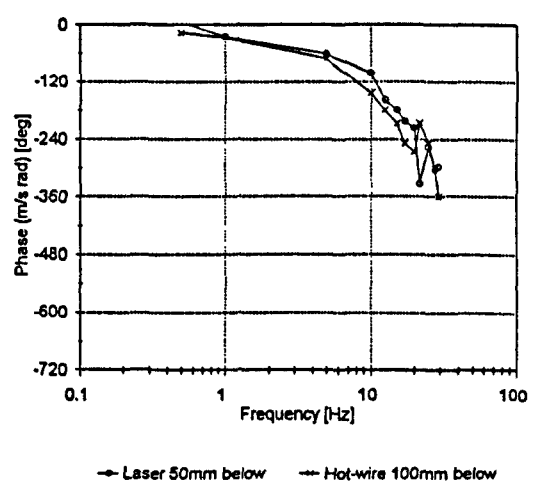

73% R

Fig. 5-20 Induced Flow Phase Response obtained from the LDA
(1200 rpm, LDA 0.05m & 0.1m below Rotor, Collective Excitation)

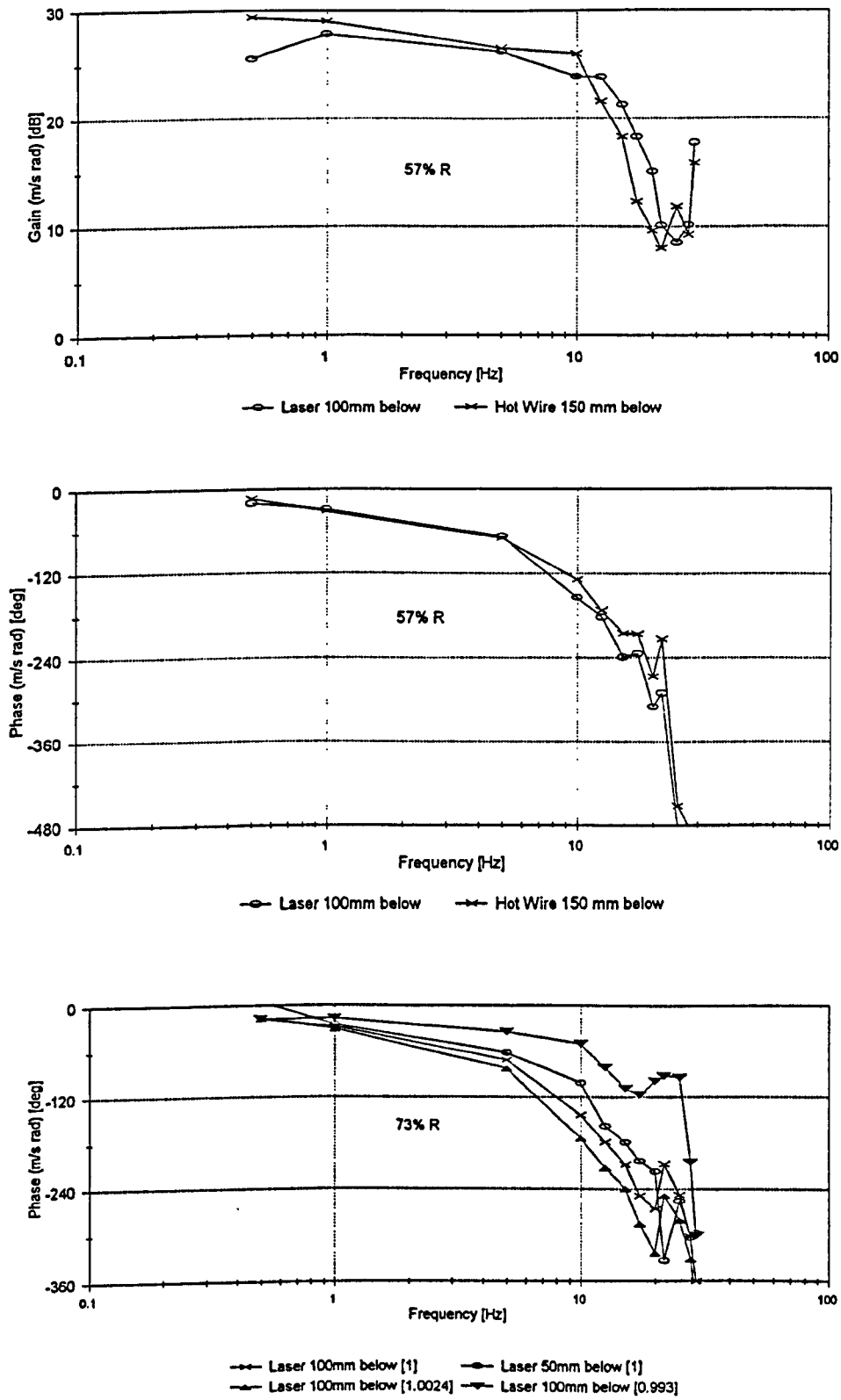

Fig. 5-21 Comparison of Induced Flow Frequency Responses obtained from the LDA & Hot Wire with the Effect of Timing Synchronisation (1200 rpm, 57% R, Collective Excitation)

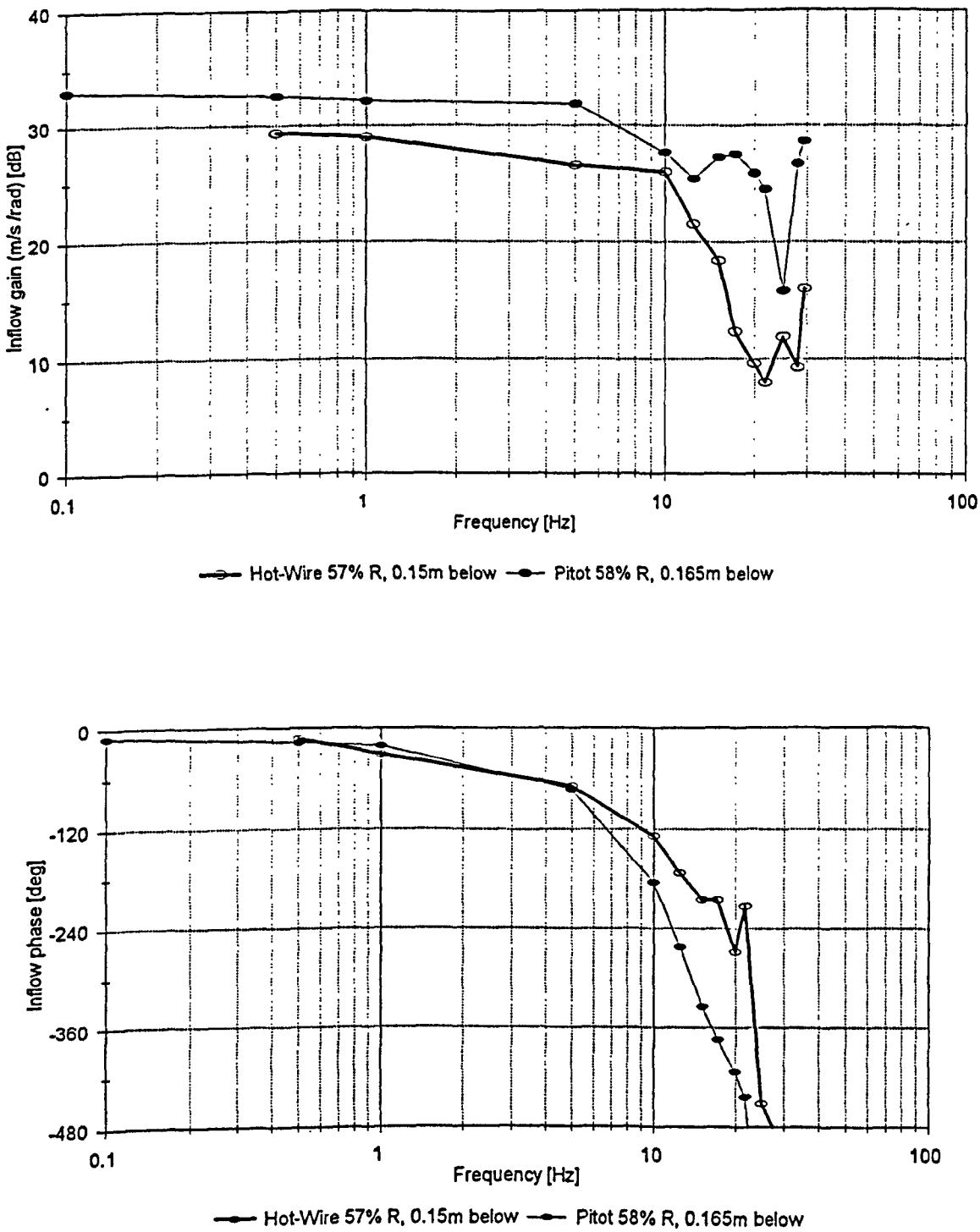

Fig. 5-22 Comparision of Induced Flow Frequency Response Measured with Hot Wires and Pitot-Static Pressure Transducers (1200 rpm, Collective Excitation)

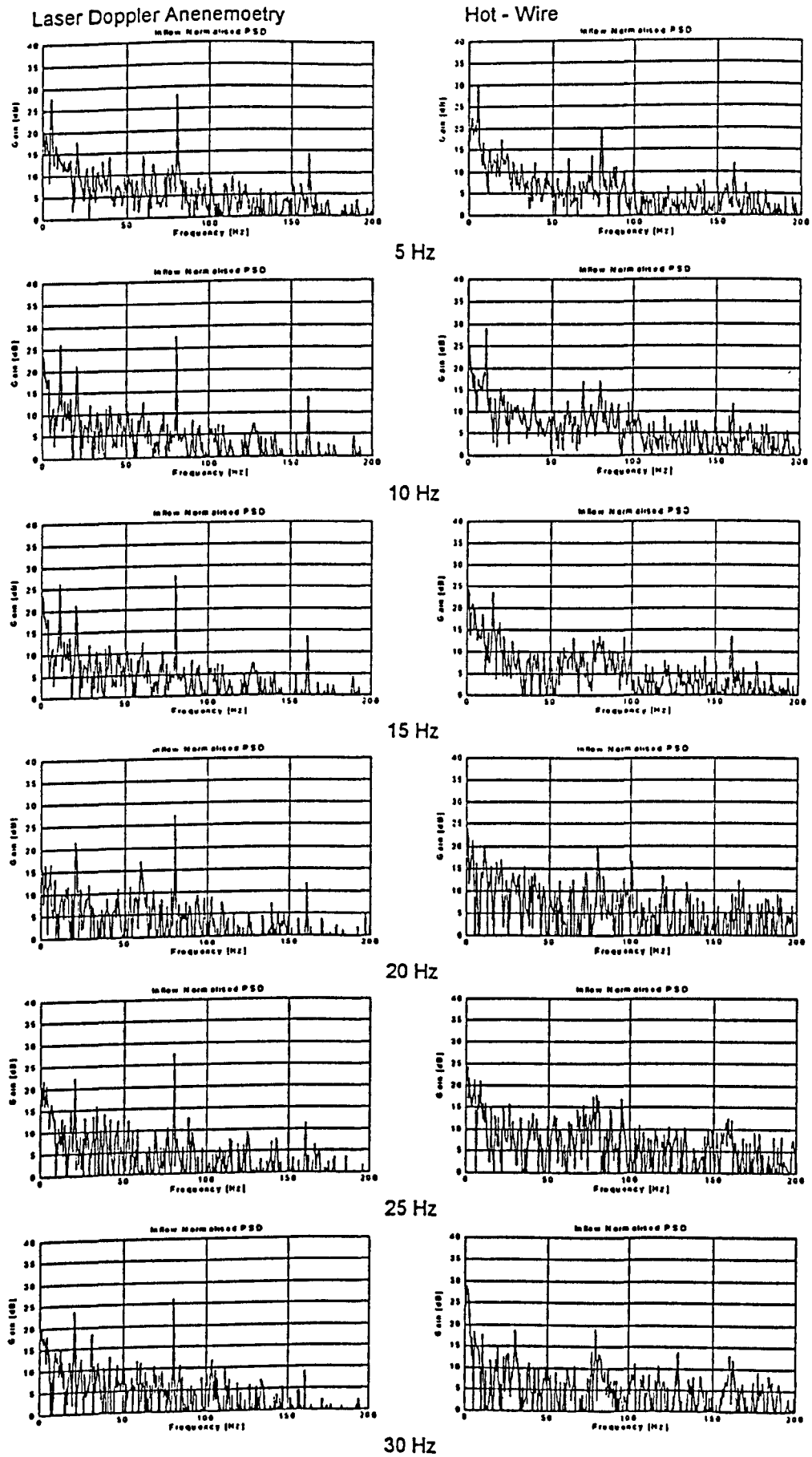

Fig. 5-23 Inflow Signal Frequency Content
(1200 rpm, 57% R, Hot Wire 0.15m & LDA 0.1m below Rotor)

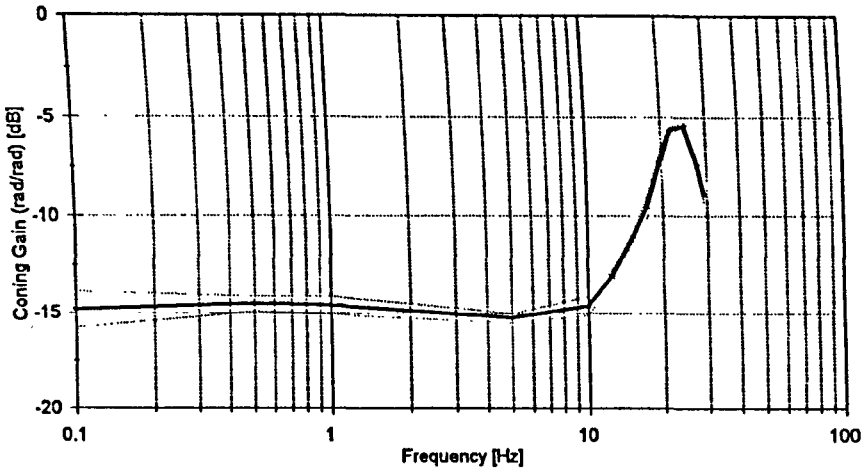

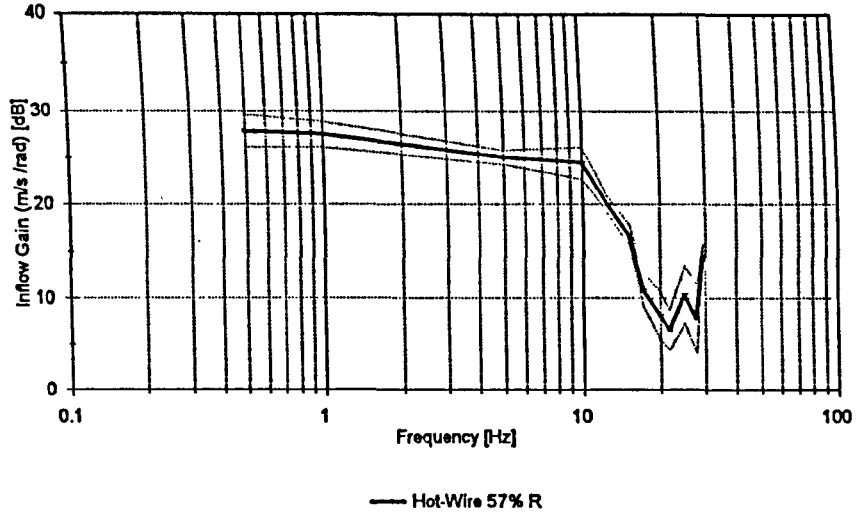

Coning

Inflow

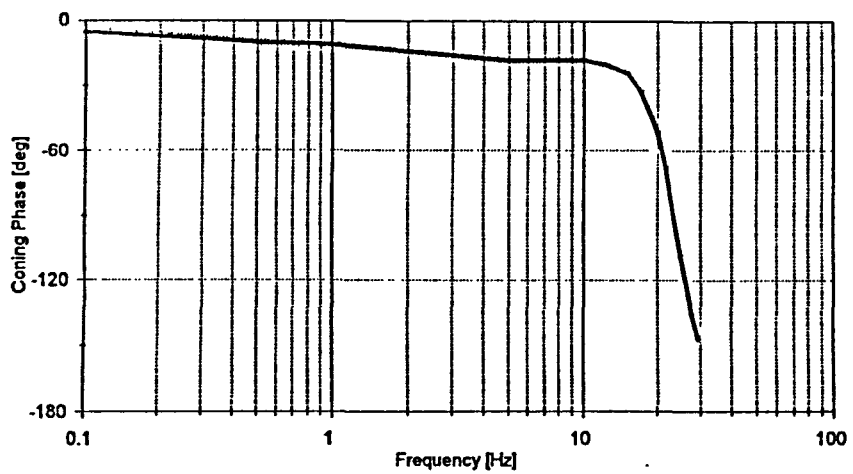

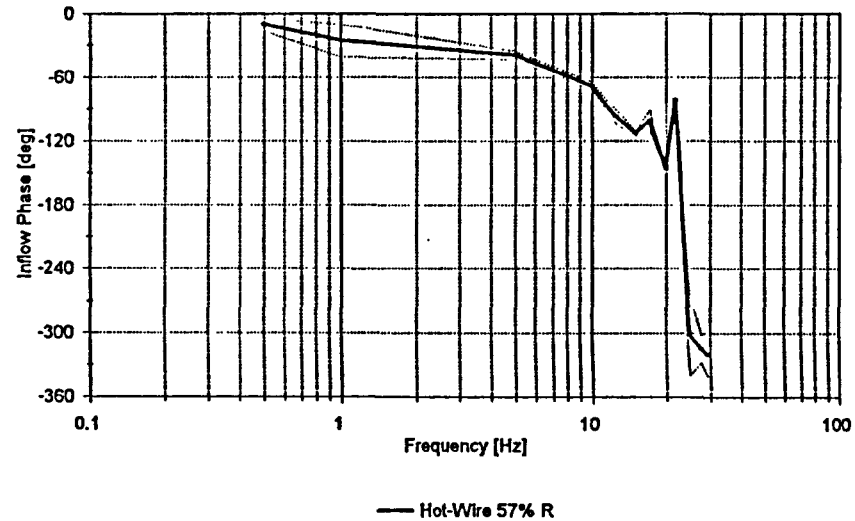

Fig. 5-24 Experimentally Determined Coning and Inflow Dynamics
(1200 rpm, Hot Wire, 0.15m below , Collective Excitation, Inflow Phase Corrected for Transmission Delays)

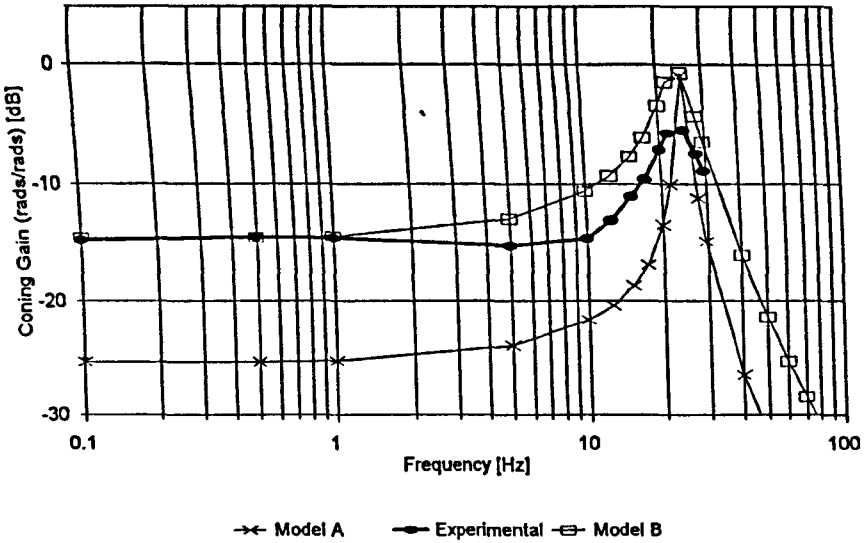

Coning

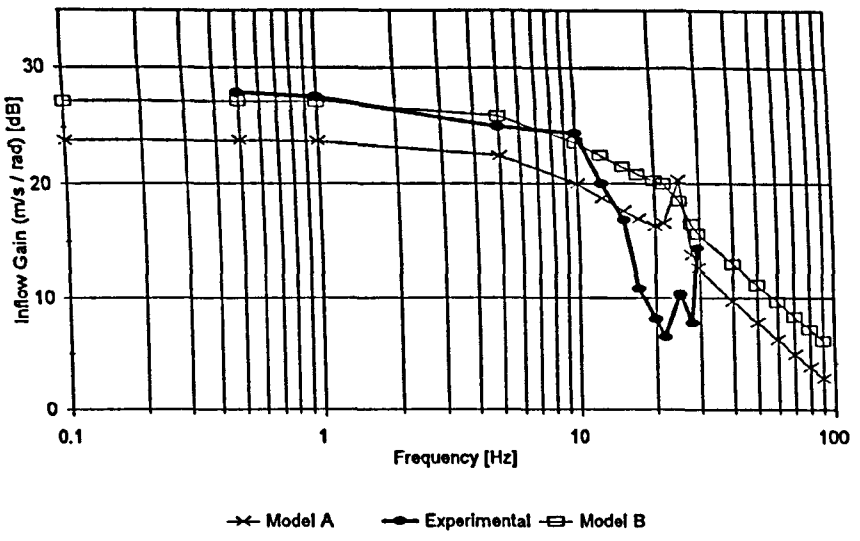

Inflow

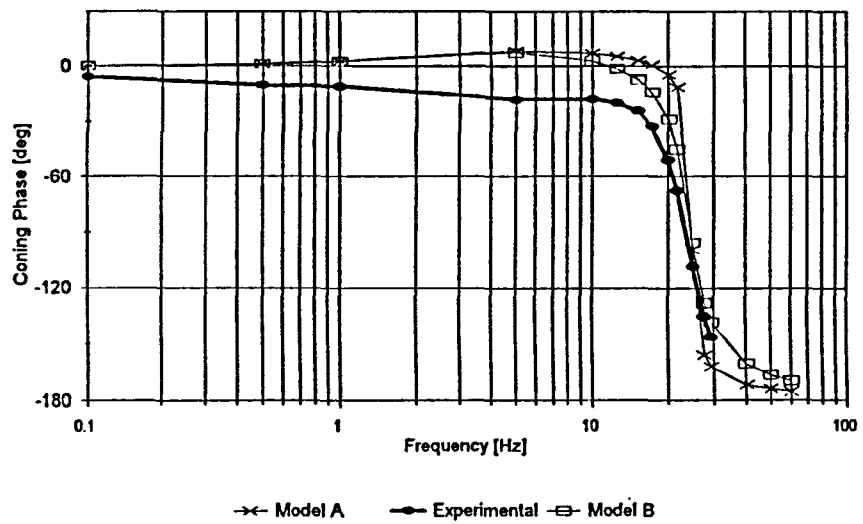

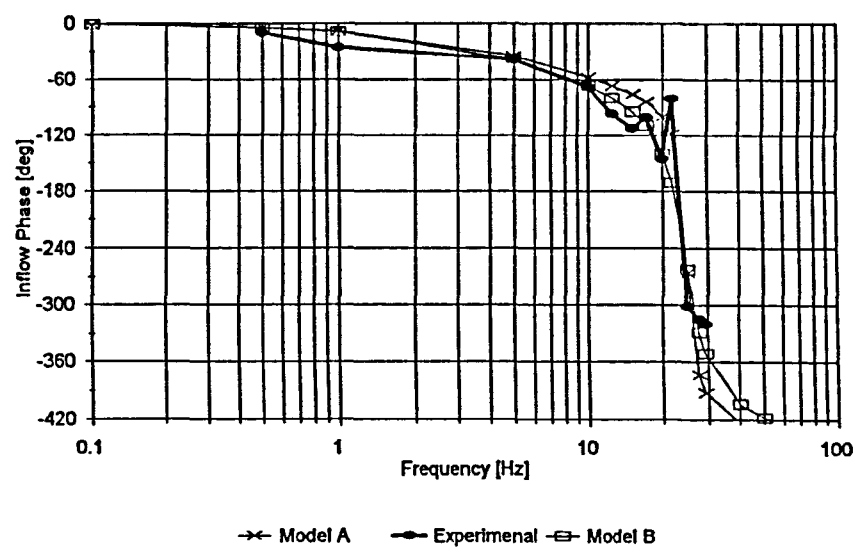

Fig. 5-25 Correlation of two Coning/Inflow Models with Experimental Data
(1200 rpm, Hot Wire, 0.15m below , Collective Excitation)

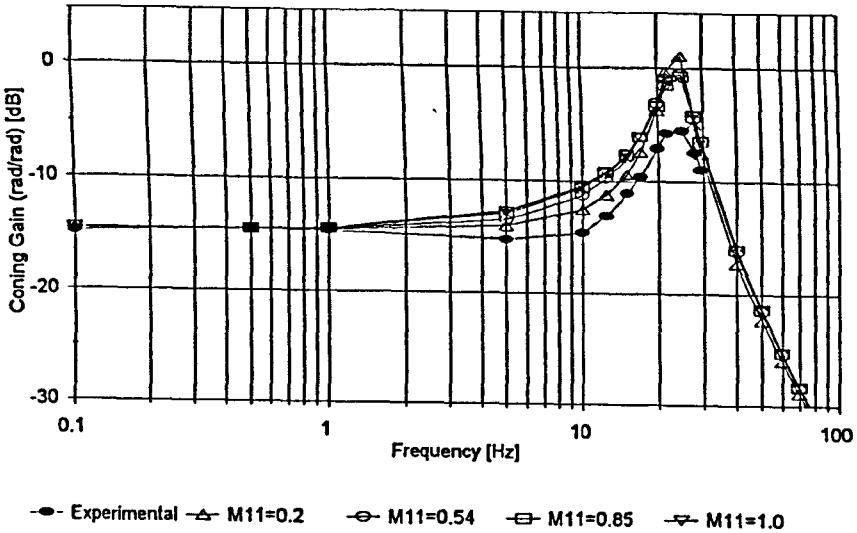

Coning

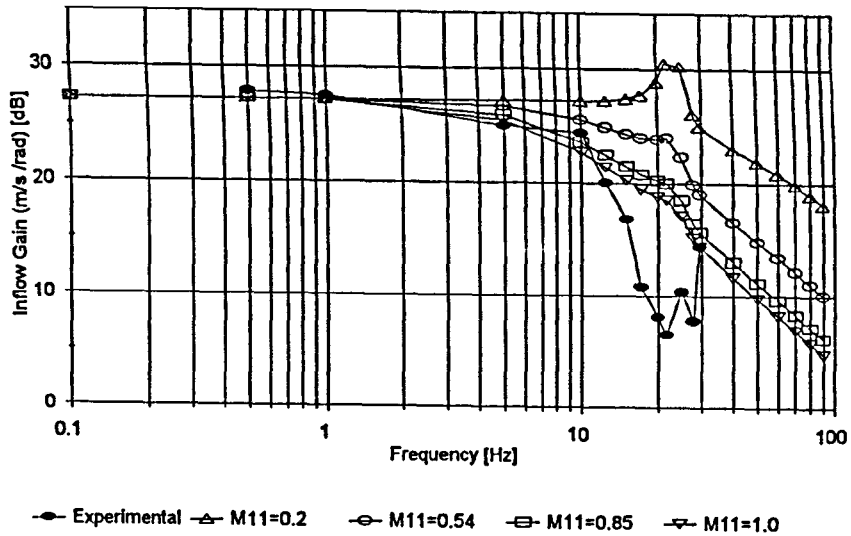

Inflow

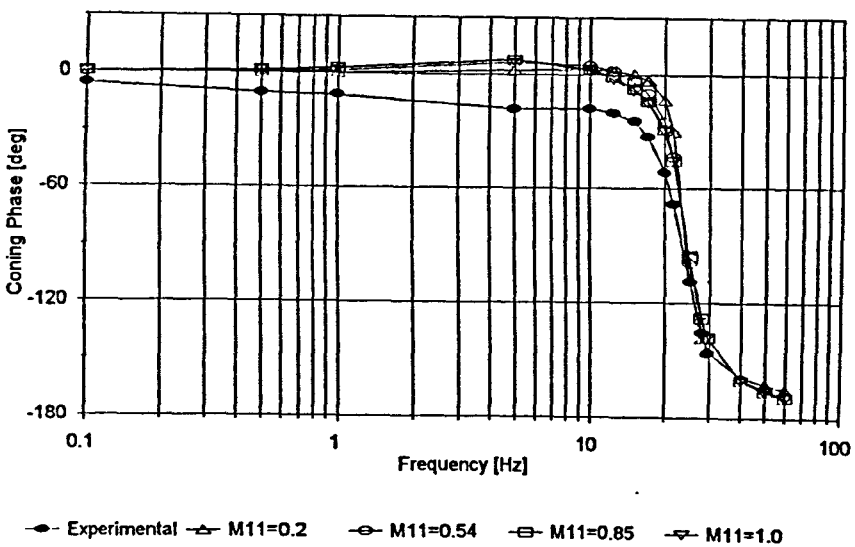

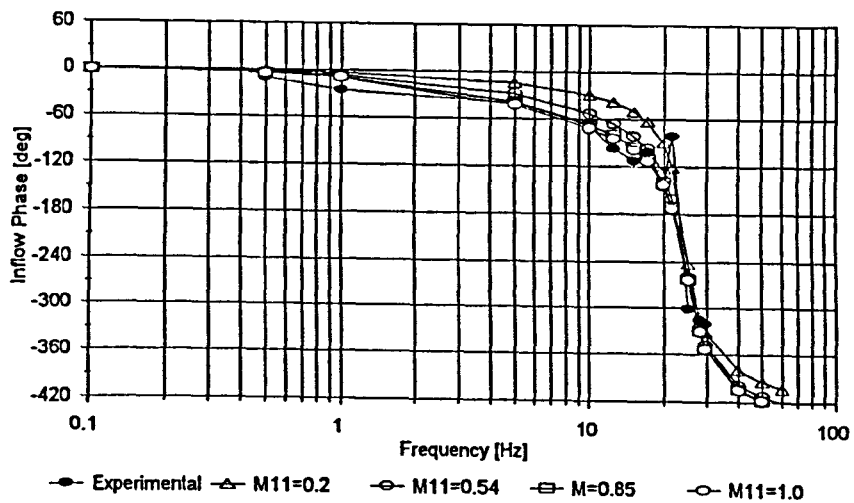

Fig. 5-26

Effect of Apparent Mass on Model B Fidelity
(1200 rpm, Hot Wire, 0.15m below , Collective Excitation)

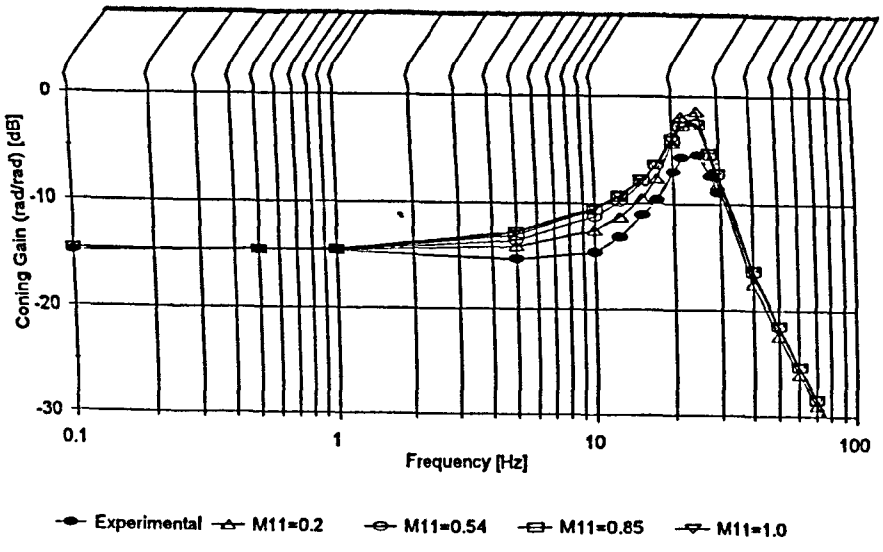

Coning Gain

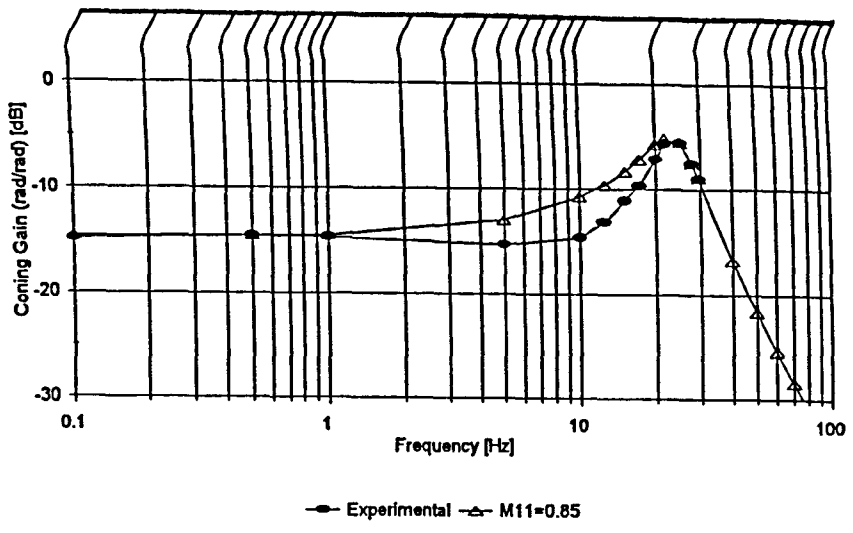

Coning Gain

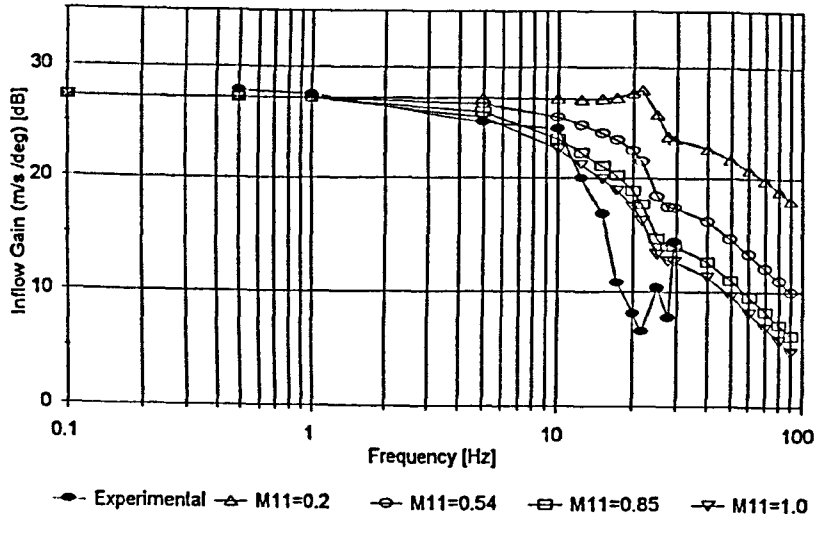

-a- Inflow Gain

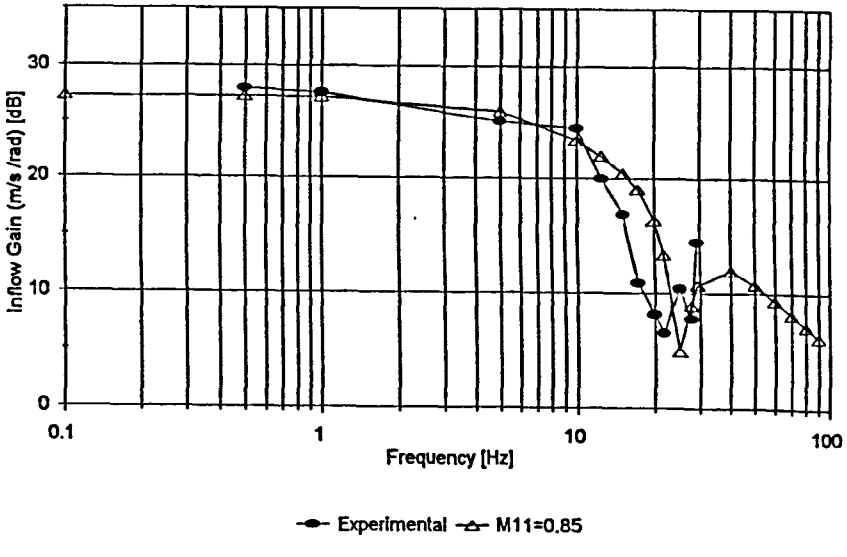

-b- Inflow Gain

Fig. 5-27 Effect of Increased Coning Damping on the Fideity of Model B
(a - Coning Damping increased by 25%, b - Coning Damping increased by 50%)
(1200 rpm, Hot Wire, 0.15m below , Collective Excitation, Inflow Phase Corrected for Transmission Delays)

Chapter 6
Inflow Due to Cyclic Excitation

6.1 Introduction

From the literature survey it was clear that there was very little published information on the induced flow field behaviour of the rotor for the case of dynamic cyclic pitch excitation. The limited information that was found [Liou & Komerath 1994] related to one specified cyclic input frequency, well above the shaft speed of the rotor. The aim of the work in this section was thus to examine the inflow response due to cyclic pitch excitation over a frequency range of 0.5 to 30 Hz.

The results are compared with the assumptions made in the Pitt and Peters [Pitt & Peters 1983] dynamic inflow model. In particular the assumptions of a linear inflow gain variation and constant phase delay with radius are examined. The first order sinusoidal azimuthal variation of the inflow response with respect to the Pitt and Peters [Pitt & Peters 1983] inflow degrees of freedom is also considered. The radial variation of the induced flow with cyclic input is compared to the distribution found with collective inputs.

Following on from the work in Chapter 5, where good correlation between the results from the Hot-Wire and LDA systems was shown, the majority of the data discussed in this chapter were taken using hot wires spaced radially and circumferentially. Some additional data were obtained using the (LDA) system, but time limitations placed restrictions on the LDA experimentation. Some data were also taken with the tunnel running at a very low speed of 2.5 m/s giving an advance ratio μ of 0.025. It was thought that this would improve the repeatability of results by reducing circulation, without affecting the overall inflow response.

Due to time constraints the work was carried out using cyclic pitch inputs which only resulted in mainly lateral flapping, i.e. side to side tilt of the tip path plane.

6.2 Cyclic Rotor Excitation

The input to the rotor was such that the maximum variation of the blade pitch occurred at 15 and 195 degrees azimuth. The minimum blade pitch variation for each blade occurred at azimuth positions offset by 90 degrees, i.e. at 105 and 285 degrees azimuth. This resulted in a predominantly lateral blade flapping response. Fig. 6-1 shows the lateral and longitudinal frequency response of the tip path plane in simulated hover. It can be seen that the rotor control phasing results in a lateral response, which is twice as large as the longitudinal response (6 dB). For comparison, the coning gain response is also shown in the top graph of Fig. 6-1. It can be seen that the collective response is approximately 30 dB smaller than the lateral response. The conclusion from this is that the cyclic inputs did result in almost pure cyclic loading of the rotor and produced minimal changes in thrust loading.

The phase of the lateral and longitudinal tip-path-plane-tilt degrees of freedom is shown in the bottom of Fig. 6-1.

The cases at low advance ratio were included because it was anticipated that this would reduce recirculation without significantly affecting the measured inflow. The low tunnel speed did not affect the dynamic flapping response as shown in Fig. 6-1. The data with low advance ratio was only taken during the test, which examined the azimuthal variation of the induced flow.

Fig. 6-2 shows the instantaneous deflection of one blade, over-plotted against azimuth position over a period of several seconds at 1200 rpm, while cyclic inputs are applied at a frequency of 5 Hz.

From the plot of the blade response, it can be seen that the blade range of movement is at a minimum at 340 degrees and 160 degrees azimuth. Less clear is the position of maximum blade response, which occurs at approximately 70 and 250 degrees azimuth. From this is can be seen that the difference between application of maximum pitch variation and maximum blade response is approximately 60 degrees. In other words, because of the stiff mounting of the blades in the hub, the delay between the maximum aerodynamic force on the blade and the

subsequent blade response has been reduced from 90 degrees (articulated rotor) to 60 degrees for the rotor under test.

6.3 Radial Inflow Frequency Response with Cyclic Excitation

For this case, the blade pitch was varied at frequencies between 0.5 and 30 Hz. The radial inflow measurements were taken at an azimuth position of 90 degrees as this was the aerodynamically least obstructed area under the rotor and allowed radial measurements between 17 and 105 % of the rotor radius. Fig. 6-3 and 6-4 show the gain and phase frequency response over the radial range. The graphs show the average and standard deviation from 5 runs, with good repeatability.

6.3.1 Inflow Dependence on Frequency of Excitation

The dynamic inflow gain response is shown in Fig. 6-3 for a range of radial stations. Once again some reduction in data quality is evident near the tip region and also near the blade root. Outside of the wake beyond 80% blade radius, turbulence impairs the repeatability. In the 25 to 80 % radial range the lowest frequency of 0.5 Hz generally has a larger standard deviation than that at other frequencies. This is almost certainly due to low frequency wake recirculation, which adversely affects the results, for the low excitation frequency.

The inflow frequency response over a range of radial stations is shown in Fig. 6-3. Generally, the gain is constant or slightly increasing between 0.5 and 1 Hz before decreasing linearly with logarithmic frequency up to 10 Hz. Above 10 Hz most of the frequency responses show a slight recovery in gain between 10 Hz and 23 Hz. The inflow frequency responses for the case of cyclic excitation are quite different to the collective (Fig. 5-6) case, where the gain remains steady for a range of frequencies between 0.5 and 10 Hz. The underlying trend of diminishing gain with frequency in the region between 1 and 5 Hz is very interesting since this band is important from the point of view of handling and control. Although the low frequency inflow gain is near 25 dB for both collective and cyclic excitation, in the cyclic case the gain reduces with frequency from 1 Hz, resulting in lower gains and smaller inflow variations at

corresponding frequencies. This might explain the slightly worse repeatability of the cyclic case, illustrated by generally larger standard deviations, particularly near the root and tip.

The phase response at various radial stations is shown in Fig. 6-4. Again between 33% R and 88% R the phase response is very repeatable. In all cases the phase falls rapidly from around 10 deg at 0.5 Hz to 120 deg at 5 Hz. Thereafter the phase recovers to approximately 60 deg over the frequency range 8 to 20 Hz.

The phase response for the cyclic case is again different in character from that of the collective case (Fig. 5-7). The inflow phase response for the collective case is similar in shape to the phase response of the blade coning mode. Similarly the shape of the inflow phase for the cyclic case has similarities with the cyclic flapping blade phase response shown in Fig. 6-1.

If a conceptual wake model based on momentum theory is used, where the local induced velocities beneath the rotor are related to the local blade loading of the rotor, then the frequency responses of the collective and cyclic cases should be similar. The only difference between the two being that in the collective case, loading changes will occur over the whole disc and in the cyclic case over only part of the disc, hence the effects on the induced velocity would be present over the whole or partial disc respectively. The fact that the character of the frequency responses is different for the collective and cyclic cases emphasises the need for an accurate wake model where the velocity components at any point beneath the rotor are given by the combined influence of the spiralling time-varying shed vortices from all the blades. In the collective case the loading changes due to pitch changes on all blades would cause shed vorticity of varying strength to be added to the spirals already beneath the rotor. In the cyclic case the amount of shed vorticity (vorticity due to time-varying blade lift) from each blade and added to the existing spiral will be determined both by the blade azimuth position and the cyclic input. From this it would be expected that the vorticity distribution in the spiralling wake would be very different from that of the collective case and this is a very likely explanation for the observed differences in the collective and cyclic inflow frequency responses.

Concluding, it seems that, as for the collective case, both the gain and phase frequency responses of the induced flow vary with radial station when the rotor is subjected to dynamic cyclic pitch inputs. Furthermore, the character of the inflow response for the collective and cyclic cases is quite different. These differences may be explained using a complex wake model were the dynamic inflow response is determined by the combined effect of the shed vorticity spirals.

6.3.2 Radial Variation of the Dynamic Inflow Response

In Fig. 6-5 the gain variation with radius is shown over a range of frequencies. The radial variation of gain was examined only at the 90 degrees azimuth position. Measurements in the axial direction would have been restricted due to the protruding base plate. The average over 5 runs and the standard deviation are shown. Repeatability is good, with the usual degradation towards the tip and root of the blade.

The graphs in Fig. 6-5 show that the induced flow gain distribution over the radius is not constant with frequency. At 0.5 Hz the response starts increasing near linearly with radius on a logarithmic gain scale. As the frequency is increased the response flattens. At 5 Hz a slight inner peak has developed at 30-40% R and a small peak is present at 88 % R. The outer peak becomes more pronounced at 10 Hz, and at 12 Hz there is a sharp outer peak and then two troughs at 25 and 65 % R. The shape for 15, 17 and 20 Hz is similar. At the higher frequencies the sharp outboard peak at 88 %R dominates the radial gain variation.

Comparison of Fig. 6-5 with the equivalent collective cases (Fig. 5-2), shows that the radial gain distributions for the cyclic and collective cases have some similarities. The cyclic radial gain variation develops a sharp gain peak at approximately 90 % R, just as in the collective case. Similarly a secondary peak - though further outboard and less sharp - appears, as in the collective case.

Although there are some similarities between the radial inflow variation in the cyclic and collective cases, in detail they are different. Again this reinforces the need for a complex wake model.

The variation of the induced flow phase with radial station is shown in Fig. 6-6. No clear pattern of the phase variation with radial station can be found. This is in contrast to the radial phase variation in the collective case, where the phase lag increases clearly with inboard station (Fig. 5-5). For the cyclic case, the induced flow phase change with radius is approximately linear over the centre blade section between 33% and 80 % R. Again these results and the differences to the cyclic case, point to a complex wake model of spiralling shed vorticity, where the vorticity is related to the time-varying loading of each blade. A simple wake model where the induced flow at a point beneath the rotor disc is related to the rotor loading at that point cannot be used to explain the complex structure of the dynamic induced wake observed in these results.

6.4 Azimuthal Inflow Measurements

The variation of the induced flow response with azimuthal position will be examined next. Again the maximum blade pitch excitation is at 15 deg azimuth and the range of azimuth positions considered between 0° and 90° azimuth. All results are for the radial station of 57% R. During this phase of the research the LDA system became available again and this was used to examine the inflow response some 5 cm closer to the blade. The effect of a low tunnel speed setting (μ=0.025) to reduce recirculation was also investigated.

6.4.1 Dynamic Inflow Frequency Response at various Azimuthal Stations

The gain response is shown in Fig. 6-7. The frequency response obtained at various azimuthal positions for both μ=0 and μ=0.025 are very similar. The most notable difference between the two is that for μ=0.025 repeatability is significantly improved, particularly at low frequency. This confirms that the low tunnel speed setting sweeps away the wake downstream of the rotor and results in much lower recirculation. Differences in the results obtained with and μ=0 and μ

=0.025 exist, particularly at 0, 15 and 30 degrees azimuth where the response for μ=0.025 drops off slightly earlier than that of the μ=0 case. This suggests that the low tunnel speed, which sweeps the rotor wake downstream of the tunnel has also affected the inflow response near the rotor disc. This reinforces the earlier results that showed that the inflow at a point beneath the disc is strongly affected by the shed vorticity in the wake spirals beneath the rotor.

The gains obtained using the Laser Doppler Anemometer (LDA) are shown in Fig. 6-8. Again graphs are presented for both the μ=0 and μ=0.025 cases, and some difference can be seen, although less than for the hot-wires further away from the rotor disc. Comparison with the hot-wire data in Fig. 6-7 is also very favourable with both methods giving very similar results, considering that the laser was measuring some 5 centimetres closer to the disc than the hot-wire. Particularly interesting is the fact that the data from the laser at 30° and 45° show the same gain recovery and flat gain response respectively as obtained from the hot-wire data.

The frequency response of the inflow phase measured at various azimuthal stations at a radial station of 57% R is shown in Fig. 6-9. Again the true hover (μ=0) and μ=0.025 cases are considered, and some differences found, which again points to the effect that sweeping the wake downstream has on the induced dynamic velocity response at the rotor disc.

Generally there is a significant variation in the shape of the phase response with azimuth. At 0 deg the phase drops off steadily. From 45 deg azimuth onwards a small recovery in the phase starts to build which increase with azimuth. At 90 degrees this recovery is very pronounced.

The phase data obtained from the LDA are shown in Fig. 6-10. Again the gradual phase recovery starting in the 30 deg case at 10 Hz and building, as azimuth is increased, can be seen and the LDA data show a similar variation in character with azimuth as found from the hot-wires. In detail the laser phase data are however somewhat different, from that taken using the hot wires, showing that the distance from the blade has an effect on the observed inflow response.

Whereas for the 0° 10 Hz case the hot-wire data have a phase delay of 120 Hz the data obtained from the LDA give only a 60° phase lag. This is the case for the 0, 15, 30 deg azimuth cases. A possible explanation might be that this is due to transmission delays with the hot wires being located some 5 cm further away from the rotor than the LDA. Work in Chapter 5, which examined the vertical variation of the induced phase for cases of collective excitation showed that a transmission type delay is present at frequencies up to 15 Hz. At 0 degrees azimuth and 10 Hz the phase difference between the LDA and hot-wire data is approximately 60 degrees and 80 degrees phase lag, for the zero and low advance-ratio cases respectively. With an average induced velocity of 10.5 m/s at a radial station of 57% R and separation difference of 0.05m, the phase difference due to transmission delays would be 360*0.05*10/10.5=17 degrees. This is much smaller than that determined experimentally. With increasing azimuth position the difference between the two decreases, which is difficult to explain from the point of view of a pure transmission delay, which would not vary with azimuthal station. The difference in phase is too large to be explained using a pure transmission delay as outlined in Chapter 5, and again illustrates the highly complex nature of the wake.

6.4.3 Azimuthal Variation of the Dynamic Inflow Response

The previous results have shown that a low wind tunnel speed giving μ as low as 0.025 is sufficient to affect the wake and the measured induced velocities near the rotor. The LDA system was used to take measurements closer to the rotor, and although similar results were obtained, the inflow response also varies with vertical separation from the blades. In this section only the hot-wire data obtained with μ=0 are used to examine the azimuthal variation of the inflow gain and phase over the range of frequencies.

The variation of the inflow gain response with azimuth is shown in Fig. 6-11. The results are those obtained from the hot wires placed 0.15m below the rotor at 7 azimuthal stations, averaged over 5 runs, with confidence intervals of 1 standard deviation.

For the lowest two frequencies considered there is a maximum of gain in the region of 45° to 60° azimuth. At 10 Hz and 12 Hz the gain drops off towards the 90° azimuth position. Assuming a momentum theory approach the highest induced velocities over the entire frequency range would have been expected to occur at the azimuth position corresponding to highest blade loading (15 deg. azimuth). Working from the assumption that the magnitude of the inflow produced by a blade is proportional to the lift produced by a blade, a sinusoidal variation of the inflow could be expected with a peak at the position where the blade loading is largest. The azimuthal inflow variation is dependent on frequency, further reinforcing that it is the wake generated over several revolutions which determines the inflow distribution. It seems to be less related to the disc loading as assumed in the Pitt and Peters inflow model. At higher frequencies the general level of the inflow gain drops with increased frequency as expected.

The phase variation of the inflow response over the azimuth from the hot-wire anemometry system is shown in Fig. 6-12 for μ=0.

For the lowest two frequency cases the azimuthal distribution of phase is virtually constant. As frequency is increased the general phase lag increases as would be expected. At 5 Hz the phase decreases from the 0 deg azimuth position towards the 90 degree position by approximately 100 degrees. For the next two frequency cases this trend is reversed and the phase lag decreases towards the 90 degree azimuth position. The response at 15 Hz again is more level with azimuth.

It is worthwhile to compare the overall pattern of the phase distribution with azimuth at these frequencies with the gain variation over the azimuth shown in Fig. 6-11. For the cases of 0.5 and 1 Hz the gain is near constant with azimuth, with only a slight peak in the mid azimuth range. The corresponding phase distribution is constant with azimuth. At 10 and 12 Hz the gain drops off significantly towards the 90° azimuth position and the phase response shows a decrease in the phase lag towards the 90° azimuth position.

At the higher frequencies, between 20 and 29 Hz, the development of a much larger phase delay at azimuth positions of 0 to 30 degrees is apparent. This corresponds to the phase

response seen in Fig. 6-9. Initially it might be thought that this significantly different gain might be due to a measurement error or rogue result. The developing nature, with the phase lag increasing between the 20 and 29 Hz cases, speaks against this. The complex changes in phase with azimuth are again not reconcilable with a simple momentum theory wake model, and must be due to the distribution of shed vorticity in the wake.

6.5 Compatibility with the Pitt and Peters Wake Description

Although the wake description used in the Pitt and Peters [Pitt & Peters 1983] dynamic inflow model is necessarily simple, it is useful to examine to what extent the approximations made relate to the experimentally observed dynamic wake. It may be argued that it is not constructive to compare the results from the Pitt and Peters [Pitt & Peters 1983] model, which utilises a simple conceptual wake model with the experimentally observed results. The wake model from Pitt and Peters has however been used to predict the inflow response [Chen & Hindson 1987] and to some extent the parameters of the Pitt and Peters inflow model are dependent on an adequate wake model.

Given a particular rotor loading, the Pitt and Peters model gives predictions of three inflow degrees of freedom, which are in turn used to find the induced velocity at any point on the rotor disc, using the Pitt and Peters wake model, given below. For further details the reader is referred to Chapter 1.

$$\lambda(\psi,r) = \lambda_0 + \lambda_s r \sin\psi + \lambda_c r \cos\psi \qquad (6\text{-}1)$$

This effectively assumes that the induced velocity perturbation due to collective hub aerodynamic loading λ_0 is uniform over the rotor disc, and varies radially for the fore-aft λ_c and side-to-side λ_s induced flow degrees of freedom.

Predicted Radial Variation

The radial variation of the induced flow due to cyclic inputs are shown in Fig. 6-5. All the results are for the 90 degree azimuth position. For this case Equation (6-1) reduces to

$$\lambda(r, \psi = 90) = \lambda_0 + \lambda_s r, \qquad (6\text{-}2)$$

where r is the non-dimensionalised radial position. The inputs to the rotor are effectively cyclic, which is confirmed by Fig. 6-1, which shows that the collective-freedom response is some 20 dB smaller than the cyclic tip-path-plane degree of freedom. As the collective inflow component λ_0 is only related to the collective (thrust) loading of the rotor in the hover condition this inflow component should be negligible during the cyclic cases. The radial inflow gain response predicted by Equation (6-2) above thus reduces to :

$$\lambda(r, \psi = 90) = \lambda_s r. \qquad (6\text{-}3)$$

Equation (6-3) is used to simulate the radial inflow variation, with two magnitudes of λ_s, to match the experimental data at *r=0.57%*. This is shown in Fig. 6-13 using the same scaling as in earlier radial variation results. The experimental results from the hot-wires at 0.5 and 5 Hz are also plotted on this graph for comparison. It can be seen that over a centre section of the blade the linear inflow response - now plotted on the logarithmic gain axis - reasonably matches the experimental data. Differences occur outside of the 85 % radial station, where the measured inflow drops off rapidly and at the innermost radial stations. The theoretical predictions however, do not change with frequency, compared to the experimental results in Fig. 6-5. At higher frequencies the experimentally obtained, radial inflow variations are much more complex than the simple wake model in the Pitt and Peters [Pitt & Peters 1983] inflow model. According to the Pitt and Peters model the induced phase does not vary with radial station and should therefore be constant.

Predicted Azimuthal Variation

Using the Pitt and Peters wake description given by Equation (6-1), the azimuthal variation in the gain and phase of the inflow can be compared to the experimental data. Figure 6-14 examines the azimuthal variation in induced flow looking both at the gain and phase.

Considering the wake description given by Equation (6-1) and applying the same arguments as before for the exclusion of λ_0, this reduces to:

$$\lambda = 0.57(\lambda_s \sin\psi + \lambda_c \cos\psi). \qquad (6\text{-}4)$$

Two special cases exist at azimuth positions of 0 and 90 degrees:

$$\lambda(\psi = 0) = 0.57(\lambda_c), \qquad \lambda(\psi = 90) = 0.57(\lambda_s) \tag{6-5}$$

The λ_c and λ_s inflow degrees will have associated with them both a gain and a phase at each frequency. If the rotor loading were known then the resultant λ_c, λ_s degrees of freedom could be obtained analytically from the Pitt and Peters model. Here λ_c, λ_s will be extracted from the experimental data in Fig. 6-14 for frequencies of 0.5 Hz and 5 Hz and are given in the table below. The lateral and longitudinal inflow degrees can be found using Equation (6-5) at 0 degrees and 90 degrees.

Frequency [Hz]	Avg. Gain [dB] @0 deg.	Avg. Phase [deg] @0deg.	Avg. Gain [dB] @90deg.	Avg. Phase [deg] @90deg
0.5	23	-30	24.0	-15
5	25	-40	20	-125
	$0.57\lambda_c$		$0.57\lambda_s$	

Table 6-1 Selected Gain and Phase of the Inflow Response at two Azimuth Positions

Using the lateral and longitudinal inflow degrees (λ_s, λ_c) found from the data shown in the above table the azimuthal variation of gain and phase can be reconstructed using the wake description of Equation (6-4) and this is also shown in Fig. 6-14 with reasonable correlation. To calculate the azimuthal variation of the inflow gain and phase, the inflow gain and phase pairs at 0 degrees and 90 degrees were changed into complex numbers and then substituted into Equation (6-2) with various azimuth values. The assumed variation of the inflow degrees of freedom w.r.t. azimuth, assumed in the Pitt and Peters model, seems to be at least plausible at low frequencies. At higher frequencies the correlation is poorer.

6.6 Conclusions

The dynamic induced flow field beneath a rotor under cyclic excitation over a range of frequencies between 0.5 and 30 Hz was examined using hot wire and Laser Doppler Anemometry equipment. It was found that the dynamic inflow response of the air varied both with radial station, azimuthal station and frequency. A low tunnel setting to reduce

recirculation affected the measured dynamic induced response. The low advance ratio test cases did reduce the standard deviation of the results, suggesting that the small tunnel speed decreased recirculation by moving the older wake downstream. The effect on the dynamic inflow response shows that even small changes to the rotor wake significantly affect the dynamic induced velocities measured at the rotor disc. The axial position for data collection with respect to the rotor disc was also found to affect the recorded dynamic inflow frequency response.

Intuitively it would be expected that the largest variations in the induced flow occur at the azimuth area of the rotor where the pitch is largest over the range of cyclic input frequencies. This is however not the case with the inflow distribution being strongly affected by the frequency of excitation.

Much more work in examining the detailed behaviour of the wake even under steady conditions, but especially under cyclic excitation needs to be done, particularly looking at vertical variations and using further lateral and longitudinal cyclic inputs. The present results indicate that the behaviour of the wake is complex and not easily modelled with a momentum theory approach.

The wake description used in the Pitt and Peters inflow model is necessarily simple, but comparison of the radial and azimuthal variations of the inflow with experimental data, show that the real wake is more complex. The assumed linear gain variation is only approximately true for the mid-span region. Although not correct at the inboard section the effect of this is probably insignificant considering the low lift and induced flows in this area. More important is the repeatedly observed strong reduction in gain in the tip region of the blade, which is not considered in the wake description. The azimuthal variation of the inflow, w.r.t. the inflow degrees of freedom, however seems to be valid within a model of the wake behaviour, at least at low frequencies.

The strength of the Pitt and Peters dynamic inflow model is that it provides a simple mechanism to capture the dynamic structure of the wake. Its wake description however was

never intended to be used for accurate predictions of the induced velocities over the disc area, but this does not detract from the usefulness of the Pitt and Peters dynamic inflow model.

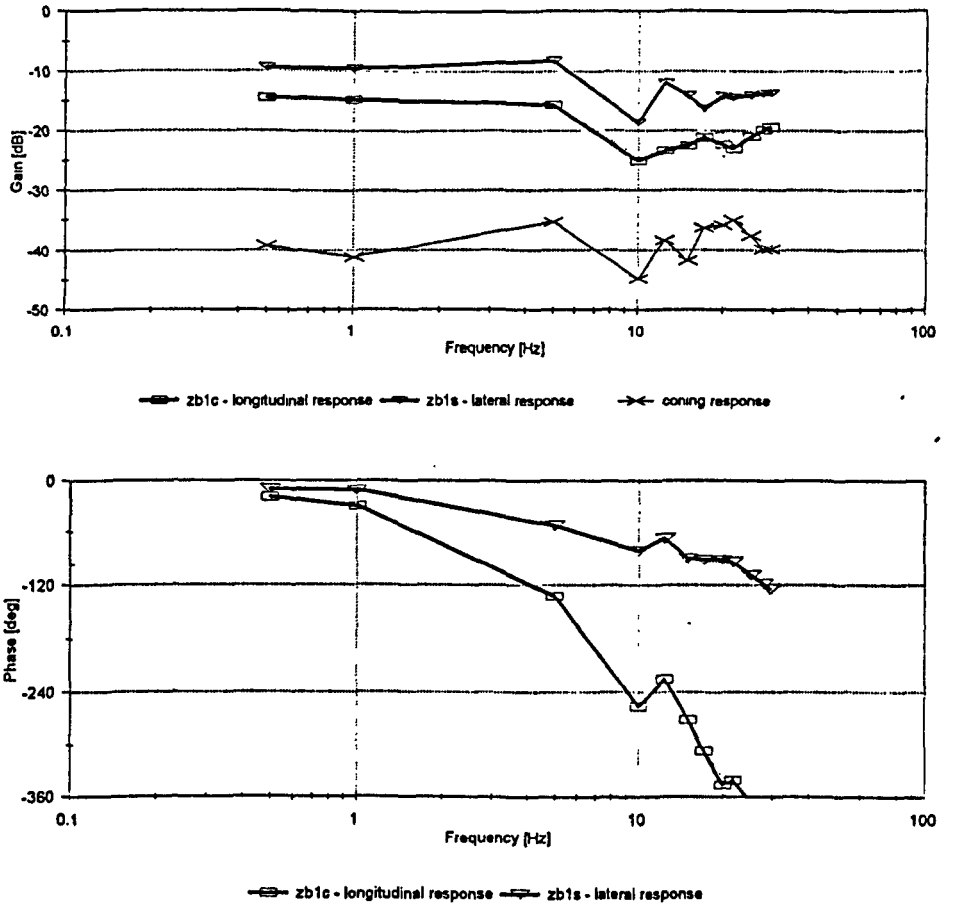

Fig. 6-1 Tip Path Plane DoF Frequency Response with Cyclic Inputs
(1200 rpm, Max. Blade Pitch at 15 deg.)

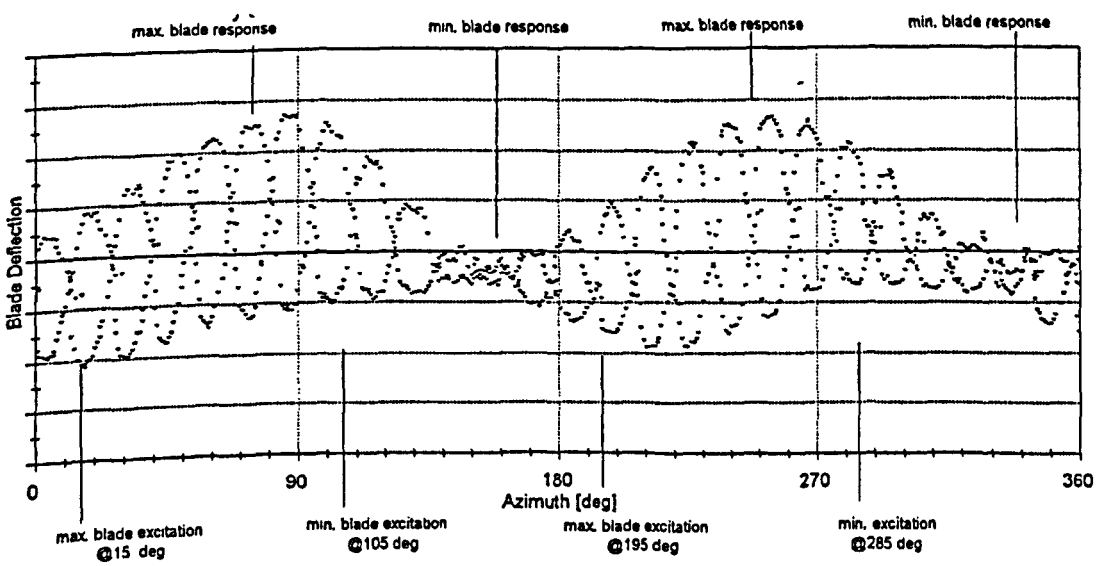

Fig. 6-2 Blade Excitation and Response
(1200 rpm, Max. Blade Pitch at 15 deg.)

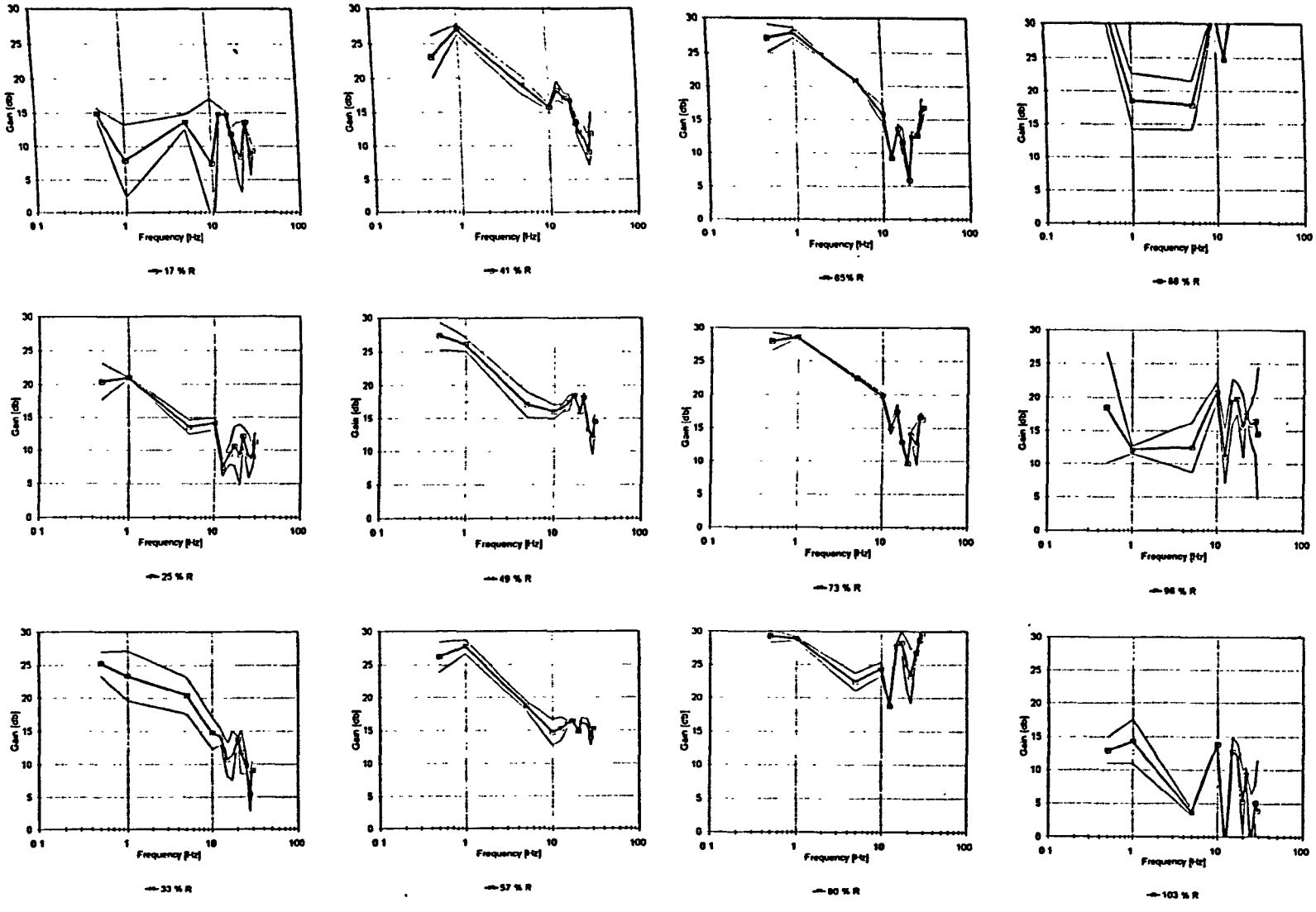

Fig. 6-3 Induced Flow Gain Response at selected Radial Stations, 90 deg. Azimuth
(1200 rpm, Hot Wire 0.15m below, Cyclic Excitation)

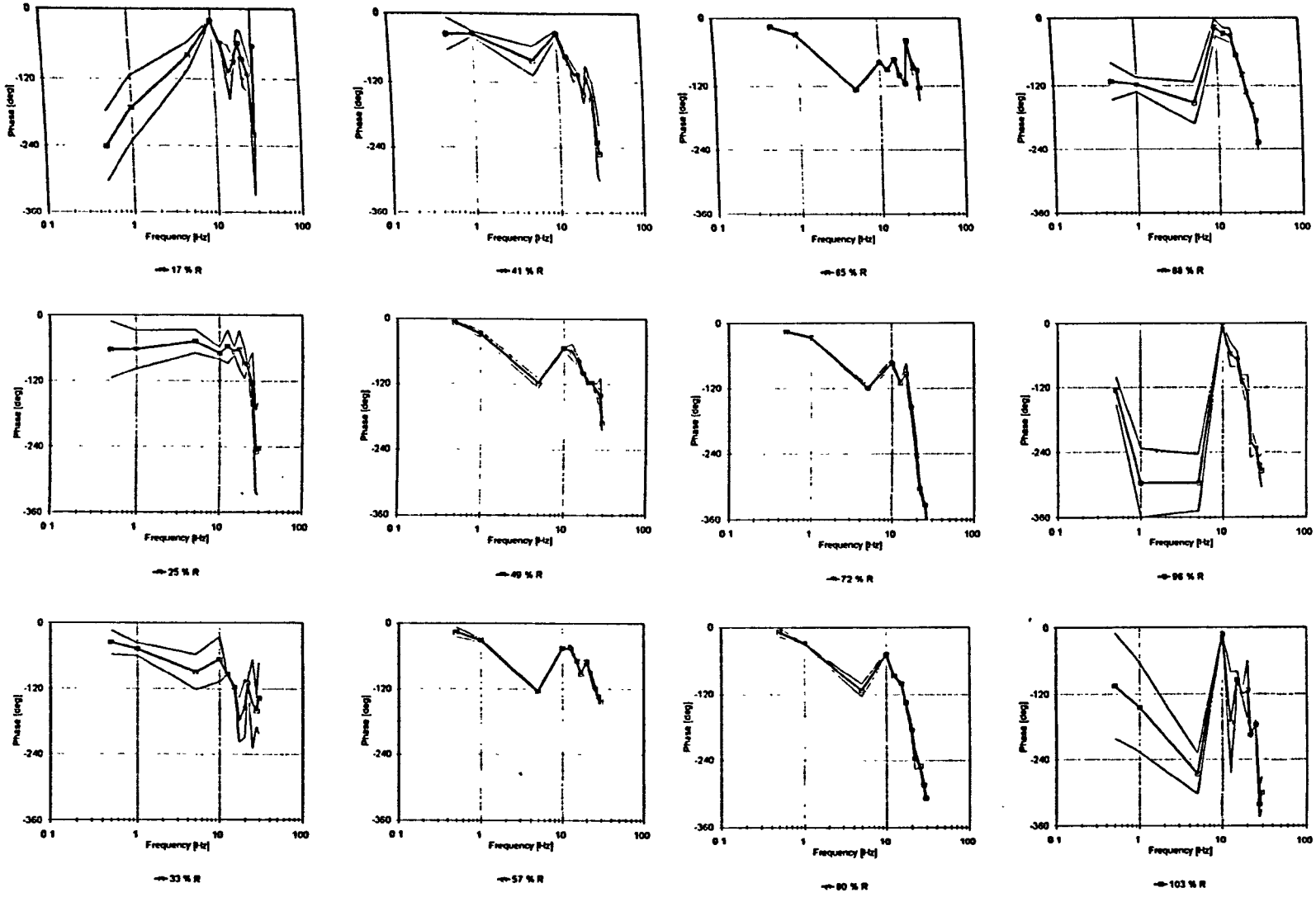

Fig. 6-4 Induced Flow Phase Response at selected Radial Stations, 90 deg. Azimuth
(1200 rpm, Hot Wire 0.15m below, Cyclic Excitation)

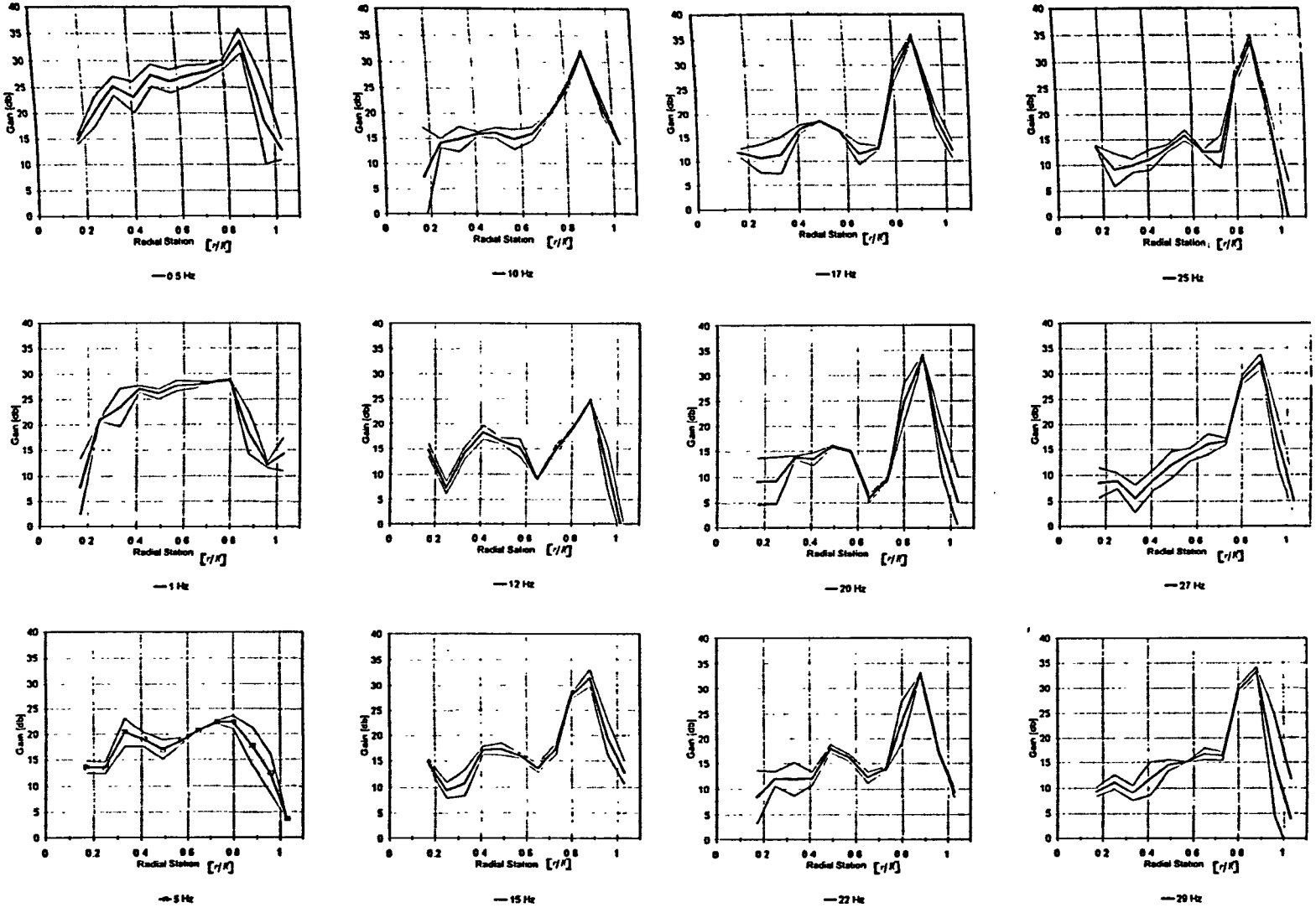

Fig. 6-5

Radial induced Flow Gain Variation
(1200 rpm, Hot Wire 0.15m below, 90 deg. Azimuth)

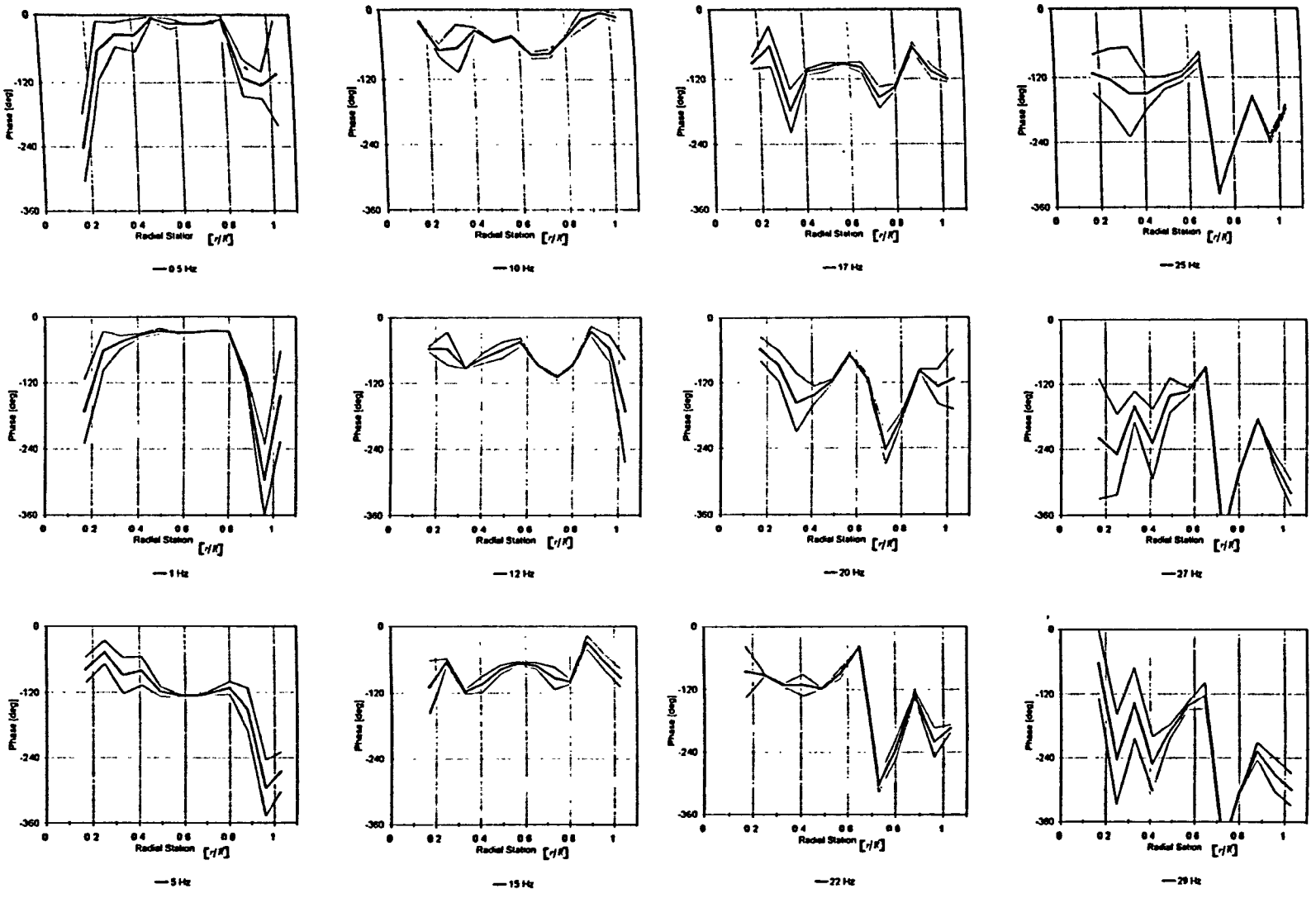

Fig. 6-6

Radial Induced Flow Phase
(1200 rpm, Hot Wire, 0.15m below, 90 deg. Azimuth)

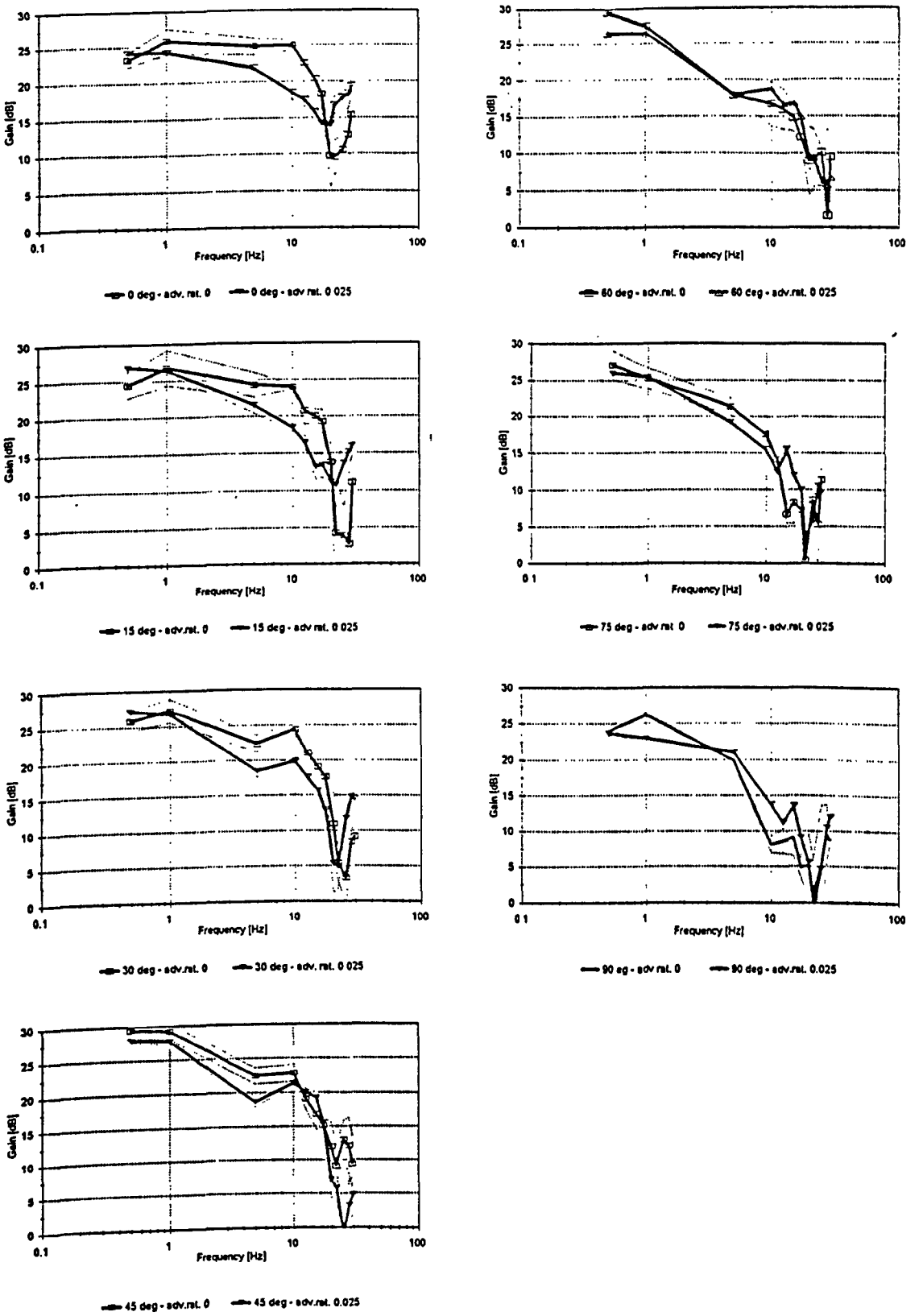

Fig. 6-7 Inflow Gain Response at various Azimuth Stations - Hot Wire
(1200 rpm, Hot Wire 0.15m below Rotor, 57% R, 0 and 0.025 adv. rat.)

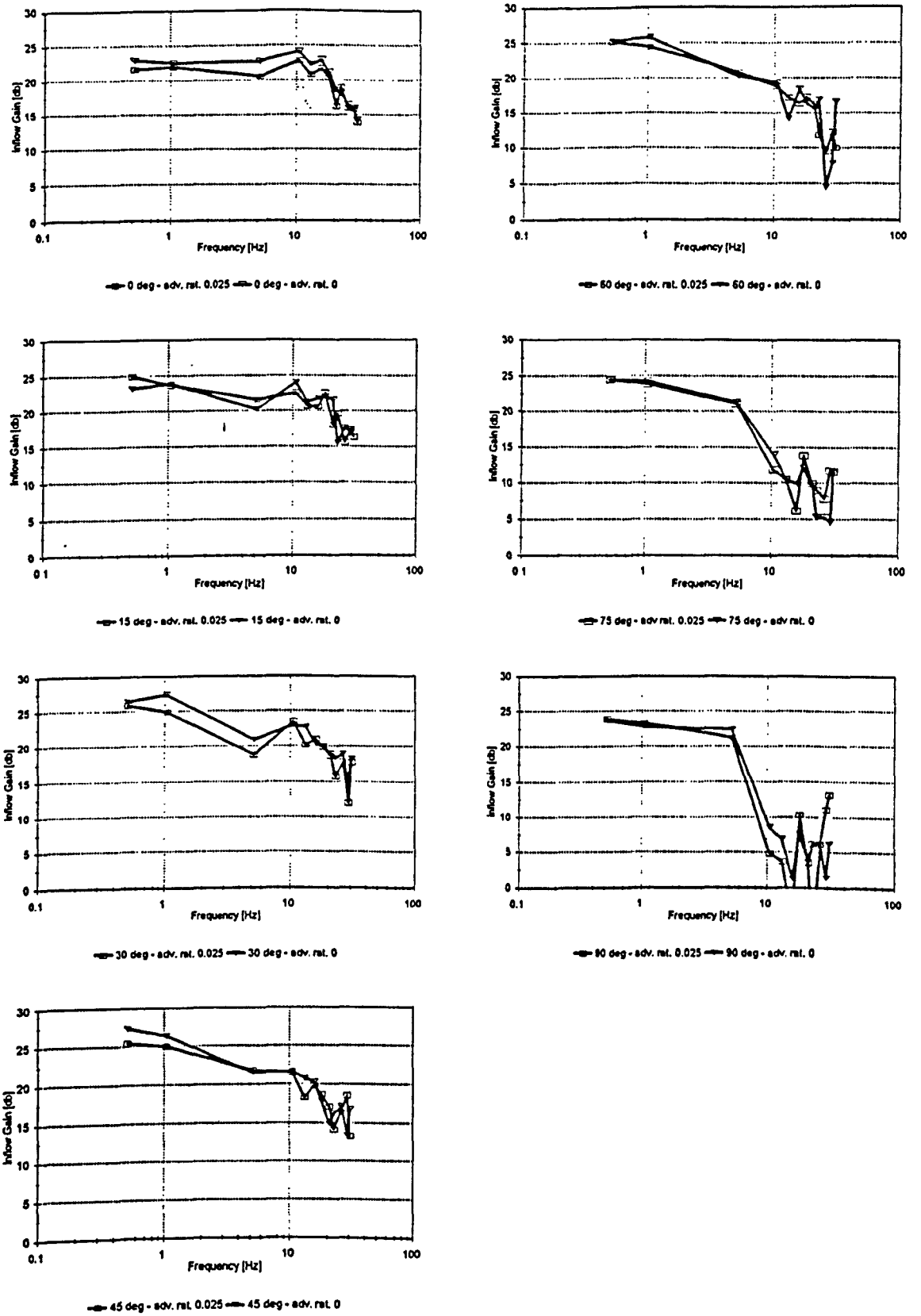

Fig. 6-8 Inflow Gain Response at various Azimuth Stations - LDA
(1200 rpm, LDA 0.10m below, 57% R, 0 and 0.025 adv. rat.)

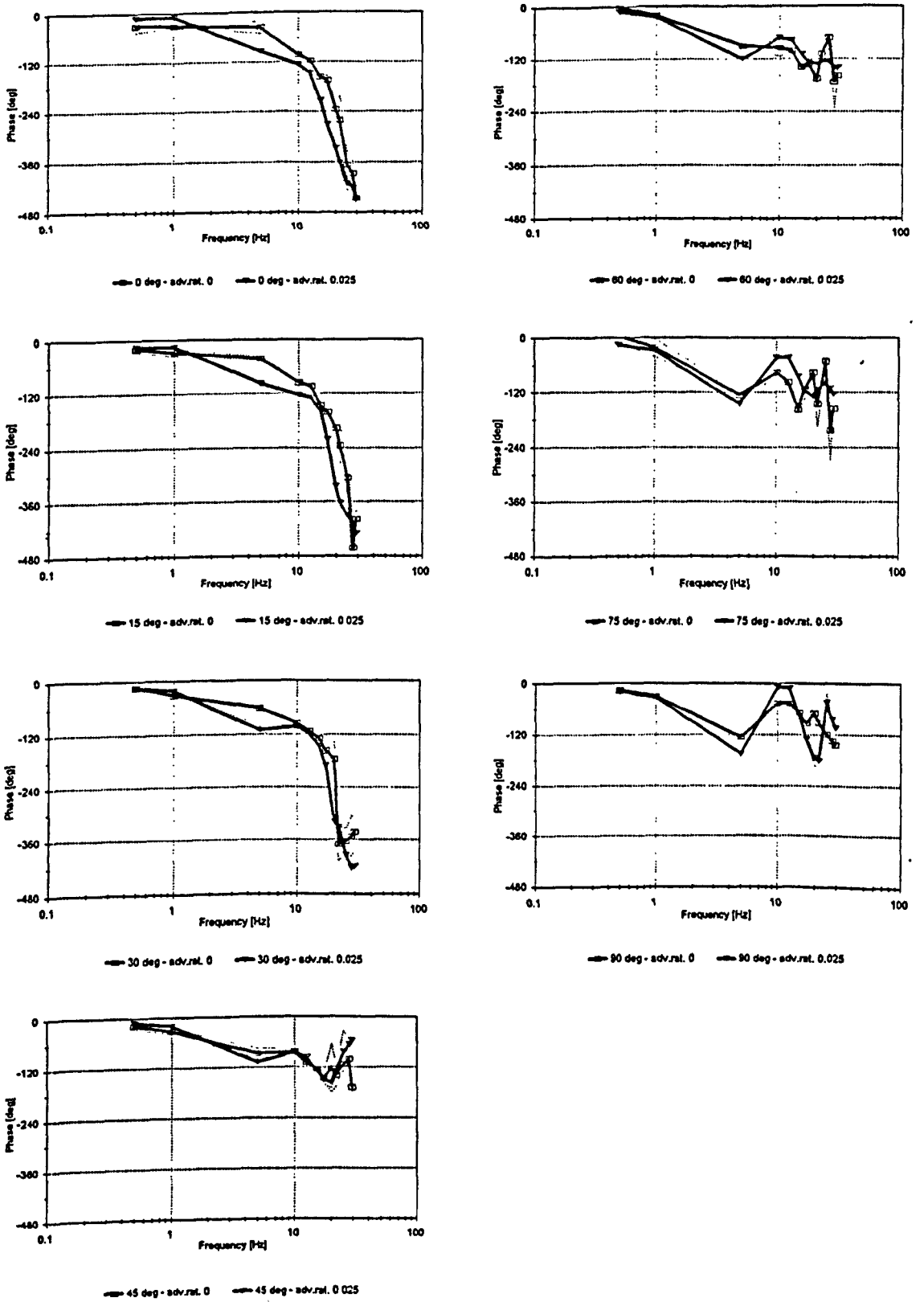

Fig. 6-9 Inflow Phase Response at various Azimuth Stations - Hot Wire
(1200 rpm, Hot Wire 0.15m below, 57% R, 0 and 0.025 adv. rat.)

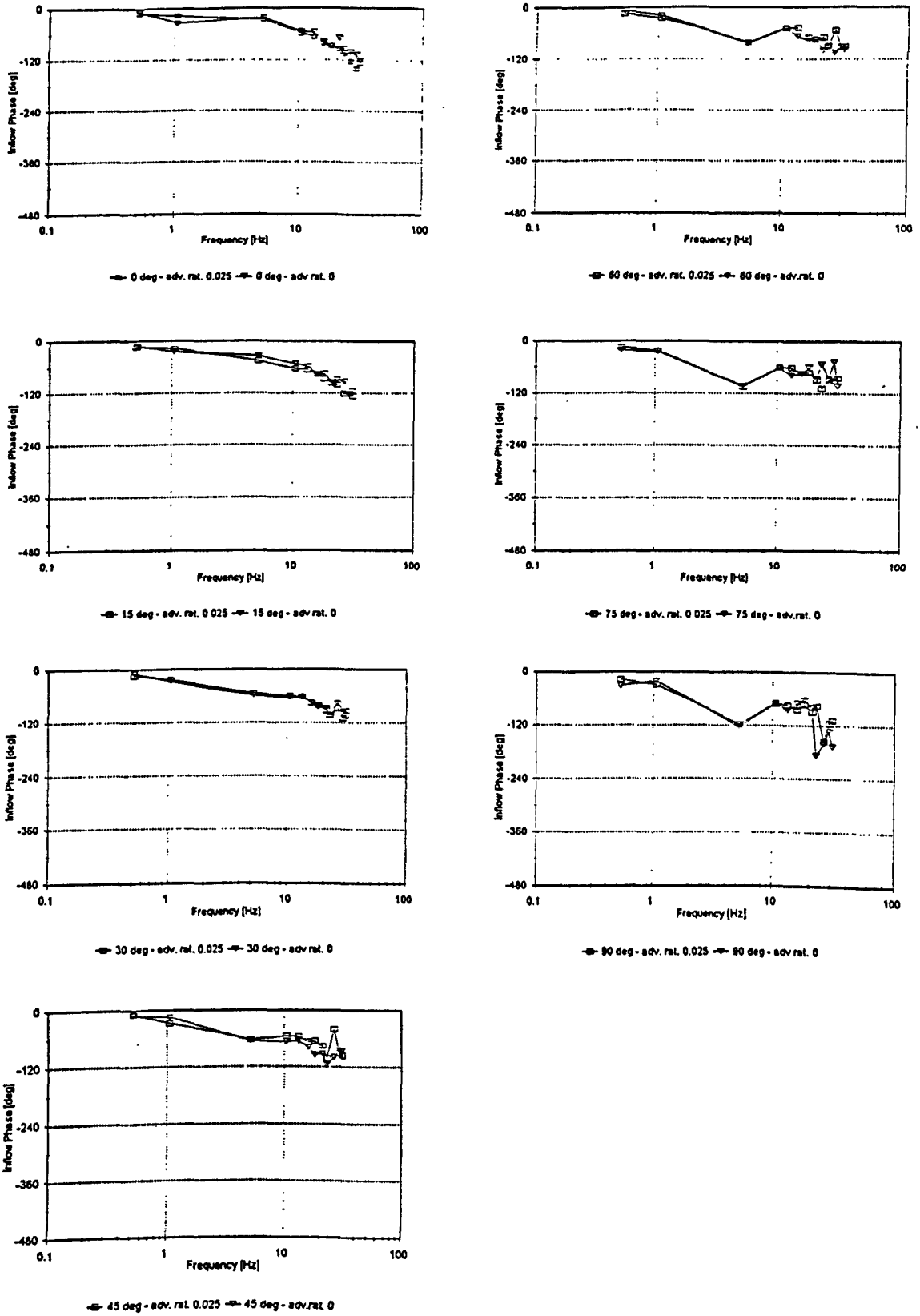

Fig. 6-10 Inflow Phase Response at various Azimuth Stations - LDA
(1200 rpm, LDA 0.10m below, 57% R, 0 and 0.025 adv. rat.)

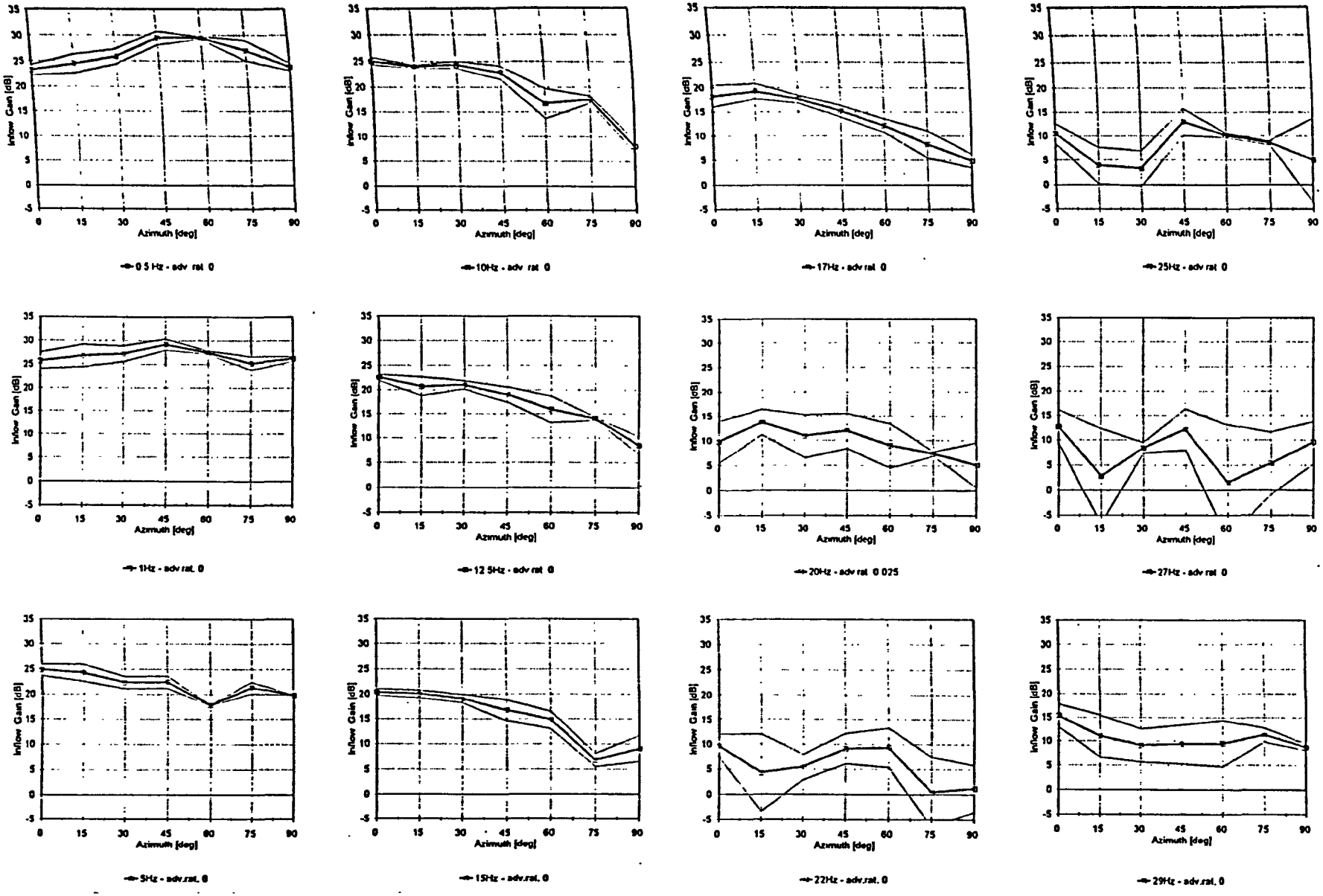

Fig. 6-11 Azimuthal Variation of the Inflow Gain at a Radial Station of 57% R - Hot Wire
(1200 rpm, Hot Wire 0.15m below, 0 and 0.025 adv. rat., Cyclic Excitation)

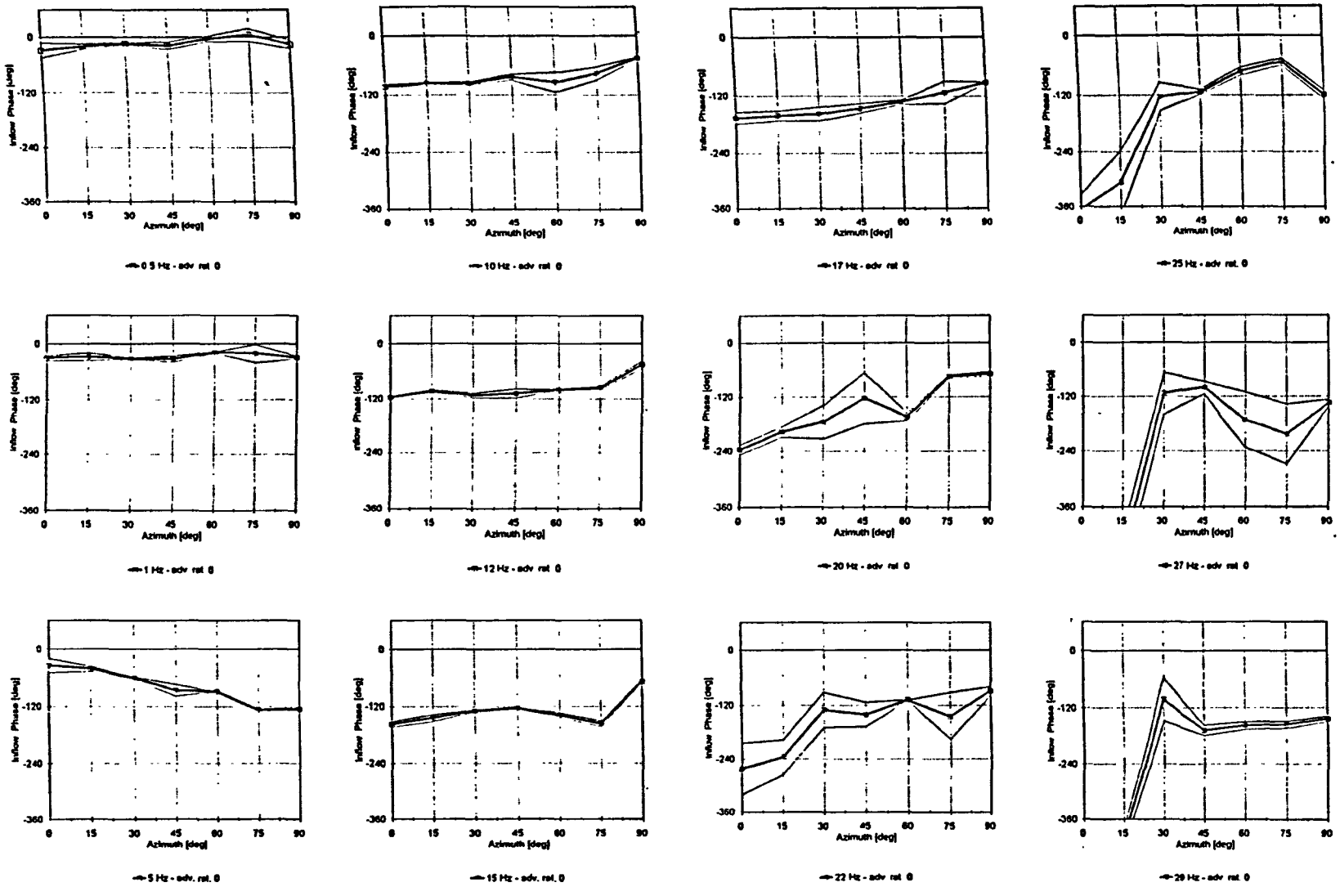

Fig. 6-12 Azimuthal Induced Flow Phase Variation at one Radial Station of 57% R - Hot Wire
(1200 rpm, Hot Wire 0.15m below, 0 and 0.025 adv. rat., Cyclic Excitation)

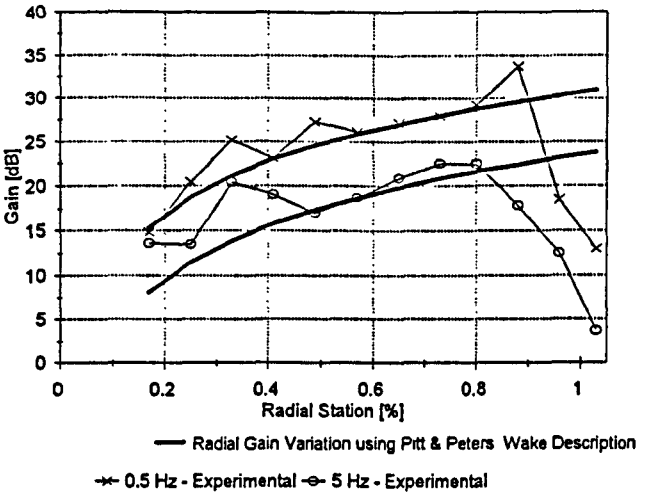

Fig. 6-13 Radial Variation of Inflow Gain compared to the Pitt & Peters Wake Description
(1200 rpm, Hot Wire 0.15m below, 0 adv. rat., 90 deg. Azimuth, Cyclic Excitation)

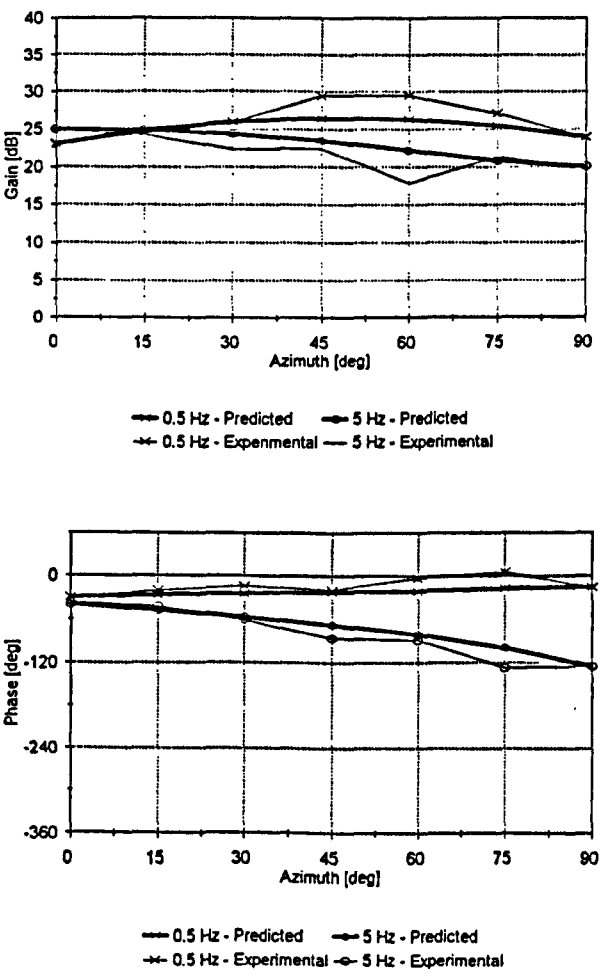

Fig. 6-14 Azimuthal Change of the Inflow Phase compared with the Pitt & Peters Wake Description
(1200 rpm, Hot Wire 0.15m below, 0 adv. rat., 57% R, Cyclic Excitation)

Chapter 7
Inflow Response using Inferred Aerodynamic Loading

7.1 Introduction

This chapter examines a method for isolating the dynamic induced flow response, so that the inflow model fidelity may be more precisely established. The approach utilises the Pitt and Peters [Pitt 1980] inflow model to relate the induced flow field to the aerodynamic rotor loading.

In Chapter 3, coning / inflow models were developed which linked the rotor coning and inflow response to the collective input of the rotor. An aerodynamic model was used to obtain the aerodynamic loads acting on the rotor for a given blade root pitch. From the aerodynamic loading the inflow and blade response can be found, which in turn affect the aerodynamics of the blade and hence the blade loading. This illustrates the closed loop nature of the inflow response, which is shown in the block diagram below.

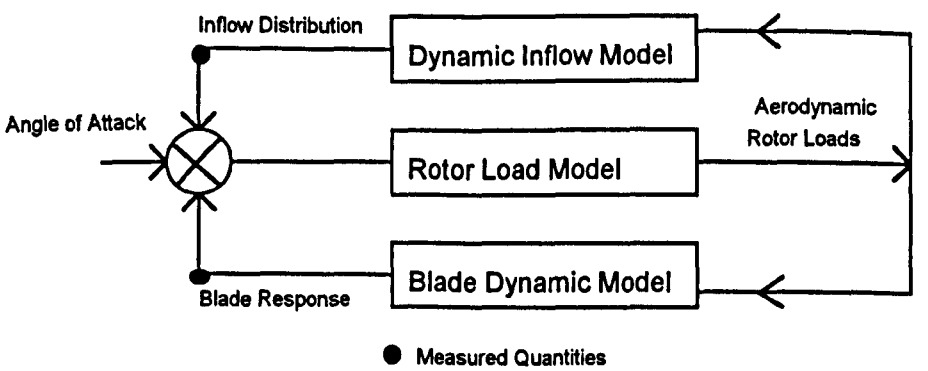

The area of greatest uncertainty is the rotor load model which relates the flow angle of attack at the blade to the *aerodynamic* loads, which also depend on the blade flapping and induced flow response. Unfortunately unless a pressure instrumented blade is used, the aerodynamic loads are not easily measured, as the total hub loads will have contributions both from the aerodynamic loads and the blade dynamics.

In this chapter the aerodynamic loading will be estimated from the blade response, as the relationship between the blade response and aerodynamic loading is well defined in the literature [Johnson 1980, Chen & Hindson 1987, Chen 1980], as long as the geometric and material properties of the blade are known. Once the aerodynamic moment has been established the inflow model is used to provide predictions of the dynamic induced velocity response and these are compared with experimental measurements. The dynamic inflow model is given by Pitt and Peters, and is the link in the model which will be examined.

7.2 Theoretical Basis

7.2.1 Dynamic Inflow Model

The Pitt/Peters Dynamic Inflow model relates the degrees of freedom which describe the inflow distribution perturbations to the aerodynamic loading on the rotor. In this open loop model the aerodynamic thrust and pitch and roll moments acting on the rotor are directly related to the inflow degrees of freedom by the L and M matrices defined by Pitt and Peters [Pitt & Peters 1980]. The model is shown below using the Pitt and Peters notation.

$$[\mathrm{M}]\begin{Bmatrix}\dot{\lambda}_0\\ \dot{\lambda}_s\\ \dot{\lambda}_c\end{Bmatrix} + [L]^{-1}\begin{Bmatrix}\lambda_0\\ \lambda_s\\ \lambda_c\end{Bmatrix} = \begin{Bmatrix}C_T\\ C_L\\ C_M\end{Bmatrix}_{aero} \qquad (7\text{-}1a,\ 1\text{-}1)$$

The time derivatives are with respect to non-dimensional time $\frac{d}{d\psi}$. The aerodynamic perturbation in roll moment in the Pitt and Peters model is C_L, which is positive for more aerodynamic loading on the left side of the rotor. Similarly C_M is the aerodynamic pitching moment defined as positive when there is more aerodynamic lift on the forward section of the rotor disc.

For the hover case where $\alpha = \frac{\pi}{2}$, this reduces the Pitt and Peters model developed in Chapter 1 to the following:

$$\begin{bmatrix} M_{11} & 0 & 0 \\ 0 & M_{22} & 0 \\ 0 & 0 & M_{33} \end{bmatrix} \begin{Bmatrix} \dot{\lambda}_0 \\ \dot{\lambda}_s \\ \dot{\lambda}_c \end{Bmatrix} + V \begin{bmatrix} 2 & 0 & 0 \\ 0 & -0.5 & 0 \\ 0 & 0 & -0.5 \end{bmatrix} \begin{Bmatrix} \lambda_0 \\ \lambda_s \\ \lambda_c \end{Bmatrix} = \begin{Bmatrix} C_T \\ C_L \\ C_M \end{Bmatrix}_{aero}. \qquad (7\text{-}2)$$

$$V = 2\lambda_m$$

Now, perturbations in thrust for example will cause perturbations in only the uniform inflow degree of freedom as both L and M matrices are diagonal and C_T, C_L, C_M are un-coupled.

7.2.2 Blade Flapping Equation

The small perturbation flapping equation for a single rotor blade in the rotating frame, for a rotor with an offset hinge and hinge restraint to model the hingeless rotor, is developed in Appendix F. It is derived by considering moments acting on the blade about the assumed offset hinge.

inertial centrifugal aerodynamic

$$\int_e^R \eta(r-e)m\mathrm{d}r\ddot{\beta} + \int_e^R \eta r m dr\beta\Omega^2\mathrm{d}r + K_\beta\beta = \int_e^R (r-e)F_z\mathrm{d}r \qquad (7\text{-}3)$$

$$\int_e^R R\frac{r-e}{R-e}(r-e)m\mathrm{d}r\ddot{\beta} + \int_e^R R\frac{r-e}{R-e} r m\mathrm{d}r\beta\Omega^2 + K_\beta\beta = \int_e^R (r-e)F_z\mathrm{d}r \qquad (7\text{-}4)$$

The equations above thus relate the aerodynamic moment due to a single blade to the flapping angles, in the rotating frame. The moment due to the blade mass has been ignored as it is a constant term and does not affect the small perturbation equations, a similar argument applies to the flapping pre-cone term. The superscript *m* indicates individual blade quantities.

$$A(m,e)\ddot{\beta}^m + B(m,e)\beta^m\Omega^2 + K_\beta\beta^m = M_{aero}{}^m. \qquad (7\text{-}5)$$

For comparison the inclusion of arbitrary 'structural' damping in the blade equation will also be considered as follows:

$$\underline{A(m,e)\ddot{\beta}^m + D\dot{\beta}^m + B(m,e)\beta^m\Omega^2 + K_\beta\beta^m = M_{aero}{}^m} \qquad (7\text{-}6)$$

The next step is to transform the above equation from the rotating to the non-rotating frame. This is discussed in Appendix G, and only the results are quoted here. The conversion involves the following new non-rotating degrees of freedom which are defined as:

$$\beta_0 = \frac{1}{4}\sum_{m=1}^{4}\beta^m,\ \beta_c = \frac{2}{4}\sum_{m=1}^{4}\beta^m \cos\psi_m,\ \beta_s = \frac{2}{4}\sum_{m=1}^{4}\beta^m \sin\psi_m \quad . \tag{7-7}$$

The linear mapping between the rotating and non-rotating system is given by:

$$\beta^m = \beta_0 + \beta_c \cos\psi_m + \beta_s \sin\psi_m. \tag{7-8}$$

In this mapping $\beta_0, \beta_c, \beta_s$ can be interpreted as the coning and longitudinal and lateral TPP tilt degrees of freedom respectively, which are functions of time. A similar mapping can be defined for the root moment of an individual blade, i.e.

$$M_{aero}{}^m = M_{aero0} + M_{aero_c} \cos\psi_m + M_{aero_s} \sin\psi_m, \tag{7-9}$$

with the following degrees of freedom:

$$\frac{1}{4}\sum_{m=1}^{4}\left(M_{aero}{}^m\right) = M_{aero},\ \frac{2}{4}\sum_{m=1}^{4}\left(M_{aero}{}^m\right)\cos\psi_m = M_{aero_c},\ \frac{2}{4}\sum_{m=1}^{4}\left(M_{aero}{}^m\right)\sin\psi_m = M_{aero_s}. \tag{7-10}$$

Now, expressions need to be found which relate the summation of time derivatives ($\frac{1}{4}\sum_{m=1}^{4}\left(\ddot{\beta}^m\right)\sin\psi_m$ etc.) to the newly defined degrees of freedom and these are [Appendix G]:

$$\begin{gathered}\frac{1}{4}\sum_{m=1}^{4}\dot{\beta}^m = \dot{\beta}_0; \\ \frac{2}{4}\sum_{m=1}^{4}\dot{\beta}^m \cos\psi_m = \dot{\beta}_c + \Omega\beta_s;\ \ \frac{2}{4}\sum_{m=1}^{4}\dot{\beta}^m \sin\psi_m = \dot{\beta}_s - \Omega\beta_c;\end{gathered} \tag{7-11}$$

$$\begin{gathered}\frac{1}{4}\sum_{m=1}^{4}\ddot{\beta}^m = \ddot{\beta}_0; \\ \frac{2}{4}\sum_{m=1}^{4}\ddot{\beta}^m \cos\psi_m = \ddot{\beta}_c + 2\Omega\dot{\beta}_s - \Omega^2\beta_c + \dot{\Omega}\beta_s;\ \ \frac{2}{4}\sum_{m=1}^{4}\ddot{\beta}^m \sin\psi_m = \ddot{\beta}_s - 2\Omega\dot{\beta}_c - \Omega^2\beta_s - \dot{\Omega}\beta_c\end{gathered} \quad . \tag{7-12}$$

The conversion from rotating to non-rotating frame has added centrifugal and Coriolis terms [Johnson 1980]. The equations which describe the flapping behaviour of a rotor in the non-rotating frame are given below:

$$A\ddot{\beta}_0 + B\Omega^2\beta_0 + K_\beta\beta_0 = \frac{1}{4}\sum_{m=1}^{4}\left(M_{aero}{}^m\right) = M_{aero0} \tag{7-13a}$$

$$A\left(\ddot{\beta}_c + 2\Omega\dot{\beta}_s - \Omega^2\beta_c + \dot{\Omega}\beta_s\right) + B\Omega^2\beta_c + K_\beta\beta_c = \frac{2}{4}\sum_{m=1}^{4}\left(M_{aero}{}^m\right)\cos\psi_m = M_{aero_c} \tag{7-13b}$$

$$A\left(\ddot{\beta}_s - 2\Omega\dot{\beta}_c - \Omega^2\beta_s - \dot{\Omega}\beta_c\right) + B\Omega^2\beta_s + K_\beta\beta_s = \frac{2}{4}\sum_{m=1}^{4}\left(M_{aero}{}^m\right)\sin\psi_m = M_{aero_s} \tag{7-13c}$$

or including the damping of Equation (7-6), give:

$$A\ddot{\beta}_0 + D\dot{\beta}_0 + B\Omega^2\beta_0 + K_\beta\beta_0 = \frac{1}{4}\sum_{m=1}^{4}\left(M_{aero}{}^m\right) = M_{aero_0} \tag{7-14a}$$

$$A\left(\ddot{\beta}_c + 2\Omega\dot{\beta}_s - \Omega^2\beta_c + \dot{\Omega}\beta_s\right) + D\left(\dot{\beta}_c + \Omega\beta_s\right) + B\Omega^2\beta_c + K_\beta\beta_c = \frac{2}{4}\sum_{m=1}^{4}\left(M_{aero}{}^m\right)\cos\psi_m = M_{aero_c} \tag{7-14b}$$

$$A\left(\ddot{\beta}_s - 2\Omega\dot{\beta}_c - \Omega^2\beta_s - \dot{\Omega}\beta_c\right) + D\left(\dot{\beta}_s - \Omega\beta_c\right) + B\Omega^2\beta_s + K_\beta\beta_s = \frac{2}{4}\sum_{m=1}^{4}\left(M_{aero}{}^m\right)\sin\psi_m = M_{aero_s}. \tag{7-14c}$$

7.2.3 Aerodynamic Loads

These are expressions which relate the flapping response, or the TPP tilt degrees of freedom (β_0, β_c, β_s), in the non-rotating frame to the non-rotating aerodynamic loads.

The aerodynamic moment in the rolling direction (positive for increased lift on the advancing side), is defined as,

$$M_{Roll} = \sum_{m=1}^{N} M_{aero}^{m}\sin\psi^m = 2M_{aero_s}. \tag{7-15}$$

Similarly the aerodynamic moment in the pitching direction (positive increased lift on the nose), is given by:

$$M_{Pitch} = -\sum_{1}^{N} M_{aero}^{m}\cos\psi^m = -2M_{aero_c}. \tag{7-16}$$

A problem remains with M_{aero_0}, this is the 'collective' aerodynamic moment. To verify the Pitt/ Peters inflow model this needs to be converted to a thrust coefficient. As the exact rotor loading is not known, there is no way of finding the *exact* thrust from M_{aero_0}.

Returning to the definition of $M_{aero}^{m} = \int_{e}^{R}(r-e)F_z dr$, the integral $\int_{e}^{R}(F_z)dr$ which represents the aerodynamic thrust on the rotor, needs to be found. Although the aerodynamic loading on the rotor will depend on factors such as the blade pitch setting, the shape of the loading should be the same for a wide range of operating conditions. In fact, this is an assumption which is also made in the Pitt and Peters [Pitt & Peters 1983] model derivation. A loading distribution whose shape is independent of the loading condition is assumed. It is suggested that the loading over the span of the rotor blade is given by the function [Pitt & Peters 1984]

$$p_u - p_0 / \rho V^2 C_T \propto \sqrt{1-\left(\frac{r}{R}\right)^2} \tag{7-17}$$

This result is useful because it suggests that the loading over the blade span has the same shape for various flight conditions, only differing in magnitude. We can thus use this to solve the integral above using the following assumptions from first principles:

$$F_Z = \text{const}\sqrt{1-\left(\frac{r}{R}\right)^2}\ ,\ M^m_{aero} = \int_e^R (r-e)F_Z dr\ ,\ T^m_{aero} = \int_e^R F_Z dr \tag{7-18a}$$

$$M^m_{aero} = T^m_{aero} * \bar{r} \text{ and hence } \bar{r} = \frac{\int_e^R (r-e)F_Z dr}{\int_e^R F_Z dr} \tag{7-18b}$$

The value of $\bar{r}$ is independent of the magnitude of the aerodynamic loading function. The above integrals were solved numerically for a rotor radius of 0.775 m and a hinge offset of 21%R and $\bar{r}$ found to be 0.28m.

Thus we can now have $T^m_{aero} = \frac{M^m_{aero}}{\bar{r}}$ or in the non- rotating frame,

$$T_{aero} = \sum_{m=1}^{4} \frac{M^m_{aero}}{\bar{r}} = \frac{1}{\bar{r}} \sum_{m=1}^{4} \left(M_{aero_0} + M_{aero_c} \cos\psi^m + M_{aero_s} \sin\psi^m \right) = \frac{4}{\bar{r}} M_{aero_0} \tag{7-19}$$

$$A\ddot{\beta}_0 + D\dot{\beta}_0 + B\Omega^2\beta_0 + K_\beta\beta_0 = M_{aero_0} \tag{7-20a}$$

$$A\left(\ddot{\beta}_c + 2\Omega\dot{\beta}_s - \Omega^2\beta_c - \dot{\Omega}\beta_s\right) + D\left(\dot{\beta}_c - \Omega\beta_s\right) + B\Omega^2\beta_c + K_\beta\beta_c = M_{aero_c} \tag{7-20b}$$

$$A\left(\ddot{\beta}_s - 2\Omega\dot{\beta}_c - \Omega^2\beta_s - \dot{\Omega}\beta_c\right) + D\left(\dot{\beta}_s - \Omega\beta_c\right) + B\Omega^2\beta_s + K_\beta\beta_s = M_{aero_s}. \tag{7-20c}$$

These can be converted to thrust and pitch/roll coefficients by dividing by $\rho A(\Omega R)^2$ and $\rho AR(\Omega R)^2$ for the thrust and pitch respectively.

The final step is to apply these equations to the experimental data to obtain the aerodynamic thrust and pitch/roll coefficients . A possible approach is to take the real time flapping degrees of freedom and their derivatives and apply the above equations to obtain the time response of the thrust and pitch/roll coefficients. Such a method however would rely on noise-free

flapping measurements. This is certainly not the case and the practical problems associated with obtaining good estimates of flapping derivatives are considerable.

A state observer or Kalman filter could be used to reconstruct the missing states from the available measurements. However, the processed flapping frequency response data have been shown to be of very high quality and therefore a frequency-domain based approach is proposed. Thus, the above equations need to be reformulated in the frequency domain. It is assumed that changes in rotor speed are small $(\dot{\Omega}=0)$. This assumption is justified by the results of Chapter 4. Taking Laplace transforms gives:

$$\beta_0 \frac{4}{\bar{r}}\left(As^2+Ds+B\Omega^2+K_\beta\right)=T_{aero_0} \tag{7-21a}$$

$$-2\left[\beta_c\left(As^2+Ds-A\Omega^2+B\Omega^2+K_\beta\right)+\beta_s(2A\Omega s+D\Omega)\right]=M_{pitch} \tag{7-21b}$$

$$2\left[\beta_s\left(As^2+Ds-A\Omega^2+B\Omega^2+K_\beta\right)-\beta_c(2A\Omega s+D\Omega)\right]=M_{roll}. \tag{7-21c}$$

The only problem left is to find suitable values for the variables in the above *transfer function.* The parameters A, B, $K\beta$ and $\bar{r}$ are all dependent on the location of the offset hinge and spring stiffness used to model the rigid hub. A check on the correct combination of the hinge offset and spring stiffness can be made by comparing the experimental coning resonance frequency with that predicted by a particular hinge-spring combination.

Johnson suggests that a suitable position for the offset hinge can be found from the flapping mode shape.[Johnson 1980] $\varepsilon=1-y_{\eta(0.75)}$, i.e. from the slope at the 75 % radial station. Using the mode shape for the first flapping mode of the rotating blade, as in Appendix H, this gives an equivalent offset hinge at 26 % R.

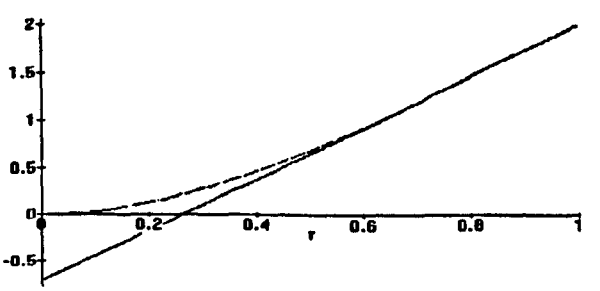

Assuming a spring stiffness of zero initially this gives a coning frequency ratio [Appendix F] of 1.23:

Nominal rpm	1000	1200	1500
Rotational Speed Ω [Hz]	16.7	20.0	25.0
Coning Resonance [Hz]	19.8	23.6	29.4
Coning Frequency Ratio f_r	1.18	1.18	1.18

Table 7-1 Experimentally Determined Coning Resonance Frequencies

From the above table it can be seen that this flap frequency ratio is higher than that found experimentally. Either a negative spring stiffness K_β could be used, which is difficult to justify physically, or the hinge offset reduced somewhat. The fact that the above method overestimates the location of the offset hinge is however understandable. The mode shapes found in Appendix H are only approximate and derived on the assumption of a non-rotating blade. Accordingly, the hinge offset is reduced to 21% which gives a flap frequency ratio of 1.18, to match the experimental results.

Now the constants A and B can be evaluated with a hinge offset of 21%.

$$A = \int_e^R R\frac{r-e}{R-e}(r-e)mdr = 0.02346 \tag{7-22}$$

$$B = \int_e^R R\frac{r-e}{R-e}rmdr = 0.03288 \tag{7-23}$$

7.3 Collective Rotor Excitation

7.3.1 Hover Case

The simplest case to consider is that of the rotor in simulated hover. Restricting excitation to the rotor to consider collective only, results in zero pitch and roll moments. Equation (7-21) thus reduces to:

$$\beta_0 \frac{4}{\bar{r}}\left(As^2 + Ds + B\Omega^2 + K_\beta\right) = T_{aero} \tag{7-24}$$

$$\frac{T_{aero}}{\rho(\pi R^2)(\Omega R)^2} = C_{T_{aero}}. \tag{7-25}$$

From the Pitt/Peters dynamic inflow model configured for the hover case the following transfer function can be derived.

$$C_{T_{aero}} = \left[\frac{M_{11}}{\Omega}s + 4\lambda_m\right]\lambda \text{ or } \lambda = \frac{C_{T_{aero}}}{\frac{M_{11}}{\Omega}s + 4\lambda_m} \tag{7-26}$$

Note that the apparent mass factor has been divided by the rotor speed, because the Pitt and Peters model is formulated w.r.t. non-dimensional time.

The block diagram in Fig. 7-1 shows the relationship between the collective input and the inflow response in transfer function form. Notice that in Fig. 7-1, the relationship between collective pitch and flapping is replaced by the experimentally determined frequency response, thus eliminating modelling errors in the most uncertain part of the coupled rotor / inflow formulation.

From this block diagram it can be noted that for the low frequency or steady state case the parameter B determines the thrust due to coning gain and that the low frequency inflow response is inversely proportional to λ_m.

7.3.2 Critical Review of Assumptions

It is now possible to reconstruct the aerodynamic thrust coefficient frequency response function from the experimentally obtained coning angle frequency response. This can then be applied to the Pitt-Peters dynamic inflow model and the resulting inflow frequency response compared to the measured inflow response. The attraction of this method is that the aerodynamics of the blade need not be modelled and this is where most modelling uncertainty exists. Some of the assumptions made however need to be examined critically before the comparison between the predicted and measured inflow response are made.

Modelling the bending of a rigidly built-in blade through the use of an offset hinge and spring restraint is a simplification, which can be assumed to be valid because it gives the correct fundamental natural flapping frequencies of the blade. This is the frequency limit to which the

above approximation is valid. Even so, this must be the area of most uncertainty. The other approximation is the conversion from moments to equivalent thrust through the use of the $\bar{r}$ parameter. As shown earlier this parameter is found from an approximate blade loading model. This limitation applies to the collective case only.

In Equation (7-18) it is assumed that the aerodynamic thrust produced by the blade is given by $\frac{1}{\bar{r}}\int_{e}^{R}(r-e)F_z dr$. This implies that only the blade section outboard of the assumed offset hinge produces lift. In reality, the section between the root cut-out and the hinge offset will produce a small amount of lift. The root cut-out is at approximately 10% of the blade span and therefore the lift produced over the length of blade between the root cut-out and offset hinge needs to be assessed. Examination of the typical loading over a blade suggests that 8% of the lift is produced in this region and is therefore unaccounted for, and a correction factor of 1.08 (approx. 0.7 dB) is applied to the lift obtained above to take this into account.

7.3.3 Effect of Parameter Variations

It has already been shown that this analysis depends on relatively few parameters, which are derived from physical arguments. In this section the effect of slight variations of the parameters on the predicted inflow response will be examined, before comparisons with the actual experimental results are made. The parameters, which will be varied are the A and B coefficients in Equation (7-21a). These represent respectively the *mass* and *spring* terms in the equation and will have most effect on the response and natural frequency. The value of $\bar{r}$ will not affect the dynamics of the inflow response, only its magnitude.

The approximate structural damping in the flapping equation was found by exciting the blade while it was not rotating and recording the damped response. This is shown in Fig. 7-2 and from it the approximate structural damping of 2.5 % can be determined. Thus the effect of adding structural damping, although small, on the flapping response was also included.

With damping, the equation which gives the relationship between the coning angle and aerodynamic loading is given below, based on Equation (7-21a):

$$\frac{\beta^m}{M^m_{aero}} = \frac{1}{As^2 + Ds + \left(B\Omega^2 + K_\beta\right)}. \tag{7-27}$$

Comparing this with the standard form of a second order system:

$$\frac{1}{s^2 + {}^{D}/_{A}\,s + {}^{\left(B\Omega^2 + K_\beta\right)}/_{A}} \tag{7-28}$$

gives the following expressions for the natural frequency and damping ratio:

$$\omega_n^2 = \frac{B\Omega^2 + K_\beta}{A} = \frac{\text{Spring term}}{\text{Inertial term}} \qquad 2\omega_n\xi = \frac{D}{A} \text{ or } D = \xi 2\omega_n A. \tag{7-29}$$

Using the values of A and B derived in 7-23 (and for $K_\beta = 0$) the coning resonance frequency at 1200 rpm can be found as $\omega_n = \sqrt{\frac{B\Omega^2}{A}} = \sqrt{\frac{0.02346}{0.03288}}\Omega = 1.18\Omega$, which is as expected and provides confidence that the values of A and B were calculated correctly.

The effect of variations of A and B on the predicted inflow response are shown in Fig. 7-3. The left hand graphs show the frequency response of the thrust transfer function (block 2 in Fig. 7-1) and the predicted induced flow response is shown on the right hand side. Firstly the values of A and B were changed individually, producing slightly different coning resonance frequencies and this is shown in Fig. 7-3. The case with no damping is also shown. The table below summarises the 5 test cases.

	A	B	Flap Freq. Ratio	Damping Ratio
1 (Datum)	0.02346	0.03288	1.18	2.5%
2	$1.2*A_{Datum}$	B_{Datum}	1.079	2.5%
3	A_{Datum}	$1.2*B_{Datum}$	1.2956	2.5%
4	A_{Datum}	B_{Datum}	1.18	0%

Table 7-2 Parameter Variations in the Sensitivity Analysis

As can be seen from Fig. 7-3 the predicted thrust and inflow responses are relatively insensitive to the changes in the parameters. The changes in the A and B parameters which are closely related to the flap frequency of the coning mode, cause the gain dip to move slightly either side of 23 Hz. The much larger peak for case 2 is due to one of the data points lying exactly at the minimum of the peak, whereas in the other cases the data points lie just either side of the sharp

trough. As can be seen by looking at the transfer function of the B parameter, this affects the steady state gain, and this can be seen for the case of the largest flap frequency ratio, which has an increase in the low frequency gain of about 1.5 dB. The effect of the no-damping case is most pronounced in the thrust transfer function phase response, causing a phase jump at the coning resonance frequency.

7.3.4 Comparison with Inflow Data

The predicted inflow response can now be compared to the measured dynamic inflow data. It has already been shown that inflow dynamics vary with radial station and this variation is not captured by the simple assumptions of the uniform inflow wake description used in the Pitt and Peters model. In Fig. 7-4a-c the theoretical inflow gain and phase response are compared with the experimental results at 6 radial stations. The lower graphs on each figure show the inflow phase. As the results were taken 0.15m below the rotor, a phase correction, assuming a pure transmission delay has been made, which was shown in Chapter 5 to approximate the axial phase correction at low frequencies. The variation in the average, steady induced velocities with radial station, as shown in Fig. 7-5, have been taken into account in determining the phase differences due to transmission delays. The value of the average induced velocity used in the Pitt and Peters model [Pitt & Peters 1983] was also found from this data as the average between the rotor centre and the 96 % radial station, which is shown as a straight line in Fig. 7-5. This is assumed to be equivalent to the average induced velocity found from momentum theory ($\lambda_m = \sqrt{\frac{C_T}{2}}$), which could not be calculated from the rotor thrust as this was not directly available. In any case, a direct measurement should be more reliable.

The conclusion is that the experimental data obtained at a radial station of 49% or 57 % match the theoretical data best. The gain response of the 49% case matches the model better whereas for the 57% the phase response is closer. The difference in low frequency gain of 2 dB is reasonable considering the approximation of a rigid blade. Away from the tip and inboard blade regions the Pitt and Peters [Pitt & Peters 1983] inflow model provides reasonable predictions of the inflow response given the aerodynamic loading.

The experimental gain tends to reduce earlier at a lower frequency and more sharply than predicted by the model and this suggests that higher order dynamics are involved in the dynamic inflow response, compared to the first order Pitt and Peters model. This lack of fidelity in the model occurs at frequencies which are likely to be of interest in flight mechanics studies.

Further comparisons will use the experimental data at 57%R and this will be the datum.

7.3.5 Effect of Average Induced Velocity & Apparent Mass Factor

The effect of varying the momentum-induced average velocity is shown in the left hand graphs of Fig. 7-6. As already discussed, the average momentum-induced velocity as used in the Pitt and Peters inflow formulation [Pitt & Peters 1983] determines the steady state inflow gain. Reducing the average inflow by 1m/s increases the gain by 1 dB. This shows that the low frequency discrepancy between the theoretical and experimental data could be reduced by adjusting the average momentum-induced velocity.

Considering the radial variation of the dynamic inflow, it might be thought that better results over the whole blade span could be achieved if the momentum-induced velocity were replaced by the actual average induced velocity at that radial station. The velocities obtained experimentally and shown in Fig. 7-5 could be used. This approach however is not used in the derivation of the Pitt and Peters model [Pitt & Peters 1983] which relies on a uniform free stream velocity in its derivation. In any case, it has to be noted that the higher the momentum induced velocity the lower the dynamic inflow response, therefore if the velocities in the radial variation are used - increasing with radial station - then the induced velocity response would decrease with radius, which is not borne out by the experimental results.

Finally the effect of varying the apparent mass factor is considered. This is shown in the right hand graphs of Fig. 7-6. It can be seen that neither increasing nor decreasing the apparent mass factor degrades the correlation. The experimentally induced velocity drops off more

steeply above 10 Hz than predicted by any of the theoretical models. Similarly the phase drops off and recovers earlier than the theoretical data at about 20 Hz.

7.3.6 Conclusions for the Collective Case

The approach which has been developed in this chapter isolates the inflow contribution to the coupled coning inflow dynamics and demonstrates that the Pitt and Peters [Pitt & Peters 1983] formulation provides good correlation between the theoretical and experimental data for the collective case. Although the Pitt and Peters formulation is based upon simplistic wake assumptions, the character of the inflow response is reasonably well captured. The model fails to capture the high 'roll-off' in gain and accompanying phase changes, which may be important in flight mechanics models. Correction of the experimental data for wake transmission type delays further improves the correlation and reinforces the conclusion of Chapter 5 that a transmission-delay correction is appropriate, particularly at frequencies below 15 Hz. The gains and apparent mass factor of 0.84 from the Pitt and Peters [Pitt & Peters 1980] inflow model provide good results.

7.4 Cyclic Rotor Excitation

7.4.1 Hover Condition

Again from the Pitt and Peters model for zero forward speed the following equation is obtained in state-space formulation:

$$\begin{bmatrix} M_{11} & 0 & 0 \\ 0 & M_{22} & 0 \\ 0 & 0 & M_{33} \end{bmatrix} \begin{Bmatrix} \dot{\lambda}_0 \\ \dot{\lambda}_s \\ \dot{\lambda}_c \end{Bmatrix} + V \begin{bmatrix} 2 & 0 & 0 \\ 0 & -0.5 & 0 \\ 0 & 0 & -0.5 \end{bmatrix} \begin{Bmatrix} \lambda_0 \\ \lambda_s \\ \lambda_c \end{Bmatrix} = \begin{Bmatrix} C_T \\ C_L \\ C_M \end{Bmatrix}_{aero} \quad (7\text{-}30)$$

$$V = 2\lambda_m$$

It can be seen that in the hover case the collective, lateral and longitudinal degrees of freedom are not coupled.

From section 7.2.3 and Equations (7-15) and (7-16) the aerodynamic pitch and roll moment coefficients are given by:

$$C_{roll} = \frac{2M_{aero\_s}}{\rho(\pi R^2)(\Omega R)^2 R} = -C_L. \tag{7-31}$$

$$C_{pitch} = \frac{-2M_{aero\_c}}{\rho(\pi R^2)(\Omega R)^2 R} = C_m \tag{7-32}$$

And noting that the aerodynamic rolling moment in the Pitt and Peters model is defined with opposite sign convention, the following can be obtained from Equation (7-30) considering only pure cyclic inputs in the hover case and taking Laplace transforms.

$$M_{22}\dot{\lambda}_s + (-0.5V)\lambda_s = C_{L_{Aero}} = -C_{roll} \text{ from which } \lambda_s = \frac{-C_{roll}}{\frac{M_{22}}{\Omega}s - 2*0.5\lambda_m} \tag{7-33}$$

$$M_{33}\dot{\lambda}_c + (-0.5V)\lambda_c = C_{M_{Aero}} = C_{pitch} \text{ and similarly } \lambda_c = \frac{C_{pitch}}{\frac{M_{33}}{\Omega}s - 2*0.5\lambda_m} \tag{7-34}$$

From the blade flapping Equation (7-14) the relationships between the lateral and longitudinal flapping and the aerodynamic loading are obtained as:

$$\left[\beta_c\left(As^2 - A\Omega^2 + B\Omega^2 + Ds + K_\beta\right) + (2A\Omega s + D\Omega)\beta_s\right] = M_{aero\_c} \tag{7-35}$$

$$\left[\beta_s\left(As^2 - A\Omega^2 + B\Omega^2 + Ds + K_\beta\right) - (2A\Omega s + D\Omega)\beta_c\right] = M_{aero\_s}. \tag{7-36}$$

The assumed inflow distribution from the Pitt and Peter [Pitt & Peters 1980] inflow model is given by $\lambda = \lambda_0 + \lambda_c r\cos\psi + \lambda_s r\sin\psi$, which simplifies to $\lambda = r(\lambda_c\cos\psi + \lambda_s\sin\psi)$ when only cyclic degrees of freedom are considered. The induced flow at any point on the disc u is then obtained by multiplying the non-dimensional induced flow by the tip speed of the rotor, and hence:

$$u = \lambda\Omega R. \tag{7-37}$$

A transfer function block diagram similar to that used for the collective case is shown in Fig. 7-7. The inputs to the system are the frequency responses of the transfer function between the lateral and longitudinal tip path plane response to the cyclic input. The actual cyclic input does

not need to be defined accurately in terms of whether it produces pure lateral or longitudinal responses, as it is only the tip path plane lateral and longitudinal responses which are used to infer the aerodynamic loading and thus the inflow response.

The basic approach follows that of the coning case. All experimental data were gathered at 90 deg azimuth since this was the aerodynamically most clean side of the rotor rig.

The frequency response of the tip path plane to cyclic inputs is shown in Fig. 7-8. The cyclic input gave maximum blade pitch variation at 15 degrees azimuth. The maximum blade response was found to occur 60 degrees later at approximately 75 degrees. The phase lag between application of pitch and response of the blades, for a rotor with hinge offset, is given by Johnson [Johnson 1980] as $\psi = \frac{\pi}{2} - \frac{12}{\gamma}\varepsilon$. The rotor Lock number is approximately 4, and the blade hinge offset is at approximately 21 %, giving a phase lag of 54 degrees. This compares well with the experimentally determined results and confirms that the correct hinge offset was chosen.

The perturbations in cyclic pitch inputs were of 1.4 degrees amplitude at the root and the gains are referenced to this. This excitation causes predominantly lateral flapping (β_{1s}) with some longitudinal flapping (β_{1c}). For the work in this chapter the exact cyclic input is immaterial, as it is the response of the tip path plane which is used to infer the aerodynamic loads, as explained above.

In Fig. 7-8 the left hand graphs show the β_{1c} degree of freedom or the longitudinal tip path plane tilt. The right hand graphs show the gain and phase of the lateral tip path plane tilt degree of freedom (β_{1s}). It can be seen from the figure that as expected the low frequency behaviour of the tip path plane is predominantly a lateral tilt, with β_{1s} being 6 dB larger than β_{1c}. The character of the tip path plane response is very much as would be expected from a hingeless rotor [Johnson 1980]. The phase of the longitudinal responses drops off more rapidly that the lateral response. It has been shown [Johnson 1980] that for the 'direct' response (longitudinal flapping due to longitudinal cyclic input or lateral flapping due to lateral cyclic input) the transfer functions have one zero, whereas the 'cross' response transfer

functions (lateral flapping due to longitudinal pitch inputs, longitudinal flapping due to lateral pitch inputs), have both a low and high frequency zero, with the low frequency zero being much more heavily damped. This explains the earlier drop off in phase of the longitudinal ('cross') response. The reader is referred to a very good discussion on the flapping dynamics of rotors by Johnson [Johnson 1980].

7.4.3 Effect of Parameter Variations

Similar to the approach for the collective case, in the cyclic case the sensitivity of the predicted inflow response to variations in the blade flapping parameters needs to be examined. In the collective case it was shown that the predicted thrust loading and resulting inflow responses were relatively insensitive to variations in the blade parameters A and B and also insensitive to the damping included in the blade flapping formulation.

Fig. 7-9 shows the aerodynamic load coefficients (C_{pitch} and C_{roll}) for the 7 cases outlined in the table below. The values of A and B are the same as for the collective case and they are varied by the same amounts respectively.

Case	A	B	Flap Freq. Ratio	Damping
1 (Datum)	0.0235	0.0328	1.18	2.5%
2	$1.2*A_{Datum}$	B_{Datum}	1.079	2.5%
3	A_{Datum}	$1.2*B_{Datum}$	1.2956	2.5%
4	A_{Datum}	B_{Datum}	1.18	10%
5	$1.2A_{Datum}$	$1.2A_{Datum}$	1.18	2.5%
6	$0.8A_{Datum}$	$0.8A_{Datum}$	1.18	2.5%

Table 7-3 Parameters used in the Cyclic Sensitivity Analysis

Maximum cyclic blade root pitch occurs at an azimuth angle of 15 degrees. Thus most of the aerodynamic loading will be at the back of the rotor disc slightly to the advancing side. The aerodynamic pitching moment coefficient (C_{pitch}) is defined positive for more aerodynamic lift

on the nose, which explains the 180 degree phase lag on the aerodynamic pitching moment frequency response.

Including structural damping of the blade, the steady-state relationship between M_{pitch} and the TPP degrees of freedom becomes $((B-A)\Omega^2)\beta_c + (D\Omega)\beta_s = {}^{-M_{pitch}}/_{I}$. Changes in the parameters A, B and the blade structural damping change the low frequency gain.

The significance of cases 5 and 6 is that changing the parameters A and B by an equal amount does not change the flap frequency ratio whereas changing only one of the parameters does. The cases with the same flap frequency ratio (3 and 4) are not shown in the phase plot as the response is indistinguishable from the datum case.

The steady state relationship between the aerodynamic loading in the rolling direction and the TPP degrees of freedom is given by, $((B-A)\Omega^2)\beta_s - (D\Omega)\beta_c = {}^{M_{roll}}/_{I}$. This is the same as that of the pitching case except for the sign changes and is also shown in Fig. 7-9.

Compared to the collective case, the aerodynamic loading predictions due to cyclic inputs are much more sensitive to parameter changes. This is disappointing as it was hoped that one of the main advantages of this method would lie in the ability to isolate aerodynamic loads from inertial blade dynamics. The sensitivity of the results to structural damping is unfortunate since this is difficult to determine precisely. Although changes in the A and B parameters were considered in the sensitivity analysis, these are also physically related to the flap frequency ratio and this is known with a reasonably high degree of confidence; therefore changes which affect only one of these parameters will be unlikely.

For the datum case, aerodynamic pitching moment gain response at low frequency is lower than the aerodynamic rolling moment response. It has already been shown that with the cyclic input used, it would be predominantly aerodynamic pitching moment, but with some rolling moment, that would be expected. This is contrary to that shown in Fig. 7-9 for the datum case. Only when the damping of the blade is increased to approximately 10% does the aerodynamic pitching moment exceed the rolling moment. Such an increase is difficult to

justify from a physical standpoint and in any case the sensitivity of the results to the parameter variations casts serious doubts upon the validity of this approach.

The sensitivity of the isolated inflow response to the same parameter variations is shown in Fig. 7-10. The left hand graphs show the longitudinal inflow degree of freedom, or the inflow which would be expected at an azimuth position of 0 degrees. In the Pit and Peters model the inflow expected at any point on the rotor disc is given by $u(r,\psi)=(\lambda_c r\cos\psi+\lambda_s r\sin\psi)\Omega R$, where u is the dimensional induced flow which is assumed to vary linearly with radius. In Chapter 6 it was shown that this linear variation of the inflow response with radius is not observed. Therefore, the results which are shown in Fig. 7-10 are the longitudinal and lateral inflow degrees of freedom (λ_c,λ_s) multiplied by the tip speed of the blade, or in other words the expected inflow at 0 and 90 degrees azimuth assuming $r=1$.

Fig. 7-10 shows that the general character of the predicted inflow response is reasonably well retained across the range of parameter variations considered. The induced flow measured at 0 and 90 degrees azimuth positions, obtained from hot-wire and LDA is shown in Fig. 7-11. Reasonable agreement between hot-wire and LDA data exists and the detailed differences are discussed in Chapter 6. Fig. 7-11 also shows the predicted inflow, with the longitudinal frequency response on the left and the lateral on the right. The match between the experimental and theoretical inflow data is very poor. Better correlation between the experimental and theoretical results is obtained for the phase response.

Altogether the results for the cyclic case are very disappointing. It is very difficult to identify whether the differences between the predicted and experimental results are due to deficiencies in the inflow model, the wake representation or the inference of the aerodynamic loads.

The general approach that has been outlined for the cyclic case failed to consolidate the Pitt and Peters inflow model cyclic degrees of freedom with experimental data. However, it is believed that it represents a valid method and should be investigated further. This is discussed in Chapter 8 and should include a close look at modelling the semi-rigid rigid hub in a more

general way, avoiding the use of the offset hinge approximation, or using an articulated rotor which would be easier to model.

7.5 Conclusions

For the collective case good agreement between the predicted inflow response using the Pitt and Peters [Pitt & Peters 1989] dynamic inflow model and aerodynamic loading inferred from blade dynamics was found. The gains in the dynamic inflow model are appropriate and the apparent mass factor, which gives good correlation, is 0.84. The experimental data obtained at a radial station of 57%R seem to give a good approximation to the response of the model, which assumes a radially uniform inflow distribution. It seems that although the wake description of the Pitt and Peters inflow model is simplistic the model itself does capture important inflow dynamics in the 'collective' mode. There is evidence that a higher order inflow representation, would improve model fidelity

For the cyclic case it was found that the aerodynamic loading prediction was very sensitive to the blade dynamic model, and attempts to isolate the cyclic inflow degrees of freedom failed to align the theoretical predictions with experimental data.

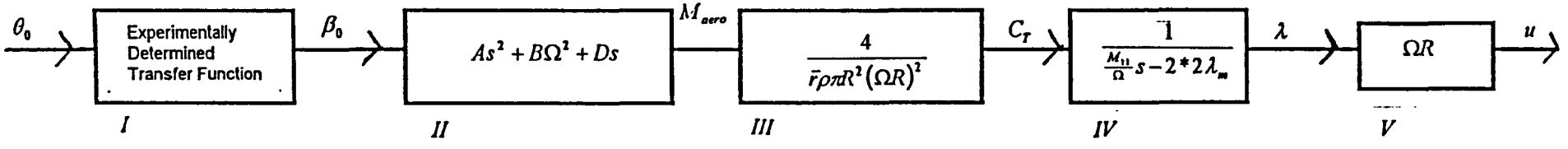

Fig. 7-1 Block Diagram of the Induced Velocity Response Inferred from Flapping Data - Collective Case

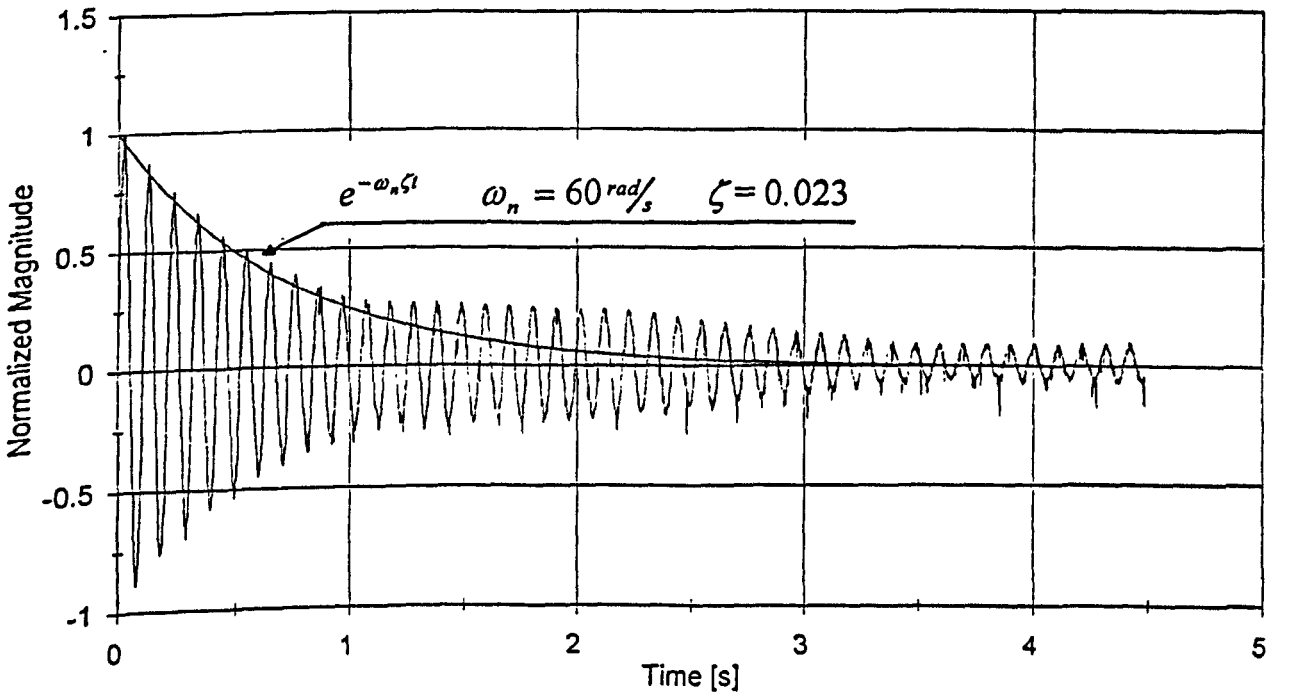

Fig. 7-2 Non-Rotating Blade Natural Frequency and Damping Ratio
(1200 rpm, Max. Blade Pitch at 15 deg.)

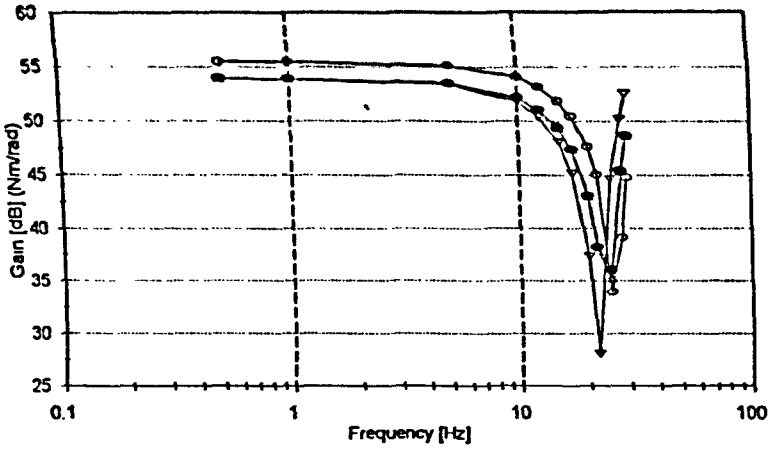

Thrust Transfer Function

	A	B	fr.	Damping
1 (Datum)	0.02346	0.03268	1.18	2.5%
2	$1.2*A_{Datum}$	B_{Datum}	1.079	2.5%
3	A_{Datum}	$1.2*B_{Datum}$	1.2958	2.5%
4	A_{Datum}	B_{Datum}	1.18	20%

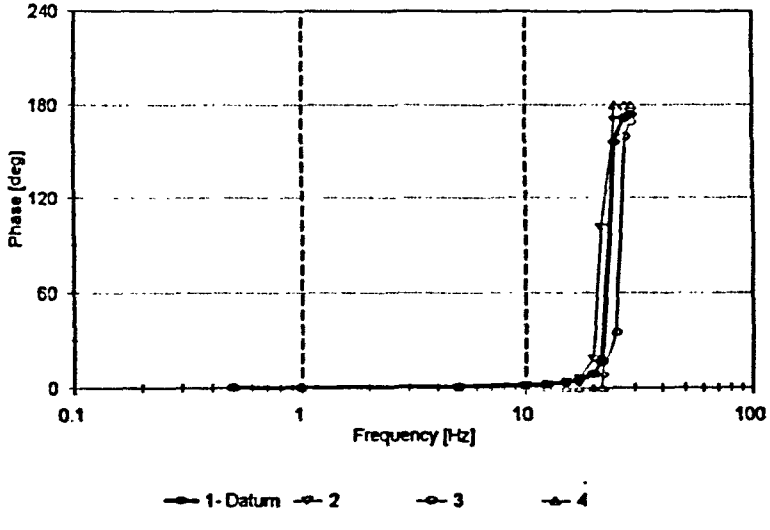

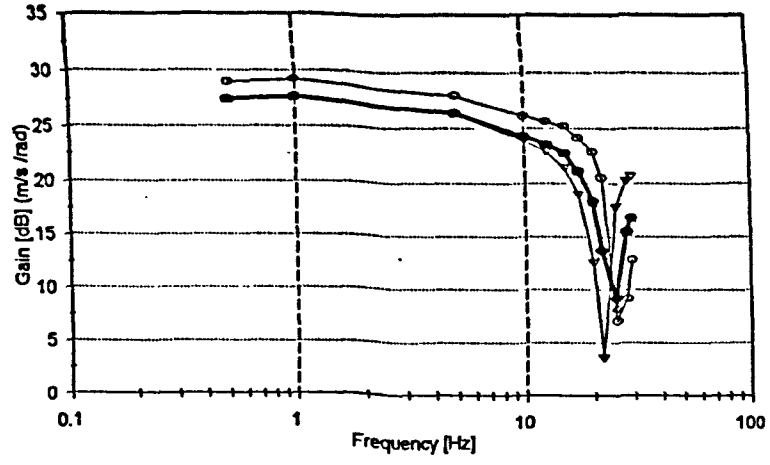

Predicted Inflow Response

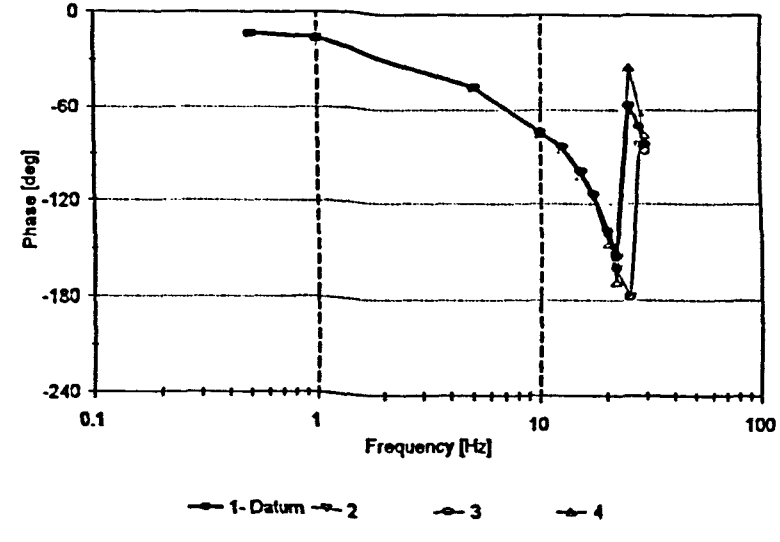

Fig. 7-3 Sensitivity of Predicted Inflow Response to Parameter Variations

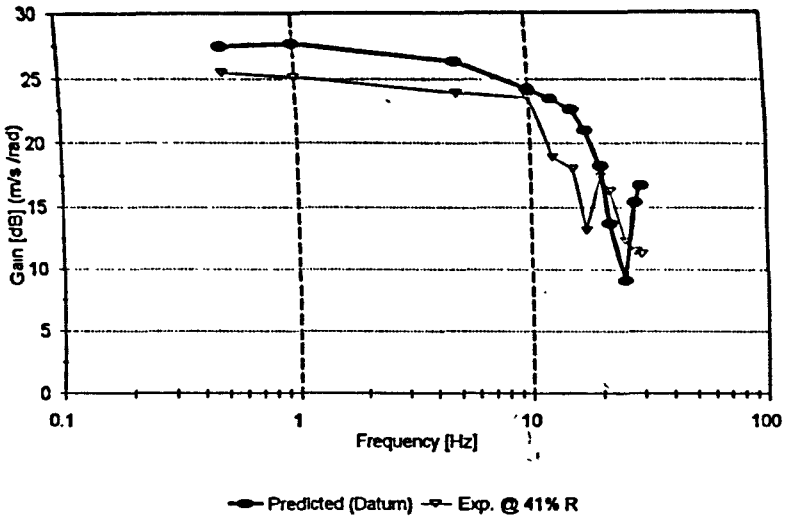

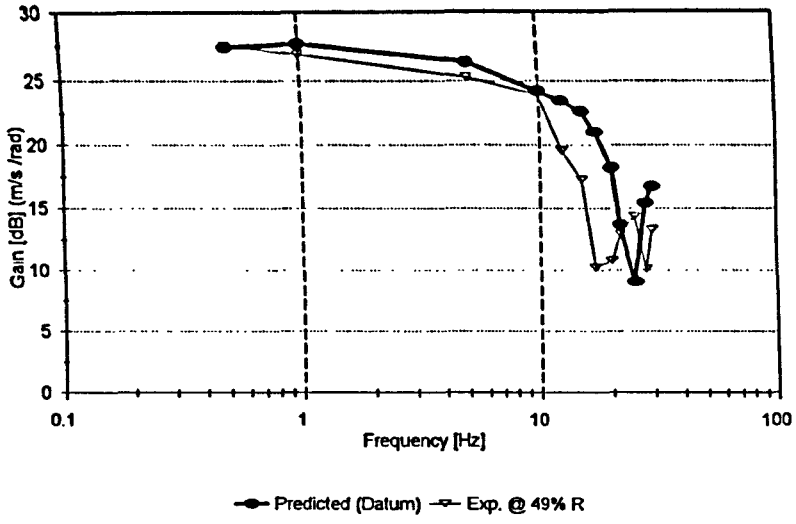

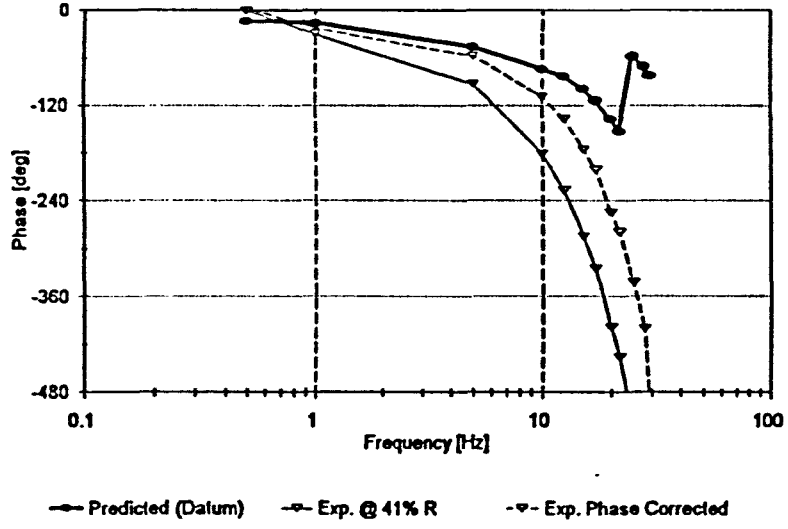

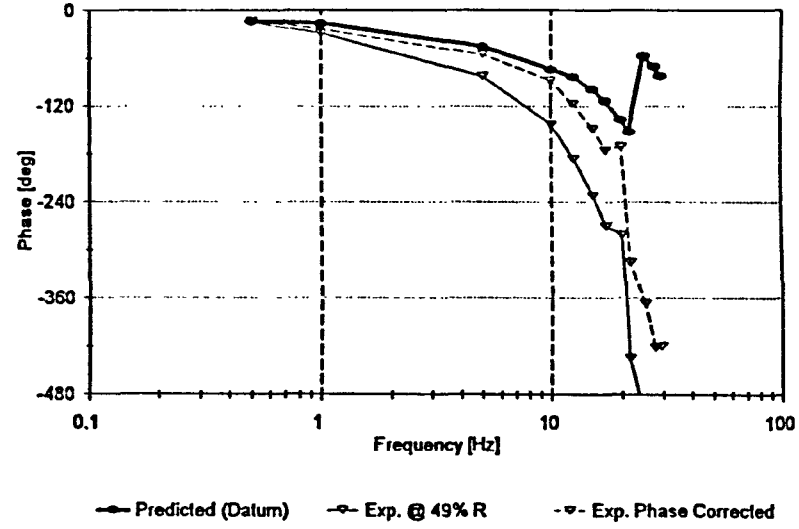

Fig. 7-4a Comparison of Predicted and Measured Inflow, R=41% & 49%
(1200 rpm, Hot Wire 0.15m below)

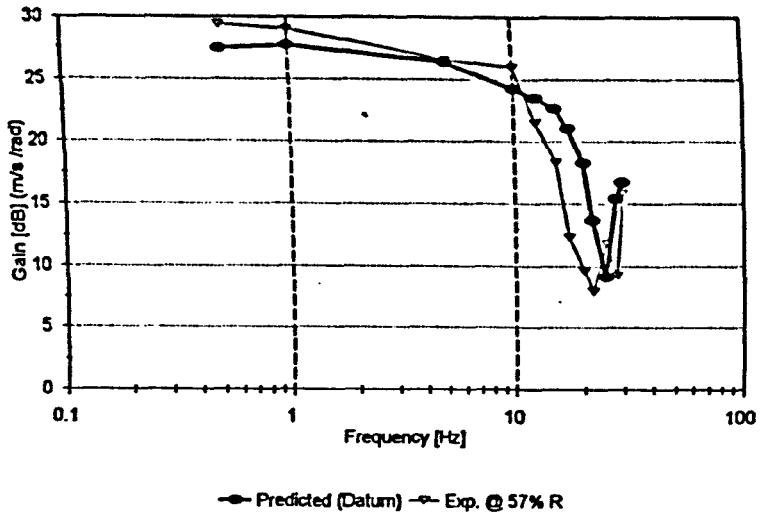

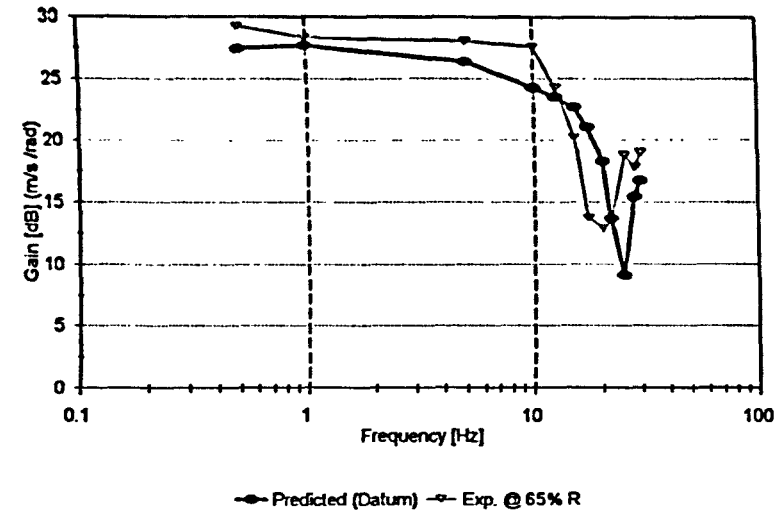

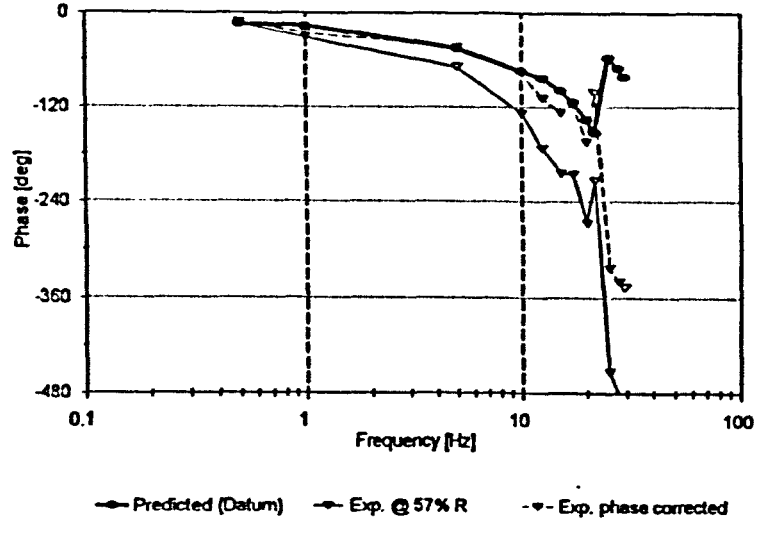

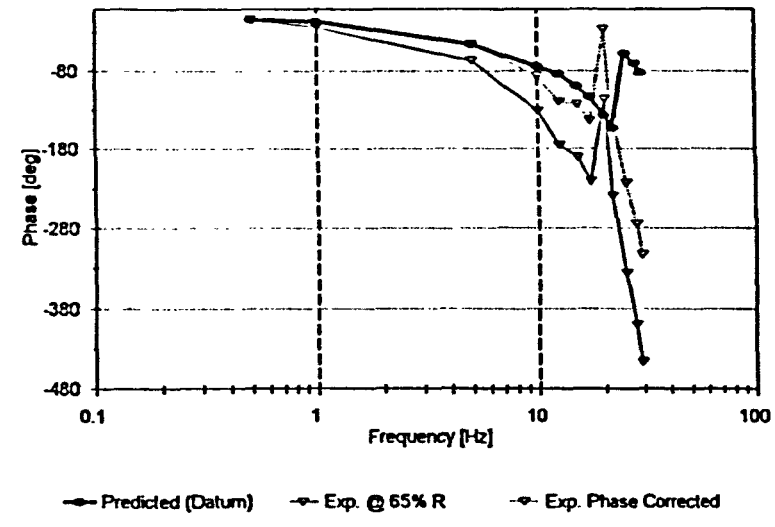

Fig. 7-4b

Comparison of Predicted and Measured Inflow, R=57% & 65%
(1200 rpm, Hot Wire 0.15m below)

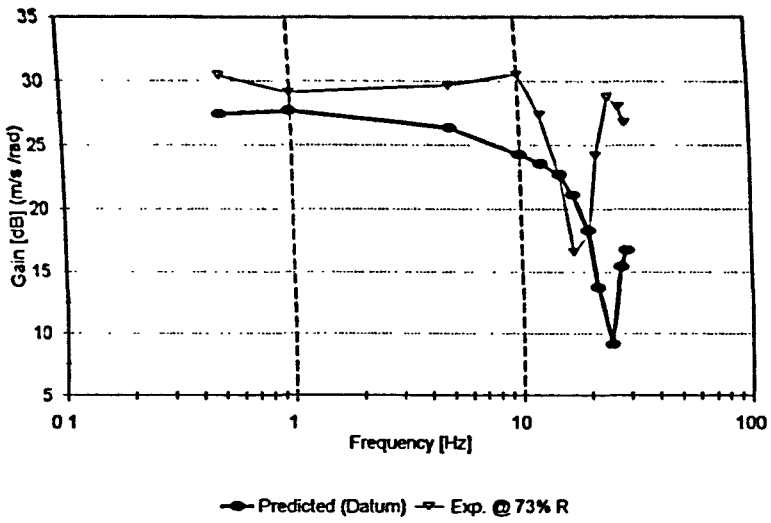

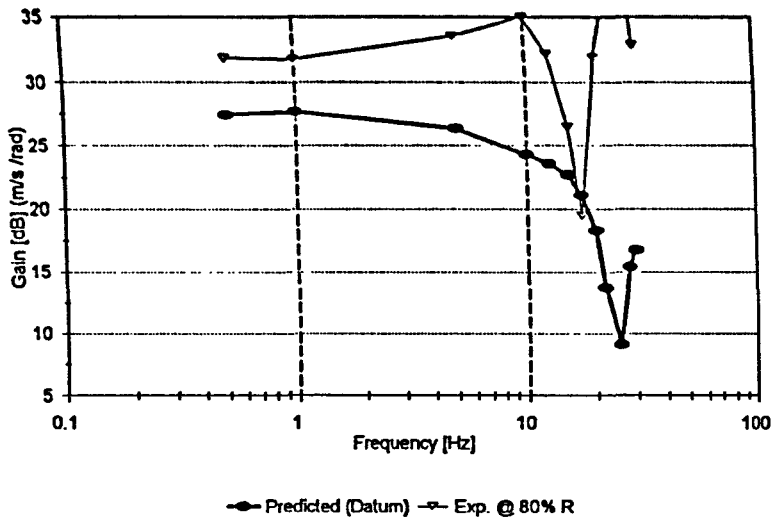

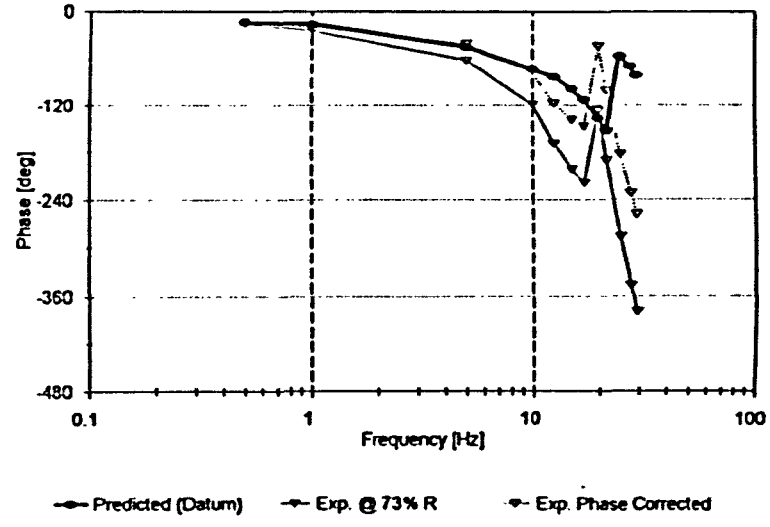

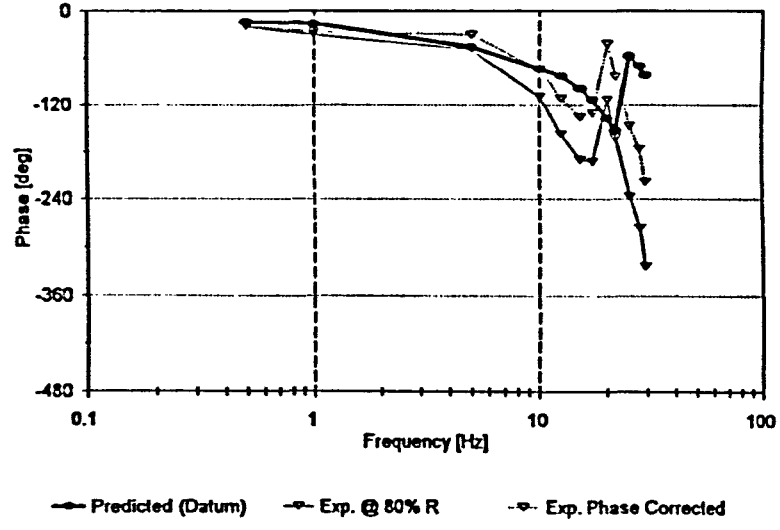

Fig. 7-4c

Comparison of Predicted and Measured Inflow, R=73% & 80%
(1200 rpm, Hot Wire 0.15m below)

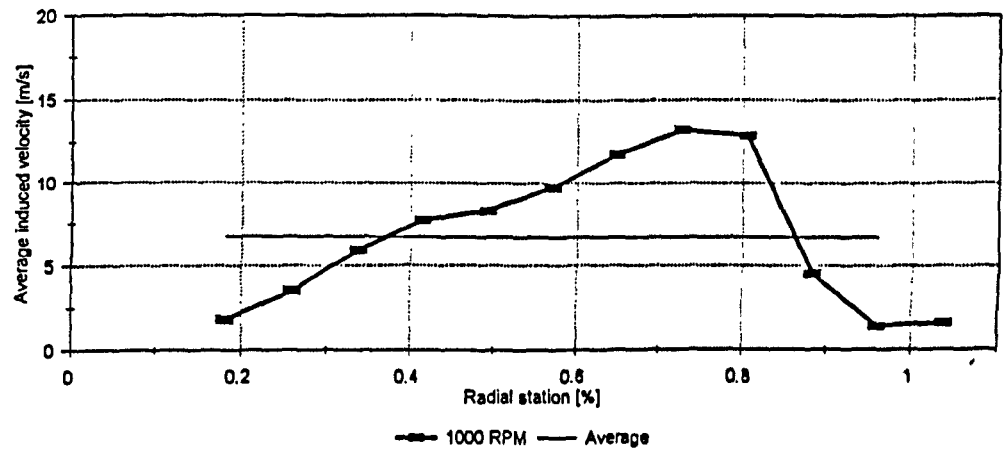

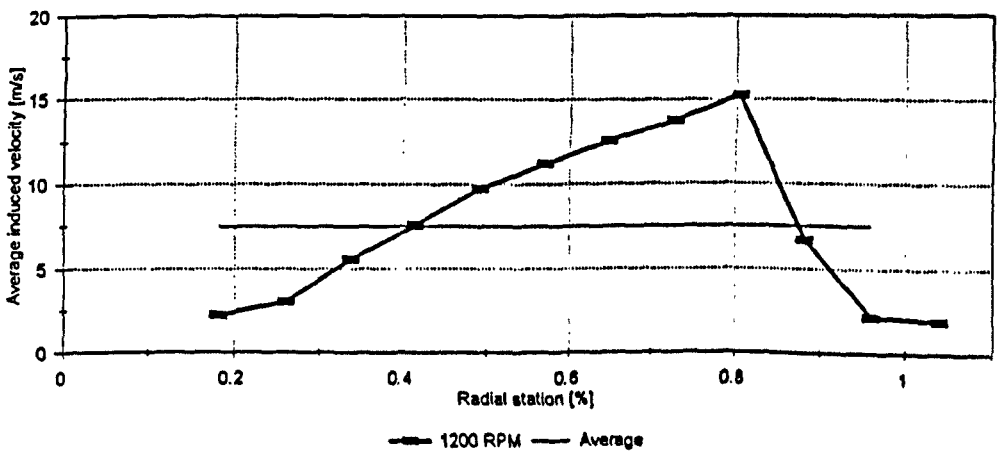

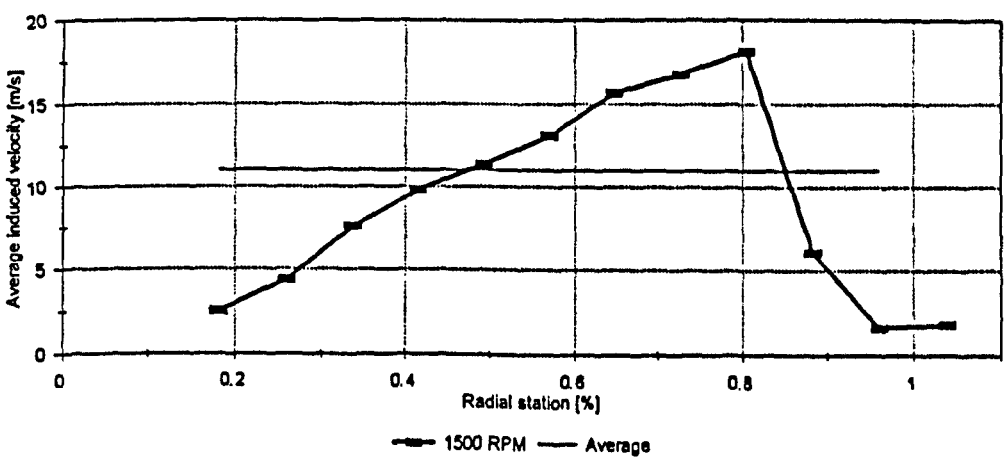

Fig. 7-5 Radial Variation of Average Induced Velocity for three Rotor Speeds
(1200 rpm, Hot Wire 0.15m below Rotor)

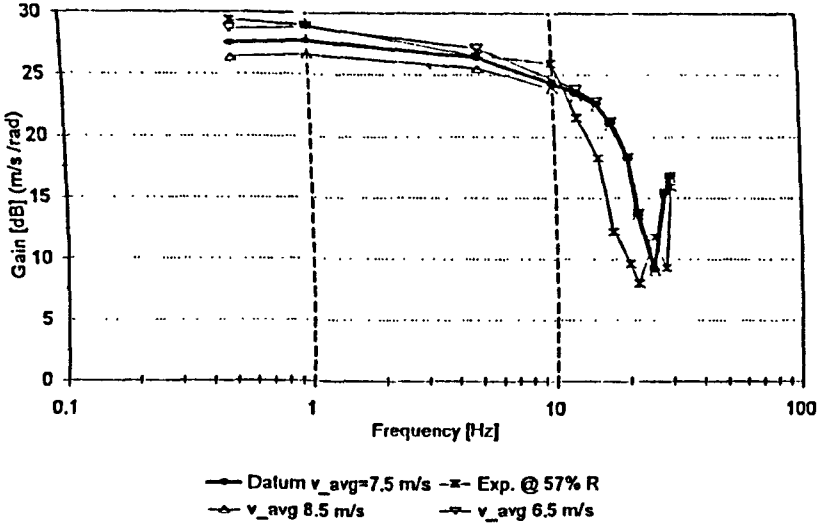

Variation of Average Induced Velocity

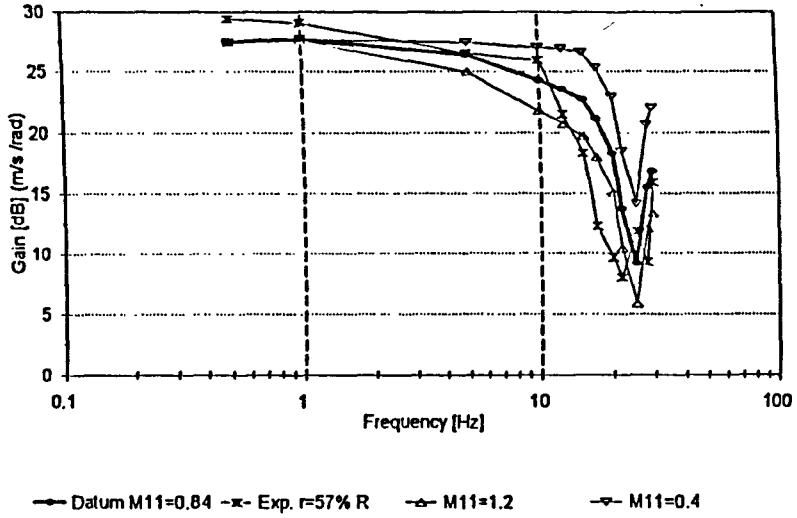

Variation of Apparent Mass

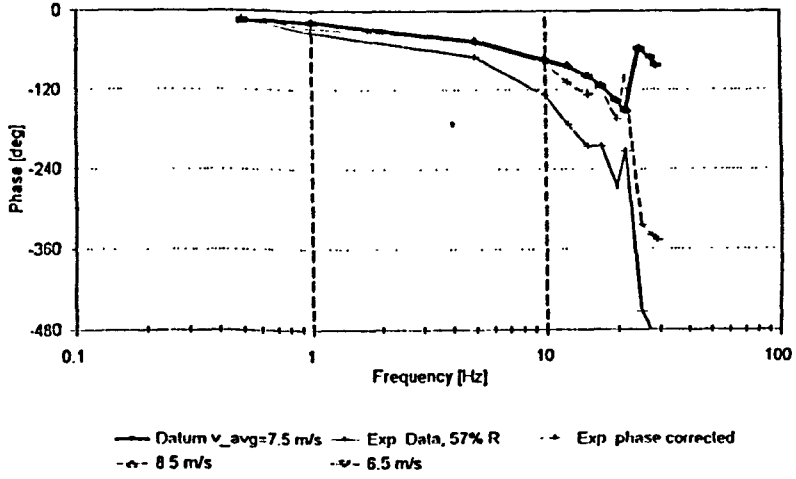

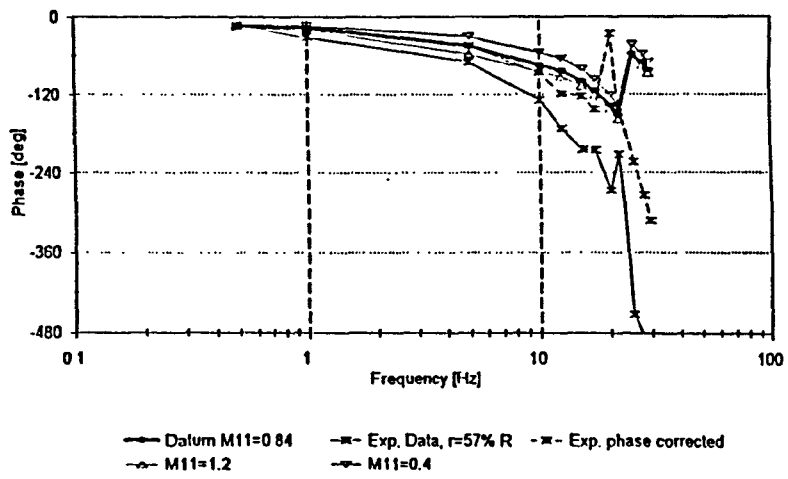

Fig. 7-6 Effect of Average Induced Velocity and Apparent Mass on Inflow Prediction
(1200 rpm, Hot Wire 0.15m below)

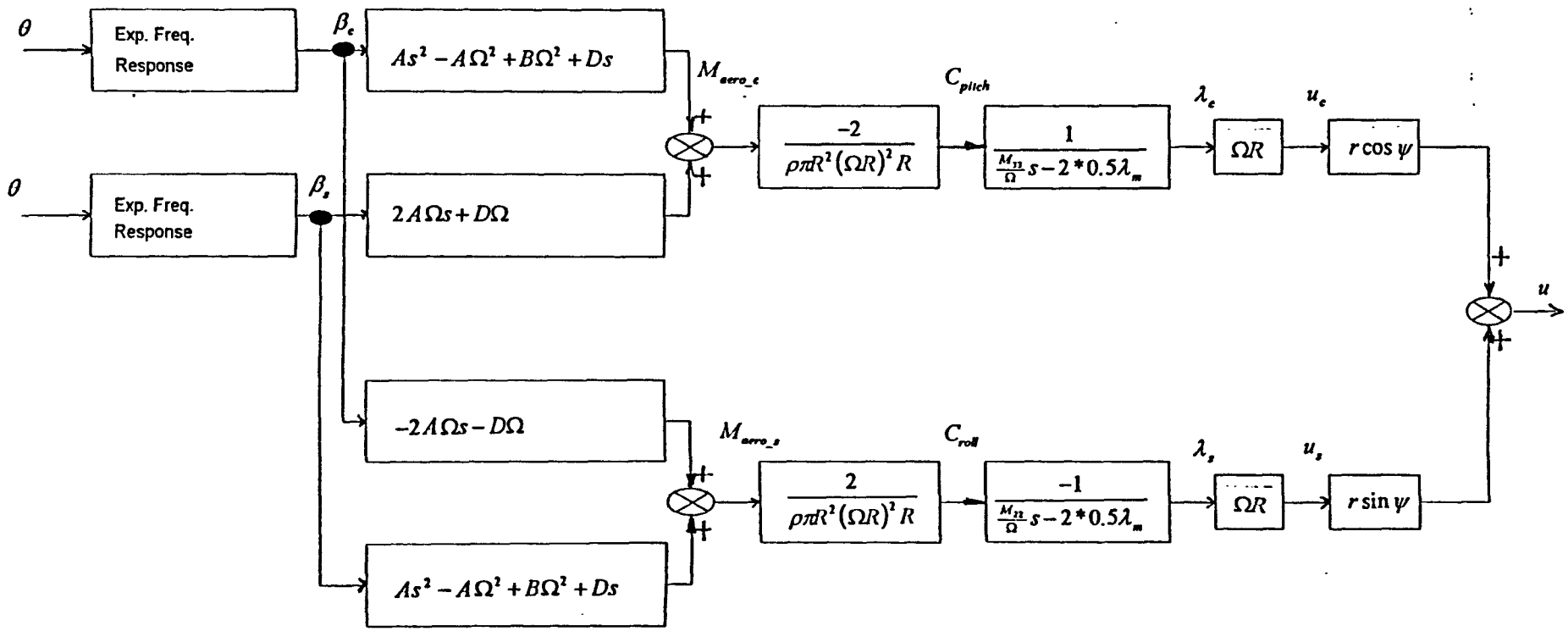

Fig. 7-7 Block Diagram of the Inferred Induced Velocity Response from Flapping Data - Cyclic Case

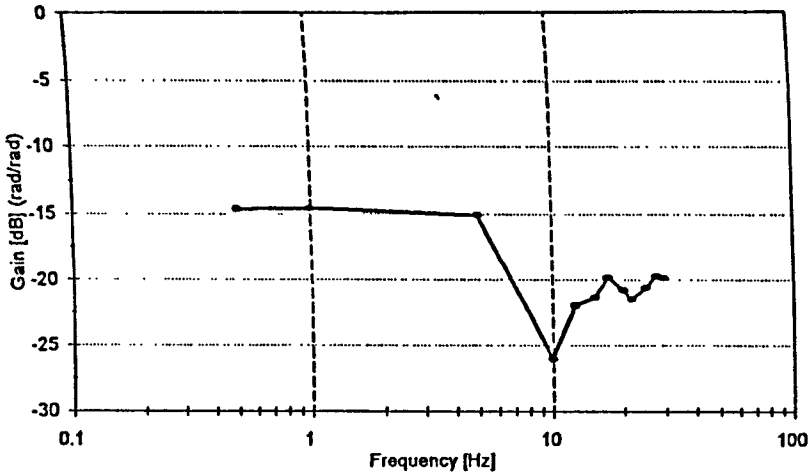

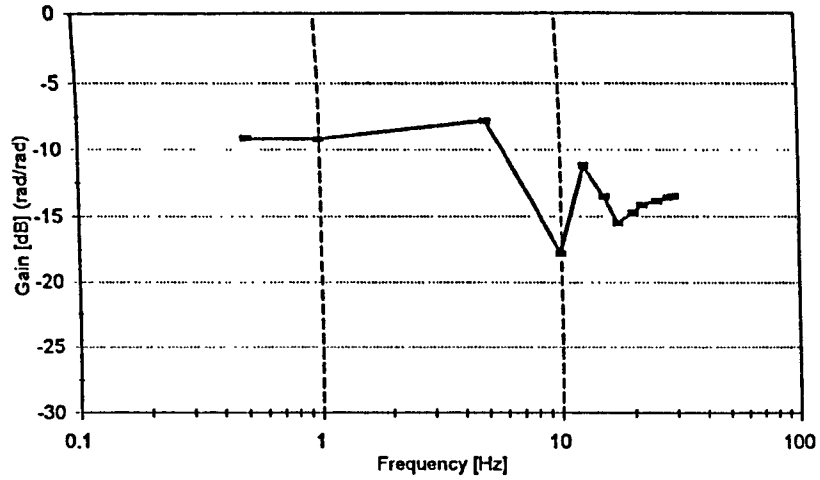

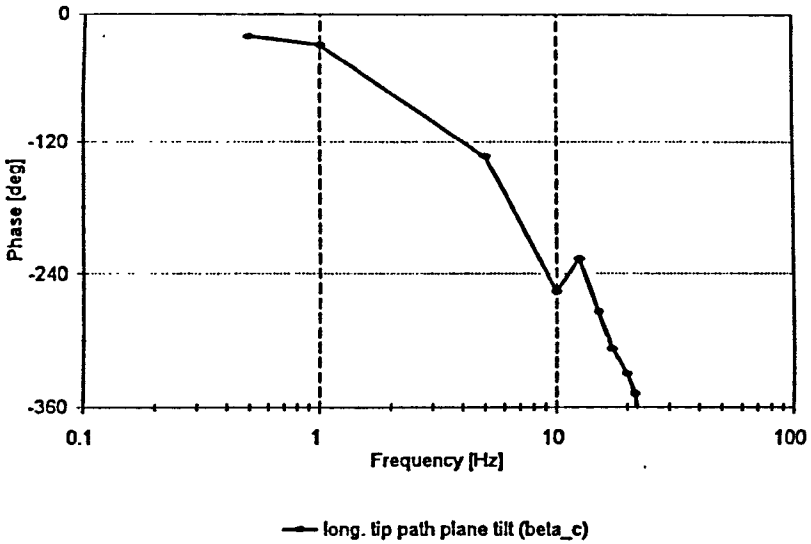

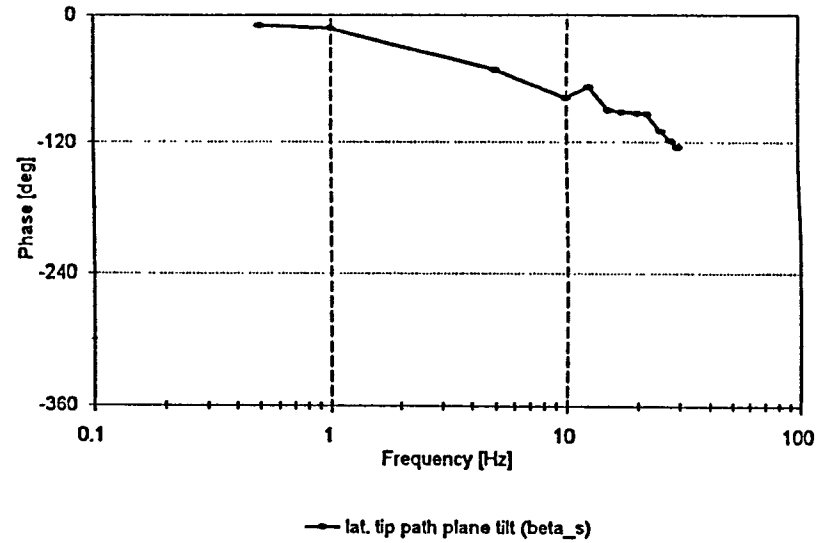

Fig. 7-8 Tip Path Plane Measured Frequency Response with Cyclic Input
(1200 rpm, Max. Blade Excitation at 15 deg. Azimuth)

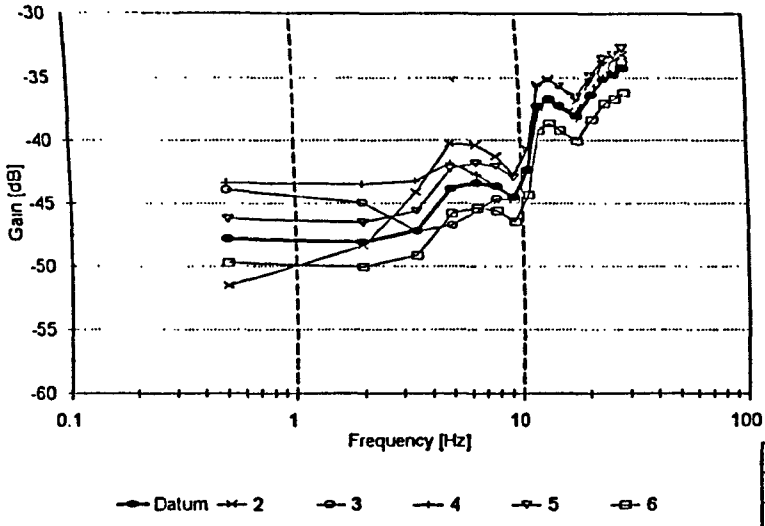

	A	B	fr	Damping
1 (Datum)	0.02346	0.03268	1.18	25%
2	$1.2*A_{Datum}$	B_{Datum}	1.079	25%
3	A_{Datum}	$1.2*B_{Datum}$	1.2958	25%
4	A_{Datum}	B_{Datum}	1.18	20%
5	$1.2*A_{Datum}$	$1.2*B_{Datum}$	1.18	25%
6	$0.8*A_{Datum}$	$0.8*B_{Datum}$	1.18	25%

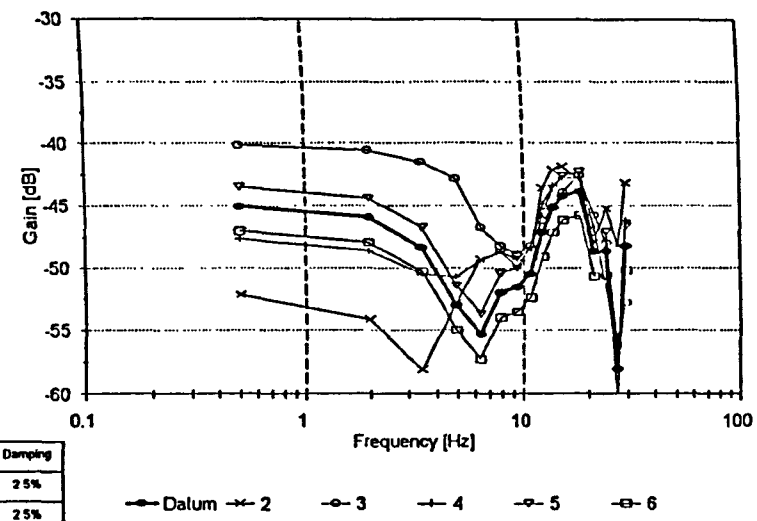

Aerodynamic Pitching Moment Coef. - Frequency Response (C_{pitch})

Aerodynamic Rolling Moment Coef. - Frequency Response (C_{roll})

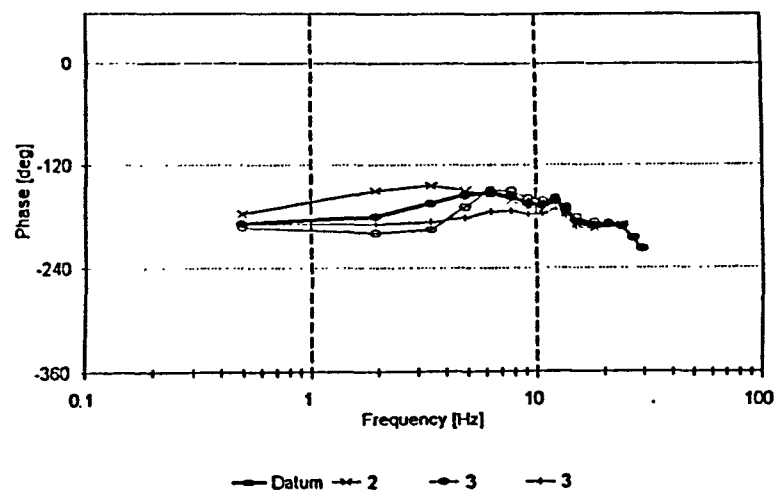

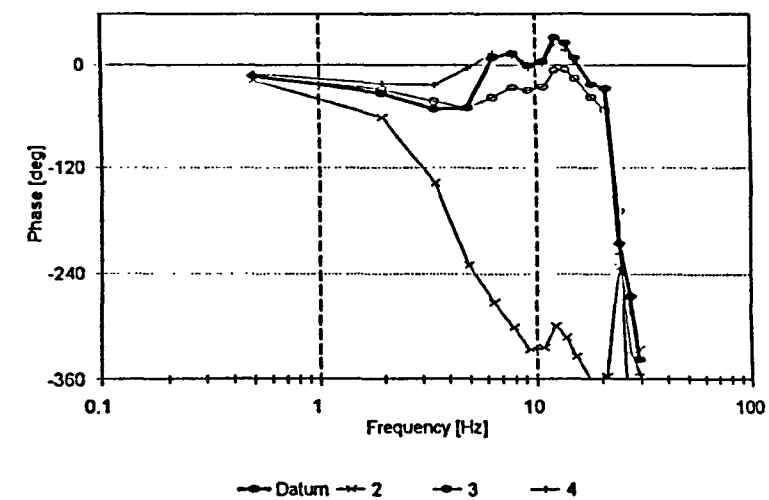

Fig. 7-9 Sensitivity of the Predicted Aerodynamic Loading to Parameter Changes
(1200 rpm, Max. Excitation at 15 deg.)

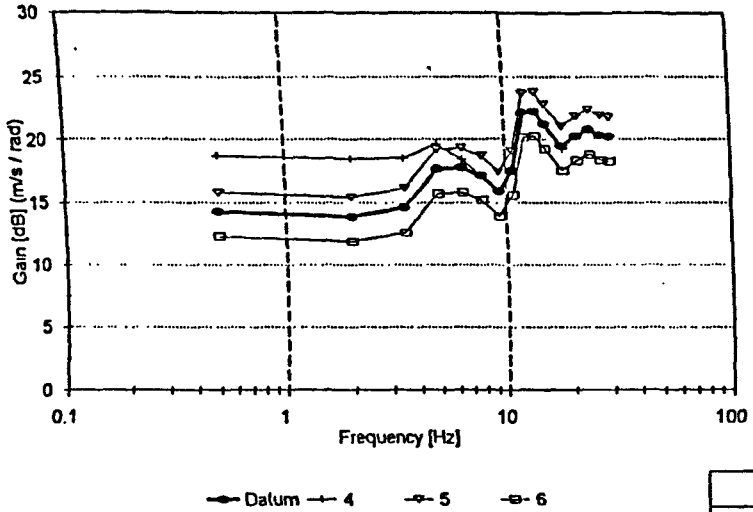

Longitudinal Velocity Component (u_c)

	A	B	fr.	Damping
1 (Datum)	0.02346	0.03288	1.18	2.5%
4	A_{Datum}	B_{Datum}	1.18	20%
5	$1.2*A_{Datum}$	$1.2*B_{Datum}$	1.18	2.5%
6	$0.8*A_{Datum}$	$0.8*B_{Datum}$	1.18	2.5%

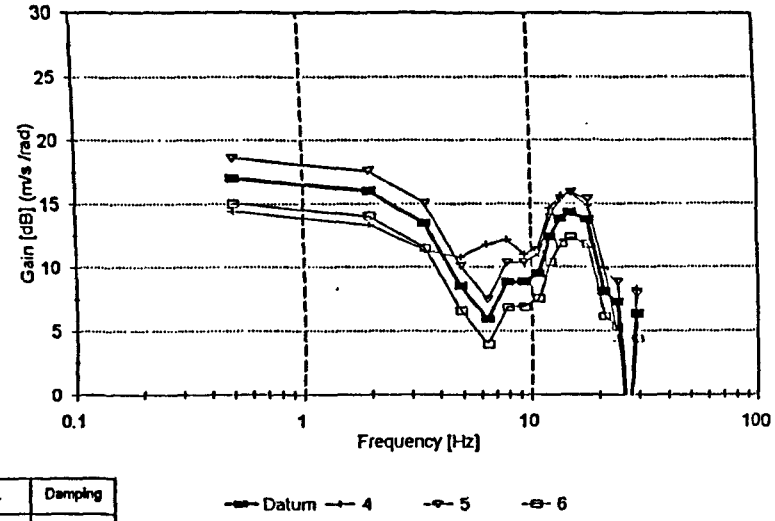

Lateral Velocity Component (u_s)

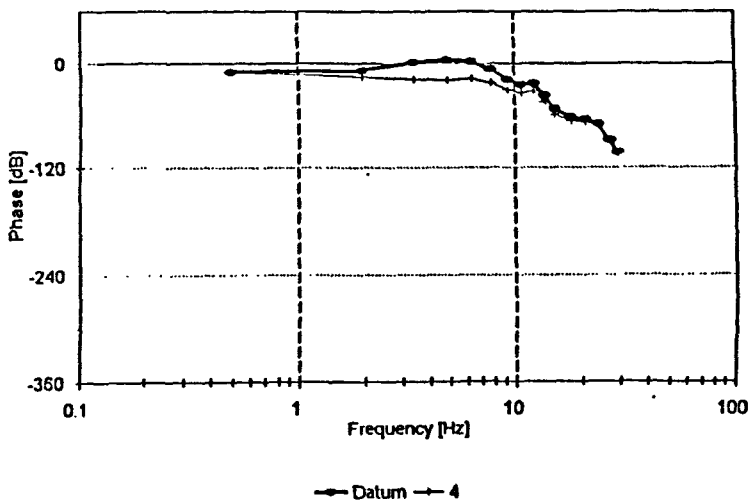

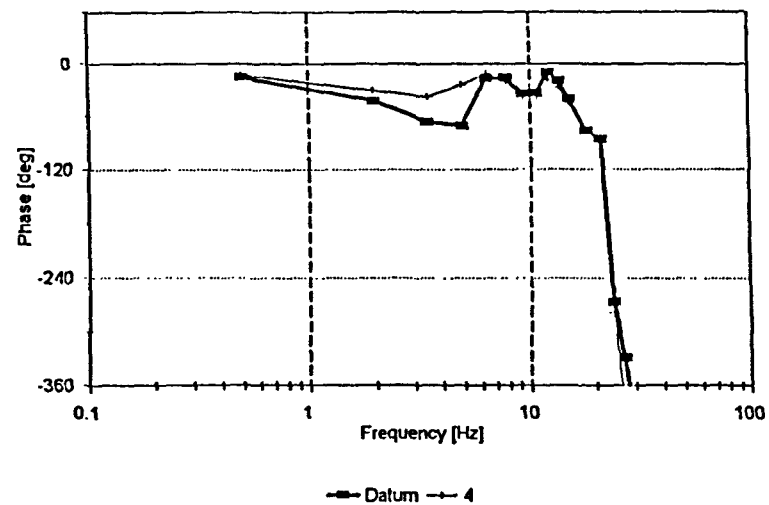

Fig. 7-10

Sensitivity of predicted Inflow to Parameter Changes
(1200 rpm, Max. Excitation at 15 deg.)

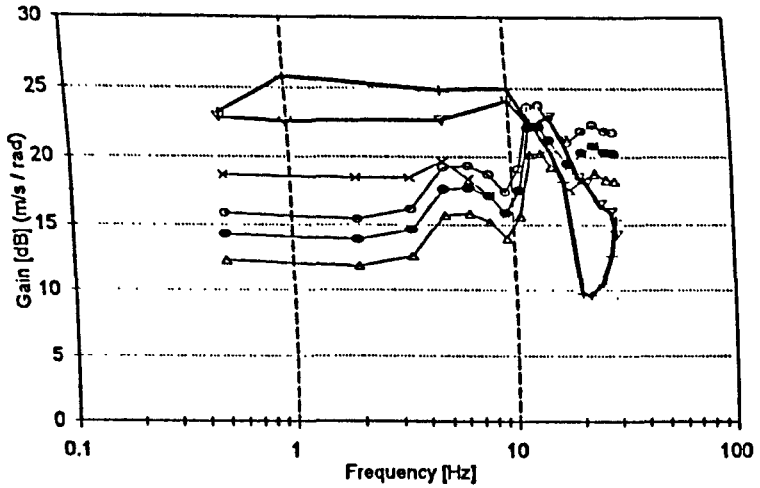

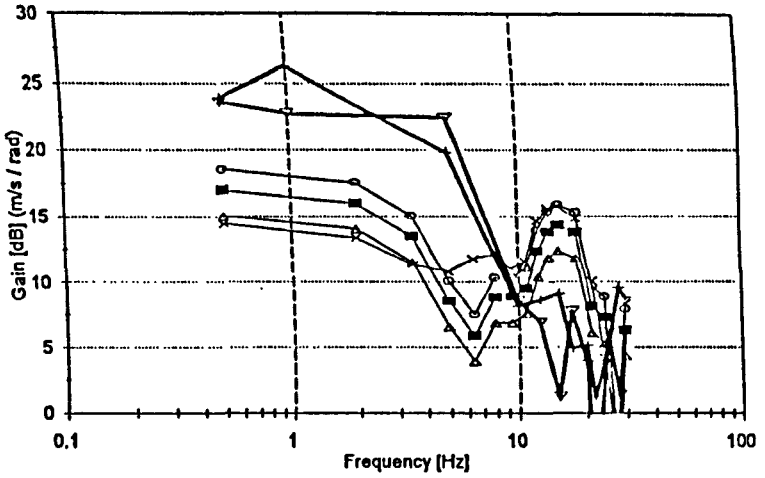

Exp. & Predicted Velocities at 0 deg. (u_c)

	A	B	fr.	Damping
1 (Datum)	0.02346	0.03288	1.18	25%
4	A_{Datum}	B_{Datum}	1.18	20%
5	$1.2*A_{Datum}$	$1.2*B_{Datum}$	1.18	25%
6	$0.8*A_{Datum}$	$0.8*B_{Datum}$	1.18	25%

Exp. & Predicted Velocities at 90 deg. (u_s)

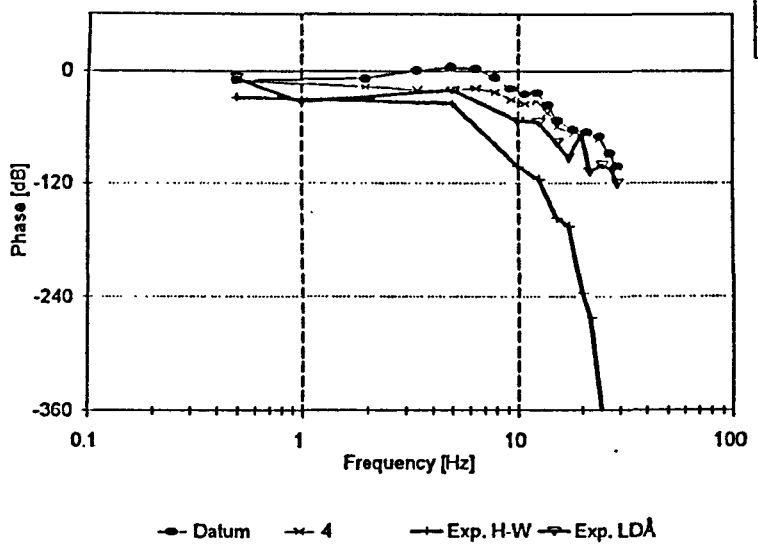

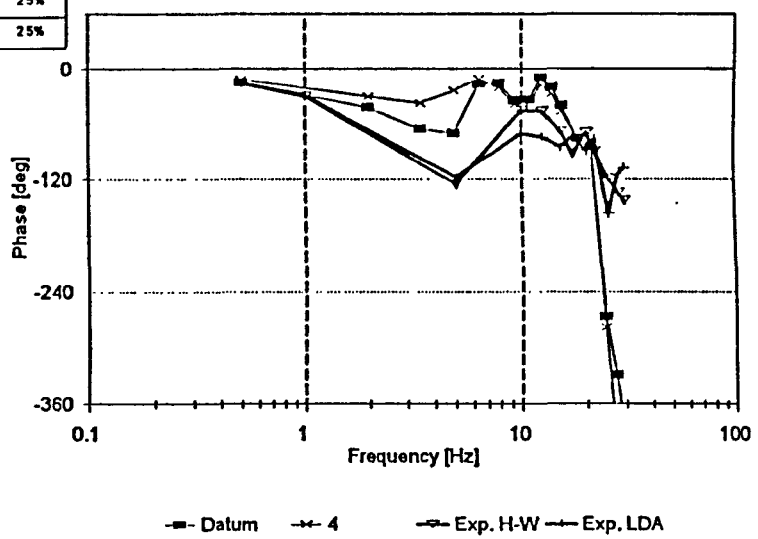

Fig. 7-11 Comparison of the Experimental Inflow at two Azimuth Positions with Theoretical Predictions
(1200 rpm, Max. pitch at 15 deg. Azimuth, 57% R, Hot Wire 0.15m and LDA 0.1m below)

Text cut off in original

Chapter 8
Summary of Experimental Findings and Future Work

8.1 Introduction

In this chapter the principal conclusions from the experimental work are summarised, with aim of providing a concise overview of the most significant results. A full discussion of results is given in the relevant preceding chapters. Areas of future work, improvements extensions of the current work, both experimental and theoretical are also discussed.

8.2 Summary of Experimental Findings

An important aspect of the experimental work was the examination of the induced flow fiel the rotor when it is subject to collective excitation. One aspect of this concerned examination of the effect of vertical separation from the rotor disc on the measured inf perturbations. Fig. 8-1a shows the inflow gain variation with vertical separation. The g variation at the three measurement points is near linear with separation distance, however gradient is frequency-dependent. From this it can be concluded that there is no sin correction factor that can be applied to the measured gain to take account of vert separation between the rotor and measurement point. Only the results for frequencies from to 15 Hz are shown in this figure, as these show a clear trend. At higher frequencies behaviour of the wake is much more complex, with no clear trends indicated, a feature whic repeated in many of the other results. In Chapter 3 it was observed that at frequencies near shaft speed the general level of the turbulence in the flow increases, and this may be a rel effect.

Fig. 8-1b examines the phase variation with vertical distance. A linear fit for the three chc measuring points beneath the rotor is also shown, and it can be seen that the phase variatio virtually linear with separation distance. The slope of the fitted line increases with freque

Both these features suggest a transmission type delay for measurements taken at different distances below the rotor disc. To confirm this, the gradient of the phase change is examined. The gradient for each of the frequency cases is plotted against frequency in Fig. 8-1c and a linear least squares line fitted to these points. The gradient of the phase variation with vertical distance is approximately 63 deg/m /Hz. The theoretical value assuming a pure phase transmission delay was found to be 44 deg/m /Hz. This suggests that although transmission type delays are involved where the wake is convected from one point to the next, these alone are not sufficient to explain the observed phase variations with vertical separation. At the lower frequencies the transmission delay correction can be used as a first approximation to the vertical phase variations. The results shown here are only for frequencies up to 17 Hz since at higher frequencies the linear relationship between separation and phase difference is no longer present. This again highlights both the change in character of the wake at frequencies above 17 Hz and the complex structure of the dynamic wake.

Fig. 8-2 shows the dependence of induced flow gain and phase on the rotational speed of the rotor. Generally, the gain increases with rotational speed and this is shown to be consistent with the Pitt and Peters inflow formulation, in Chapter 5. The phase delay decreases at a given excitation frequency as the rotational speed is increased and this is consistent with the theoretical inflow model. Again, these trends are only clearly shown for the frequency range between 0.5 Hz and 17 Hz.

The inflow frequency responses at three radial stations are shown in Fig. 8-3. The full set of data covering radial stations from 17% to 103% is given in chapter 5. Clearly both the gain and the phase response change significantly with radial station. The results of Fig. 8-3 have been averaged over 5 runs and excellent repeatability can be seen to be achieved. The effect is more clearly shown in Fig. 8-4, where the inflow gain is plotted against radial station, for a selection of frequencies between 0.5 Hz and 29 Hz. Plotting gain against radial station and frequency on one graph results in the 3 dimensional carpet plot shown in Fig. 8-5. These results were repeated at lower and higher rotor speeds of 1000 rpm and 1500 rpm respectively and the results are given in Chapter 5. Fig. 8-6 shows the phase response at both speeds and at

three radial stations. The repeatability is again very good, and a similar trend can be seen in both cases. At higher excitation frequencies the predominant changes in the induced velocity occur in the outboard regions of the blade.

Fig. 8-7 shows the phase variation with radial station for the 1200 rpm case. Only the range between 40% and 80% radial station is shown for a reduced frequency set of 0.5 Hz. to 15 Hz. Clearly visible is the increasing phase lag, from the outboard region of the blade, which is not modelled in the Pitt and Peters inflow model. A possible explanation of this might be that the inflow response is significantly affected by the circulation of the tip vortex. Further inboard of the circulation centre, the flow takes longer to respond.

An important result from this work is the high dependence on frequency and radial variation of the dynamic inflow response. Finally, in Chapter 5 the induced flow response predicted from coning/inflow models, developed in Chapter 3, is compared with experimental results. Although these models assume the Pitt and Peters inflow model wake description, which does not allow for radial inflow variations, good agreement is achieved using inflow measurements at a near mid-span position of 57 % R and an apparent mass factor of 0.81. The results are dramatically improved if the damping of the coning mode is increased and this is shown in Fig. 8-8. A detailed discussion of the results and justification for increased damping is given in Chapter 5 and illustrates the closed-loop connection between the blade geometric pitch, blade flapping response and dynamic inflow, which determine the effective aerodynamic blade angle of attack and hence the aerodynamic loads on the rotor.

The inflow response due to cyclic excitation is examined in Chapter 6. The area of the wake that could be examined ranged from 0 degrees to 90 degrees azimuth. Fig. 8-9 shows the inflow gain and phase response, measured at an azimuth position of 90 degrees, at three radial stations. It can be seen that the character of the response changes with radial station. Plotting inflow against blade radius in Fig. 8-10, shows that the radial shape is also dependent on the excitation frequency.

The inflow variation with azimuth was also examined at a radial station of 57%. Fig. 8-11 shows the gain and phase response observed at four azimuth stations between 0 degrees and 90 degrees. It can be seen that the shape of the frequency response changes with azimuth position. For the 0 deg azimuth position the gain response is flat up to and above 10 Hz and then reduces. At 90 degrees the gain response falls sharply from 5 Hz onwards. At around 30 degrees azimuth a dip in the gain at 5 Hz and subsequent recovery is shown.

To examine the azimuthal variation of the inflow more easily the frequency response data taken at 7 azimuth positions, using hot-wires, is plotted against azimuth in Fig. 8-12. The azimuthal variations are small and no peak in gain is seen at the azimuth position (15 deg) where the blade pitch is at its maximum. A simple momentum theory approach suggests that the maximum induced velocities occur at the azimuth position corresponding to maximum blade pitch.

An examination of the induced velocity response due to cyclic pitch changes has shown that the radial dynamic inflow distribution is dependent on the frequency of excitation. Furthermore, the induced flow response varies significantly with azimuth and the azimuthal distribution is also dependent on frequency. The results do not show the intuitively expected higher velocities at azimuth positions corresponding to larger blade root pitch and hence blade loading. The results point to a complex wake structure, where the dynamic induced velocities at a point are determined from the distribution of shed vorticity in the wake. This again is dependent on the frequency of excitation and the location of the measuring point. A simple sinusoidal variation of the inflow response is accounted for in the Pitt and Peters wake description, but similar to the collective case, a radial variation with frequency is not included.

The aerodynamic loading on the rotor is inferred from the blade flapping data in Chapter 7, which is then used to drive the Pitt and Peters dynamic inflow model to provide theoretical predictions of the inflow response. The aim of this method was to use the blade flapping response to obtain reliable predictions for the aerodynamic hub loads, which are not easily obtained experimentally, and hence to use the aerodynamic loading to predict the inflow

response using the Pitt and Peters dynamic inflow model. The complete analysis is carried out in the frequency domain. Fig. 8-13 shows the results obtained for the case of collective rotor pitch excitation, in the hover conditions. The estimation of the aerodynamic loading depends on accurate estimation of blade dependent parameters, and these are in turn dependent on the blade dynamic model. The upper two graphs of Fig. 8-13 show the sensitivity of the inflow prediction to variations in blade parameters. Confidence in the correct value of the blade parameters is high as these give correct predictions of the coning resonance frequency. Nonetheless the results are relatively insensitive to model parameters. The lower graphs of Fig. 8-13 compare the predicted and measured inflow response at two radial stations of 57% R and 65% R, and very good agreement is found, with the predicted inflow showing the same sharp dip in gain as the experimental results. The dynamic model of the inflow response assumed in the Pitt and Peters model, for the collective excitation case in hover, is in essence correct throughout the frequency range of interest.

A similar approach was taken for the cyclic rotor pitch excitation cases. The mathematical relationship, in the frequency domain, of the blade response and aerodynamic loading is given in Chapter 7, but is more complicated than that of the collective case, because of the coupling between the lateral and longitudinal TPP degrees of freedom. Fig. 8-14 shows the results from the analysis, predicting the inflow response at 0 degrees and 90 degrees azimuth, or in other words the Pitt and Peters longitudinal and lateral inflow degrees of freedom. Unlike the collective case, the inflow response is very sensitive to the chosen parameters, and this was disappointing. The lower graphs of Fig. 8-14 compare the inflow predictions with experimental data at 0 degrees and 90 degrees azimuth, with poor correlation.

The dynamic induced flow measurements have shown that for both collective and cyclic excitation the induced flow field varies with radius, azimuth and frequency, and is thus more complicated than previously assumed. The complex dynamic induced velocity field is likely to be due to the distribution of time-varying shed vorticity and trailing vorticity in many spirals beneath the rotor. A computational fluid dynamics approach for a rotor under collective and

cyclic excitation over a range of frequencies should be attempted to reproduce the dynamic inflow behaviour.

The Pitt and Peters dynamic inflow model includes a wake description which is much more simple than the real wake structure. The main purpose of the Pitt and Peters model was not to model the structure of the wake accurately but to include degrees of freedom in more complicated rotor models, which allowed for the dynamic nature of the induced flow. The simplified wake model does however make it difficult to make direct comparisons with experimental data. The Pitt and Peters model seems to fit well in the 'collective' sense. Apart from the wake structure, the first order Pitt and Peters model does not capture the high roll-off in inflow response at frequencies near shaft speed, and a higher-order inflow representation should yield better results.

8.3 Areas for Further Research

During this research many areas of possible future investigation became apparent and these are detailed below. Most of these suggestions are extensions and refinements of the completed work that would improve the knowledge of dynamic inflow, which could not be pursued because of time and equipment limitations.

i) Inflow Measurements at Vertical Stations above the Rotor

Further measurements of dynamic induced flow should be made at stations above the rotor. A transmission type delay effect has been identified for inflow phase measurements at frequencies below 17 Hz beneath the rotor. It would be interesting to see if this is the case above the rotor. The advantage of measurements taken above the rotor is that the airflow should be less turbulent. Hot wire and pitot static measurements were not taken above the rotor because of the significant difficulties associated with mounting the sensors safely. The Laser Doppler Anemometer system could not be used to obtain measurements above the rotor as its vertical range was insufficient.

ii) Hub Load Measurements

On the present rig, the aerodynamic thrust and pitch/roll moments have to be inferred from the blade response data. Direct measurements of the thrust and pitch/roll moments would be desirable as it would be easy to correct these using blade flapping data to obtain only the aerodynamic loading. Thrust measurements were difficult to obtain as the pitch and roll degrees of freedom of the rig meant that the supporting structure of the gimbal had to be very stiff and was therefore not suitable for strain gauge location. The only possible position for strain gauges would be on the rotor shaft, however this again was also so stiff that the non-amplified signal would be lost in the noise of the slip-ring assembly. Measurements of the pitch and roll moments acting on the base plate when it is not free to pitch and move would be obtained from load cells. Time limitations prevented this from being done.

iii) Azimuthally Spaced Inflow Sensors

With many more hot-wires, measurement positions could be spaced at regular intervals around the complete azimuth, thus allowing a larger region of the wake to be examined during collective or cyclic excitation of the rotor. The advantage of this would be that a more complete survey of the wake, particularly during cyclic excitation, could be obtained with fewer experiments. With sufficient sensors around the azimuth it might also be possible to track a specific blade around the azimuth and observe the development of the induced flow.

The equipment requirements for this approach are considerable. With a spacing of fifteen degrees, sixteen hot-wire channels and sixteen analogue to digital converters (ADC) would be needed. On the present rig it was possible to gather twelve channels of data. This was limited both by the multiplexer on the ADC and the time it needed to convert the analogue data to digital form, which had to be completed within the two mili-seconds frame time of the rig. These had to include the signals from the strain gauges mounted on the rotor blades and other analogue signals needed in the operation of the rig. In total eight analogue input channels were available for inflow data of which four were used. To accommodate more analogue inflow channels faster ADC converters and more channels would be required.

iv) Inflow Measurements in the Rotating Frame using a Laser Doppler Anemometer

Another aspect of the experimental work that could not be included in this study due to time and equipment limitations was the measurement of the induced flow in the rotating frame using Laser Doppler Anemometry. For this, the six laser beams used to obtain the 3 dimensional flow information would follow the blade, measuring the flow at the same position relative to the blade. This could be achieved with a de-rotation mirror mounted at the centre of the rotor hub, rotating at exactly half the speed of the rotor. The laser beams would be focused through the mirror arrangement to a point behind the blade. As the rotor turned, the rotating mirror would keep the beams following the blade and thus allow measurement of the induced flow in the rotating frame, while the blades were excited dynamically.

This seemingly simple method requires the solution to a number of complex problems. The six laser beams are already difficult to focus on one single spot. With the rotating mirror the beams need to be aligned through the rotating mirror and then focused on a point near the rotor blade. The azimuth covered by one side of the mirror will be somewhat less than 180 degrees because there will be no information when the mirror is edge-on onto the incoming beams. The mirror needs to be constantly kept at half the azimuthal position of the rotor blade it is trying to follow, with high precision. To maintain the beams within 1 mm of the desired measuring point at say a radial station of 0.7m would require an azimuthal accuracy of the mirror of 0.041 degrees at around 1200 rpm. An advantage of using the LDA in a rotating frame is that 3 dimensional flow information can be obtained and that forward flight cases can be investigated without difficulty.

v) Step Inputs in the Time Domain

All the investigations of the inflow response in this work were conducted in the frequency domain. It was possible to excite the rotor for lengthy periods with sinusoids of different frequencies and then to extract the dynamic inflow response from the noisy data using a correlation procedure. The disadvantages of time-domain techniques were that the pitch inputs into the rotor had to be kept reasonably small to protect the mechanical integrity of the

blades/hub and hence the resultant inflow changes were also small. To identify the inflow response to step inputs confidently these would have to be repeated and averaged several times to produce reliable results. Some experimental step responses were run and the results indicated that this was feasible, but time constraints did not allow further work in this area.

vi) 'Shadow-Graph' Visualisation of the Tip Vortex Cores

Interesting work could be done in the field of shadow-graph flow visualisation of the vortex cores particularly when the blade pitch is changed dynamically. Studying the effects of the vortex core of the rotor in the dynamic case should show how significant the vortex core is in affecting the dynamic variation of the induced flow as observed in Chapters 5 and 6. Shadow-graph flow visualisation relies on the different refractive indices of air of different density. A very strong point light source casts a shadow image on a reflective screen, which can be photographed or filmed. In the dynamic case it would be interesting to observe if the spacing or position of tip vortex cores are affected by dynamic changes in blade pitch.

vii) Different Rotor Configurations

To complement the work carried out using a semi-rigid 4-bladed rotor, other rotor configurations and their effect on the induced flow need to be examined. Amongst the factors that should be varied are the number of rotor blades, the blade geometry and the blade mounting. For rotors at the same operating point, the number of blades should not influence the induced velocity response according to the Pitt and Peters [Pitt 1983] dynamic inflow model, and this could be verified. Varying the blade chord but otherwise maintaining the same operating conditions affects the reduced frequency ($k = \frac{b\omega}{n\Omega}$), and it was suggested in Chapter 5 that this may be a main element in the radial and frequency variation of the induced flow.

Using a hub with articulated rotor blades should greatly simplify the inference of the aerodynamic loading from the blade response as per Chapter 7. The position of the hinge off-set would be clearly defined in this case and the rest of the blade can be better approximated as a rigid beam. The analysis using two degree of freedom coning / inflow models as in Chapter 3 should also be simplified for the same reason.

iix) Forward Flight Regime

The current work concentrated on the rotor in the simulated hover condition. This should be extended to the forward flight regime. However, the measurement of the induced flow response in forward flight poses further difficulties. In the hover condition it could be assumed that the predominant induced flow direction near the rotor and away from the tip regions was vertically downward. This assumption cannot be made in forward flight where the rotor wake will be swept back. If measurements of both the magnitude and direction of the induced flow are desirable, this would necessitate 3 dimensional (3 channel hot wire probes or Laser Doppler Anemometry) flow measurements. Investigation of the forward flight case should allow the assumptions made in the Pitt and Peters model about the variation of the L and M matrix elements with wake angle to be compared with experimental data. The forward flight case is more complicated than the hover case due to the coupling of the thrust and pitch aerodynamic loading to both the uniform and fore-aft-variations in forward flight.

ix) Aerodynamic Loading from a Pressure Instrumented Blade

A blade instrumented with pressure transducers along the span of the blade would allow the aerodynamic loading acting on the rotor to be determined without the need for flapping measurements. Once the aerodynamic loading of the rotor can be determined this can be used to correlated the induced flow measurements with the dynamic inflow model by Pitt and Peters [Pitt 1983]. A further advantage of this approach would be that the blade loading would be available as a function of the radial station, the accuracy of which is limited only by the number of sensors spaced along the blade. This would allow the examination of recent, more complicated dynamic inflow models [Peters & He 1989], which allow radial and azimuthal variations of the induced flow and link these directly to the local aerodynamic loading of the blade. This would also allow the work of Lal [Lal et al , 1994], which looked at the chord-wise pressure distribution on a rotor blade at one collective excitation frequency, to be extended to a range of frequencies.

x) System Identification using Inflow Data

Many researchers [Harding 1992; Leith, Bradly & Murray-Smith 1991; Bradly, Black & Murray-Smith 1989], have concluded that the identification of dynamic inflow in rotor/body/inflow models would be greatly improved if high quality blade flapping, and particularly inflow, data were available. Once inflow data are available an equation error approach is likely to provide good results [Bradly, Black & Murray-Smith 1986]. This is an area in which the data from the rotor rig could be applied.

xi) Comparison of Experimental Results with CFD Results

The experimental results presented here need to be compared with the predictions from computational fluid dynamics simulations. Several different methods are available for the calculation of the flow field of the rotor using an iterative approach. An initially assumed flow field is used to examine the rotor loading, this in turn is used to make a better prediction of the flow field which in turn affects the loading. When the flow field has converged a solution is found. Methods range from a lifting line theory, where the trailing vorticity of the rotor using either a geometrically prescribed or free wake is used to find the flow at the rotor using the Biot Savart law to panel methods where a suitable grid of sources, sinks and doublets is used to fulfil the boundary conditions at the blade. Other methods are available such as lifting surfaces, using a lifting mesh with vortex rings, and Euler methods, where a 2 or 3 dimensional grid is used to solve the Euler equations for the flows. Using these methods, the dynamic circulation produced by the rotor needs to be modelled.

These methods need to give predictions of the dynamic flow field. This could be in terms of a direct time or frequency response of the flow. Once this is possible the radial, azimuthal and vertical variations in the dynamic induced flow response can be compared with the experimental data.

8.4 Conclusions

A unique experimental facility for the study of dynamic inflow has been developed. This allowed examination of the dynamic induced velocity field of a model rotor under controlled excitation over a frequency range up to 1.5 times rotor shaft speed, while keeping rotor speed variations to a minimum.

- The dynamic response of the induced flow field was found to be highly complex, dependent on both the radial and vertical measurement position and the frequency of excitation.

- The frequency response of the induced flow was compared to theoretical models including dynamic inflow theory, based on the work by Pitt and Peters [Pitt & Peters 1981]. The overall dynamic characteristics of the flow are captured reasonably well by the theory for the 'collective' case. In this case the inflow dynamics were also successfully isolated, suggesting that the Pitt and Peters apparent mass model with M_{11}=0.8 is in essence correct. However, the results suggest that the wake description used in the Pitt and Peters inflow model does not capture important features of the real wake, such as a strong radial variation of the dynamic inflow response, which is dependent on the frequency of excitation. For the case of cyclic excitation the correlation between theoretical models and experimental results was disappointing. For this case a significant azimuthal variation of the dynamic induced flow with frequency was also found.

- The results highlight changes in character of the inflow response at frequencies above 15 Hz to 17 Hz, which deserve further investigation. An increase in turbulence was also observed at frequencies near the shaft speed. The complex structure of the dynamic wake can probably be attributed to the distribution of shed vorticity in the wake beneath the rotor, which will be affected by the frequency of rotor excitation.

- The initial theoretical coning/inflow models did not capture the magnitude of the coning resonance peak accurately and modifications to the theoretical model, based on physical

arguments, are proposed improving the correlation. There is a strong observed coupling between the coning damping and the inflow response near the resonance frequency.

This work has produced valuable insights into the complex dynamic structure of the wake, which it is hoped - together with the literature survey, review of the Pitt and Peters model and discussion of future work - will offer guidance to future researchers working in the area of dynamic inflow.

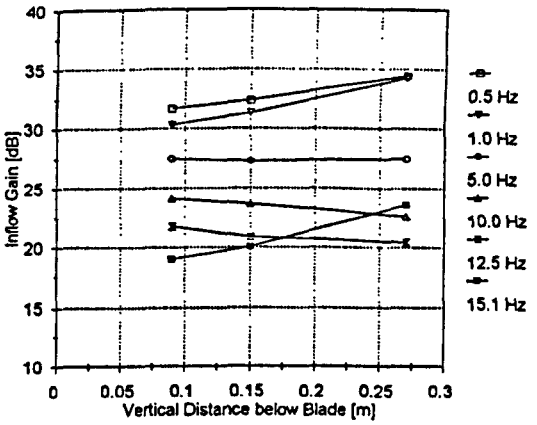

Fig. 8-1a Axial Gain Variation

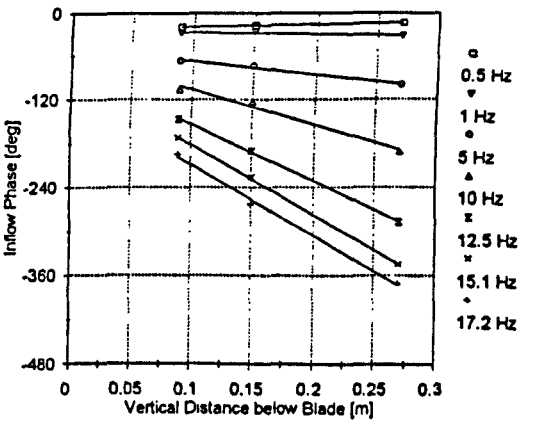

Fig. 8-1b Axial Phase Variation

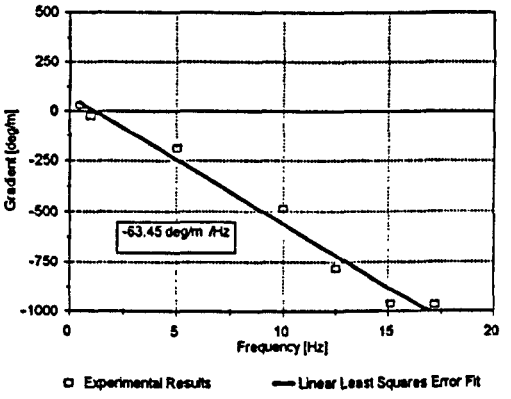

Fig. 8-1c Phase Gradient as a Function of Frequency

Fig. 8-1 Transmission Delay for the Vertical Inflow Phase Variation
(1200 rpm, 57% R, Hot Wire 0.15m below, Collective Excitation)

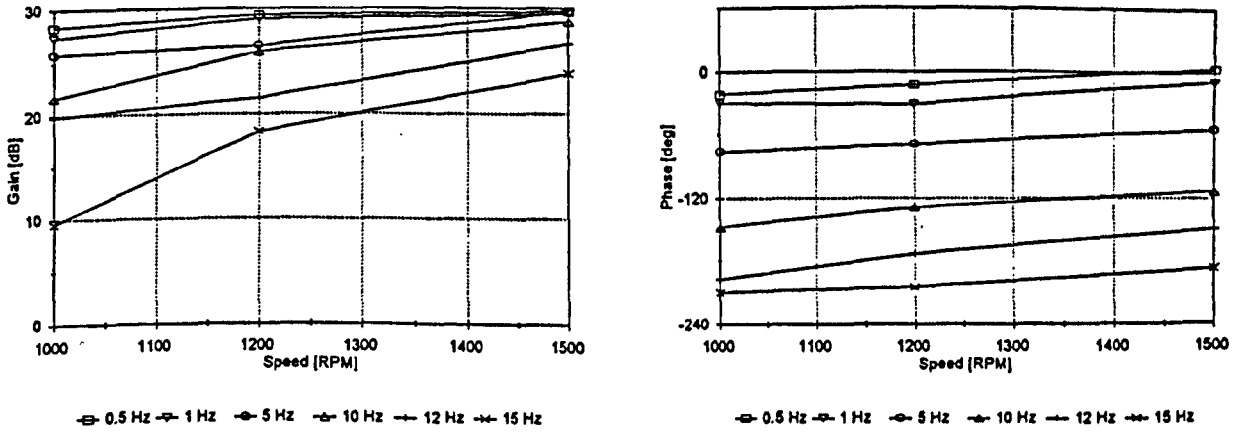

Fig. 8-2 Variation of the Inflow Phase and Gain with Rotor Speed
(57% R, Hot Wire 0.15m below, Collective Excitation)

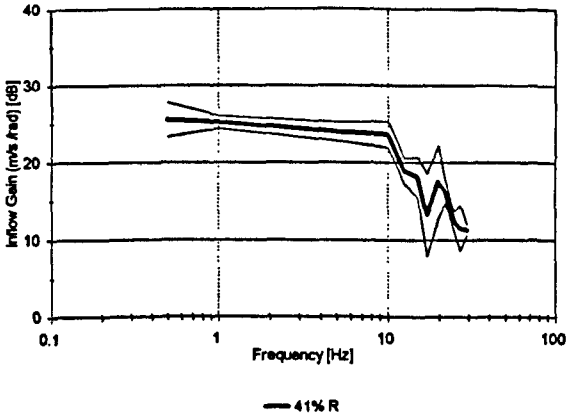

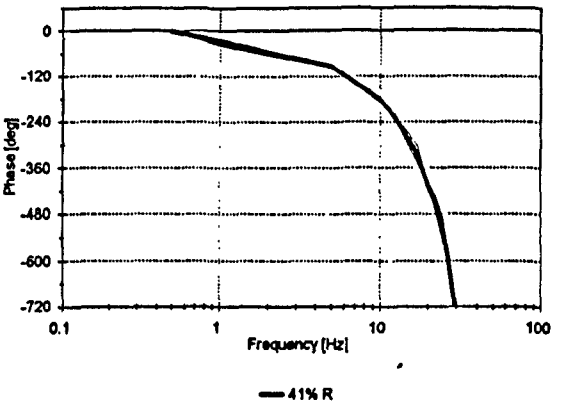

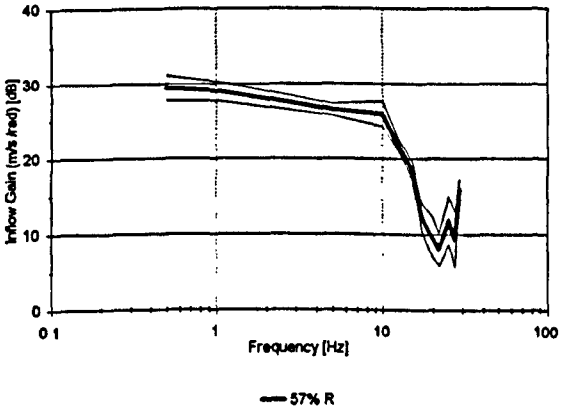

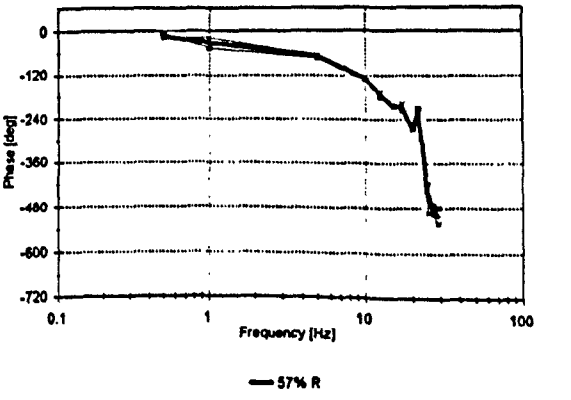

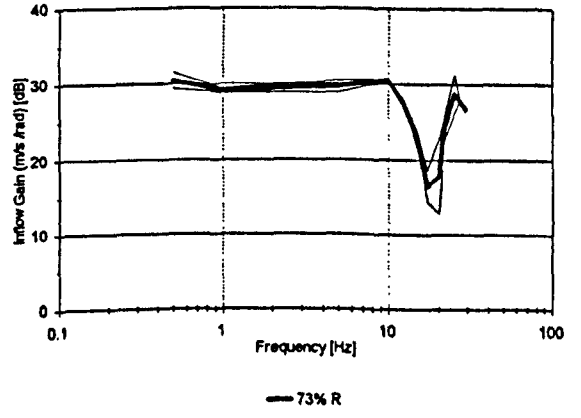

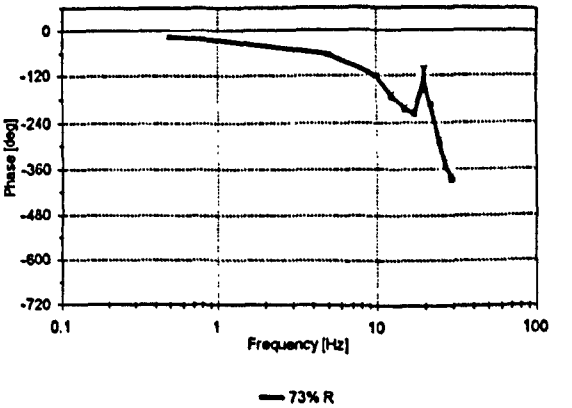

Fig. 8-3 Change in Inflow Frequency Response with Radial Station
(1200 rpm, Hot Wire 0.15m below, Collective Excitation)

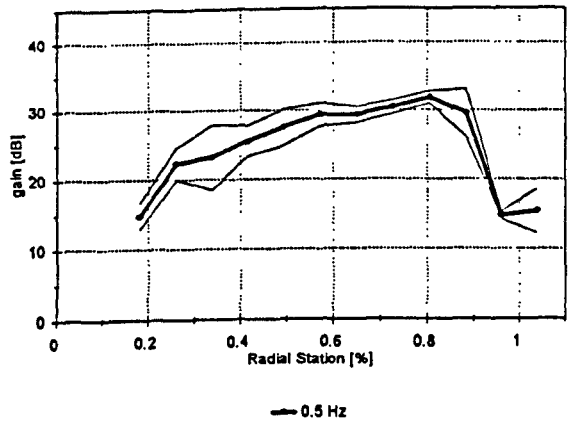

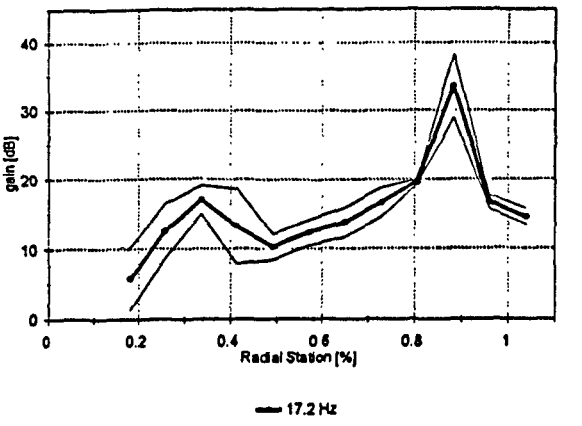

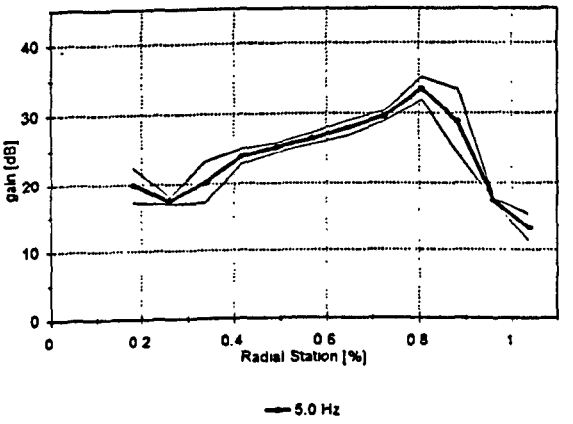

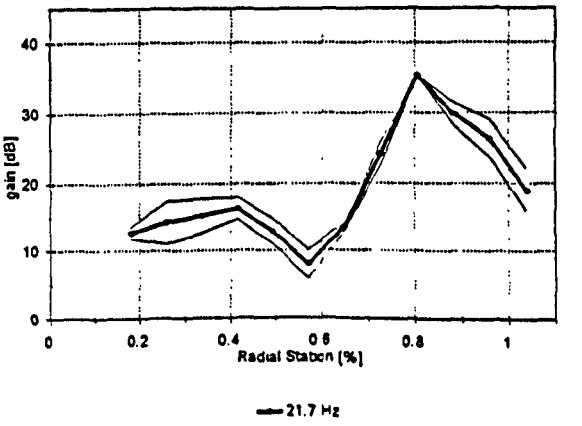

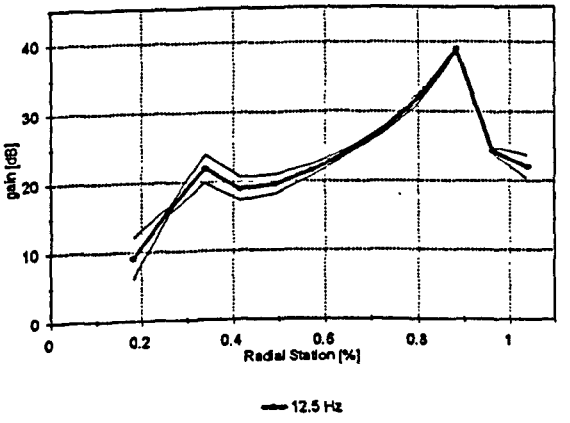

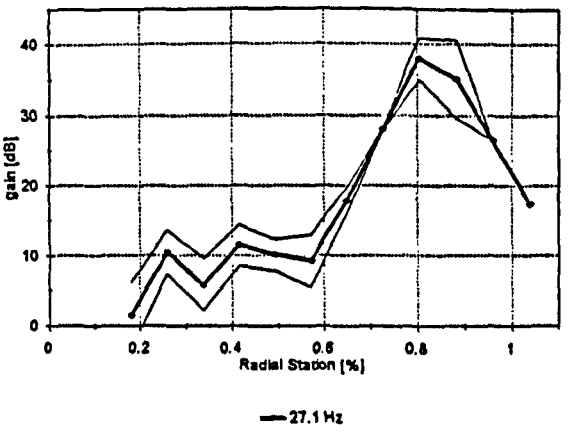

Fig. 8-4 Radial Variation of the Inflow Gain at selected Frequencies
(1200 rpm, Hot Wire 0.15m below)

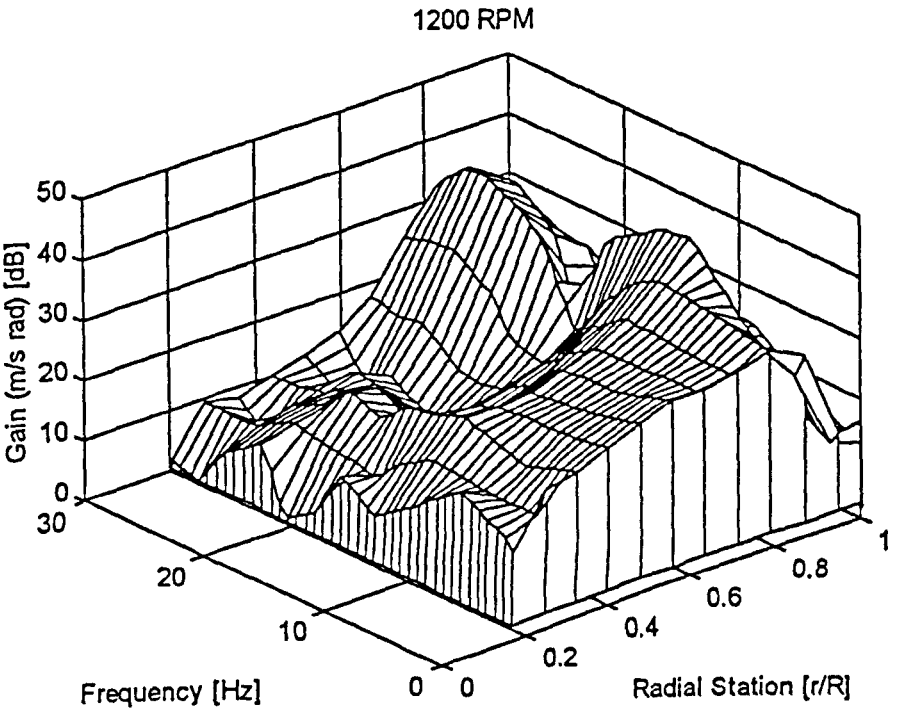

Fig. 8-5 Radial Distribution of the Induced Velocity Response variation with Frequency
(1200 rpm, Hot Wire 0.15m below, Collective Excitation)

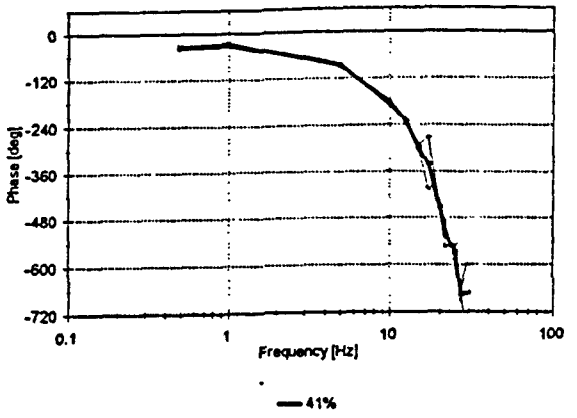

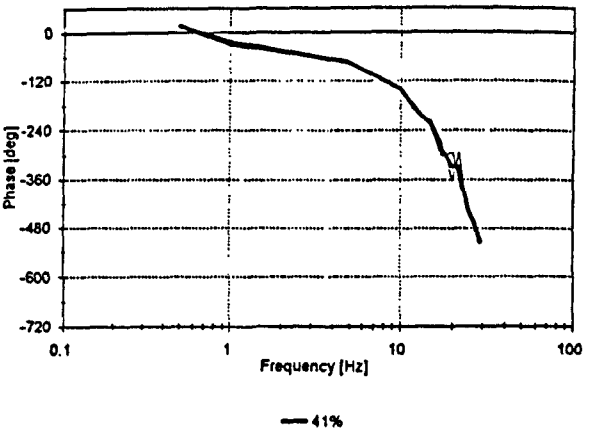

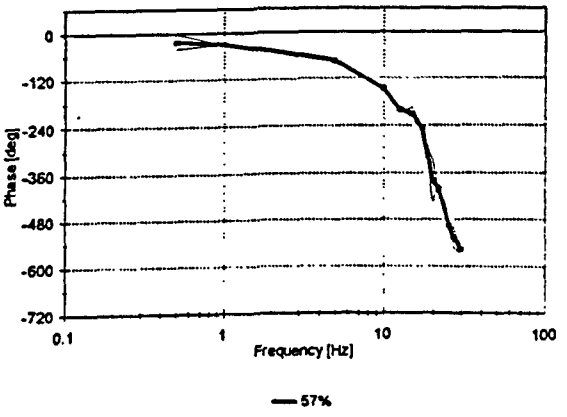

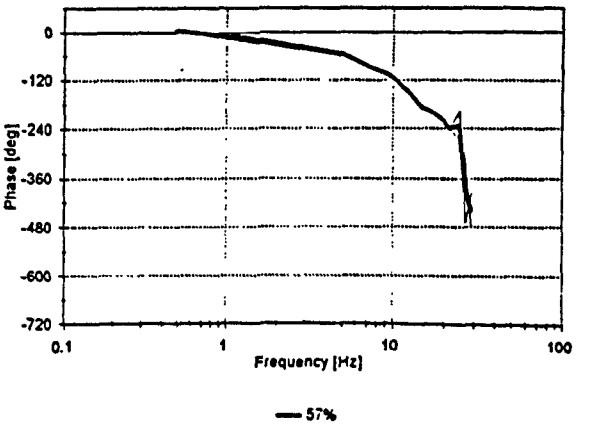

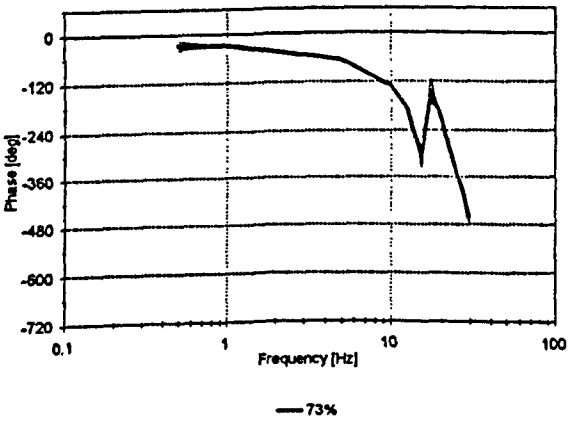

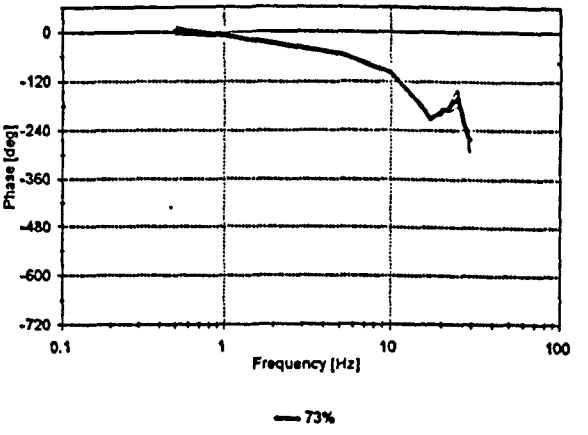

1000 RPM

1500 RPM

Fig. 8-6 Inflow Phase Response at three Radial Stations & two Rotor Speeds
(1200 rpm, Hot Wire 0.15m below, Collective Excitation)

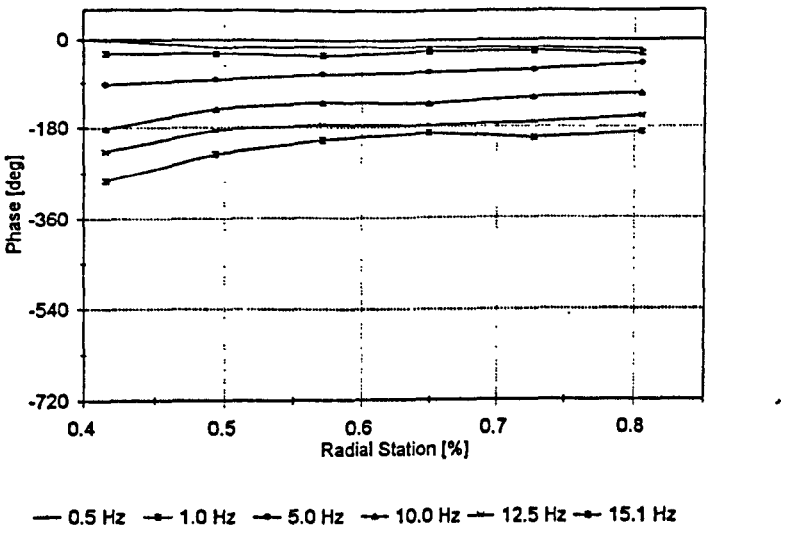

Fig. 8-7 Inflow Phase decreases towards the Tip Region
(1200 rpm, Hot Wire 0.15m below Rotor, Collective Excitation)

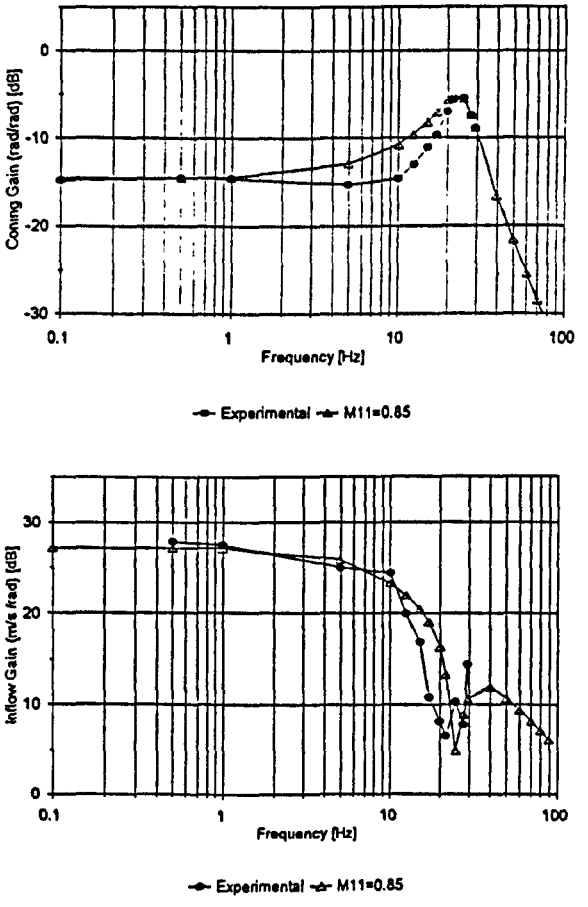

Fig. 8-8 Correlation between the Experimental and Predicted Inflow Response using 2 DoF Coning/Inflow Models with artificially Increased Coning Damping
(1200 rpm, Hot Wire 0.15m below, Collective Excitation, M_{11}=0.85)

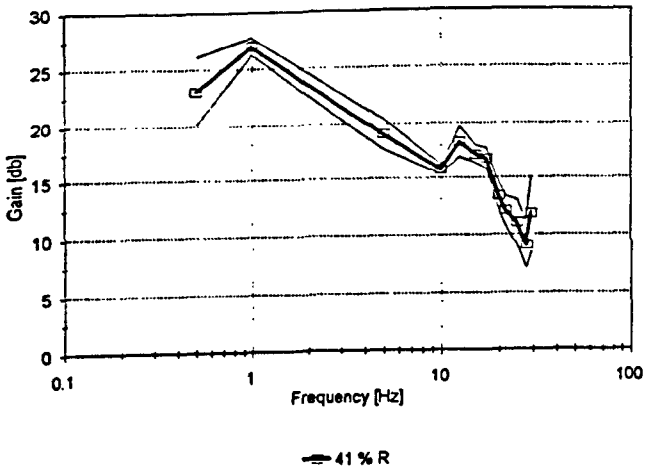

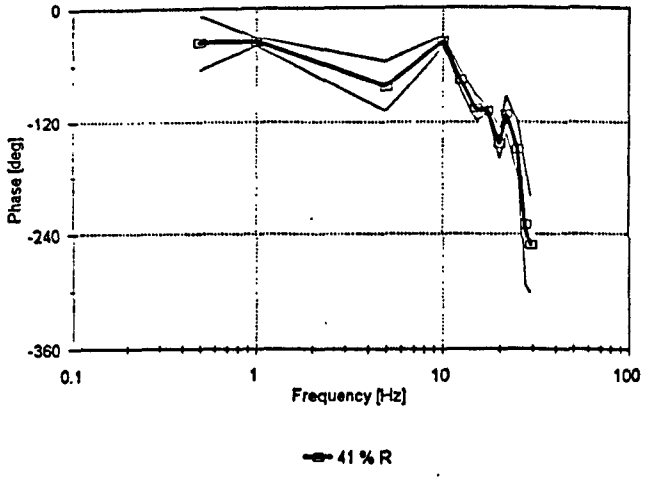

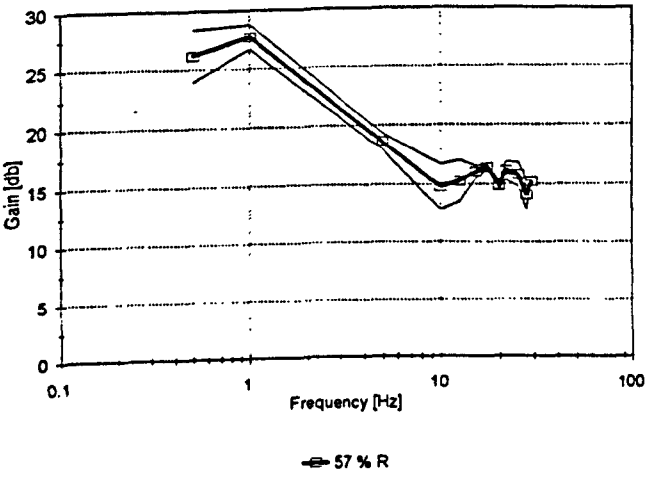

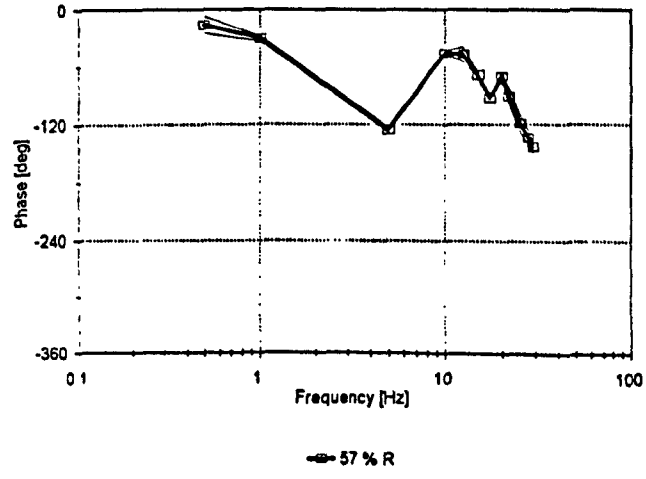

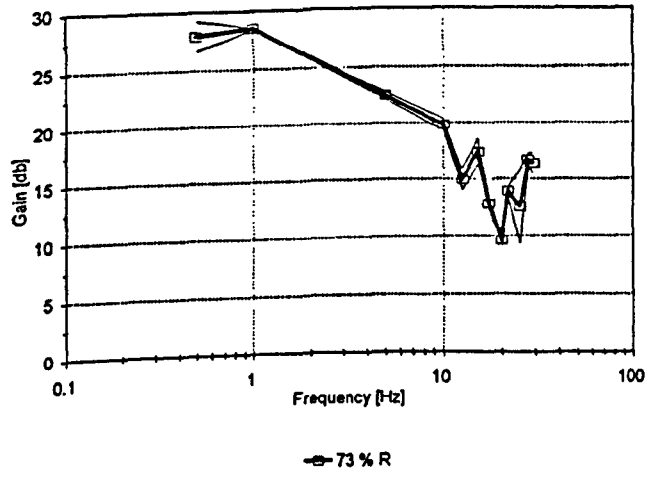

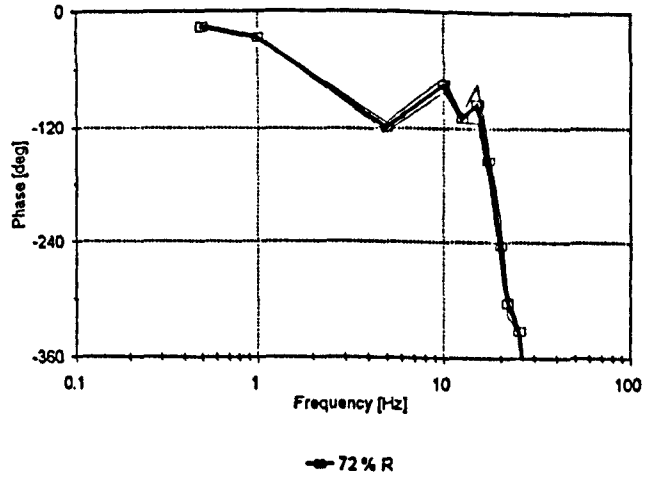

Fig. 8-9 Variation of the Inflow Frequency Response with Radial Station Cyclic Excitation
(1200 rpm, Hot Wire 0.15m below, 90 deg. Azimuth

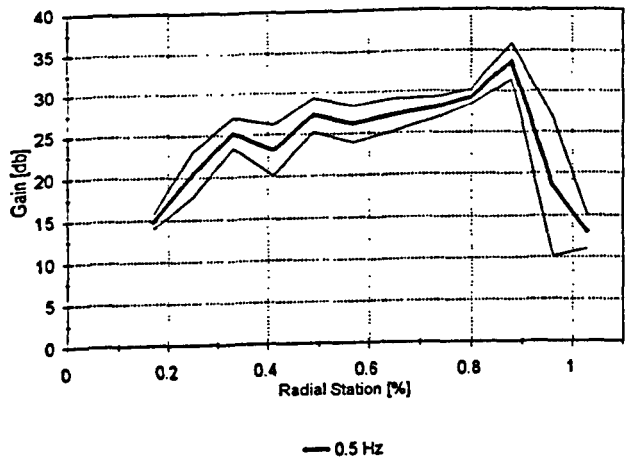

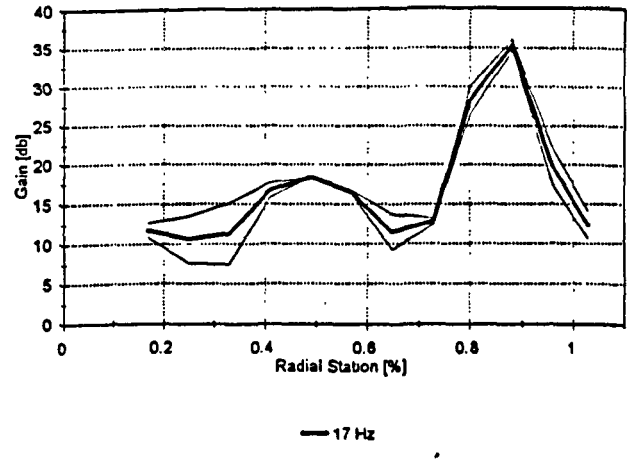

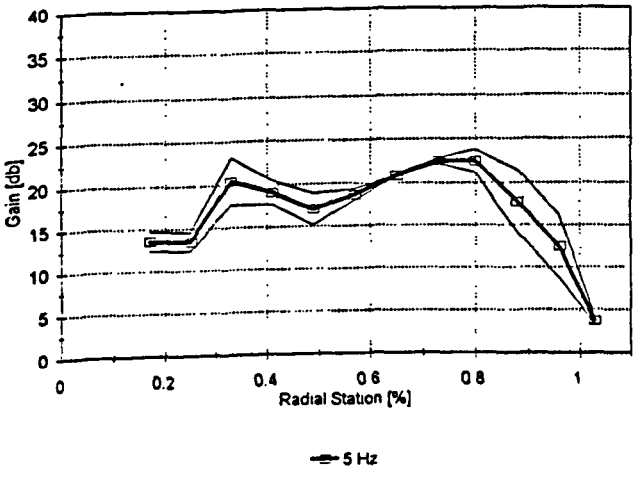

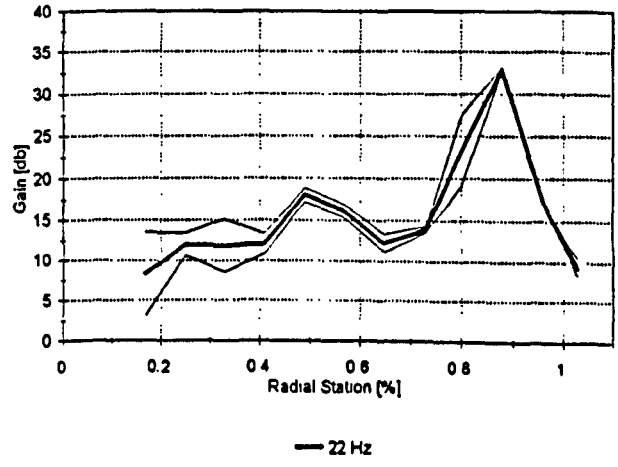

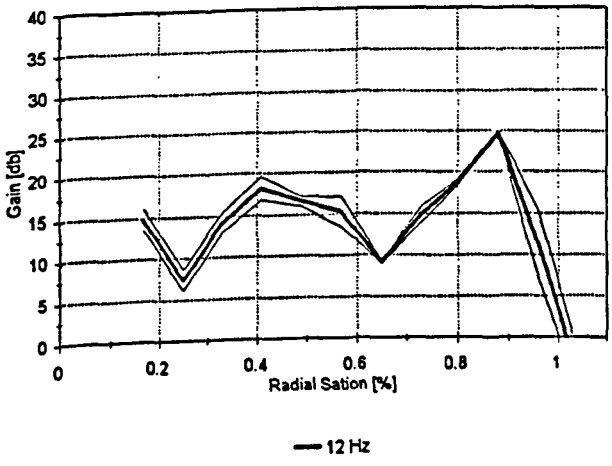

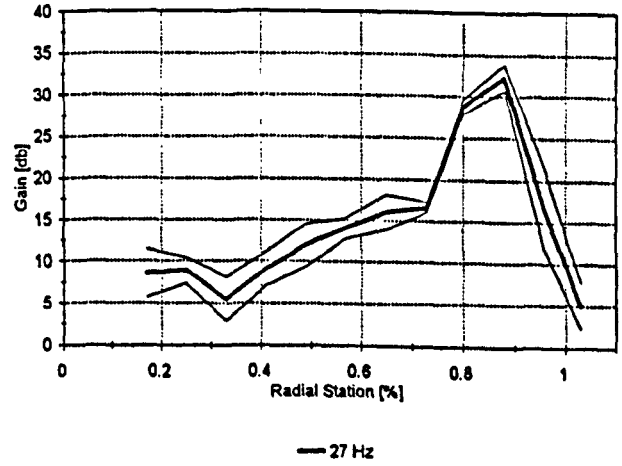

Fig. 8-10 Effect of Frequency on the Radial Inflow Distribution
(1200 rpm, Hot Wire 0.15m below, 90 deg. Azimuth)

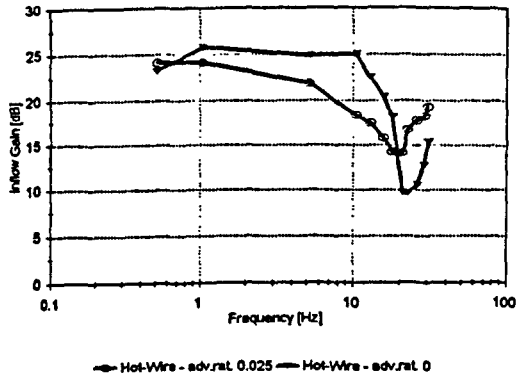

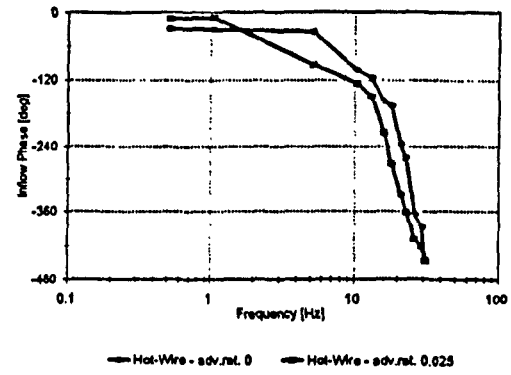

0 deg

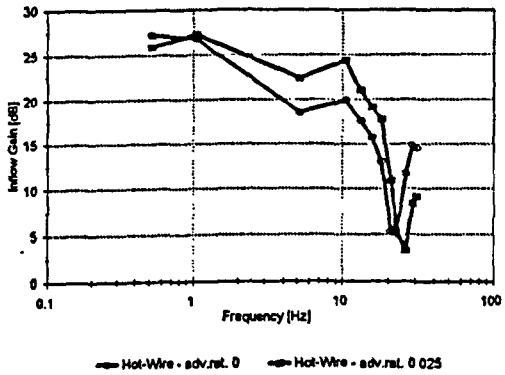

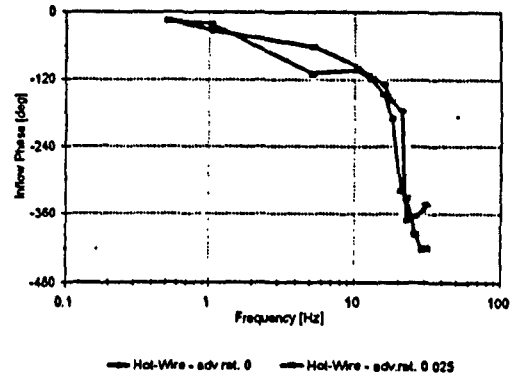

30 deg

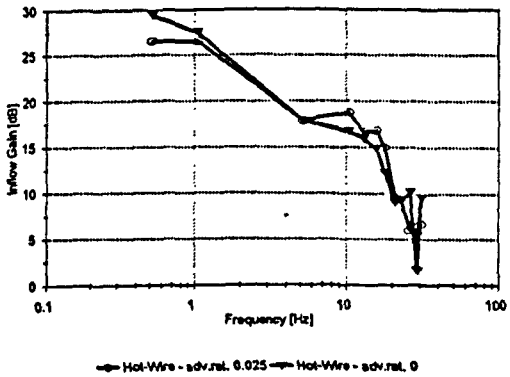

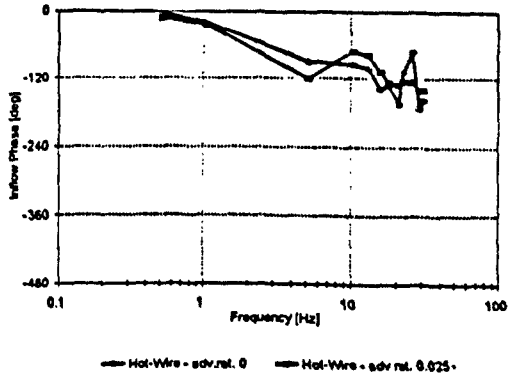

60 deg

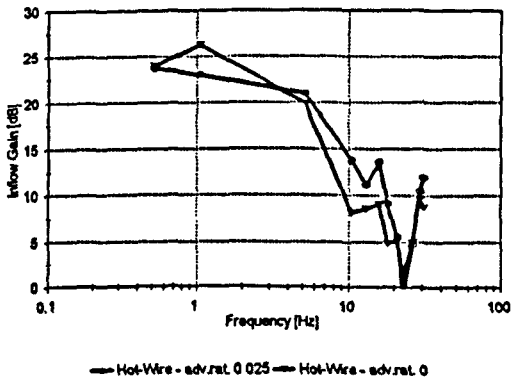

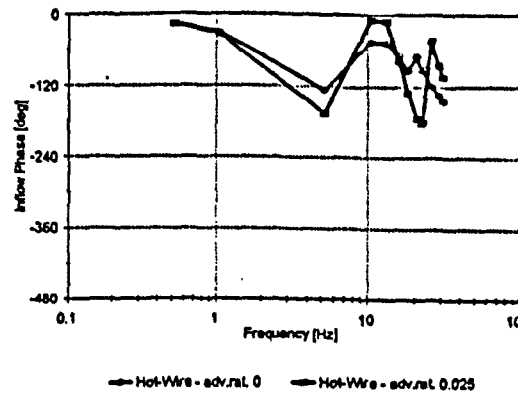

90 deg

Fig. 8-11 Inflow Frequency Response obtained at four Azimuth Positions
(1200 rpm, Hot Wire 0.15m below, 57% R)

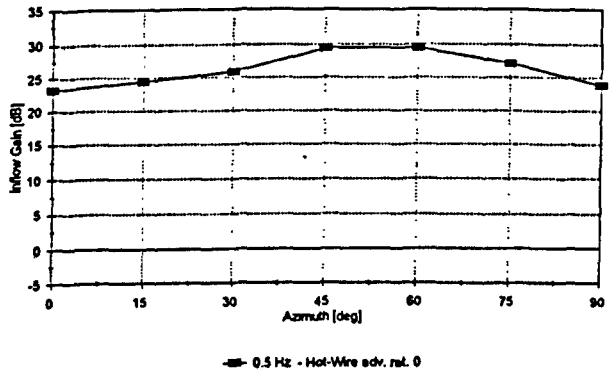

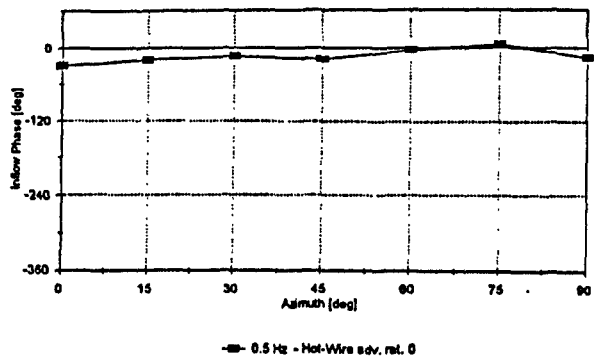

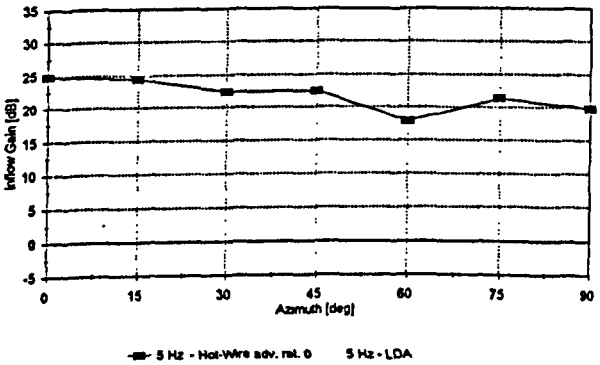

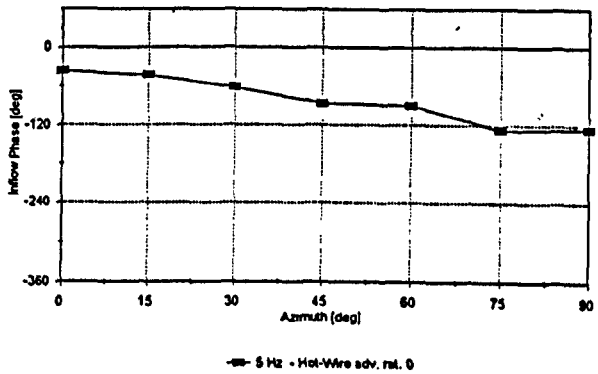

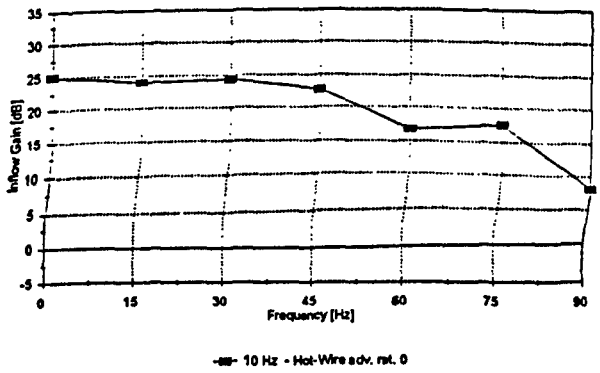

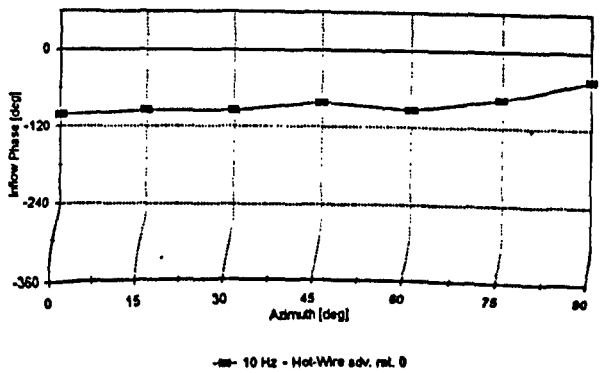

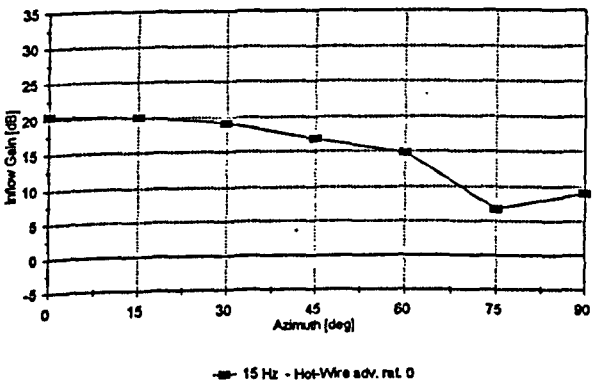

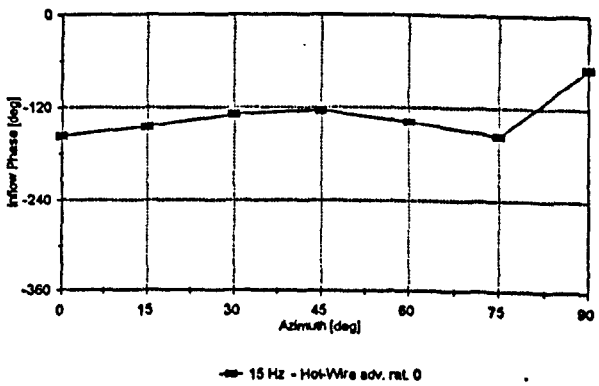

Fig. 8-12 Inflow Response Variation with Azimuth at selected Frequencies
(1200 rpm, Hot Wire 0.15m below, 57% R)

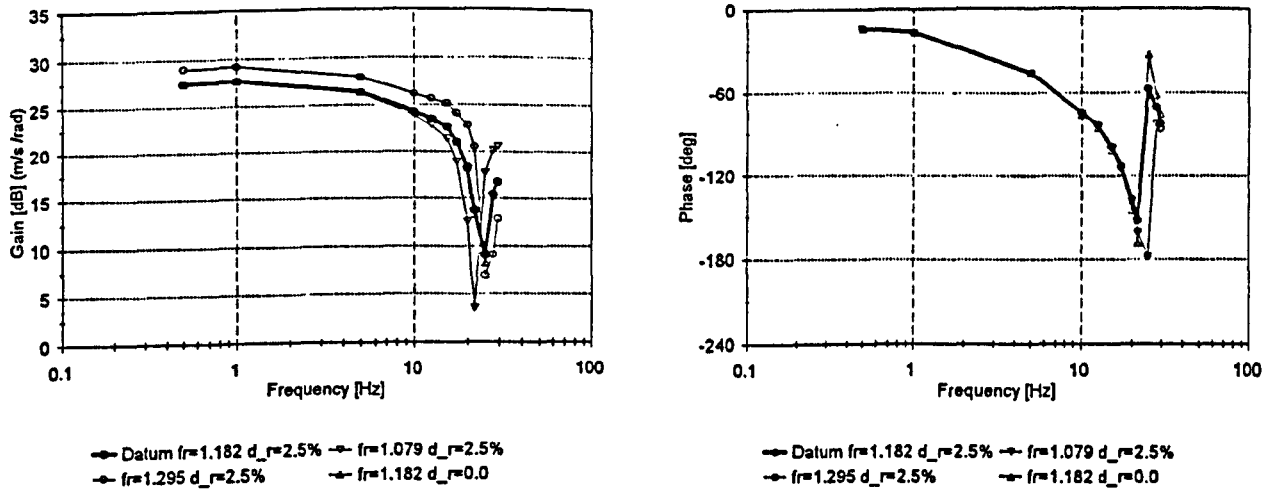

Sensitivity of the Inflow Response to Parameter Changes

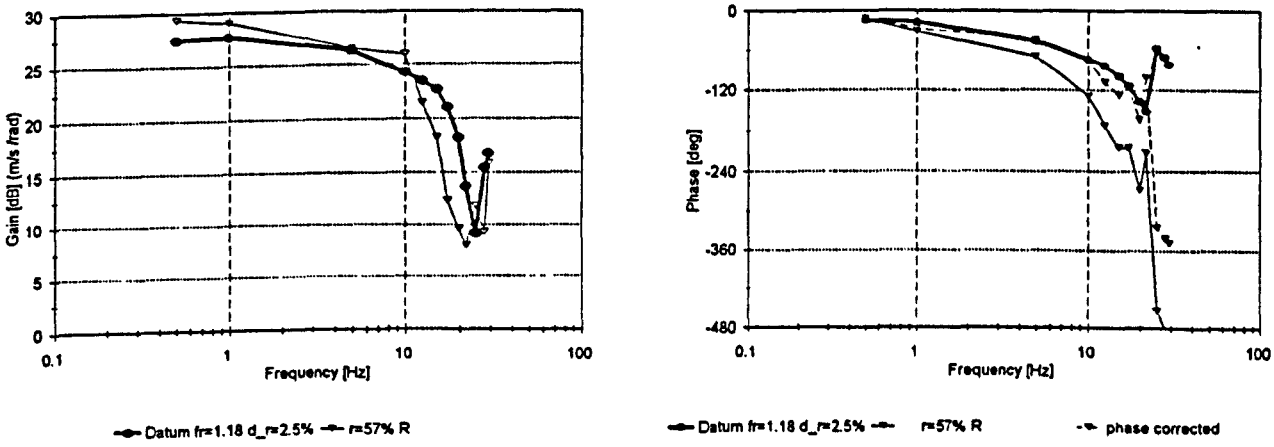

Inflow Response at 57% Radial Station

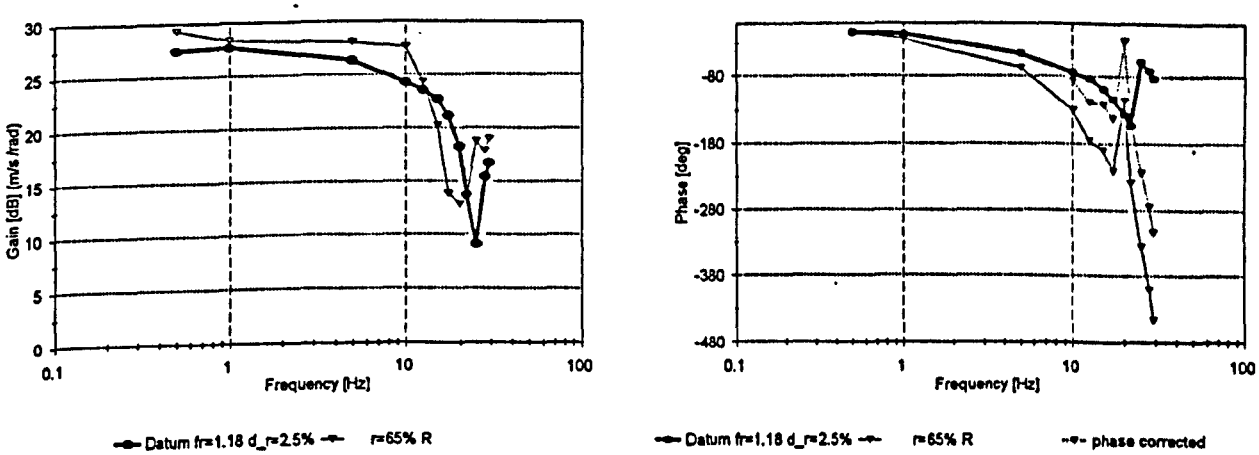

Inflow Response at 65% Radial Station

Fig. 8-13 Inferred Inflow Response Correlation with Experimental Results
Collective Case
(1200 rpm, Hot Wire 0.15m below,)

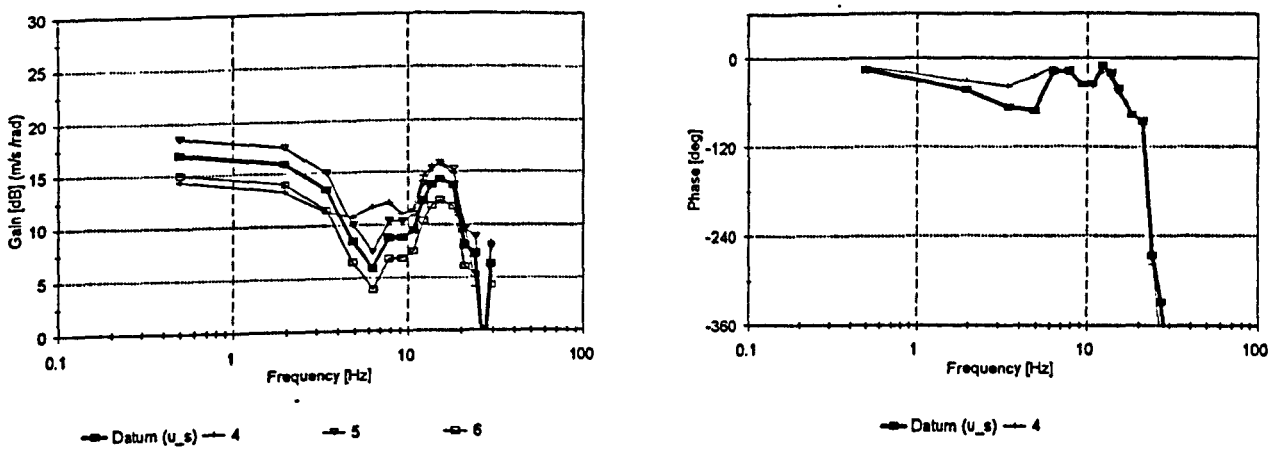

Sensitivity of the Inflow Response to Parameter Changes (90 deg)

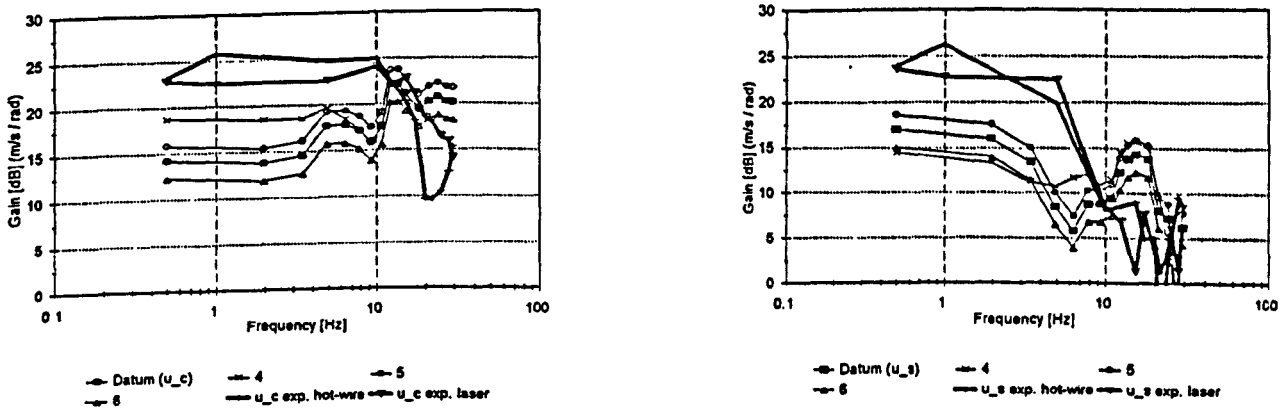

0 degrees Azimuth

	A	B	kr.	Damping
1 (Datum)	0.02346	0.03288	1.18	2.5%
4	A_{Datum}	B_{Datum}	1.18	20%
5	$1.2*A_{Datum}$	$1.2*B_{Datum}$	1.18	2.5%
6	$0.8*A_{Datum}$	$0.8*B_{Datum}$	1.18	2.5%

90 degrees Azimuth

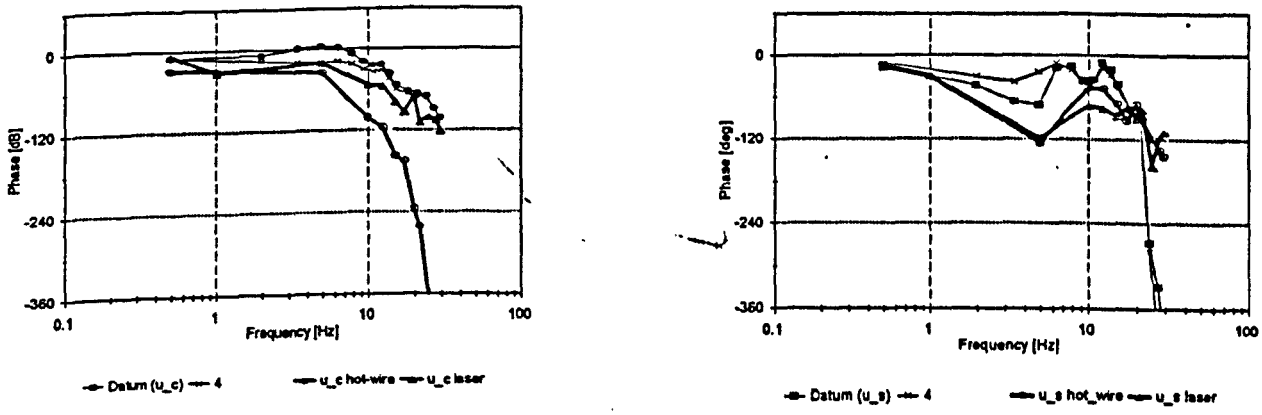

Fig. 8-14 Correlation of Inferred Inflow Response with Experimental Results Cyclic Case
(1200 rpm, Hot Wire 0.15m & LDA 0.1m below)

References

Bannerjee D., Crews S.T., Hohenemser K., Yin S., 1977. *Identification of State Variables and Dynamic Inflow from Rotor Model Dynamic Tests.* Journal of the American Helicopter Society, **(22)**.

BERGH H., TIJDEMAN H., 1965. *Theoretical and Experimental Results for the Dynamic Response of Pressure Measuring Systems.* Netherlands: NLR Report NLR-TR F.228.

BLEVINS R.D., 1979. *Formulae for Natural Frequency and Mode Shape.* New York: ISBN 0-89874-791-0.

BRADLEY R., BLACK C.G., MURRAY-SMITH D.J., 1989. *Glauert Augmentation of Rotor Inflow Dynamics.* Amsterdam: 15th European Rotorcraft Forum.

BRADLEY R., BLACK C.G., MURRAY-SMITH D.J., 1986. *System Identification Strategies for Helicopter Rotor Models Incorporating Induced Inflow.* Vertica, 13 (3).

BRAMWELL A.R., 1976. *Helicopter Dynamics.* London: E. Arnold. ISBN 0-7131-3753-8.

BRINSON P.R., 1991. *Experimental Investigation of Coupled Helicopter Rotor/Body Control.* Berlin: 17th European Rotorcraft Forum.

BUNNISS P.C., 1984. *Sprotan Rotor Performance Prediction Code.* Bristol: University of Bristol. Department of Aerospace.

CARPENTER P.J., FRIDOVICH B., 1953. *Effect of a Rapid Blade Pitch Increase on Thrust and Induced Velocity Response of a full-scale Helicopter Rotor.* NACA TN3044.

CHEN R.T., 1979. *A simplified rotor system math model for piloted flight dynamics simulation.* NASA TM 78575.

CHEN R.T., 1980. *Effects of Primary Rotor Parameters on Flapping Dynamics.* NASA TP 1431.

CHEN R.T., 1989. *A Survey of Non-uniform Inflow for Rotorcraft Flight Dynamics and Control and Control Applications.* Amsterdam: 15th European Rotorcraft Forum.

CHEN R.T., HINDSON W.S., 1987. *Influence of Dynamic Inflow on the Helicopter Vertical Response.* Vertica **(11)** 1.

ELLENRIEDER T.J., 1993. *Correlation of 2 Degree of Freedom Coning / Inflow Helicopter Rotor Models with Data Obtained from a Hover Stand.* Bristol: University of Bristol. Department of Aerospace.

ELLENRIEDER T.J., BRINSON P.R., 1994. *Experimental Investigation of Helicopter Coning / Inflow Dynamics in Hover.* Amsterdam: Twentieth European Rotorcraft Forum.

GAONKAR G.H., PETERS D.A., 1984. *A Review of Dynamic inflow and its Effect on Experimental Correlation.* California: American Helicopter Society. Second Decennial Specialists Meeting on Rotorcraft Dynamics.

GAONKAR G.H., PETERS D.A., 1986. *Effectiveness of Current Dynamic Inflow Models in Hover and Forward Flight.* Journal of the American Helicopter Society, **(31)** 2.

HARDING J.W., 1992. *Frequency Domain Identification of Coupled Rotor/Body Models of an Advanced Attack Helicopter.* American Helicopter Society. 48th Annual Forum.

HOHENEMSER K.H., CREWS S.T., 1973. *Model Tests on Unsteady Rotor Wake Effects.* Journal of Aircraft. (10) 1.

HOUSTON S.S, 1989. *Identification of Factors Influencing Rotorcraft Heave Axis Damping and Control Sensitivity in the Hover.* Royal Aircraft Establishment. AE Technical Report 88067.

HOUSTON S.S., 1993. *Informal Communication.*

HOUSTON S.S., BLACK C.G., 1990. *On the Identifiability of Helicopter Models incorporating Higher Order Dynamics.* Royal Aircraft Establishment. Tech Memo Fm37.

HOUSTON S.S., TARTELLIN P.C., 1989. *Theoretical and Experimental Correlation of Helicopter Aeromechanics in Hover.* Royal Aircraft Establishment. Tech. Memo Fm 20.

IFEACHOR E., JERVIS B., 1993. *Digital Signal Processing, A practical Approach.* Addison Wesley. ISBN 0-201-54413-x.

JOGLEKAR M., 1970. *An Actuator Disc Analysis of Helicopter Wake Geometry and Corresponding Blade Response.* California: USAAVLABS Tech. Rep. 69-66.

JOHNSON W., 1980. *Helicopter Theory.* Princeton University Press. ISBN 0-691-07971-4.

LAL M.K., 1994. *Measurement Around a Rotor Blade Excited in Pitch. Part 2: Unsteady Surface Pressure.* Journal of the American Helicopter Society, (39) 2.

LEITH D.J., BRADLY R., MURRAY-SMITH D.J., 1991. *The Identification of Coupled Flapping/Inflow Models for Hovering Flight.* 17th European Rotorcraft Forum .

LIOU S.G., KOMERATH M., ET AL, 1994. *Measurements Around a Rotor Blade Excited in Pitch. Part 1: Dynamic Inflow.* Journal of the American Helicopter Society, (39) 2.

MANGLER K.W., SQUIRE H.B., 1953. *The Induced Velocity Field of a Rotor.* Aeronautical Research Council, RM No. 2642.

ORMISTON R.A., 1972. *An Actuator Disc Theory for Rotor Wake Induced Velocities.* France: AGARD Specialists meeting on the Aerodynamics of Rotary Wings.

ORMISTON R.A., 1976. *Application of Simplified Inflow Models to Rotor Craft Dynamic Analysis.* Journal of the American Helicopter Society, (21) 3.

OWER E., PANKHURST R.C., 1977. *The Measurement of Airflow.* Oxford: Pergamon Press, ISBN: 0-08-021282-4.

PETERS D.A., 1988. *The Importance of Steady and Dynamic Inflow on the Stability of Rotor Body Systems.* NASA. CP10007.

PETERS D.A., BOYD D.D., HE C.J., 1989. *Finite-State Induced-Flow Model for Rotors in Hover and Forward Flight.* Journal of American Helicopter Society, (34) 4.

PETERS D.A., CHEN S.Y., 1982. *Momentum Theory, Dynamic Inflow and the Vortex Ring State.* Journal of the American Helicopter Society, (27).

PETERS D.A., GAONKAR G.H., 1988. *Review of Dynamic Inflow Modelling for Rotorcraft Flight Dynamics.* Vertica, (12) 3.

PETERS D.A., HAQUANG N., 1988. *Dynamic Inflow for Practical Applications.* Journal of the American Helicopter Society, (33) 4.

PETERS D.A., HE C.J., 1989. *Comparison of Measured Induced Velocities with Results from a Closed Form Finite State Dynamic Inflow Model.* American Helicopter Society. 45th Annual Forum.

PETERS D.A., HE C.J., 1987. *A Closed Form Unsteady Aerodynamic Theory for Lifting Rotors in Hover and Forward Flight.* American Helicopter Society. 43rd Annual Forum.

PITT D.M., PETERS D.A., 1981. *Theoretical Prediction of Dynamic Inflow Derivatives.* Vertica, (5) 2.

PITT D.M., PETERS D.A., 1983. *Rotor Dynamic Inflow Derivatives and Time Constants from Various Inflow Models.* 9th European Rotorcraft Forum.

PROUTY R.W., 1992. *Even More Helicopter Aerodynamics.* Potomac: Rotor & Wing International. Phillips Publishing Inc.

ROSEN A., BEIGELMAN Z., 1983. *A Simplified Model of the Influence of Blade Elastic Pitch Variations on Helicopter Rotor Flapping Dynamics.* Vertica, (7) 4.

SISSINGH G.J., 1951. *The Effect of Induced Velocity on Helicopter Rotor Damping in Pitch And Roll.* Aeronautical Research Council (Great Britain). A.R.C. Technical Report C.P. No. 101.

SOUTHWELL R.V., GOUGH B.S., 1921. *On the Free Transverse Vibration of Air Screw Blades.* Aeronautical Research Council, RM 766.

STRINGER J., 1976. *Hydraulic Analysis: An Introduction.* New York: Wiley. ISBN: 0-470-83377-7.

SU A., YOO K.M., PETERS D.A., 1992. *Extension and Validation of an Unsteady Wake Model for Rotors.* Journal of Aircraft, (29) 3.

SWALES C., RICKARDS J., BRAKE C.J., BARRETT R.V., 1993. *Development of an Improved Technique for the Alignment of Three-dimensional Laser Doppler Anemometers.* Bristol: Bristol University. Dept. of Aerospace Engineering.

TEMPLE G., BICKLEY W.G., 1956. *Rayleigh's Principle.* New York: Dover Publications.

Bibliography

BANNERJEE D., CREWS S.T., HOHENEMSER K.H., 1979. *Parameter Identification Applied to Analytic Hingeless Rotor Modelling.* Journal of the American Helicopter Society, (24) 1.

BERRY J.D, HOAD D.R., ALTHOFF S.L., 1987. *Helicopter Rotor Induced Velocities Theory and Experiment,* Texas: American Helicopter Society Specialist's Meeting on Aerodynamics and Aero-acoustics.

BERRY J.D., ALTHOFF S.C., 1990. *Inflow Perturbations due to Fuselage Effects in the Presence of a Fully Iterative Wake.* Annual Forum Proceedings. American Helicopter Society, (46) 2.

BIGGERS J.C., ORLOFF K.L., 1975. *Laser Velocimeter Measurements of the Helicopter Rotor Induced Flow Field.* California: NASA. Ames Research Centre.

BIGGERS J.M., CHU S., ORLOFF K.L., 1975. *Laser Velocity Measurements of Rotor Blade Loads and Vortex Roll-up.* American Helicopter Society. 31st Annual National Forum.

BISHOP R.E.D., JOHNSON D.C., 1960. *The Mechanics of Vibration.* London: Cambridge University Press.

BRITISH STANDARDS INSTITUTION, 1990. *Recommendations for the Presentation of Theses and Dissertations.* BS 4821.

BRITISH STANDARDS INSTITUTION, 1990. *Recommendations for Citing and Referencing Published Material.* BS 5605.

BRYER D.W., PANKHURST R.C., 1971. *Pressure Probe Methods for Determining Wind Speed and Flow Direction.* London: HMSO. ISBN 0-11-480012-x.

CARADONNA F.X., TUNG C., 1981. *Experimental and Analytical Studies of a Model Helicopter Rotor in Hover.* Vertica, (8) 1.

CARLSON R.G., BLACKWELL R.H., 1974. *Dynamic Stall Modelling and Correlation with Experimental Data on Airfoils and Rotors.* NASA Specialists Meeting on Rotorcraft Dynamics. NASA SP 352.

CHEESEMAN I.C., C. HADDOW C., 1988. *An Experimental Investigation of the Downwash Beneath a Lifting Rotor at low Advance Ratios.* Italy: 14th European Rotorcraft Forum.

CREWS S.T., HOHENEMSER K.H., ORMISTON R.A., 1973. *Unsteady Wake Model for a Hingeless Rotor.* Journal of Aircraft, (10) 12.

CROWSE G.C., LEISHMAN J.G., BI NAIPEI, 1990. *Theoretical & Experimental Study of Unsteady Rotor / Body Aerodynamic Interactions.* 46th Annual Forum of the American Helicopter Society.

CURTISS H.C., MCKILLIP R.M., 1990. *Coupled Rotor-Body Equations of Motion in Hover Flight - Interim Report 1989-90.* NASA CR 186710.

CURTISS H.C., SHOPE N.K., 1971. *A Stability and Control Theory for Hingeless Rotors.* American Helicopter Society. 27th Annual National Forum.

CURTISS H.C., ZHAO X., 1988. *A Linearized Model of Helicopter Dynamics Including Correlation with Flight Test.* American Helicopter Society. 2nd International Conference on Rotorcraft Basic Research.

DU VAL R., BRUHIS O., GREEN J., 1986. *Identification of a Coupled Flapping/Inflow Model for the Puma Helicopter from Flight Test Data.* Vertica, (13) 3.

ELLIOT J.W, ALTHOFF S.L., SAILEY R.H. 1984. *Inflow Measurements made with a Laser Velocimeter in Forward Flight.* American Helicopter Society. 2nd Decennial Specialist's Meeting on Rotorcraft Dynamics.

FAY J., 1987. *The Helicopter: History, Piloting, How it Flies*, Newton Abbot: David & Charles ISBN: 0-7153-890-8.

FEIK R.A., PERRIN R.H., 1989. *Identification of an Adequate Model for Collective Response Dynamics of a Sea King Helicopter in Hover.* Vertica **(12)** 3.

FUNG Y.C., 1955. *An Introduction to the Theory of Aeroelasticity.* New York: John Wiley & Sons Inc.

GAONKAR G.H., ET AL, 1983. *The Use of Actuator Disc Dynamic Inflow For Helicopter Flap-Lag Stability.* Journal of the American Helicopter Society, **(28)** 3.

GOODWIN C., PAYNE L., 1977. *Dynamic System Identification Experiment, Design, & Data.* New York: Academic Press. ISBN 0-12-289750-1.

HEYSON H.H., KATZHOFF S, 1957. *Induced Velocities Near a Lifting Rotor with Non-Uniform Disc Loading.* NACA Report 1319.

HOAD D.R., 1990. *Rotor Induced Inflow Ratio Measurements and Camrad Calculations.* NASA TP2940.

HOAD D.R., ALTHOFF S.C., ELLIOT J.W., 1988. *Rotor Inflow Variability with Advance Ratio.* American Helicopter Society. 44th Annual Forum.

JOHNSON W., 1986. *Recent Developments in the Dynamics of Advanced Rotor Systems.* Vertica **(10)** 2.

LEPICOVSKY J., BELL W.A., 1984. *Aerodynamic Measurements About a Rotating Propeller with a Laser Velocimeter.* Journal of Aircraft. **(21)** 3.

ORMISTON R.A., PETERS D.A., 1972. *Hingeless Helicopter Rotor Response with Non-Uniform Inflow and Elastic Blade Bending.* Journal of Aircraft, **(9)** 10.

PADFIELD G.D., 1981. *A Theoretical Model of Helicopter Flight Mechanics for Application to Piloted Simulation.* RAE TR 81048.

PERRY A.E., 1982. *Hot Wire Anemometry.* Oxford: Clarendon Press. ISBN: 0-19-856327-2.

PETERS D.A., 1987. *The Importance of Aerodynamics on Dynamics.* Texas: American Helicopter Society. National Specialist's Meeting on Aerodynamics and Aeroacoustics.

PETERS D.A., GAONKAR G.H., 1980. *Theoretical Flap-Lag Damping with Various Dynamic Inflow Models.* Journal of the American Helicopter Society, **(25)** 3.

PHELPS A.E., BERRY J.D., 1987. *Description of the U.S. Army 2 Metre Scale Rotor Test System.* NASA TM 87762.

PROUTY R.W., 1985. *Helicopter Aerodynamics.* Rotor & Wing International. PJS Publishing Inc.

PROUTY R.W., 1988. *More Helicopter Aerodynamics.* Rotor & Wing International. PJS Publishing Inc.

SCHRAGE D.P., PETERS D.A., PRASAD J.V.R., 1988. *Helicopter Stability and Control Modelling Improvements and Verification on Two Helicopters.* Italy: 14th European Rotorcraft Forum.

SEDDON J., 1990. *Basic Helicopter Aerodynamics.* American Institute of Aeronautics and Astronautics: AIAA Education Series. ISBN 0-930403-67-3.

TANGLER J.L., WOHLFELD K., MILEY S.J., 1973. *An Experimental Investigation of Vortex Stability, Tip Shapes, Compressibility and Noise for Hover.* NASA CR 2305.

WILSON J.C., 1992. *Experimental Evaluation of a Flat Wake Theory For Predicting Rotor Inflow Wake Velocities.* NASA TM 4334.

YOUNG M.I., 1962. *A Simplified Theory of Hingeless Rotors with Application to Tandem Helicopters.* American Helicopter Society. 18th Annual National Forum.

Appendix A - Précis of Reports

In this section précis for certain reports, which were considered of prime importance to the modelling, effects and measurement of dynamic inflow will be presented. The summaries concentrate on issues which are most relevant to the investigation and development of dynamic inflow theory and should in any future investigations of dynamic inflow save considerable time in locating relevant papers. They were obtained from many sources over a period of 3 years. The papers have been put in chronological order to give an indication of the temporal evolution of the theory.

Sissingh G.J. 1951,
The Effect of Induced Velocity on Helicopter Rotor Damping in Pitch and Roll
The report showed that variations of the thrust distribution over the rotor disc with respect to azimuth caused variations of induced flow around the disc which affected the damping in pitch and roll motions. This theory was substantiated by limited test data. The variations in induced flow distribution were assumed to be instantaneous.

Carpenter P.J. & Fridovich B. 1953,
Effect of a Rapid Blade Pitch Increase on Thrust and Induced Velocity Response of a Full-scale Helicopter Rotor
Experimental data on the thrust and induced velocity response of a helicopter rotor to collective pitch inputs was compared to theoretical results based on the concept of an apparent additional mass which is affected by the rotor disc. This was shown to introduce an apparent time delay between application of pitch changes and the resulting changes in induced velocity, which matched the experimental data well. To find the apparent mass term, the analogy between the rotor, idealised as a disc, and the air affected by an accelerating impervious disc was used. To further examine the blade coning dynamics associated with a sudden increase in collective pitch, the momentum derived thrust was equated to that found from a blade element approach. Together with the differential equations governing the blade motion the blade response could be found. Good correlation is found between the experimental coning and thrust data and the proposed theory. This paper firstly attempts to model the dynamics associated with the rotor inflow. Some flow visualisation results are also shown.

Mangler K.W., Squire H.B. 1953
The Induced Velocity Field of a Rotor
The rotor is treated as a circular disc with a pressure discontinuity across it. A pressure distribution which satisfies Laplaces equation and also gives a pressure discontinuity (i.e. lift) was given by Kinner in 1937 in terms of Legendre functions with an elliptical co-ordinate system. Using an assumed load distribution which gives the desired thrust, the induced velocity field can be determined. This is essentially the method used in the later Pitt and Peters model [Pitt & Peters 1983] , except that Pitt and Peters use the potential flow field to determine the degrees of freedom of a simple harmonic inflow distribution, and then extended their analysis to take apparent mass effects into account. Mangler considers two load distributions, where the second gives both the desired thrust and fulfils the zero load conditions at the centre and periphery of the rotor disc.

Ormiston R.A. 1972
An Actuator Disc Theory for Rotor Wake Induced Velocities
A generalised theory for calculating the time-averaged induced velocity distribution is presented but not completed. It is attempted to determine this using actuator or potential flow theory and simultaneously solving the equations of circulation distribution, downwash distribution and blade flapping dynamics.

Ormiston R.A., D. A. Peters D.A. 1972
Hingeless Helicopter Rotor Response with Non-Uniform Inflow and Elastic Blade Bending
A generalised harmonic balance theory is used to examine the steady-state, linear, response of a hingeless rotor in forward flight and the results are compared with experimental data. It was shown that a significant improvement in correlation with experimental data can be made by using non uniform, but quasi steady (i.e. no inflow dynamics) models for the induced velocity, that were derived using momentum and vortex theory. An empirical inflow model showed good agreement for low advance ratios. A result of the inflow models is that the change of inflow due to pitch/roll moments or thrust decreased with increasing overall thrust or forward speed. Thus the effect of quasi steady induced flow will be greatest for low disc loading. The forcing functions for the inflow are the aerodynamic loading of the rotor. Lacking in this inflow model representation is an analytical variation of the coupling terms between the loading and resulting inflow with increasing forward speed, starting at the hover.

Biggers J.C., Orloff K.L. 1975
Laser Velocimeter Measurements of the Helicopter Rotor Induced flow Field
Using a laser velocimeter both instantaneous and time averaged data velocities in the wake of a 2.13 m diameter rotor were obtained. From this the location and size of the tip vortex was determined.

Ormiston R.A., 1976

Application of Simplified Inflow Models to Rotor Craft Dynamic Analysis

The paper looks at the effect of including dynamic inflow models in eigen-analyses of rotors, such as flight dynamic stability or blade aeroelastic stability. In the paper the specific case of flapping dynamics is examined. The unsteady terms in the dynamic model are found from the analysis of the air affected by an impervious disc. For quasi-steady inflow a modified Lock number is sufficient. Quasi steady inflow reduced the off axis tip path plane response to cyclic inputs at low pitch, the more so for hingeless rotors. The effects on the flapping response are most significant at low pitch settings. The paper concludes that dynamic inflow can change the transient rotor flapping dynamics, particularly at low collective pitch settings and also reduces the regressing flap mode damping. The inflow mode is found to be low frequency, highly damped and well separated from the flapping modes. The effect of including dynamic inflow in the models is similar for both semi-rigid and articulated rotors. Dynamic inflow may adversely affect the stability of marginally stable systems, such as ground resonance of hingeless rotors by reducing flap damping.

Bannerjee D., Crews S.T., Hohenemser K.H. 1979

Parameter Identification Applied to Analytic Hingeless Rotor Modelling

Two inflow models one based on an equivalent Lock number, i.e. quasi steady, and a model including a dynamic inflow degree of freedom are identified from experimental data. The former model performs well for advance ratios down to 0.4. At lower advance ratios the dynamic inflow model performs better. The experimental data are obtained from a model rotor, but no inflow measurements are available.

Peters D.A., Gaonkar G.H., 1980

Theoretical Flap-Lag Damping with Various Dynamic Inflow Models

The paper examines the effect of dynamic inflow on the flap-lag dynamics of a rotor, by considering various inflow models in a dynamic rotor analysis. The models considered, include those based on no dynamic inflow, quasi steady momentum theory, unsteady momentum theory, empirical inflow and equivalent Lock number approaches. It concludes that dynamic inflow reduces the expected lift for the flapping mode and increases the expected drag for the lagging mode. These effects can be approximated using a reduced Lock number and modified profile drag coefficient. The effects of dynamic inflow are primarily on the regressing mode.

Chen R.T. 1980

Effects of Primary Rotor Parameters on Flapping Dynamics.

A rotor model for flapping dynamics is developed which includes as parameters flapping hinge offset, flapping hinge restraint, pitch-flap coupling and blade Lock Number. The effect of the parameters on flapping is studied. More importantly, this report derives the flapping equation

on which many body/coning/inflow models rely [Houston 1989, Houston & Tartellin 1989, Houston & Black 1990].

Pitt D.M., Peters D.A. 1981
Theoretical Prediction of Dynamic Inflow Derivatives

(This paper is reviewed in depth in Chapter 1)

Peters D.A., Chen S.Y., 1982
Momentum Theory, Dynamic Inflow and the Vortex Ring State
The time constant in the Pitt and Peters dynamic inflow model is related to a flow parameter. Certain combinations of forward speed, downward speed and loading of the rotor can make this parameter negative and thus predict instability in the induced flow. The paper examines the connection between this flow parameter and the helicopter, vortex ring state and windmill operating states of the rotor and finds that the predicted instability coincides with the vortex ring state, thus providing indirect verification dynamic inflow theory.

Pitt D.M., Peters D.A., 1983
Rotor Dynamic Inflow Derivatives and Time Constants from Various Inflow Models
The report provides a detailed history of the development of dynamic inflow modelling and the Pitt and Peters model. Two different models for the induced velocity response are considered. One assumes that the induced flow is related to the rotor loading by a complex gain matrix, i.e. containing gain and phase information, whose elements are functions of frequency and angle of attack. This assumes that the pressure field is always mutually in-phase and the method is termed superposition of velocities. The second approach assumes that the velocities are always mutually in-phase and the pressures are a complex superposition, hence the term superposition of pressures. The relationship between the induced flow and loading is then given by a real gains matrix and an apparent mass matrix which adds the dynamic component, or in other words gives the required phase delay. In this formulation which is used in the Pitt and Peters [Pitt & Peters 1981] dynamic inflow model, some parameters are a function of angle of attack, but not frequency.

Particular attention is again given to the results and dynamic inflow obtained from the assumptions of superposition of pressures and velocities, and significant differences found. The true rotor should behave somewhere between the two methods. The superposition of pressure method however is computationally simpler, and to be preferred as it allows analytical expressions for the L elements as functions of angle of attack to be found. None of the elements are functions of frequency as is the case in the superposition of velocities approach. The overall conclusion is that the differences between both methods are not significant enough to justify the abandonment of the simpler method. Another approach is considered in finding the elements of the L matrix. This time-only steady actuator disc theory, i.e. no inflow

dynamics, is considered. The conclusions are that the elements are independent of lift distribution and in hover are the same as momentum theory. The L matrix is invertable at all times as required in the inflow formulation. Finally a discrete vortex analysis, also called lifting line theory is used to find the elements of the L matrix. This process is essentially a computational aerodynamics approach, where the vorticity in the wake (assumed to be rigid) is integrated to find the induced flow at the disc. From this the equivalent L matrix elements are obtained. This analysis is interesting because it includes the effects of wake contraction, skew and finite number of blades, but is again only concerned with the steady case. The analysis produces some cross coupling terms, $L_{3,2}$ and $L_{2,3}$, which are due to wake rotating, but small compared to the diagonal terms (<10%).

Gaonkar G.H., Peters D.A., 1983
The Use of Actuator Disc Dynamic Inflow For Helicopter Flap-Lag Stability
Dynamic inflow is defined as the low frequency properties of the wake under unsteady conditions in contrast to conventional high frequency unsteady aerodynamics, such as flutter. The work compares the results for the prediction of flap-lag damping from 13 models. These are based on time-delayed unsteady momentum theory with first harmonic inflow, unsteady actuator disc theory (first and second order inflow distributions) and simple lift deficiency functions. Potential theory as used by the Pitt and Peters inflow description, yields better results than that obtained using models based on unsteady momentum theory. At high advance ratios quasi steady inflow models are sufficient. The use of corrected or uncorrected lift distributions to give the correct hub loading boundary conditions have little effect on the flap-lag damping.

Gaonkar G.H. & Peters D.A. 1984
A review of Dynamic inflow and its Effects on Experimental Correlation
The report gives a detailed account of the historical development of dynamic inflow and examines the correlation between experimental data and theoretical models including dynamic inflow. The report then focuses on the development of the Pitt and Peters [Pitt & Peters 1983] dynamic inflow model and the fact that it recovers momentum theory results in hover. Results from both a superposition of velocities and superposition of pressures approach [Pitt & Peters 1983] are compared, and it is concluded that both provide similar results, justifying the use of the simpler superposition of pressure formulation used in the Pitt and Peters model. The report also suggests, but does not develop the idea further, that the effects of tip loss can be incorporated in the L and M matrices. Results showing the roll and pitch moment response of a rotor due to cyclic excitation up to frequencies of 1.2 shaft speed are compared to the predictions of models including no inflow, quasi steady and dynamic inflow. The results highlight the improvement gained through the use of dynamic inflow.

Elliot J.W., Althoff S.L., Sailey R.H., 1984

Inflow Measurements Made with a Laser Velocimeter in Forward Flight

Inflow measurements were made with a Laser Doppler Anemometer on a 2 bladed rotor. The data gathered 1 chord above the tip path plane of the rotor at an advance ratio of 0.3 at 180 locations spaced around the azimuth. The pitch of the rotor was not changed dynamically.

Gaonkar G.H., Peters D.A, 1986

Effectiveness of Current Dynamic Inflow Models in Hover and Forward Flight

The report gives a very good historical development of dynamic inflow theory. Observations in 1950 showed that the theoretical pitch-roll damping did not agree with flight results. Sissingh showed that a roll rate results in side to side variations in thrust distribution ,which in turn could cause perturbations of the induced flow field. These could affect the damping in roll and pitch. The induced flow perturbations could be taken into account by using an equivalent Lock number in flight dynamics examinations. So far it had been assumed that the variation of induced flow occurred instantaneously with changes in thrust. In 1953 Carpenter and Fridovich [Carpenter & Firdovitch 1953] introduced a time delay in the cause and effect relationship. The time delay was based on the apparent mass that an impervious disc would accelerate. Eventually in 1972 time delays were introduced, not only for the uniform induced flow, but also the side to side variations. The mathematical relationship between the induced flow variations and thrust perturbations was determined in 1981 by Pitt and Peters for flight conditions ranging from hover to edgewise flow by using actuator disc theory. The report then further examines the effectiveness of current dynamic inflow models. Experimental data of the frequency response of coning in hover, in response to cyclic pitch inputs is compared to theory including the Pitt and Peters [Pitt & Peters 1983] inflow models and good correlation is found. Data for advance ratios of 0.27, 0.36 and 0.51 are also considered. Good correlation between the experimental and theoretical frequency responses of roll and pitch moments, due to changes in cyclic pitch, is found.

Peters D.A., 1987

The Importance of Aerodynamics on Dynamics

The paper uses dynamic inflow theory as an illustration of the effects of aerodynamics on rotor dynamics. It stresses the importance of feedback loops between the lift generated by a blade and the resulting inflow and blade response which both affect the generated lift. A good introduction to the theory of dynamic inflow is given. The effects of dynamic inflow are illustrated by examining the effect on the rotor roll and pitch response, due to cyclic inputs. It concluded that it is not sufficient to model dynamic inflow as a lift deficiency function but it needs to be included as separate degrees of freedom in a rotor analysis.

Chen R.T., Hindson W.S., 1987

Influence of Dynamic Inflow on the Helicopter Vertical Response

The report examines the effect of dynamic inflow on the helicopter's vertical response and blade flapping in hover. Linearised versions of the Pitt and Peters [Pitt & Peters 1983] and Carpenter [Carpenter & Fridovich 1957] dynamic inflow models were incorporated into simple rotor body models and the effect of variations in thrust coefficient and Lock number investigated. The essential difference between the models is the assumed value of the apparent mass factor, the Carpenter model having a higher value than the corrected mass value from the Pitt and Peters model [Pitt & Peters 1983]. The rotor body model was based on a four bladed articulated rotor, with no hinge offset or blade twist, developed by Chen [Chen 1979]. Comparisons were also made between the linear analysis and transient data from a CH-47B helicopter. It was found that dynamic inflow destabilises the flapping mode and introduces an inflow mode which results in large initial overshoots in flapping due to step inputs in collective. Inclusion of dynamic inflow reduces both the frequency and damping of the flapping mode compared to the uncoupled flapping response with no dynamic inflow. The Pitt and Peters [Pitt & Peters 1983] model generally produces more oscillatory responses and has a smaller time constant due to its smaller apparent mass value. Reducing the apparent mass to zero provides a quasi steady description of the inflow with a time constant of zero. It was also used to model the step input in collective of the CH-47B research helicopter, with good correlation, initially and towards the end of the time record. The worse correspondence after the initial response is attributed to poor rotor speed governing.

Cheeseman I.C., Haddow C., 1988

An Experimental Investigation of the Downwash Beneath a Lifting Rotor at low Advance Ratios

Using tri-axial hot wires the flow beneath a rotor was examined successfully. Strain gauges on the blade provided information on flapping and hub moments. For accurate results the bending modes of the blade had to be considered. Within a prescribed incidence range the tri-axial hot wire probe was able to determined the three dimensional flow within the wake. Consideration of the time averaged data shows that Glauert's formula for the distribution of steady induced flow is not ideal. The frequency content of the wake was also considered and contained mainly rotor blade passage harmonics. Strength and position of the bound circulation and tip vortex roll up was also determined.

Peters D.A., Gaonkar G.H., 1988

Review of Dynamic Inflow Modelling for Rotorcraft Flight Dynamics.

The Pitt/Peters dynamic inflow model which is based on unsteady actuator disc theory is compared to models derived from simple, extended momentum theory and a prescribed-wake, lifting line, discrete vortex analysis and those derived empirically. The primary emphasis of the work is on linear, small perturbation formulations of dynamic inflow in matrix form, although

non-linear versions for use in time-history applications are also considered. The report concludes that the, "Pitt model stands out as a premier dynamic model" when predicting the global behaviour of the air mass flow. It is derived from first principles, reduces to momentum theory in hover and has been verified on a basis of flapping response data. Strong points of this report are it systematic development of the L matrix from momentum theory, empirical models and finally extended momentum theory: the Pitt and Peters [Pitt and Peters 1983] dynamic inflow model. If apparent-mass effects are not considered, i.e. only the L matrix, then the response of the inflow degrees of freedom to the rotor loading is instantaneous. This is called quasi steady inflow theory. In quasi steady theory, the inflow response to loading changes will decrease lift and increases drag. The report shows that this can be taken account of by an equivalent Lock number and increased drag coefficient. The equivalent Lock number is identical to Loewy's lift deficiency functions. The historical development of the M matrix is also outlined, and the early interpretation of the apparent-mass elements in terms of the non dimensional reaction forces and moments of an impermeable disc under acceleration or rotation, are given. Higher harmonic inflow models are also considered.

The problem of validating dynamic inflow models is also addressed, because of the difficulty in isolating the induced flow effects. In the absence of direct inflow data, pure flapping data are considered best for the validation of dynamic inflow models. Finally the report deals with common misconceptions in Dynamic Inflow Modelling: the use of the correct mass flow parameter, the relevance of dynamic inflow not only to stiff rotor hubs, the lift deficiency approximation to quasi steady inflow and not dynamic inflow, and the use of tip loss factors in the L and M matrices. The item on tip loss factors is very interesting. Previously it was suggested by Gaonkar [Gaonkar & Peters 1984] that the tip loss effects could be included in the L and M matrices through appropriate factors. In this paper it is argued that the tip loss is already implicitly accounted for in that blade loading function, which is zero at the tip.

Peters D.A., HaQuang N., 1988
Dynamic Inflow for Practical Applications
The Pitt and Peters dynamic inflow model which is usually presented as a small perturbation model in the wind axis system in terms with no hub motion is reformulated to be more usable for practical applications, in a rotor co-ordinate frame and allowing for hub motions. The model is given in non-linear and perturbation form and allows for sideways flight. The sign definition used in this paper is different to that used in the original Pitt and Peters model [Pitt & Peter 1983] and this results in sign changes to the L and M matrices.

Houston S.S. 1989

Identification of Factors Influencing Rotorcraft Heave Axis Damping and Control Sensitivity

A model of the Puma helicopter using quasi steady rotor approximations was used to predict its response in heave. The results showed that the quasi steady model was unsatisfactory, overestimating vertical gain and damping by 50% and 100% respectively. In an attempt to resolve this matter a 3 Degree of Freedom body/ coning/ inflow model based on work by Chen and Hindson [Chen & Hindson 1987] was identified from flight tests and compared to theoretical predictions. Significantly, the inflow dynamics were inferred from coning and vertical acceleration data as no direct measurement of inflow was possible. The 3 DOF model needs to be improved to take into account unsteady wake effects and the limitations of the simplification of a rigid blade. The magnitude of the apparent air mass term identified from flight test data is in good agreement with that proposed by Carpenter and Fridovich.

Houston S.S, Tartellin P.C, 1989

Theoretical and Experimental Correlation of Helicopter Aeromechanics in Hover

The paper describes a validation tool kit and database for the development of an appropriate mathematical model for helicopter response to collective in hover, using a 3 D.O.F body/coning/inflow model based on initial work by Chen and Hindson [Chen & Hindson 1987]. The paper uses in its representation of dynamic inflow the Carpenter/Fridovich term for the apparent mass, as this gives better results than that of the *corrected* Pitt and Peters [Pitt & Peter 1983] model. Using system identification by transfer function matching in the frequency domain the need of a 3 D.O.F body/coning/inflow model is emphasised. The identified model parameters suggest that the model will be substantially in error unless real wake effects and blade flexibility are incorporated in the model. Real wake effects were introduced using correction factors, but these are generic to every rotor. The limited range of the linear model could be demonstrated by increasing the size of step responses, which resulted in decreasing correlation with theory, although this can to some extent be attributed to poor rotor speed governing of the Puma helicopter. It was also shown that models with the same structure, but significantly different model parameters, can produce similar frequency responses over a limited frequency range. The use of a Research Instrumented Blade analysis (RIB) which utilised a blade with local pressure sensors on the leading and trailing edges was also used to gain a better understanding of inflow on the actual rotor. This analysis gave information of local induced velocities and angle of attack on the blade over the azimuth range after a step input in collective. It was shown that the distribution of incidence is essentially uniform over 86% of the blade span. Outboard of this, blade vortex effects cause loading peaks which account for half the rotor thrust. The same is true for the inflow distribution. These findings question the validity of simple momentum based flight mechanics.

Bradly R., Black C.G., Murray-Smith D.J., 1989

System Identification Strategies for Helicopter Rotor Models Incorporating Induced Inflow

A frequency domain method using output error system identification is developed to validate rotor models including dynamic inflow. The models considered include second order flapping and first order inflow. The main advantage of frequency domain techniques is that a frequency range over which the identification is carried out and over which the model is valid can be defined. It is concluded that equation error identification methods cannot be used as there is no available inflow measurement, and thus an output error method needs to be adopted. Only flapping data gained in hover are used to identify the models. No particular advantage in using models with dynamic inflow dynamics could be found, and reduced order models gave good results. This is thought to be due to the considered flight condition of fast forward flight where the effects of dynamic inflow would be small.

Peters D.A., Boyd D.D., He C.J., 1989

Finite-State Induced Flow Model for Rotors in Hover and Forward Flight

A dynamic induced inflow theory for rotors with a finite number of blades is presented for forward flight and hover. The coefficients of the Fourier and Legendre functions which describe the azimuthal and radial inflow distribution form the finite states of the model. These can be linked by differential equations to the circulatory lift distribution. The model is derived from first principles based on actuator disc theory, which utilises a pressure distribution with a discontinuity about the rotor plane, but which otherwise satisfies Laplace's equation. Account is taken of the individual pressure peaks caused by the blade passage. The number of harmonics and shape functions used to describe the induced flow field is determined by the user, but an aerodynamic model, which gives the aerodynamic loading, must match the complexity of the dynamic model. The model shows good correlation with the thrust and blade flapping response obtained from collective frequency responses. The main difference between this model and the Pitt and Peters model [Pitt and Peters 1983] is that the forcing function is no longer the aerodynamic hub loading but the pressure coefficients of the assumed loading obtained from circulatory blade lift. The chordwise variation of pressure should also be available but may be replaced by an approximate function. The authors consider it to be particularly useful in the area of aeroelasticity and the design of higher harmonic controller models. It is less suitable for use in flight dynamic models, as accurate inflow estimates are only available from models providing accurate blade loading predictions, and these are difficult to produce in real time.

Chen R.T., 1989

A Survey of Non-uniform Inflow Models for Rotorcraft Flight Dynamics and Control Applications

The text charts the development of rotor inflow models, from the initial uniform, time invariant models, through to non-uniform and finally dynamic inflow models. Several non uniform inflow models are examined, with particular attention being given to uses in flight dynamics and control applications. Simple first harmonic inflow models are compared to more sophisticated methods developed for performance and airload computations based on free, prescribed and flat wake methods, but only in the static sense. Comparison with experimental data show that the Pitt and Peters [Pitt & Peters 1983] first harmonic dynamic inflow model works well overall.

Houston S.S., Black C.G., 1990

On the Identifiability of Helicopter Models Incorporating Higher Order Dynamics

A three degree of freedom body/coning/inflow model based on work by Chen and Hindson [Chen & Hindson 1987] was examined w.r.t. identifiability and robustness as frequency range, parameter constraints, a priori estimates and identification methods were varied. An output error method in the frequency domain and a time series analysis for transfer function matching were used. Both methods provided similarly good fits, but for the output-error method the derivatives in the inflow equation had to be fixed, as no inflow data were experimentally measured. It was found that the model parameters were sensitive to the frequency range used and to any a priori estimates made to initiate iterative processes. The transfer function method also showed sensitivity to the test run.

Leith D.J., Bradly R., Murray-Smith D.J., 1991

The Identification of Coupled Flapping/Inflow Models for Hovering Flight

The optimum experiments needed to identify flapping/inflow models for hover are examined. For a second order flapping, first order inflow representation, all parameters can only be obtained when inflow measurements are available. If these are not available then some of the parameters need to be determined by a priori information. The required frequency content and power distribution of the input signals for optimum identification are also considered. It was found that for a second order flapping, first order inflow representation, low frequency information is of prime importance when no inflow data are available, and in any case frequencies up to the rotor shaft frequency need to be considered. When inflow data are available this zero frequency component is not as important. The report also highlights the problems when using pilot generated frequency sweeps and step inputs as regards accurate frequency content, particularly frequencies above 1Hz.

Su A., Yoo K.M., Peters D.A., 1992

Extension and Validation of an Unsteady wake Model for Rotors

This report continues the previous development of a three-dimensional, finite state, generalised wake model. Similar to the Pitt and Peters model [Pitt and Peters 1983] it is based on actuator-disc theory which has been extended. The input to the model is the circulatory lift distribution along the blade. The flow field is described by the coefficients of the azimuthal harmonics and radial shape functions, these are the degrees of freedom of the model. The number of harmonics or shape functions used is decided by the user and by the necessary fidelity of the required flow field. These states are linked by ordinary differential equations to the circulatory lift distribution. It follows that the complexity of the lift distribution must match the required detail of the induced flow field. The basis for finding a link between the rotor loading and flow field is Prandtl's acceleration potential function, which satisfies Laplace's equation and gives a pressure discontinuity across the disc. This is similar to the Kinner pressure distribution used in the Pitt and Peters model except that time varying coefficients are added. Similarly the wake model now also includes coefficients which vary with non-dimensional time, and are the basis for predicting the effect of blade passage on the induced flow. Further details of the model's development and application are given by Peters [Peters & He 1987] and Boyd [Peters, Boyd & He 1989].

This paper further considers the extension of the linear model to include the application in the hover condition through the used of appropriate mass flow parameters. Subsequently the model is extended to take account of the steady and perturbation thrust and inflow. Hence the linear model has been extended to the non-linear case which considers the total resulting flow through the disc. This is analogous to the non-linear inflow model of Pitt and Peters [Pitt & Peters 1981]. Finally, provision is made to examine the induced flow in the rotating frame by using a reference blade. This is particularly relevant in the hover condition. For the results generated in this paper the circulatory lift at a radial station on any blade was found from quasi-steady two dimensional aerodynamics. The lift at a section on along the blade is dependent on the local angle of attack and lift curve of the blade. In this way unsteady effects are considered through the time varying angle of attack. Lift theories that already include a factor to account for unsteady effects, such as lift deficiency factors, are not suitable, as they do not allow for the feedback loop between dynamic induced flow and blade lift.

Finally the paper examines the predicted flow field for various special cases. Firstly the radial inflow variation for a one-bladed rotor at low collective pitch setting (1 deg.), under steady conditions is examined, and the effect of the chosen number of radial shape and azimuthal harmonics examined. Significantly, the inflow distribution increases sharply at the tip, contrary to the expected drop of inflow near the tip due to tip effects and wake contraction.

Next a case with large collective pitch (10 deg), representing the hover case is examined. Several iterations are needed to find the induced average flow and therefore the induced flow states. It is found that the model converges only slowly to a theoretical solution in the tip and root regions as the number of radial shape functions is increased.

The difference between the flow fields predicted for steady and unsteady pitch are also examined. For the unsteady case the pitch is varied at four times the rotational speed, at a collective setting of 4 degrees with an oscillatory pitch of one degree. As the excitation frequency is an exact multiple of the rotational frequency a link between azimuth and blade root pitch can be established. By examining the inflow response at various azimuth positions a picture of the time-varying inflow response can be built up, and this is presented.

Limited experimental data for the validation of the model were available from a two bladed teetering Bell 212 tail rotor. Comparisons of the induced flow at two radial stations under steady conditions show that, the model predicts the spikes seen in experimental inflow data caused by the passing of the blade over the measuring position well, if sufficient azimuthal harmonics (about 24) are allowed. Finally experimental data obtained from the bell tail rotor at a collective pitch setting of 4 degrees and unsteady pitch of 1 degree at four-per-rev. is presented. There is little observed difference from the data with steady pitch. The predicted inflow response for both cases again shows negligible difference between the steady and unsteady case.

Liou S.G., Komerath M., 1994
Measurement Around a Rotor Blade Excited in Pitch, Part 1: Dynamic Inflow
A two-bladed rotor in hover is subjected to controlled pitch excitation at four times the rotational frequency of 10 Hz. Inflow data were taken at one position beneath the rotor using a laser Doppler anemometry system. Spectral analysis of the inflow data shows multiple harmonics of the excitation frequency. It is found that the resulting inflow response is subject to hysteresis effects which reduce with outboard station. The dynamic inflow response also strongly decreases in the tip region. An open chamber is used to reduce recirculation effects. Due to blade fatigue considerations the examined test cases are limited and the input amplitude restricted to 2 degrees peak-to-peak. Since the excitation frequency is an exact multiple of the rotational frequency, long record lengths can be effectively used with the laser system, and the blade pitch position is fixed with respect to azimuth. This limits the available input excitations. The observed hysteresis is radially dependent and inflow response decreases rapidly in the tip region.

Appendix B - Derivation of Coning / Inflow Models

B1 The Chen & Hindson Coning / Inflow Model- Model 1

The general model of helicopter rotor response to collective input in hovering flight using first order inflow and second order coning is given in state space form below:

$$\dot{x} = Ax + Bu,$$

$$A = \begin{bmatrix} \upsilon_\upsilon & 0 & \upsilon_{\dot\beta} \\ 0 & 0 & 1 \\ \beta_\upsilon & \beta_\beta & \beta_{\dot\beta} \end{bmatrix}; \quad B = \begin{bmatrix} \upsilon_\theta \\ 0 \\ \beta_\theta \end{bmatrix}$$

$$x = \begin{bmatrix} \upsilon & \beta & \dot\beta \end{bmatrix}, \; u = \theta_0$$

(B-1)

The flapping equation with no hinge offset, flap-pitch coupling, or flap stiffness for an articulated rotor is taken from Chen [Chen & Hindson 1987, Equation (9)] and given below, for the case of no aircraft motion.

$$\ddot{\beta} = -\frac{\Omega^2\gamma}{6}\frac{\upsilon}{\Omega R} - \Omega^2\beta - \frac{\Omega\gamma}{8}\dot{\beta} + \frac{\Omega^2\gamma}{8}\theta_0. \tag{B-2}$$

From this the three coning derivatives in Equation (B-1) are obtained.

$$\beta_\upsilon = -\frac{\Omega\gamma}{6R}\;;\; \beta_\beta = -\Omega^2\;;\; \beta_{\dot\beta} = -\frac{\Omega\gamma}{8}\;;\; \beta_\theta = \frac{\Omega^2\gamma}{8}. \tag{B-3}$$

The inflow response due to transient thrust in hover is given by Pitt & Peter [Pitt 1981, Chen & Hindson 1987, Equation (4)] as :

$$C_T = \frac{M_{11}}{\Omega}\dot{\lambda} + 2V_T\lambda; \text{ where } \lambda = \frac{\upsilon}{\Omega R}. \tag{B-4}$$

This is the non-linear version of the Pitt/Peters [Peters 1988] model where V_T is the total normalised velocity at the rotor and M_{11}=0.543 , assuming that a 'corrected' pressure distribution (zero blade loading at blade root and tip) is used. M_{11} can be interpreted as the fraction of the mass of air of a sphere of rotor radius which participates in the acceleration process of the air, non-dimensionalized by $\rho\pi R^3$. When evaluating V_T, the velocity due to the coning motion of the rotor disc with respect to the tip path plane is considered. This is found by considering the flow through an annulus moving with velocity $\dot\beta r$ relative to the rotor hub. This is then non-dimensionalized on rotor speed and area [Chen & Hindson 1987]. The resulting integration gives: $\frac{1}{(\Omega R)}\frac{1}{(\pi R^2)}\int_0^R (2\pi r)(\dot\beta r)dr = \frac{2\dot\beta}{3\Omega}$.

Assuming no aircraft motion, V_T can be written as (from Equation (5) Chen & Hindson 1987]: $V_T = \lambda + \frac{2\dot{\beta}}{3\Omega}$; and substituting into Equation (B-4), gives:

$$C_T = M_{11}\frac{\dot{\lambda}}{\Omega} + 2\lambda(\lambda + \frac{2\dot{\beta}}{3\Omega}). \tag{B-5}$$

An identical equation was derived by Carpenter and Fridovich [Carpenter 1953], except that their apparent mass value was 0.851. For a hovering rotor and accounting for blade flapping the expression for the instantaneous thrust is given as (Chen & Hindson 1987, from Equation (1)):

$$T = 0.637\rho\left(\tfrac{4}{3}\pi R^3\right)\dot{\upsilon} + 2\left(\pi R^2\right)\rho\upsilon(\upsilon + \frac{2\dot{\beta}R}{3}). \tag{B-6}$$

Dividing by $\rho\pi R^2(\Omega R)^2$ and expressing this in terms of a thrust coefficient gives:

$$C_T = 0.849\frac{\dot{\lambda}}{\Omega} + 2\lambda(\lambda + \frac{2\dot{\beta}}{3\Omega}); \tag{B-7}$$

By comparing Equations (B-5) and (B-7) we can see that the only difference is in the value of the apparent mass, with Carpenter and Fridovich suggesting M_{11}=0.849 and Pitt and Peters suggesting 0.543 for a *corrected* pressure distribution.

Linearizing Equation (B-5) or (B-7) about the initial conditions of $\lambda = \lambda_m$ and $\dot{\beta} = 0$ gives the following perturbation equation for the thrust coefficient (Note: No new notation is used for small perturbation quantities):

$$C_T = M_{11}\frac{\dot{\upsilon}}{\Omega^2 R} + 4\lambda_m\frac{\upsilon}{\Omega R} + \frac{4\lambda_m\dot{\beta}}{3\Omega} \qquad \text{where } \lambda_m = \sqrt{\frac{C_T}{2}} \tag{B-8}$$

Another expression for the rotor thrust can be obtained using blade element theory, the local velocities, angle of attack and lift characteristics of the blade. In the Chen and Hindson model the blade angle of attack is assumed constant (no twist), the chord uniform and the induced velocity invariant with rotor radius. The differential thrust produced by an elemental annulus on the rotor disc can be expressed as:

$$dT = \left(\tfrac{1}{2}\rho(\Omega r)^2\right)bca(\theta_0 - \frac{\dot{\beta}r}{\Omega r} - \frac{\upsilon}{\Omega r})dr. \tag{B-9}$$

Integrating over the rotor radius this gives:

$$T = \left(\tfrac{1}{2}\rho\Omega^2\right)(bca)\frac{R^3}{3}(\theta_0 - \frac{3\upsilon}{2\Omega R} - \frac{\dot{\beta}}{\Omega}). \tag{B-10}$$

In terms of a perturbation thrust coefficient this becomes:

$$C_T = \frac{\sigma a}{6}(\theta_0 - \frac{3\upsilon}{2\Omega R} - \frac{\dot{\beta}}{\Omega}). \tag{B-11}$$

Equating the small perturbation Equations (B-8) and (B-11) gives:

$$\dot{\upsilon} = -\frac{4\Omega}{M_{11}}(\lambda_m + \frac{\sigma a}{16})\upsilon - \frac{4\Omega R}{3M_{11}}(\lambda_m + \frac{\sigma a}{8})\dot{\beta} + \frac{4\Omega^2 R}{3M_{11}}\frac{\sigma a}{8}\theta_0. \tag{B-12}$$

The corresponding derivatives are :

$$\upsilon_\upsilon = -\frac{4\Omega}{M_{11}}(\lambda_m + \frac{\sigma a}{16}) \; ; \; \upsilon_{\dot{\beta}} = -\frac{4\Omega R}{3M_{11}}(\lambda_m + \frac{\sigma a}{8}) \; ; \; \upsilon_\theta = \frac{4\Omega^2 R\sigma a}{3M_{11}8}; \tag{B-13}$$

$$A = \begin{bmatrix} -\frac{4\Omega}{M_{11}}(\lambda_m + \frac{a\sigma}{16}) & 0 & -\frac{4\Omega R}{3M_{11}}(\lambda_m + \frac{a\sigma}{8}) \\ 0 & 0 & 1 \\ -\frac{\Omega\gamma}{6R} & -\Omega^2 & -\frac{\Omega\gamma}{8} \end{bmatrix} \quad B = \begin{bmatrix} \frac{4\Omega^2 Ra\sigma}{3M_{11}8} \\ 0 \\ \frac{\Omega^2\gamma}{8} \end{bmatrix}. \tag{B-14}$$

This is the same model as given by Chen [Chen & Hindson 1987] albeit with a slightly different notation.

B2 The DRA Coning / Inflow Model - Model 2

Work at the DRA in 1990 [Houston 1989] showed that significant improvements in correlation between flight and theory could be achieved if the following effects were considered in the model.

A correction factor to the momentum based uniform component is introduced to account for tip losses and wake non-uniformity. Unsteady aerodynamic effects are taken into account by lift and thrust deficiency factors.

The suggested flapping equation including the lift deficiency factor C^* given by Johnson [Johnson 1980, p515] and a factor to account for flap frequency ratio (f_R) then becomes:

$$\ddot{\beta} = -\frac{\Omega^2\gamma C^*}{6}\frac{\upsilon}{\Omega R} - \Omega^2 f_R\beta - \frac{\Omega\gamma C^*}{8}\dot{\beta} + \frac{\Omega^2\gamma C^*}{8}\theta_0. \tag{B-15a}$$

The according derivatives are:

$$\beta_\upsilon = -\frac{\Omega\gamma}{6R}C^* \; ; \; \beta_\beta = -\Omega^2 f_R \; ; \; \beta_{\dot{\beta}} = -\frac{\Omega\gamma}{8}C^* \; ; \; \beta_\theta = \frac{\Omega^2\gamma}{8}C^*$$
$$\text{with } C^* = \frac{1}{1 + \pi\sigma/(4\nu_0)} \tag{B-15b}$$

Equation (B-6) is amended to include a thrust deficiency factor $C*$ [Johnson 1980, p527] and an empirical momentum correction factor k giving the following expression for the momentum thrust (for comparison see Equation (B-6)).

$$T = m_a \dot{v} + 2\rho(\pi R^2) v \frac{C_*}{k}\left(\frac{v}{k} + \frac{2\dot{\beta}R}{3}\right)$$
$$\text{where } C_* = \frac{1}{1 + a\sigma/(16\lambda_m)} \quad . \tag{B-16}$$

Expressing this in terms of a thrust coefficient (B-17) and then linearizing (B-18) about initial conditions gives:

$$C_T = M_{11}\frac{\dot{\lambda}}{\Omega} + 2\lambda\frac{C_*}{k}\left(\frac{\lambda}{k} + \frac{2\dot{\beta}}{3\Omega}\right); \tag{A-17}$$

$$C_T = M_{11}\frac{\dot{v}}{\Omega^2 R} + 4\lambda_m\frac{C_*}{k^2}\frac{v}{\Omega R} + \frac{4\lambda_m C_*\dot{\beta}}{3k\Omega} \quad . \tag{B-18}$$

The expression for the instantaneous thrust as given by blade element theory [Houston & Black 1990, Equation (7)] is:

$$T = 0.25\Omega R\rho a\sigma(\pi R^2)\left(\frac{2}{3}\Omega R\theta - v - \frac{2}{3}R\dot{\beta}\right); \tag{B-19}$$

$$T = \left(\tfrac{1}{2}\rho\Omega^2\right)(bca)\frac{R^3}{3}\left(\theta_0 - \frac{3v}{2\Omega R} - \frac{\dot{\beta}}{\Omega}\right). \tag{B-10}$$

This is the same as Equation (B-10) and is similarly converted to small perturbation coefficient form and equated to Equation (B-18), giving:

$$C_T = \frac{\sigma a}{6}\left(\theta_0 - \frac{3v}{2\Omega R} - \frac{\dot{\beta}}{\Omega}\right); \tag{B-20, B-11}$$

$$\dot{v} = -\frac{4\Omega}{M_{11}}\left(\frac{C_*}{k^2}\lambda_m + \frac{\sigma a}{16}\right)v - \frac{4\Omega R}{3M_{11}}\left(\frac{C_*}{k}\lambda_m + \frac{\sigma a}{8}\right)\dot{\beta} + \frac{4\Omega^2 R}{3M_{11}}\frac{\sigma a}{8}\theta_0. \tag{B-21}$$

The corresponding derivatives are :

$$v_v = -\frac{4\Omega}{M_{11}}\left(\frac{C_*}{k^2}\lambda_m + \frac{\sigma a}{16}\right) \; ; \; v_{\dot{\beta}} = -\frac{4\Omega R}{3M_{11}}\left(\frac{C_*}{k}\lambda_m + \frac{\sigma a}{8}\right) \; ; \; v_\theta = \frac{4\Omega^2 R\sigma a}{3M_{11}8}; \tag{B-22}$$

$$A = \begin{bmatrix} -\frac{4\Omega}{M_{11}}\left(\frac{C_*}{k^2}\lambda_m + \frac{a\sigma}{16}\right) & 0 & -\frac{4\Omega R}{3M_{11}}\left(\frac{C_*}{k}\lambda_m + \frac{a\sigma}{8}\right) \\ 0 & 0 & 1 \\ -\frac{\Omega\gamma}{6R}C^* & -\Omega^2 f_R{}^2 & -\frac{\Omega\gamma}{8}C^* \end{bmatrix} \quad B = \begin{bmatrix} \frac{4\Omega^2 Ra\sigma}{3M_{11}8} \\ 0 \\ \frac{\Omega^2\gamma}{8}C^* \end{bmatrix}. \tag{B-23}$$

B3 Equivalent Non-Articulated Rotor Models - Models 3 and 4

A flapping equation for an articulated rotor with hinge offset and hinge spring stiffness is given by Chen [Chen 1980]. Appropriate values for the hinge stiffness and offset can then be used to represent a rotor with a rigid rotor hub:

$$\ddot{\beta} = -\Omega^2 \frac{\gamma}{2}(\frac{1}{3} - \frac{\varepsilon}{2})C^* \frac{\upsilon}{\Omega R} - \Omega^2 f_R{}^2 \beta - \Omega\gamma(\frac{1}{8} - \frac{\varepsilon}{3} + \frac{\varepsilon^2}{4})C^* \dot{\beta} + \Omega^2 \frac{\gamma}{8}(1 - \frac{4}{3}\varepsilon)C^* \theta_0. \tag{B-24}$$

From this the appropriate derivatives are given by:

$$\beta_\upsilon = -\frac{\Omega\gamma}{2R}(\frac{1}{3} - \frac{\varepsilon}{2})C^* \; ; \; \beta_\beta = -\Omega^2 f_R \; ; \; \beta_{\dot{\beta}} = -\Omega\gamma(\frac{1}{8} - \frac{\varepsilon}{3} + \frac{\varepsilon^2}{4})C^* \; ; \; \beta_\theta = \Omega^2 \frac{\gamma}{8}(1 - \frac{4}{3}\varepsilon)C^*. \tag{B-25}$$

The flapping equation can be modified to take a tip loss factor into account [Rosen 1982] and the derivatives then become:

$$\beta_\upsilon = -\frac{\Omega\gamma C^*}{2R}(\frac{B^3}{3} - \frac{B^2\varepsilon}{2}) \; ; \; \beta_\beta = -\Omega^2 f_R{}^2 \; ; \; \beta_{\dot{\beta}} = -\Omega\gamma C^*(\frac{B^4}{8} - \frac{B^3\varepsilon}{3} + \frac{B^2\varepsilon^2}{4}) \; ; \; \beta_\theta = \Omega^2 \frac{\gamma C^*}{8}(B^4 - \frac{B^3 4}{3}\varepsilon). \tag{B-26}$$

Again strip theory , based on work by Johnson [Johnson 1980] is used to find the expression for the rotor thrust. The elemental thrust produced by an annular segment is:

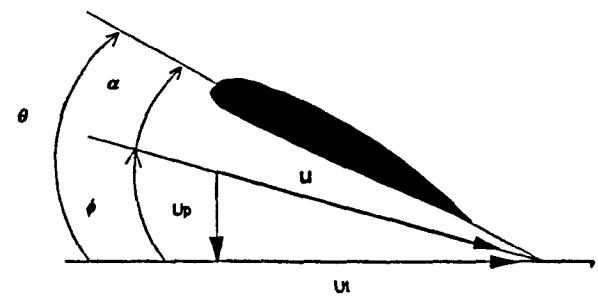

$$dT = (\tfrac{1}{2}\rho U_T{}^2)bca(\theta - \frac{U_P}{U_T})dr, \text{ with } U \cong U_T, \; \phi \cong \frac{U_P}{U_T}$$
$$dT = \tfrac{1}{2}\rho bca(\theta U_T{}^2 - \frac{U_P U_T{}^2}{U_T})dr \tag{B-27}$$

Expressing this in coefficient form normalised by air density, rotor radius and rotor speed, i.e. dividing by $\rho(\pi R^2)(\Omega R)^2$, gives:

$$dC_T = \frac{\sigma a}{2}(\theta \frac{U_T{}^2}{\Omega^2 R^2} - \frac{U_P U_T}{\Omega^2 R^2}) \, d(\frac{r}{R}). \tag{B-28}$$

The velocity component U_T is given by the radial velocity at a certain radial station and U_P by the induced velocity. The induced velocity as seen by the blade is augmented by the flapping motion of the blade.

$$U_P = \upsilon + \dot{\beta} r; \; U_T = \Omega r. \tag{B-29}$$

Inserting Equation (B-29) into Equation (B-28) gives:

$$dC_T = \frac{\sigma a}{2}(\theta(\frac{r}{R})^2 - \lambda(\frac{r}{R}) - \frac{\dot{\beta}}{\Omega}(\frac{r}{R})^2)\, d(\frac{r}{R}). \tag{B-30}$$

Integrating this over the rotor diameter, with $\left(\frac{r}{R}\right)$ going from 0 to 1, gives at the tip, gives:

$$C_T = \frac{\sigma a}{2}\left(\frac{\theta_0}{3} - \frac{\lambda}{2} - \frac{\dot{\beta}}{3\Omega}\right), \tag{B-31}$$

which is the same as Equation (B-11). It is interesting to note that if a linear variation in blade pitch, as with a twisted blade, is incorporated in Equation (B-28), the thrust coefficient expression in Equation (B-29) is augmented with a constant term. However, in small perturbation formulations, terms which were originally constant will disappear. Accounting for root cut-out and a tip loss factor changes the limits of the integration and gives, in perturbation form:

$$\begin{aligned} C_T &= \frac{\sigma a}{2}\int_{C_R}^{B} \theta\bar{r}^2 - \lambda\bar{r} - \frac{\dot{\beta}}{\Omega}\bar{r}^2 \; d\bar{r}, \text{ where } \bar{r} = \frac{r}{R}, \\ C_T &= \frac{\sigma a}{2}[\frac{\theta}{3}(B^3 - C_R{}^3) - \frac{\upsilon}{2\Omega R}(B^2 - C_R{}^2) - \frac{\dot{\beta}}{3\Omega}(B^3 - C_R{}^3)] \end{aligned} \tag{B-32}$$

Again the non-linear Pitt/Peters model modified to take account of blade flapping is used and linearised about initial conditions:

$$C_T = M_{11}\frac{\dot{\lambda}}{\Omega} + 2\lambda(\lambda + \frac{2\dot{\beta}}{3\Omega}) \tag{B-5}$$

$$C_T = M_{11}\frac{\dot{\upsilon}}{\Omega^2 R} + 4\lambda_m\frac{\upsilon}{\Omega R} + \frac{4\lambda_m\dot{\beta}}{3\Omega}, \tag{B-8}$$

Equating Equations (B-8) and (B-32) gives:

$$\dot{\upsilon} = [-\frac{4\lambda_m\Omega}{M_{11}} - \frac{\sigma a\Omega}{4M_{11}}(B^2 - C^2)]\upsilon + [-\frac{4\lambda_m\Omega R}{M_{11}} - \frac{\sigma a\Omega R}{6}(B^3 - C^3)]\dot{\beta} + [\frac{\sigma a\Omega^2 R}{6M_{11}}(B^3 - C^3)]\theta, \tag{B-33}$$

$$\upsilon_\upsilon = -\frac{4\Omega}{M_{11}}(\lambda_m + \frac{\sigma a}{16}(B^2 - C^2)) \; ; \; \upsilon_{\dot{\beta}} = -\frac{4\Omega R}{3M_{11}}(\lambda_m + \frac{\sigma a}{8}(B^3 - C^3)) \; ; \; \upsilon_\theta = \frac{4\Omega^2 R\sigma a}{3M_{11}8}(B^3 - C^3). \tag{B-34}$$

This will be know as model 3.

$$A = \begin{bmatrix} -\frac{4\Omega}{M_{11}}(\frac{C_*}{k^2}\lambda_m + \frac{a\sigma}{16}(B^2 - C^2)) & 0 & -\frac{4\Omega R}{3M_{11}}(\frac{C_*}{k}\lambda_m + \frac{a\sigma}{8}(B^3 - C^3)) \\ 0 & 0 & 1 \\ -\frac{\Omega\gamma}{2R}(\frac{1}{3} - \frac{\varepsilon}{2})C^* & -\Omega^2 f_R & -\Omega\gamma(\frac{1}{8} - \frac{\varepsilon}{3} + \frac{\varepsilon^2}{4})C^* \end{bmatrix} B = \begin{bmatrix} \frac{4\Omega^2 Ra\sigma}{3M_{11}8}(B^3 - C^3) \\ 0 \\ \frac{\Omega^2\gamma}{8}\left(1 - \frac{4}{3}\varepsilon\right)C^* \end{bmatrix} \tag{B-35}$$

Using the flapping equation with a tip loss factor and no lift deficiency factor, as suggested by Houston [1989], produces model 4.

$$A=\begin{bmatrix} -\frac{4\Omega}{M_{11}}\left(\frac{C_o}{k^2}\lambda_m+\frac{a\sigma}{16}(B^2-C^2)\right) & 0 & -\frac{4\Omega R}{3M_{11}}\left(\frac{C_o}{k}\lambda_m+\frac{a\sigma}{8}(B^3-C^3)\right) \\ 0 & 0 & 1 \\ -\frac{\Omega\gamma}{2R}\left(\frac{B^3}{3}-\frac{B^2\varepsilon}{2}\right) & -\Omega^2 f_R{}^2 & -\Omega\gamma\left(\frac{B^4}{8}-\frac{B^3\varepsilon}{3}+\frac{B^2\varepsilon^2}{4}\right) \end{bmatrix} \quad B=\begin{bmatrix} \frac{4\Omega^2 Ra\sigma}{3M_{11}8}(B^3-C^3) \\ 0 \\ \frac{\Omega^2\gamma}{8}\left(B^4-\frac{4B^3\varepsilon}{3}\right) \end{bmatrix} \tag{B-36}$$

B4 Rotor Model with Quasi Steady Inflow - Model 5

In this section the non articulated rotor model is restated including a quasi steady inflow approximation, which effectively assumes that the apparent mass factor is zero and changes in inflow due to thrust perturbations occur instantaneously. From Equation (B-24) & (B-26) the flapping equation is given as:

$$\ddot{\beta}=-\Omega^2\frac{\gamma C^*}{2}\left(\frac{B^3}{3}-\frac{B^2\varepsilon}{2}\right)\frac{\upsilon}{\Omega R}-\Omega^2 f_R\beta-\Omega\gamma C^*\left(\frac{B^4}{8}-\frac{B^3\varepsilon}{3}+\frac{B^2\varepsilon^2}{4}\right)\dot{\beta}+\Omega^2\frac{\gamma C^*}{8}\left(B^4-\frac{B^3 4}{3}\varepsilon\right)\theta_0. \tag{B-37}$$

The expression for the rotor thrust obtained from blade element theory remains unchanged and is given in appropriate form by Equation (B-32):

$$C_T=\frac{\sigma a}{2}\left[\frac{\theta}{3}(B^3-C_R{}^3)-\frac{\upsilon}{2\Omega R}(B^2-C_R{}^2)-\frac{\dot{\beta}}{3\Omega}(B^3-C_R{}^2)\right]. \tag{B38}$$

The thrust expression due to Pitt & Peters or Carpenter & Fridovich is given by Equation (B-18):

$$C_T=M_{11}\frac{\dot{\upsilon}}{\Omega^2 R}+4\lambda_m\frac{C_o}{k^2}\frac{\upsilon}{\Omega R}+\frac{4\lambda_m C_o\dot{\beta}}{3k\Omega}. \tag{B-18}$$

This is reduced to the following if the apparent mass factor is set to zero:

$$C_T=4\lambda_m\frac{C_o}{k^2}\frac{\upsilon}{\Omega R}+\frac{4\lambda_m C_o\dot{\beta}}{3k\Omega}. \tag{B 39}$$

Equating (B-39) and (B-18) gives:

$$\upsilon=\frac{-4\lambda_m C_o R}{3Dk}\dot{\beta}+\frac{\sigma a\Omega R\left(B^3-C^3\right)}{6D}\theta-\frac{\sigma a R\left(B^3-C^3\right)}{6D}\dot{\beta}$$
$$D=\left(\frac{4\lambda_m C_o}{k^2}+\frac{\sigma a\left(B^2-C^2\right)}{4}\right) \tag{B-40}$$

This is then substituted in Equation (B-24)

$$\ddot{\beta}=\frac{2\Omega\gamma\lambda_m C_o C^*}{3kD}\left(\frac{B^3}{3}-\frac{B^2\varepsilon}{2}\right)\dot{\beta}-\frac{\gamma\sigma a\Omega^2 C^*}{12D}\left(\frac{B^3}{3}-\frac{B^2\varepsilon}{2}\right)\left(B^3-C^3\right)\theta_0$$
$$+\frac{\gamma\sigma a\Omega C^*}{12D}\left(\frac{B^3}{3}-\frac{B^2\varepsilon}{2}\right)\left(B^3-C^3\right)\dot{\beta}-\Omega^2 f_R\beta-\Omega\gamma C^*\left(\frac{B^4}{8}-\frac{B^3\varepsilon}{3}+\frac{B^2\varepsilon^2}{4}\right)\dot{\beta}+\frac{\Omega^2\gamma C^*}{8}\left(B^4-\frac{B^3 4}{3}\varepsilon\right)\theta_0 \tag{B-41}$$

Rewriting Equation (B-41) with $\varepsilon = C_* = C^* = 0$ and $k = B = 1$ gives the following equation which is the same as given by Chen & Hindson [Chen 1987]:

$$\ddot{\beta} = \frac{\Omega\gamma}{8}\left(\frac{8\lambda_m + \sigma a}{18\left(\lambda_m + \frac{\sigma a}{16}\right)} - 1\right)\dot{\beta} + \frac{\Omega^2\gamma}{8}\left(1 - \frac{\sigma a}{18\left(\lambda_m + \frac{\sigma a}{16}\right)}\right)\theta_0 - \Omega^2 f_R \beta. \tag{B-42}$$

From Equation (B-41) the following derivatives can be obtained:

$$\beta_\beta = -\Omega^2 f_R \; ; \; \beta_{\dot{\beta}} = \Omega\gamma\left[\frac{2\lambda_m C_* C^*}{3kD}\left(\frac{B^3}{3} - \frac{B^2\varepsilon}{2}\right) + \frac{\sigma a C^*}{12D}\left(\frac{B^3}{3} - \frac{B^2\varepsilon}{2}\right)\left(B^3 - C^3\right) - C^*\left(\frac{B^4}{8} - \frac{B^3\varepsilon}{3} + \frac{B^2\varepsilon^2}{4}\right)\right]$$

$$\beta_\theta = \Omega^2\gamma\left[-\frac{\sigma a C^*}{12D}\left(\frac{B^3}{3} - \frac{B^2\varepsilon}{2}\right)\left(B^3 - C^3\right) + \frac{C^*}{8}\left(B^4 - \frac{4B^3}{3}\varepsilon\right)\right] \tag{B-43}$$

In state-space form this then becomes:

$$A = \begin{bmatrix} 0 & 1 \\ -\Omega^2 f_R^{\,2} & \Omega\gamma\left[\frac{2\lambda_m C_* C^*}{3KD}\left(\frac{B^3}{3} - \frac{B^2\varepsilon}{2}\right) + \frac{\sigma a C^*}{12D}\left(\frac{B^3}{3} - \frac{B^2\varepsilon}{2}\right)\left(B^3 - C^3\right) - C^*\left(\frac{B^4}{8} - \frac{B^3\varepsilon}{3} + \frac{B^2\varepsilon^2}{4}\right)\right] \end{bmatrix}$$

$$B = \begin{bmatrix} 0 \\ \Omega^2\gamma\left[\frac{-\sigma a C^*}{12D}\left(\frac{B^3}{3} - \frac{B^2\varepsilon}{2}\right)\left(B^3 - C^3\right) + \frac{C^*}{8}\left(B^4 - \frac{4B^3}{3}\varepsilon\right)\right] \end{bmatrix}$$

$$x = \left(\beta, \dot{\beta}\right)' \tag{B-44}$$

Appendix C - A Note on Spectral Analysis

The spectrum plots in this thesis were produced using the mathematical analysis package, 'Matlab'. For an in-depth mathematical background to spectral analysis the reader is referred Ifeachor [Ifeachor 1993] or the many other textbooks on this subject. For completeness the method by which the spectral plots were obtained will be briefly described.

The 'Spectrum' function in 'Matlab' can be used to find the power spectrum estimate of a data sequence using the 'Welch' method of power spectrum estimation. The data series is divided into a number of sequence N points long, where N is a power of two. A 'Hanning' window is applied to each section to reduce spectral leakage, before a fast-Fourier-transform and averaging is utilised.

The more sections that are averaged, the more accurate the resulting spectral estimate will be. It is shown in Ifeachor [Ifeachor 1993] that the standard deviation of the error of the estimate decreases with increasing number of sections. For a fixed length record this would imply that the best results are obtained using many short sections. However, the resolution, i.e. accuracy in frequency, of a estimate is directly proportional to the length of the sequences.

Therefore, a compromise between accuracy and resolution has to be found. Further functions in the Matlab package are used to normalise the power spectrum so that the estimated amplitudes correspond to the signal component amplitudes. Without the normalisation, the units on the power spectrum are, assuming the input signal to be in Volts, [$Volts^2/Hz$].

Appendix D - State Space Equations from Transfer Functions

For the simulation of the dynamic model it was desirable to provide a state-space description of each block. There are various methods to obtain a state-space formulation from the transfer function form and the following method is called *Direct Phase Variable Form* and is illustrated using a 2nd order transfer function. The state variables are the outputs of the integrators $\left(\frac{1}{s}\right)$. The transfer function below (D-1) is split into a denominator and a numerator part (D-2). The denominator part is rearranged to have the highest power of s on the left (D-3).

$$\frac{y}{u} = \frac{b_2 s^2 + b_1 s + b_o}{s^2 + a_1 s + a_0} \tag{D-1}$$

$$\frac{w}{u} = \frac{1}{s^2 + a_1 s + a_0} \qquad \frac{y}{w} = b_2 s^2 + b_1 s + b_o \tag{D-2}$$

$$ws^2 = -a_1 sw - a_0 w + u \tag{D-3}$$

From (D-3) the left hand side of the diagram below is derived. The remaining right hand part of the diagram is constructed using the numerator part of Equation (D-1), i.e. (D-2)..

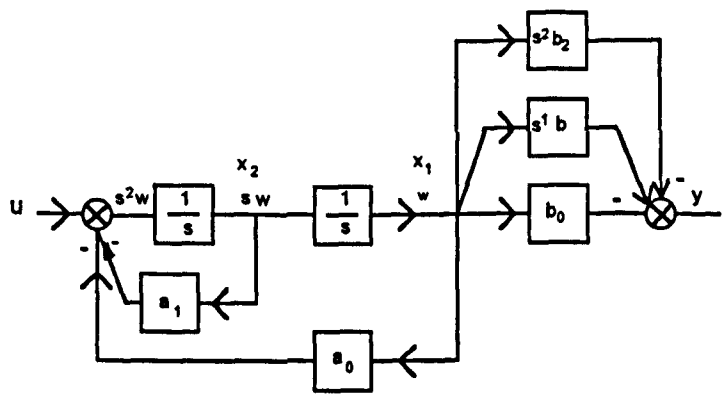

A little manipulation then gives the complete diagram below, from which the state space equations below are easily derived.

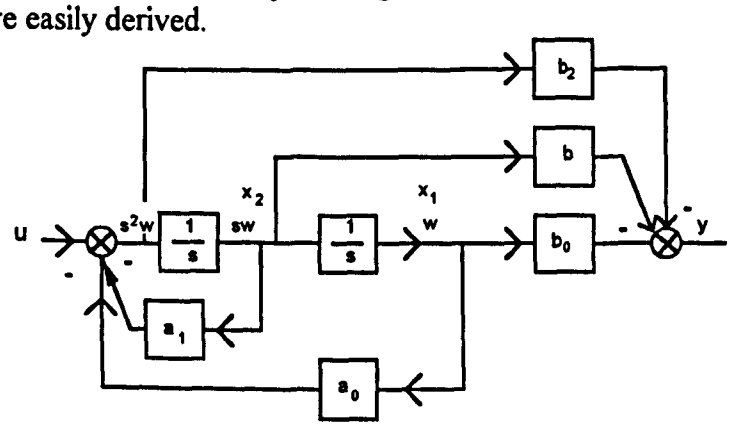

The outputs from the integrators are now assigned the state variables x_1 and x_2.

$$\begin{aligned} y &= b_0 x_1 + b_1 x_2 + b_2 (u - a_1 x_2 - a_2 x_1) \\ \dot{x}_1 &= x_2 \;,\; \dot{x}_2 = u - a_1 x_2 - a_2 x_1 \end{aligned} \tag{D-3}$$

Equation (D-3) can then be easily converted into the usual state space form:

$$\begin{pmatrix} x_1 \\ x_2 \end{pmatrix}' = \begin{bmatrix} 0 & 1 \\ -a_2 & -a_1 \end{bmatrix} \begin{pmatrix} x_1 \\ x_2 \end{pmatrix} + \begin{bmatrix} 0 \\ 1 \end{bmatrix} u \qquad \text{(D-4)}$$

$$y = \begin{bmatrix} b_0 - b_2 a & b_1 - b_2 a_1 \end{bmatrix} \begin{pmatrix} x_1 \\ x_2 \end{pmatrix} + (b_2) u$$

Appendix E - Hydraulic Resonance Frequency

The inertia of moving parts and fluid compressibility in a hydraulic system are a source of oscillations and can be considered analogous to a mass spring system with a natural frequency. The hydraulic frequency is determined by the bulk modulus and inertia of parts in the hydraulic system. The compressibility of a fluid σ is defined as the change in volume per unit volume for unit change in pressure. Bulk modulus N is the reciprocal of compressibility, with units [N/m^2]. The bulk modulus can be significantly reduced by air in the system or the dilation of hydraulic piping under pressure. For a hydraulic motor attached to a flow control valve with an inertial load J and pressures p_1, p_2 and trapped volumes V_1, V_2 either side of the motor the following analysis is valid. If the motor shaft is slightly rotated then the volume on one side of the rotor would be increased, and decreased on the other by $\theta_m \delta_m$, where δ_m is the volumetric displacement of the rotor, which will increase and decrease the pressure either side respectively, by:

$$\frac{V_1}{N}\Delta P_1 = \delta_m \theta_m \Rightarrow \Delta P_1 = \frac{\delta_m \theta_m N}{V_1} \; ; \; \frac{V_2}{N}\Delta P_2 = -\delta_m \theta_m \Rightarrow \Delta P_2 = -\frac{\delta_m \theta_m N}{V_2} \tag{E-1}$$

The total pressure difference ΔP across the rotor with $V_1 = V_2 = \frac{V_t}{2}$ is $\Delta P_1 + \Delta P_2$:

$$\Delta P = \frac{4\delta_m \theta_m N}{V_t} \; . \tag{E-2}$$

The torque required to achieve this is equal to the product of the pressure difference across the motor and its volumetric displacement, which is the work done per radian of motion.

$$\delta_m (\Delta P) = J\ddot{\theta}_m . \tag{E-3}$$

The torque of the motor is reacted by inertial loads, in the absence of friction, and the governing differential equation gives the following undamped oscillatory system by substituting (E-2) into (E-3), with its resonance frequency.

$$\theta_m = -\frac{V_t J \ddot{\theta}_m}{4N\delta_m^2} \Rightarrow \omega_h = \sqrt{\frac{4N\delta_m^2}{V_t J}} . \tag{E-4}$$

This gives the undamped natural frequency of the hydraulic system. The bulk modulus will be difficult to calculate accurately for a real system and the above expression thus gives a guide to the frequencies of vibration likely to be seen. This also sets an upper limit on the bandwidth of the speed control system for the motor.

Appendix F - Flapping Equation Derivation

F1 Flapping Equation for a Rigid Blade

In this appendix the flapping equation for a single blade will be derived from first principles The rigid hub will be approximated by an offset hinge with hinge restraint

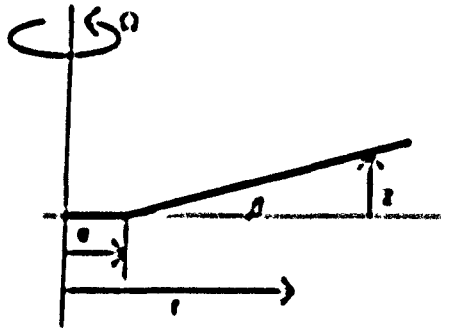

The radial station along the blade is denoted by r and runs from zero at the hub to R at the blade tip If a non-dimensional analysis is followed such as Johnson [Johnson 1980] the radial blade co-ordinate lies between zero and unity at the tip. The real hinge offset is denoted by e and the non-dimensional hinge off-set by ε The blade deflection is denoted by z and is a function of the radial station and of the blade deflection degree of freedom β The blade deflection is then given by

$$z = \psi(r)\beta$$

$$\psi(r) = \begin{cases} 0 & r < e \\ \dfrac{R(r-e)}{R-e} & r \geq e \end{cases} \qquad 0 < r < R \tag{F-1}$$

For zero hinge offset, the above mode shape simplifies to $\psi(r) = r$ and $z = r\beta$, which is just rigid blade rotation about the rotor centre The mode shape $\psi(r)$ can be thought of as a different co-ordinate system with runs along the rotational plane of the blade A graph of $\psi(r)$ for R=1, e=0 0, 0 2 and 0 4 as a function of radial station is shown below At the tip R=1 $\psi(r)=1$

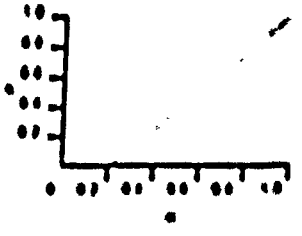

Further discussion of the use of this mode shape is given by Johnson [Johnson 1980].

The analysis here will use only the dimensional mode shape and dimensional quantities. This is to be preferred to the non-dimensional analysis performed by Johnson [Johnson 1980], where physical significance is not always immediately apparent.

The forces acting on an elemental section of the blade at a location defined by z and r are, an aerodynamic force $F_z(r)dr$ acting vertically upwards with a moment arm of $(r-e)$, an inertial force $m(r)dr * \ddot{z}$ with a moment arm of $(r-e)$ and a centripetal force $(m\Omega^2 R)$ with moment arm z. A gravity term also acts on the blade, but is ignored in this analysis as it is significantly smaller that the other terms and is eliminated in a perturbation analysis. For similar reasons the rotor pre-cone angle is also ignored but a hinge spring K_β term is included.

The above moments caused by the loads on an elemental section of the blade can be integrated along the span of the blade and the following expression is obtained, remembering $z = r(r)\beta$.

Inertial Centripetal Aerodynamic

$$\int_e^R r(r-e)mdr\ddot{\beta} + \int_e^R rmdr\beta\Omega^2 + K_\beta\beta = \int_e^R (r-e)F_z dr \tag{F-2}$$

$$\int_e^R R\frac{r-e}{R-e}(r-e)mdr\ddot{\beta} + \int_e^R R\frac{r-e}{R-e}rmdr\beta\Omega^2 + K_\beta\beta = \int_e^R (r-e)F_z dr \tag{F-3}$$

$$A\ddot{\beta} + B\beta\Omega^2 + K_\beta\beta = M_{F_{aero}}$$

$$A = \int_e^R R\frac{r-e}{R-e}(r-e)mdr;\ B = \int_e^R R\frac{r-e}{R-e}rmdr\beta\Omega^2 \tag{F-4}$$

F2 Flap Frequency Ratio

The natural frequency of a centrally hinged rigid rotating blade is equal to the rotational shaft speed. For a blade with a rigid hub mounting, modelled by a blade with an offset hinge and hinge restraint, the natural frequency is higher than that of the shaft speed. The phase lag between excitation and blade response is therefore reduced to less than 90 degrees. In the following analysis the derivation of the natural flapping frequency of a blade with offset hinge and hinge restraint will be developed. The results will be compared with those of the non-dimensional analysis obtained by Johnson [Johnson 1980]

$$A\ddot{\beta} + B\beta\Omega^2 + K_\beta\beta = M_{F_{aero}}. \tag{F-5}$$

The above differential equation represents an oscillating motion. If the equation is rearranged to the following form the frequency of oscillation is given by $\sqrt{\Omega^2 f_r^2}$.

$$\ddot{\beta}+\underbrace{{}^{B}/_{A}}_{f_r^2}\Omega^2\beta+{}^{K_\beta}/_{A}\beta=... \tag{F-6}$$

Then, in order to find an explicit expression for the flap frequency, the coefficients above are replaced by,

$$\int_e^R R\frac{r-e}{R-e}(r-e)mdr\ddot{\beta}+\int_e^R R\frac{r-e}{R-e}rmdr\beta\Omega^2+K_\beta\beta=... \tag{F-7}$$

$$\ddot{\beta}+\left(\frac{K_\beta+\Omega^2\int_e^R R\frac{r-e}{R-e}rmdr}{\int_e^R R\frac{r-e}{R-e}(r-e)mdr}\right)\beta=... \tag{F-8}$$

and if it is noted that,

$$I_B=\int_e^R\frac{R^2}{(R-e)^2}(r-e)^2mdr=\int_e^R\eta^2mdr=\frac{R^2(R-e)^3}{3(R-e)^2}m \tag{F-9}$$

(assuming m is constant with radial station)

$$\ddot{\beta}+\left(\frac{K_\beta R}{(R-e)I_B}+\frac{\frac{\Omega^2R^2}{R-e}\int_e^R\frac{r-e}{R-e}rmdr}{\frac{R^2m(R-e)^3}{3(R-e)^2}}\right)\beta=... \tag{F-10}$$

$$\ddot{\beta}+\left(\frac{K_\beta R}{(R-e)I_B}+\Omega^2\left[1+\frac{3e}{2(R-e)}\right]\right)\beta=... \tag{F-11}$$

$$\ddot{\beta}+\Omega^2\left(\frac{K_\beta R}{(R-e)I_B\Omega^2}+1+\frac{3e}{2(R-e)}\right)\beta=... \tag{F-12}$$

and comparing this form with Equation (F-6), note that,

$$f_r^2=1+\frac{3e}{2(R-e)}+\frac{K_\beta R}{I_\beta(R-e)\Omega^2}. \tag{F-13}$$

The first term is the centrifugal spring term, the next the offset hinge effect and the last term the hinge restraint spring. To check this result a dimensional comparison is made: $\frac{\left[Kg\frac{m}{s^2}m/rad\right][m]}{\left[Kgm^2\right]\left[\frac{1}{s^2}\right][m]}=1$. Using dimensionless quantities with respect to rotor radius we obtain $f_r^2=1+\frac{3\varepsilon}{2(1-\varepsilon)}+\frac{K_\beta}{I_\beta(1-\varepsilon)\Omega^2}$, which is the result given by Johnson [Johnson 1980]. It has to be

remembered that now the dimensionless definitions for I_B and K_b normalised w.r.t. R have to be used, with units of $[Kg]$ and $[Kg/s^2]$ respectively, which is not easy to interpret physically.

Appendix G - Conversion of the Flapping Equations to the Non-rotating Frame

In helicopter aerodynamics it is often necessary to transfer equations of motion from a rotating to non-rotating frame. This will be demonstrated here with the use of the individual blade flapping equation. For an in-depth discussion on the mathematics of rotating systems the reader is referred to Johnson [Johnson 1980]. Equation G-1 is the general flapping equation for a single blade.

$$A(m,e)\ddot{\beta}^m + B(m,e)\beta^m\Omega^2 + K_\beta\beta^m = M_{aero}{}^m \tag{G-1}$$

The first step is to apply each of the following summation operators, to Equation G-1 in turn. The summation operators will be later used in introducing the new degrees of freedom in the non-rotating frame. In the rotating frame β uniquely defines the position of the blade in space. In the non-rotating frame the position of the blades in space is described by the tip-path-plane (TPP) that the blade tips describe and this is defined in terms of TPP degrees of freedom, which will be introduced later. The summation operators are:

$$\frac{1}{N}\sum_{m=1}^{N}(...),\quad \frac{2}{N}\sum_{m=1}^{N}(...)\cos n\psi_m,\quad \frac{2}{N}\sum_{m=1}^{N}(...)\sin n\psi_m. \tag{G-2}$$

Applying the summation operators gives three differential equations:

$$A(m,e)\frac{1}{N}\sum_{m=1}^{N}\left(\ddot{\beta}^m\right) + B(m,e)\Omega^2\frac{1}{N}\sum_{m=1}^{N}\left(\beta^m\right) + K_\beta\frac{1}{N}\sum_{m=1}^{N}\left(\beta^m\right) = \frac{1}{N}\sum_{m=1}^{N}\left(M_{aero}{}^m\right) \tag{G-3a}$$

$$A(m,e)\frac{2}{N}\sum_{m=1}^{N}\left(\ddot{\beta}^m\right)\cos n\psi_m + B(m,e)\Omega^2\frac{2}{N}\sum_{m=1}^{N}\left(\beta^m\right)\cos n\psi_m + K_\beta\frac{2}{N}\sum_{m=1}^{N}\left(\beta^m\right)\cos n\psi_m = \frac{2}{N}\sum_{m=1}^{N}\left(M_{aero}{}^m\right)\cos n\psi_m \tag{G-3b}$$

$$A(m,e)\frac{2}{N}\sum_{m=1}^{N}\left(\ddot{\beta}^m\right)\sin n\psi_m + B(m,e)\Omega^2\frac{2}{N}\sum_{m=1}^{N}\left(\beta^m\right)\sin n\psi_m + K_\beta\frac{2}{N}\sum_{m=1}^{N}\left(\beta^m\right)\sin n\psi_m = \frac{2}{N}\sum_{m=1}^{N}\left(M_{aero}{}^m\right)\sin n\psi_m \tag{G-3c}$$

Next the degrees of freedom in the rotating frame need to be converted to the non rotating frame and the following new non-rotating degrees of freedom are defined. These define the position of the TPP in space:

$$\beta_0 = \frac{1}{N}\sum_{m=1}^{N}\beta^m,\ \beta_{nc} = \frac{2}{N}\sum_{m=1}^{N}\beta^m\cos n\psi_m,\ \beta_{ns} = \frac{2}{N}\sum_{m=1}^{N}\beta^m\sin n\psi_m\ . \tag{G-4}$$

The linear mapping between the rotating and non-rotating system is given by:

$$\beta^m = \beta_0 + \sum_n \beta_{nc}\cos n\psi_m + \sum_n \beta_{ns}\sin n\psi_m\,. \tag{G-5}$$

In this mapping β_0, β_{1c}, β_{1s} can be interpreted as the coning and TPP tilt degrees of freedom respectively, which are functions of time. For an even-bladed rotor with N blades the summation goes from 1 to (N-2)/2.

Now expressions need to be found which relate the summation of time derivatives ($\frac{1}{N}\sum_{m=1}^{N}(\ddot{\beta}^m)\sin n\psi_m$ etc.) to the newly defined degrees of freedom. Taking the initial mapping between the rotating and non-rotating frame and differentiating twice:

$$\beta^m = \beta_0 + \sum_n \beta_{nc}\cos n\psi_m + \sum_n \beta_{ns}\sin n\psi_m \tag{G-6a}$$

$$\dot{\beta}^m = \dot{\beta}_0 + \sum_n \left(\dot{\beta}_{nc} + n\Omega\beta_{ns}\right)\cos n\psi_m + \sum_n \left(\dot{\beta}_{ns} - n\Omega\beta_{nc}\right)\sin n\psi_m \tag{G-6b}$$

$$\ddot{\beta}^m = \ddot{\beta}_0 + \sum_n \left(\ddot{\beta}_{nc} + 2n\Omega\dot{\beta}_{ns} + n\dot{\Omega}\beta_{ns} - n^2\Omega^2\beta_{nc}\right)\cos n\psi_m + \sum_n \left(\ddot{\beta}_{ns} - 2n\Omega\dot{\beta}_{nc} - n\dot{\Omega}\beta_{nc} - n^2\Omega^2\beta_{ns}\right)\sin n\psi_m . \tag{G-6c}$$

Now comparing coefficients with the definitions for the individual blade derivatives, using the summation operators:

$$\dot{\beta}^m = \frac{1}{N}\sum_{m=1}^{N}\dot{\beta} + \sum_n\left(\frac{2}{N}\sum_{m=1}^{N}\dot{\beta}^m\cos n\psi_m\right)\cos n\psi_m + \sum_n\left(\frac{2}{N}\sum_{m=1}^{N}\dot{\beta}^m\sin n\psi_m\right)\sin n\psi_m \tag{G-7a}$$

$$\ddot{\beta}^m = \frac{1}{N}\sum_{m=1}^{N}\dot{\beta}^m + \sum_n\left(\frac{2}{N}\sum_{m=1}^{N}\ddot{\beta}^m\cos n\psi_m\right)\cos n\psi_m + \sum_n\left(\frac{2}{N}\sum_{m=1}^{N}\ddot{\beta}^m\sin n\psi_m\right)\sin n\psi_m . \tag{G-7b}$$

From this it follows that

$$\frac{1}{N}\sum_{m=1}^{N}\dot{\beta}^m = \dot{\beta}_0;\quad \frac{2}{N}\sum_{m=1}^{N}\dot{\beta}^m\cos n\psi_m = \dot{\beta}_{nc} + n\Omega\beta_{ns};\quad \frac{2}{N}\sum_{m=1}^{N}\dot{\beta}^m\sin n\psi_m = \dot{\beta}_{ns} - n\Omega\beta_{nc}; \tag{G-8a}$$

$$\frac{1}{N}\sum_{m=1}^{N}\ddot{\beta}^m = \ddot{\beta}_0;\quad \frac{2}{N}\sum_{m=1}^{N}\ddot{\beta}^m\cos n\psi_m = \ddot{\beta}_{nc} + 2n\Omega\dot{\beta}_{ns} - n^2\Omega\beta_{nc} + n\dot{\Omega}\beta_{ns}$$

$$\frac{2}{N}\sum_{m=1}^{N}\ddot{\beta}^m\sin n\psi_m = \ddot{\beta}_{ns} - 2n\Omega\dot{\beta}_{nc} - n^2\Omega^2\beta_{ns} - n\dot{\Omega}\beta_{nc} \tag{G-8b}$$

The conversion from rotating to non-rotating frame has added centrifugal and inertial terms to the second flapping derivatives:

$$A\ddot{\beta}_0 + B\Omega^2\beta_0 + K_\beta\beta_0 = \frac{1}{N}\sum_{m=1}^{N}\left(M_{aero}{}^m\right) = M_{aero0} \tag{G-9a}$$

$$A\left(\ddot{\beta}_{nc} + 2n\Omega\dot{\beta}_{ns} - n^2\Omega^2\beta_{nc} + n\dot{\Omega}\beta_{ns}\right) + B\Omega^2\beta_{nc} + K_\beta\beta_{nc} = \frac{2}{N}\sum_{m=1}^{N}\left(M_{aero}{}^m\right)\cos n\psi_m = M_{aero_{nc}} \tag{G-9b}$$

$$A\left(\ddot{\beta}_{ns} - 2n\Omega\dot{\beta}_{nc} - n^2\Omega^2\beta_{ns} - n\dot{\Omega}\beta_{nc}\right) + B\Omega^2\beta_{ns} + K_\beta\beta_{ns} = \frac{2}{N}\sum_{m=1}^{N}\left(M_{aero}{}^m\right)\sin n\psi_m = M_{aero_{ns}} . \tag{G-9c}$$

The above equations express the flapping behaviour of an N bladed rotor in the rotating frame. The analysis is significantly more complicated if the coefficients A, B etc. or the aerodynamic moment contain periodic terms (as in forward flight), but this case will not be considered here and the reader is referred to Johnson [Johnson 1980].

Appendix H - Calculation of the Blade Modes

H1 Introduction

In this Appendix some equations will be introduced which will allow the natural frequencies and mode shapes of a rotating rotor blade to be determined. The analytical prediction of these, particularly of the flap bending modes can be very complicated. Therefore the emphasis will be on developing expressions which relate measured mode shapes and frequencies of the non-rotating blade to that of the rotating blade. The method by which these were determined will be discussed below. The theory and many of the results are discussed in depth by Bramwell [Bramwell 1976].

H2 Torsional Mode

Bramwell [Bramwell 1976] shows that the mode shape equations governing blade torsion in the form $\theta = A(r/R)T(t)$, which varies with span and time, is given by:

$$\frac{d}{dr}\left(E_S J \frac{dA}{dr}\right) + C(\omega_\theta^2 - \Omega^2)A = 0 \; ; \; \frac{d^2T}{dt^2} + \omega_\theta^2 T = 0. \qquad \text{(H-1)}$$

Where C the torsional moment of inertia per unit length, θ the angle of twist and $E_S J$ the torsional rigidity. The above Equation (H-1) is homogenous (R.H.S.=0) as the aerodynamic loading is assumed not to vary with span.

From Equation H-2 it can be seen that the torsional stiffness , the restoring moment part of the equation, is determined only by $E_S J$ and not influenced by the rotor speed. From this it follows that the associated mode shape and $\frac{d}{dr}\left(E_S J \frac{dA}{dr}\right)$must be constant with rotor speed. Hence $\omega_\theta^2 - \Omega^2 = \text{constant}$ for all rotor speeds. When the rotor speed is zero ω_θ must equal ω_0, the non-rotating torsional frequency. Thus the squared rotor speed and square of the non-rotating natural torsional frequency added together give the rotating natural frequency of torsion:

$$\omega_\theta^2 = \omega_0^2 + \Omega^2. \qquad \text{(H-2)}$$

H3 Flapping Mode

From first principles it is shown by Bramwell [Bramwell 1976] that the equation governing the flapwise bending of a rotating blade is given by

$$\frac{\partial^2}{\partial r^2}\left(EI\frac{\partial^2 Z}{\partial r^2}\right)-\frac{\partial}{\partial r}\left(G\frac{\partial Z}{\partial r}\right)+m(r)\frac{\partial^2 Z}{\partial t^2}=-\frac{\partial F(r)}{\partial r}, \tag{H-3}$$

where Z is the vertical blade deflection at a given radial station, EI the bending stiffness, m the mass distribution and F the blade loading. If the blade loading is neglected to find the equation governing the free motion $\frac{\partial F}{\partial r}$ can be set to zero. Let $Z = S(r)\phi(t)$ be a solution which satisfies the above equation, where the deflection Z is a function of the radial position and time. Substituting this into the above partial differential Equation (H-3) and then dividing by mS, gives the ordinary differential equation:

$$\frac{d^2}{dr^2}\left(EI\frac{d^2 S}{dr^2}\phi\right)-\frac{d}{dr}\left(G\frac{dS}{dr}\phi\right)=-m\frac{d^2}{dt^2}\phi S \tag{H-4}$$

$$\text{or } \frac{1}{mS}\frac{d^2}{dr^2}\left(EI\frac{d^2 S}{dr^2}\right)-\frac{1}{mS}\frac{d}{dr}\left(G\frac{dS}{dr}\right)=-\frac{d^2\phi}{dt^2}\frac{1}{\phi}. \tag{H-5}$$

Each side of the Equation (H-5) is a function of time or radial station alone and must therefore be equal to a constant, or they would not equate. Noting that $\phi(t)$ is a function of time, and assuming that time is measured in seconds the units of the required constant are $[s^{-2}]$. A convenient arbitrary constant would then be $\lambda^2\Omega^2$. Splitting both sides of the ordinary differential equation and setting each equal to the constant gives the following two equations:

$$\frac{d^2}{dr^2}\left(EI\frac{d^2 S}{dr^2}\right)-\frac{d}{dr}\left(G\frac{dS}{dr}\right)-mS\lambda^2\Omega^2=0\ ;\ \frac{d^2\phi}{dt^2}+\lambda^2\Omega^2\phi=0. \tag{H-6}$$

Solutions for the two factors of Z form the Equation (H-6), with appropriate boundary conditions for the mode shape S, need to be found. Even for the simplest case where a uniform distribution of stiffness and mass is assumed along the blade, a closed form solution does not exist. This is in contrast to a non-rotating beam where closed form solutions exist. There are many approximate numerical methods which allow the modes shapes $S_n(x)$ and associated mode frequencies $\lambda_n\Omega$ to be found and these are given in the literature [Bramwell 1976].

An interesting result of one of these methods, the Rayleigh-Ritz procedure [Temple 1956], is that it allows a relationship between the non-rotating blade natural frequency ω_0 and the rotating blade frequency ω_θ to be found as long as a reasonable mode shape for the non rotating blade is known. This was developed by Southwell [Southwell 1921] and the pertinent equations are given below, where α_i is found from the approximate non-rotating mode shape, assuming a constant mass distribution:

$$\omega_i = \lambda_i^2\Omega^2 = \omega_{nr}^2 + \alpha_i\Omega^2 \tag{H-7a}$$

$$\alpha_i = \int_0^1 (0.5 - 0.5x^2)\left(\frac{dS_i}{dx}\right)dx \Big/ \int_0^1 S_i^2 dx. \tag{H-7b}$$

This then gives a relationship between the rotating and non-rotating natural frequencies of the blade. Approximate mode shapes and α_i are given in the literature [Southwell 1921]. For the first rigid-blade mode of a pinned blade $S_1(x) = ax$ and α_1 equals unity. Remembering that for a rigid pinned beam with no external loading there is no natural frequency associated with pure rotation about the pin and thus ω_0^2 is zero. Thereafter the classical result for the coning resonance of a centrally hinged rotor is obtained:

$$\omega_\theta^2 = \alpha_i\Omega^2 = \Omega^2. \tag{H-8}$$

H4 Non-rotating Blade Frequencies and Mode shapes

The non-rotating natural blade frequencies were found experimentally, by mounting a small shaker near the root of the blade. A frequency sweep over a range of frequencies from 1 to 400 Hz was input into the shaker and the blade. The resulting blade response was examined using a strobe and lightweight metal pin. The pin could be lightly rested on the vibrating blade and used to find the nodal points and positions of maximum vibration. Using this technique the first two flapping and first torsional mode were found. The first flapping mode was found to be 11 Hz and the second at 61 Hz. The first torsional mode was found at 166Hz.

Closed form solutions for the natural frequencies f_i and mode shapes y_i of a cantilevered beam are given by Blevins [Blevins 1979]. The rigid hub arrangement of the rotor allowed the blade end restraint to be effectively modelled as a cantilever end, for which the first free solutions are:

$$\text{frequencies: } f_i = \frac{\lambda_i^2}{2\pi L^2}\left(\frac{EI}{m}\right)^{0.5};\ i = 1,2,3... \qquad \text{[H-9]}$$

$$\text{mode shapes: } y_i\left(\frac{x}{L}\right) = \cosh\frac{\lambda_i x}{L} - \cos\frac{\lambda_i x}{L} - \sigma_i\left(\sinh\frac{\lambda_i x}{L} - \sin\frac{\lambda_i x}{L}\right) \qquad \text{[H-10]}$$

$$\lambda_1 = 1.875, \lambda_1 = 4.694, \lambda_1 = 7.854\ ;\ \sigma_i = 0.734, \sigma_i = 0.1.018, \sigma_i = 0.999. \qquad \text{[H-11]}$$

The value of the blade stiffness and second moment of inertia EI were found by applying a tip load to the blade and measuring the tip deflection. Classical engineering beam theory gives the following relationship between tip deflection y, applied load P and EI as $y = -\frac{PL^3}{3EI}$, where L is the total beam length. The resultant value for EI was then found to be 14.13 Nm^2. This compares well with the value for EI approximated from material properties and geometry, of 16.2 Nm^2. The table below compares the first three experimental and analytical natural frequencies of the blade.

Mode	Exp. Freq. [Hz]	Analyt. Freq. [Hz]	Theoretical Mode Shape
1	11	10.3	$y_1\left(\frac{x}{L}\right) = \cosh 1.87\frac{x}{L} - \cos 1.87\frac{x}{L} - 0.73\left(\sinh 1.87\frac{x}{L} - \sin 1.87\frac{x}{L}\right)$
2	61	64.9	$y_1\left(\frac{x}{L}\right) = \cosh 4.69\frac{x}{L} - \cos 4.69\frac{x}{L} - 1\left(\sinh 4.69\frac{x}{L} - \sin 4.69\frac{x}{L}\right)$
3	-	181.9	$y_1\left(\frac{x}{L}\right) = \cosh 7.85\frac{x}{L} - \cos 7.85\frac{x}{L} - \left(\sinh 7.85\frac{x}{L} - \sin 7.85\frac{x}{L}\right)$

Table H-1 Experimental and Analytical Flap Modes for the Non-Rotating Blade

The good approximation between the experimental and analytical natural frequencies suggests that the analytical mode shapes can now be used in Southwell's formula to approximate the natural frequencies of the rotating blade. Equation (H-7b) is then integrated numerically using the mode above shapes. For the first three flapping modes α_i was found to be 1.19, 5.56 and 17.76 respectively. The table below summarises the non-rotating and rotating natural frequencies of the rotor blade at a rotor speed of 1200 rpm, using Equation (H-7b).

Mode	Non-Rot. Freq. (Exp.)	Non-Rot. Freq. (Anal.)	α_i	Rotating Freq@1200 rpm $\omega_i^2 = \omega_{nr}^2 + \alpha_i\Omega^2$
1st Flap.	11 Hz	10.3 Hz	1.19	24.4 Hz (exp.), 24.1 Hz(anal.)
2nd Flap	61 Hz	64.9 Hz	5.56	77 Hz (exp.), 80.2 Hz(anal.)
3rd Flap		181 Hz	17.76	199.5 Hz(anal)
1st Torsion	166 Hz	---	$\omega_\theta^2 = \omega_0^2 + \Omega^2$	167 Hz(exp.)

Table H-2 Rotating Natural Frequencies at 1200 rpm

The first flap mode is at about 24 Hz, which corresponds to the experimentally observed coning resonance frequency, and thus verifies the above analytical and numerical results. The modes shapes of the non-rotating beam are a good approximation to the mode shapes of the rotating beam.